Title

Ribbons, bridges, and microtubules: unraveling the structure of Giardia's spiraling ventral disc

Author

Hilton, Nicholas

Publication Date

2024

Peer reviewed|Thesis/dissertation

Ribbons, bridges, and microtubules: unraveling the structure of *Giardia*'s spiraling ventral disc

By

NICHOLAS ANTHONY HILTON
DISSERTATION

Submitted in partial satisfaction of the requirements for the degree of

DOCTOR OF PHILOSOPHY

in

Microbiology

in the

OFFICE OF GRADUATE STUDIES

of the

UNIVERSITY OF CALIFORNIA

DAVIS

Approved:

Scott C. Dawson, Chair

Sean Collins

Richard J. McKenney

Committee in Charge

2024

Dedication

I dedicate this work to my family.

Abstract

Cellular morphology plays a key role in cellular function, and cytoskeletal elements are key to defining and maintaining cell shape. Eukaryotic parasites of humans and other animals often possess unique microtubule (MT) organelles. Understanding how these distinctive cytoskeletal features are built and maintained may help us in our battle against these parasites. One source of MT organization is the Striated Fibers (SFs), filamentous structures often found in association with MTs and present across diverse eukaryotic clades. Notably, SFs possess the ability to self-assemble, which extends the possibility that these structures help drive cellular organization. Comprising SFs are a family of proteins called Striated Fiber Assemblins (SFAs).

Giardia lamblia is a protist parasite that utilizes a combination of MTs and SFAs to form a unique organelle called the ventral disc. *Giardia* colonizes the small intestine and causes diarrheal disease worldwide. Motile trophozoites attach to the extracellular surface of intestinal villi with the cup-shaped ventral disc. A current model of attachment proposes that a flexible disc modulates its dome shape to create a seal on the host cell surface. The base of the ventral disc is a highly ordered and complex spiral MT array. The microribbon-crossbridge (MR-CB) complex, a novel protein complex, binds to the disc MTs at regular intervals, almost completely coating all MT protofilaments. The three *Giardia* SFA homologs localize to the MRs; their role and the functional and structural roles of the MR-CB complex has remained unknown. During interphase, the disc is hyperstable and has limited MT dynamics, and it remains unclear how the *Giardia* SFAs, or other disc-associated proteins (DAPs) confer these properties.

To better understand SFAs through their evolutionary history, we have undertaken a phylogenetic analysis of this protein family, and describe three primary groups which we label Group I, Group II, and Group III. The presence of SFA homologs in the majority of flagellated supergroup lineages implies that SFA homologs were present in the last universal common

ancestor and subsequently lost in several linages. SFA structure is highly conserved among excavates, which may indicate that the role of SFAs in this clade is also conserved.

To investigate mechanisms of disc MT hyperstability, we screened 14 CRISPRi-mediated DAP knockdown (KD) strains for defects in hyperstability and MT dynamics, and identified two strains – DAP5188KD and DAP6751KD – with discs that dissociate following high-salt fractionation. Discs in the DAP5188KD strain were also sensitive to treatment with the MT-polymerization inhibitor nocodazole. Thus, we confirm that at least two of the known DAPs confer hyperstable properties to the disc MTs.

Additionally, we show that SFAs in the MR-CB complex play a role in maintaining disc spiral structure and stabilizing disc conformation required for parasite attachment. We create stable CRISPR knockouts (KO) of the three MR SFA proteins – beta-giardin, delta-giardin, and SALP1 – and evaluate mutant disc structure and function with light microscopy and biophysical attachment assays. Functional studies of the MR-CB complex have been hampered by the small number of known MR-CB proteins. Therefore, we conducted a co-immunoprecipitation assay on beta-giardin and delta-giardin to identify MR-CB candidate proteins. We localized these candidates using fluorescent tags and targeted them with CRISPRi KD and CRISPR KO. A protein called 15376 is potentially a new MR protein. Understanding the MR-CB complex will shed light on the disc as a whole and guides us towards key insights into how the disc functions during attachment. This work also contributes to our knowledge of how cells construct and maintain complex MT organelles and helps to define the role of SFAs in complex MT structures.

Acknowledgements

Thank you to Scott, for guiding me scientifically, supporting me, and opening a door to the fascinating world of *Giardia*. Thank you to the members of the Dawson lab, especially Kari, for their advice, their help, and the many conversations shared in lab, both scientific and not. Thank you to the Microbiology Graduate Group for administrative support. Thank you to the Molecular and Cellular Biology T32 grant, for training, career advice, and financial support.

Table of Contents

Chapter 1

The Striated Fiber Assemblin family organizes the cytoskeleton of numerous protist organisms; a phylogenetic analysis illustrates the wide spread of this protein family and confirms their consistent coiled-coil rod structure

Nicholas Hilton and Scott C. Dawson

Abstract

Cellular morphology plays a key role in cellular function, and cytoskeletal elements are key to defining and maintaining cell shape. Eukaryotic parasites of humans and other animals often possess unique microtubule (MT) organelles, such as the subpellicular MTs of *Plasmodium* and *Trypanosoma*, the conoid of *Toxoplasma*, or the ventral disc of *Giardia*. Understanding how these distinctive cytoskeletal features are built and maintained may help us in our battle against these parasites. One potential source of MT organization is the Striated Fibers (SFs), filamentous structures often found in association with MTs. Similar to MTs, SFs are present across diverse eukaryotic clades, such as: green algae, ciliates, and metamonads. In some species where SFs have been studied, they provide a physical support network, organizing or bracing other cellular elements. Notably, SFs possess the ability to self-assemble, which extends the possibility that these structures help drive cellular organization.

Comprising SFs are a family of proteins called Striated Fiber Assemblins (SFAs). Similarly to SFs themselves, SFAs are present in diverse eukaryotic lineages, although SFAs are absent from plants, animals, and fungi. To better understand SFAs through their evolutionary history, we have undertaken a phylogenetic analysis of this protein family using homologs from diverse flagellated protists. In this work, we find that the overall structure of the SFA gene family is described by three primary groups which we label Group I, Group II, and Group III. Each primary group is then further subcategorized into subgroupings according to support for each clade, and most subgroupings were defined by sequences associated with one eukaryotic phylum. The presence of SFA homologs in the majority of flagellated supergroup lineages implies that SFA homologs were present in the last universal common ancestor and subsequently lost in several linages.

Additionally, I examine the structure and conservation of excavate SFAs in detail, based on our SFA multiple sequence alignment. The key to SFA function may lie in its protein

structure: a series of coiled-coil heptad repeats, out of which groups of four heptads (28 amino acids) are broken up by a skip residue (number 29). These repeating coiled-coils form a C-terminal rod domain, while the remaining protein sequence forms an unorganized head domain at the N-terminus. SFA structure is highly conserved among excavates, which may indicate that the role of SFAs in this clade is also conserved. This structural characterization is foundational toward understanding the underpinning mechanisms of SFA function and SF formation, and will aid in defining roles for the head and tail domains in various branches of the SFA family.

Striated Fibers were first described as being in close association with MTs, and SFAs possess the ability to self-associate into filamentous structures. It is possible that this family of proteins is a key element driving cytoskeletal architecture in protist organisms. Our understanding of how the cytoskeletal architecture is formed in protists is formed and maintained may be deepened with further study of this protein family.

Introduction

Cellular morphology plays a key role in cellular function, and cytoskeletal elements are key to defining and maintaining cell shape. Much study has been devoted to microtubules and actin filaments, two key types of structural proteins found in a wide variety of eukaryotic species. Furthermore, eukaryotic parasites of humans and other animals often possess unique microtubule organelles, such as the subpellicular microtubules of *Plasmodium* and *Trypanosoma*, the conoid of *Toxoplasma*, or the ventral disc of *Giardia*[1,2]. Understanding how these distinctive cytoskeletal features are built and maintained may help us in our battle against these parasites. Generally, microtubule organization is thought to be driven by microtubule associated proteins, post-translational modifications, or a combination of both[2].

One potential source of microtubule organization, as well as cytoskeletal morphology in general, is the Striated Fibers (SFs) (also called Striated Microtubule Associated Fibers), filamentous structures often found in association with microtubules[3]. Similar to microtubules, Striated Fibers are present across diverse eukaryotic clades; green algae[3] (where they are also known as system I fibers), ciliates[4] (kinetodesmal fibers), metamonads[5], and other flagellated protists[6]. The presence of Striated Fiber structures across a diversity of species suggests an ancient origin, and perhaps a presence in an early eukaryotic ancestor. In some species where Striated Fibers have been studied, they provide a physical support network, organizing or bracing other cellular elements[3,4,6,7]. Notably, known Striated Fibers possess the ability to self-assemble[3,8,9], which extends the possibility that these structures help drive cellular organization[10].

To better understand the mechanisms behind Striated Fiber activity, we can examine the proteins that comprise these fibers. The first SF-assemblin component identified as such was in the green alga *Spermatozopsis similis*, and was named Striated Fiber Assemblin (SFA) after its ability to self-assemble[3]. Similarly to Striated Fibers themselves, SFA homologs are present in diverse eukaryotic lineages, although they are notably absent from plants, animals, and fungi[10,11]. In *Spermatozopsis* and other green alga, such as *Chlamydomonas reinhardtii*, SFA is associated with the flagellar root microtubules[12], which help organize the flagella and coordinate the cytoskeleton during mitosis[13]. The amino acid sequence of Striated Fiber Assemblin is primarily comprised of a series of heptad repeats, out of which groups of four heptads (28 amino acids) are broken up by a skip residue (number 29). These repeating heptad tetrads form a coiled-coil rod domain[12]. The remaining SFA sequence forms an unorganized head domain at the N-terminus[12]. A rod domain consisting of heptad repeats lacking skip residues is modeled to contain a twisting hydrophobic seam, requiring supercoiling to maintain consistent hydrophobic contacts[14]. In contrast, SFA's pattern of four heptads, followed by a skip residue is theorized to

disrupt the coil's hydrophobic seam, and preventing supercoiling[14]. In *Spermatozopsis* and *Chlamydomonas*, the skip residue is usually glutamate[14]. Additionally, there is structural similarity amongst SFA homologs from different eukaryotic clades, but also extensive sequence divergence[15,16].

Further structural analysis on Striated Fiber Assemblin examined protein extracted from *Chlamydomonas*, and the ability to self-assemble *in vitro* into Striated Fibers when subjected to various residue manipulations and deletions[9]. Deletion of either the N-terminal unstructured head domain or the third and fourth heptad tetrads prevented proper fiber formation[9], leading the authors to propose a mechanism of assembly whereby the adjacent SFA head and coil domains interact with each other. Alteration or removal of the skip residues did not prevent fiber formation[9], but was thought to alter the coiling properties[14].

Striated Fibers in the ciliate *Tetrahymena thermophila*, also called kinetodesmal fibers in this organism, are necessary for proper cytoskeletal organization by providing physical bracing against the forces of ciliary beating[4]. The *Tetrahymena* exterior is coated with highly organized rows of cilia, each of which connect to a basal body sitting just below the cell's surface[17,18]. This basal body network is connected by striated fibers[17,18]. *Tetrahymena* also possesses ten SFA homologs, one of which is named DisAp[4,10]. DisAp is necessary for proper spacing of the basal body array. When a mutated, nonfunctional, form of DisAp is expressed, cells develop a disorganized array when exposed to elevated temperatures[4,10]. Cells with disorganized arrays were able to recover array organization when complemented with wild-type DisAp[10], suggesting that the self-assembly property of SFA homologs might drive cytoskeletal organization in some organisms. The Striated Fibers in *Tetrahymena* are also dynamic in length and respond to increased or decreased ciliary beat force[10].

Seventy-two SFAs have also been identified in the ciliate *Paramecium tetraurelia*[6,10]. Possessing a similar cellular body plan to *Tetrahymena*, *Paramecium* SFAs play an important

role in maintaining proper ciliary organization with support via the kinetodesmal fibers. Knockdown cell lines targeting various SFAs result in similar mutant phenotypes to the *Tetrahymena* studies, with a disorganized ciliary array and inhibited swimming pattern[6], highlighting the importance of the SFA family of proteins to the ciliate phylum.

SFA homologs can also be found in the early-branching eukaryote *Giardia lamblia*[5,16,19]. *Giardia* is a parasitic protist that infects humans and other mammals[20]. The lifecycle of this organism consists of an environmentally resistant cyst that gets ingested by a host via the fecal-oral pathway and excysts into a trophozoite form upon reaching the small intestine[20]. The *Giardia* trophozoite has a teardrop-shaped cell body, eight flagella, two nuclei, and a novel microtubule organelle, the ventral disc, which is thought to be essential for attachment[20]. The ventral disc is a spiral of roughly 100 parallel microtubules that spiral clockwise. Disc MTs scaffold a dense protein complex called the Microribbon-Crossbridge (MR-CB) complex, that extends dorsally above the MT spiral[21]. *Giardia* has three SFA homologs, termed beta-giardin, delta-giardin, and SALP1[16,19]. All SFAs localize to the Microribbon-Crossbridge complex of the disc.

The role of the SFA homologs In *Giardia*, and the MR-CB complex in general, is less clear. Nonetheless, beta-giardin, delta-giardin, and SALP1 are proposed to polymerize into the initial MR complex that enables other MR-associated proteins to later assemble into the MR-CB complex[22]. Aside from the three SFA homologs, only one other protein, gamma-giardin, is known to be part of the microribbons[23]. There are currently no confirmed Crossbridge proteins. Yet it is presumed that there are additional proteins associated within the MR structure, as well as microtubule-binding proteins that connect the MRs with the ventral disc MT spiral.

Striated Fiber Assemblin homologs are present in apicomplexan parasites as well[24]. In the parasite *Toxoplasma gondii*, SFA homologs are only expressed during cell division, and are an essential element of the cell division cycle[25]. In *Toxoplasma*, SFA homologs form fibers that

connect the apical ends of the developing daughter cells with the microtubule organizing center in the parent cell[25]. Knockout mutant parasites lacking either TgSFA2 or TgSFA3 (two *Toxoplasma* SFA homologs) can successfully undergo mitosis but fail to complete cellular division[25]. Notably, the microtubule organizing center in apicomplexans is thought to be orthologous to the microtubule rootlet assembly in green algae[25], which is associated with Striated Fiber Assemblin as described above.

SFA homologs were identified in *Trichomonas vaginalis and T. gallinarum*[7]. Proteomic analysis found these proteins to be in association with extracted *T. gallinarum* cytoskeletons, and tagging performed in *T. vaginalis* found some to localize to filamentous cytoskeletal elements[7].

To better define the evolutionary history of Striated Fiber Assemblins, we have undertaken a phylogenetic analysis of this protein family using homologs from diverse flagellated protists. While SFAs are present in a wide array of eukaryotes, their function has been characterized in only a handful of organisms as described above. Additionally, I examine the structure and conservation of excavate SFAs in detail, based on our SFA multiple sequence alignment. This structural characterization is foundational toward understanding the underpinning mechanisms of SFA function and will aid in defining roles for the head and tail domains in various branches of the SFA family.

Results

The SF-assemblin gene family is divided into three primary groups

The overall structure of the SF-assemblin paralogous gene family is described by three primary groups which we label Group I (A,B), Group II (A-J), and Group III (A-F) SF-assemblins (Figure

1.1). Each primary group is subcategorized into subgroupings according to support for each clade (e.g., Group II-A). Group I-A includes the first characterized SFA protein, from *C. reinhardtii*[9]. All SF-assemblin homologs derive from five eukaryotic supergroups that include flagellated morphotypes. SF-assemblins homologs have been lost, however, in multicellular plants, fungi, metazoans, and red algae that have flagellated forms. Notably, genomes of four Rhizarian species each have one SFA homolog, yet no flagellated stage has been documented. There is additional evidence, however of flagellated forms in Rhizaria based on a full complement of flagellar assembly proteins in this phylum (PMID: 24332546).

Most SFA subfamily groupings were defined by one phylum

To define modes of SFA evolution within subfamilies, we compared the composition of each subfamily with respect to species- and phylum-level affiliations. Each flagellated species ranged from having one SFA homolog (e.g., *C. reinhardtii*) to over 70 homologs (*Paramecium tetraurelia)*. Paralogous SFAs in the same species were present in one to four SFA subfamilies. Most subgroupings were defined by sequences associated with one eukaryotic phylum. Two exceptions are Group IID which is composed of SFA homologs from three supergroups, and Groups IA and B, Groups IIE and IIJ, and Group IIIE which are comprised of SFAs from two supergroups (see Table 1.1). Ciliates, stramenopiles, dinoflagellates, and alveolates include homologs in five or six subfamilies and excavate SFA homologs are represented in five subfamilies.

Excavate SFA proteins are structurally conserved

To connect SFA protein structure with subgroup clustering, we performed a structural prediction analysis and annotation of the excavate SFA proteins based on the above alignment (Figure 1.2). Excavate proteins were present in the five subgroups II-A, II-B, II-C, II-E, and II-G. All proteins were analyzed in the context of prior work[15,19], and were found to follow the repeating

coiled-coil heptad pattern broken by skip residues every four heptads described in those papers. All excavate SFAs had either 7 or 8 full heptad tetrads, and skip residues were glutamate in the majority of sequences (Figure 1.3). Proteins which were out of alignment with the rest of the group were not included when describing general group structure (Figure 1.4A). AlphaFold software protein prediction models were also employed when available to predict SFA and compare structures (Figure 1.5).

Groups II-A and II-B SFAs have seven or eight full tetrads, with a three heptad remainder at C terminus

Beta-giardin, a *Giardia* protein belonging to group II-B, was among the first characterized SFAs[19]. Beta-giardin was described as consisting of a 19 residue N terminal, unstructured head domain, and eight full coiled-coil heptad tetrads, followed by three coiled-coil heptads (Figure 1.4A). Later work by Lechtreck[9,15] described the beta-giardin head domain as 27 amino acids long, reducing the first tetrad to a triple heptad. However, functional work found that deletion of the first 19 residues was enough to disrupt self-assembly[9]. Analysis of delta-giardin revealed a 31 residue head domain, and seven complete coiled coil tetrads. The final *Giardia* SFA, SALP1, was similar in structure, with a 30 residue head domain and seven complete tetrads. Delta-giardin and SALP1 lack a hydrophobic residue at the at the alignment site where beta-giardin begins its initial three heptads (Figure 1.4A). The remaining II-B proteins aligned with the delta-giardin template, lacking hydrophobic residues were beta-giardin has one, and have head domains of 24 to 57 residues long (Figure 1.4A).

In general, Group II-A SFAs were longer in sequence than Group II-B SFAs, and had variable length for head domains, ranging from 26 to 98 amino acids. All Group II-A SFAs had seven full tetrads, with an initial 3 heptads, and C-terminal three heptads (Figure 1.4A). Groups II-A and II-B were more similar in sequence than to other excavate SFA subgroups (Figure 1.4A).

Groups II-C, II-E, II-G had reciprocal 18 residue gaps out of alignment with Groups II-A and II-B

Groups II-C, II-E, and II-G were more similar to each other than the remaining two excavate SFA groups. In particular, II-C, II-E, and II-G had an 18 residue gap 10 residues into the seventh tetrad (Figure 1.4B). This gap was not aligned with any heptad or tetrad, and corresponded to an identical gap seven residues into the first tetrad of Groups II-A and II-B (Figure 1.4B). The middle four tetrads aligned for all excavate groups.

Groups II-C, II-E, II-G have eight full tetrads and variable head domain sizes

The C-termini of proteins in Groups II-C, II-E, and II-G have four full heptads after the final skip residue (Figure 1.4A). Coiled coil tetrads in these three groups were immediately preceded by head domains, without a three heptad insertion (Figure 1.4A). There was striking variation of head domain length within Groups II-C and II-E, with head domains ranging from 16 – 62 residues and from 21 – 61 residues, respectively (Figure 1.4A). Group II-G SFA head domains were consistently smaller, ranging from 15 – 26 amino acids in length (Figure 1.4A).

AlphaFold predictions of SFA structure show consistency across clades

Protein structure predictions were accessed from the AlphaFold Protein Structure Database (https://alphafold.ebi.ac.uk/). Example SFAs from green algae (Figure 1.5A), excavates (Figure 1.5B), and apicomplexans (Figure 1.5C) were accessed to gauge the consistency of structural predictions. AlphaFold predicted a short, unstructured, N-terminal head domain in all example SFA, with the exception of *Spironucleus salmonicida* SF-assemblin (Figure 1.5B). AlphaFold also predicted a highly-coiled tail region comprising most of the amino acid length in all example SFAs.

Discussion

The presence of SFA homologs in the majority of flagellated supergroup lineages implies that SFA homologs were present in the last universal common ancestor and subsequently lost in several linages including the Opistokonts. Subsequently, inherited SFA homologs from each eukaryotic phylum duplicated and diverged independently, resulting in new subfamilies of SFAs. In other words, SFA duplication is lineage-specific, with SFA evolution mirroring the evolution of flagellated species.

SFA functional divergence is also associated with specific subfamilies. Although the majority of SFA functions have not been described for the SFA homologs in our phylogeny, multiple functions have been determined for SFAs in *Giardia* (excavates), *Chlamydomonas* (chlorophytes), multiple ciliates, and apicomplexans (SAR). In *Giardia* and the ciliates *Tetrahymena* and *Paramecium*, SFAs are responsible for supporting and organizing structures such as the ventral disc (*Giardia*) (see Chapter 3) and the ciliary array[4,6,10] (*Tetrahymena* and *Paramecium*). To contrast, SFAs in *Chylamydomonas* and the apicomplexan *Toxoplasma* are involved with cytoskeletal organization during mitosis[12,13,25].

SF-assemblin structure is highly conserved among excavates, despite sequence divergence (Figure 1.4A). Among the excavates, only *Giardia*'s SFA homologs have been functionally characterized to have roles in assembling and maintaining the fiber-like microribbons in the ventral disc[8,19,26] (see Chapter 3). However, perhaps the conserved sequence and structures of excavate SFAs indicates that the role of SFAs in this clade is also conserved. One divergence that we noticed among our alignment is that some excavate subgroups were shifted relative to each other, meaning that coil tetrads 2 – 5 in groups II-A and II-B aligned with coil tetrads 3 – 6 in groups II-C, II-E, and II-G (Figure 1.4B). This misalignment was 18 residues long, which does not correspond to either a full tetrad (28 residues), or a whole multiple of a coil heptad. Additionally, the site at which the shift occurred did not line up with a

full tetrad or whole multiple of a heptad. Therefore, we do not see this shift as the site of an insertion or deletion of tetrad or heptad repeats, but rather a reflection of sequence divergence among the subgroups that may have functional consequences.

SFA head domain sizes among the excavate SFAs were also maintained in a fairly consistent range, with the exception of group II-G head domains being smaller. In general, heads ranged from 15 – 98 residues long, for proteins with an average length of roughly 275, that would put heads at approximately 5% – 33% of the total length. It is unknown whether the size of the head domain has an impact on the possible mechanisms of fiber assembly or head-tail interaction as described by Lechtreck[9].

Striated Fibers were first described as being in close association with microtubules[3], and SFAs possess the ability to self-associate into filamentous structures[8,9]. It is possible that this family of proteins is a key element driving cytoskeletal architecture in protist organisms. Many cytoskeletal structures uniquely found in protists are comprised of SFAs[4,5,7], and our understanding of how these structures are formed and maintained may be deepened with further study of this protein family.

Materials and Methods

Creation of the SFA phylogenic tree

The multiple sequence alignment of 531 SF-assemblin (SFA) homologs was created using the MUSCLE software package (https://doi.org/10.1186/1471-2105-5-113). For some taxa (e.g., *Paramecium tetraurelia*) only one example of an SFA homolog was included when it had 100% amino acid identity to another homolog within the same species.

Phylogenetic trees were inferred using RaxML with bootstrapping and the PROT+IG amino acid substitution model that includes invariant positions and a gamma distribution (https://doi.org/10.1093/bioinformatics/btu033).

Analysis of excavate SFA head and tail domains

Jalview software (jalview.org) was used to align and visualize the excavate SFAs according to amino acid similarity. Previous annotations of beta-giardin head domain and the skip residues of its tail domain[15,19] were used as a template for annotating the other excavate SFAs. Tail domains were identified by the presence of a preferentially glutamate[14] skip residue every 28 amino acids (heptad tetrad), as well as amino acids with a hydrophobic side chain at the *a* and *d* positions of the *abcdefg* heptad repeat needed to form coiled coils[27]. Head domains were defined as the N-terminal region not belonging to the tail domain. AlphaFold predictions of SFA structure were retrieved from the AlphaFold Protein Structure Database (https://alphafold.ebi.ac.uk/).

Acknowledgements

This work was supported by an R01AI077571 award to SCD.

Figures

Figure 1.1. SF-assemblin subfamilies are present in most flagellated eukaryotic lineages

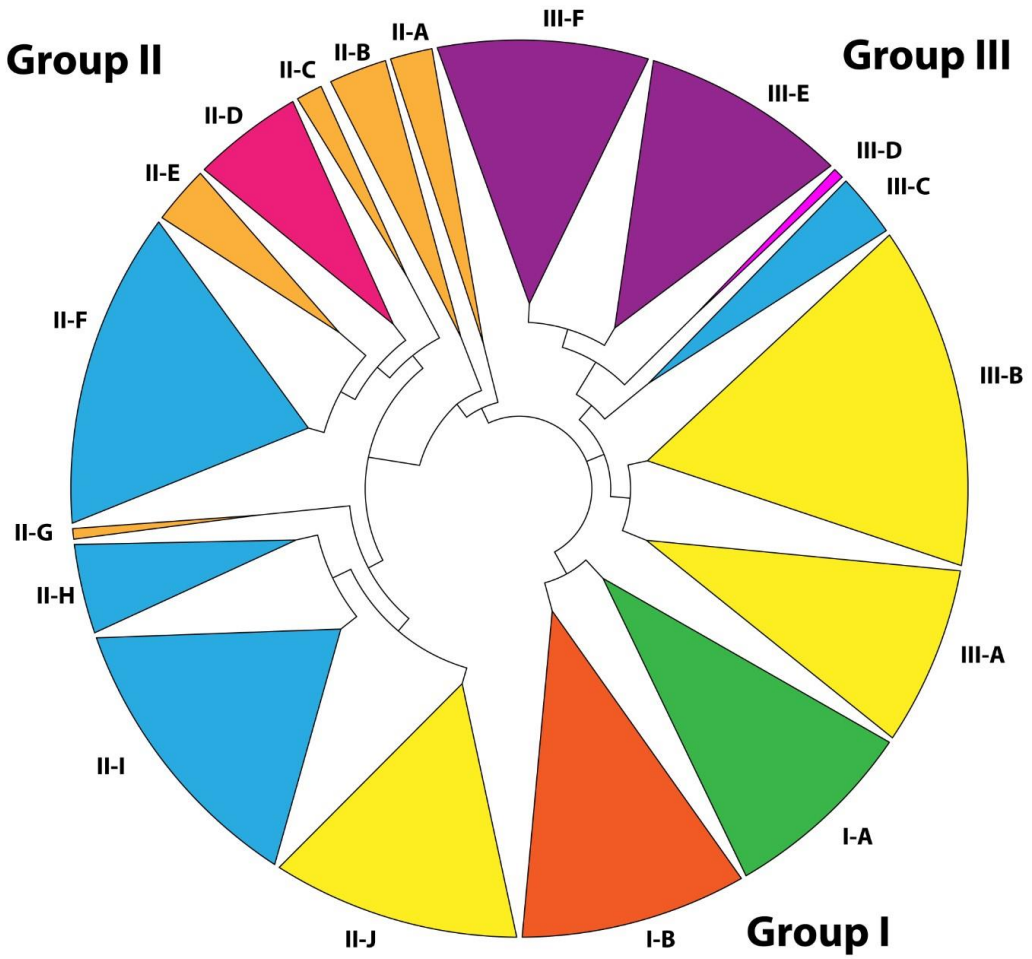

Schematic SFA phylogenetic tree showing primary SFA groupings and subfamilies. SFA subfamilies are named and homologs are color-coded according to supergroup affiliation (Excavates = orange; Chlorophytes = green; Cryptophytes and Haptophytes = red; Stramenopiles = purple; Rhizarians = pink; Ciliates = teal; Alveolates (free-living, parasitic apicomplexans, and dinoflagellates = yellow).

Figure 1.2: Excavate SFA homologs are comprised of five different subfamilies

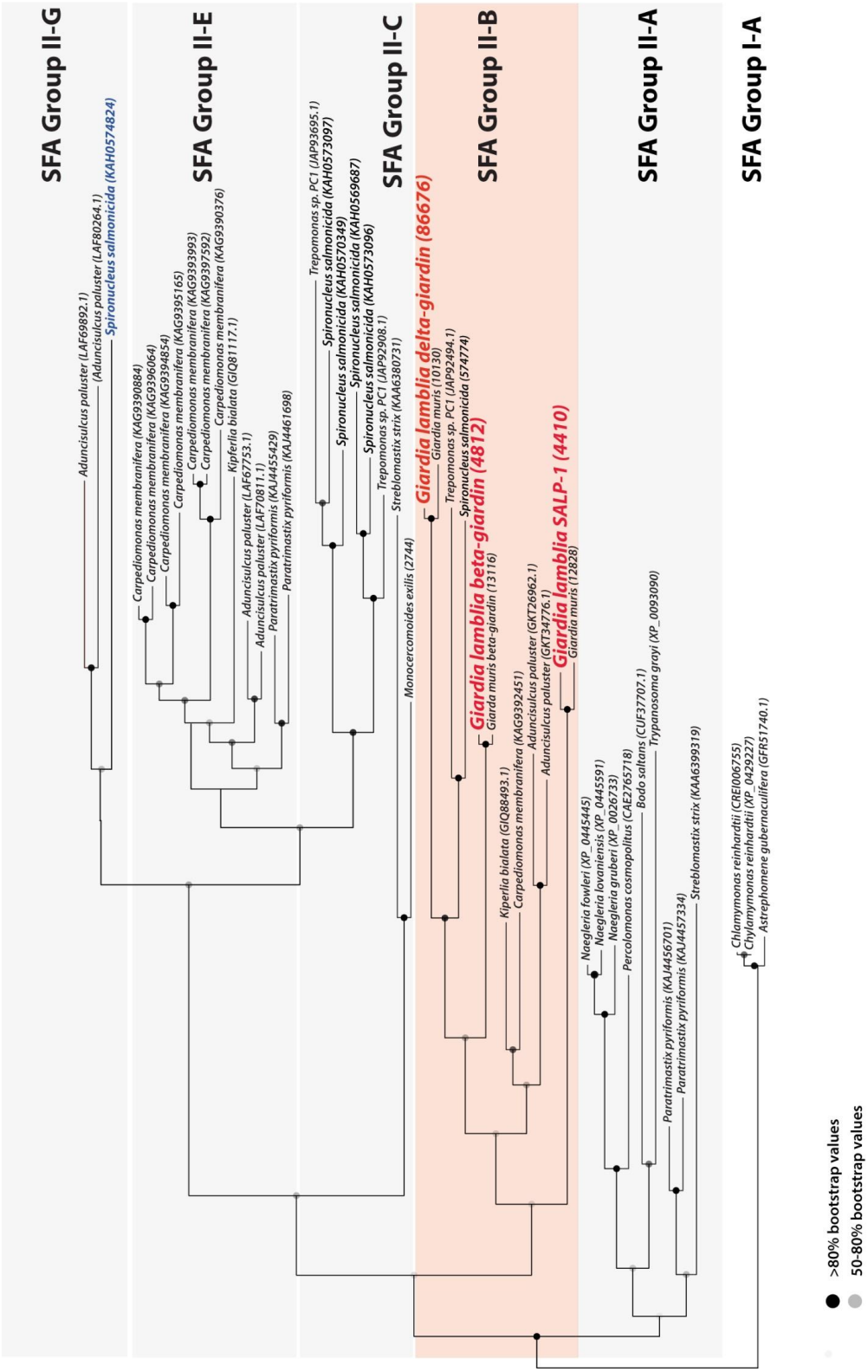

Consensus bootstrapped RAxML (PROTI+G) phylogenetic subtree of SFA homologs in excavates. *Giardia* SFA homologs (SFA-Group II-B) are highlighted in red. Black filled circles indicate nodes with bootstrap support > 80% and gray circles 50-80% support.

Figure 1.3: Jalview annotation highlights consistent skip pattern across excavate SFAs

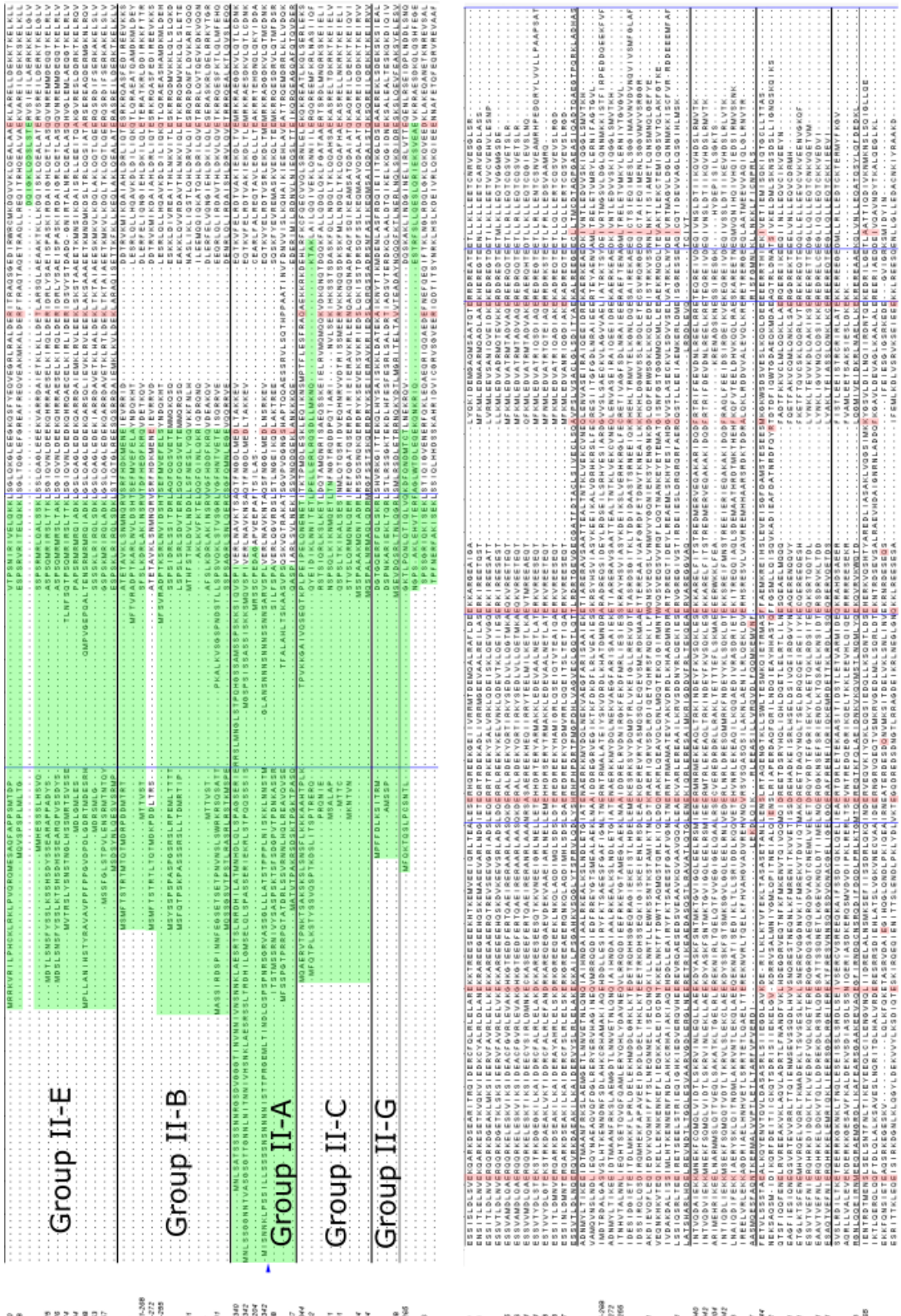

Excavate SFAs are aligned in Jalview and displayed on two rows. Head domains are highlighted in green and skip residues in red. Tail domain tetrads comprise all unhighlighted sequence until the final skip residue. Head domains were determined by the absence of a hydrophobic residue at the *a* site of an *abcdefg* heptad repeat necessary to form a coiled-coil. Head domains from other proteins in the same subgroup also affected head domain annotation.

Figure 1.4: Excavate SFAs are structurally conserved

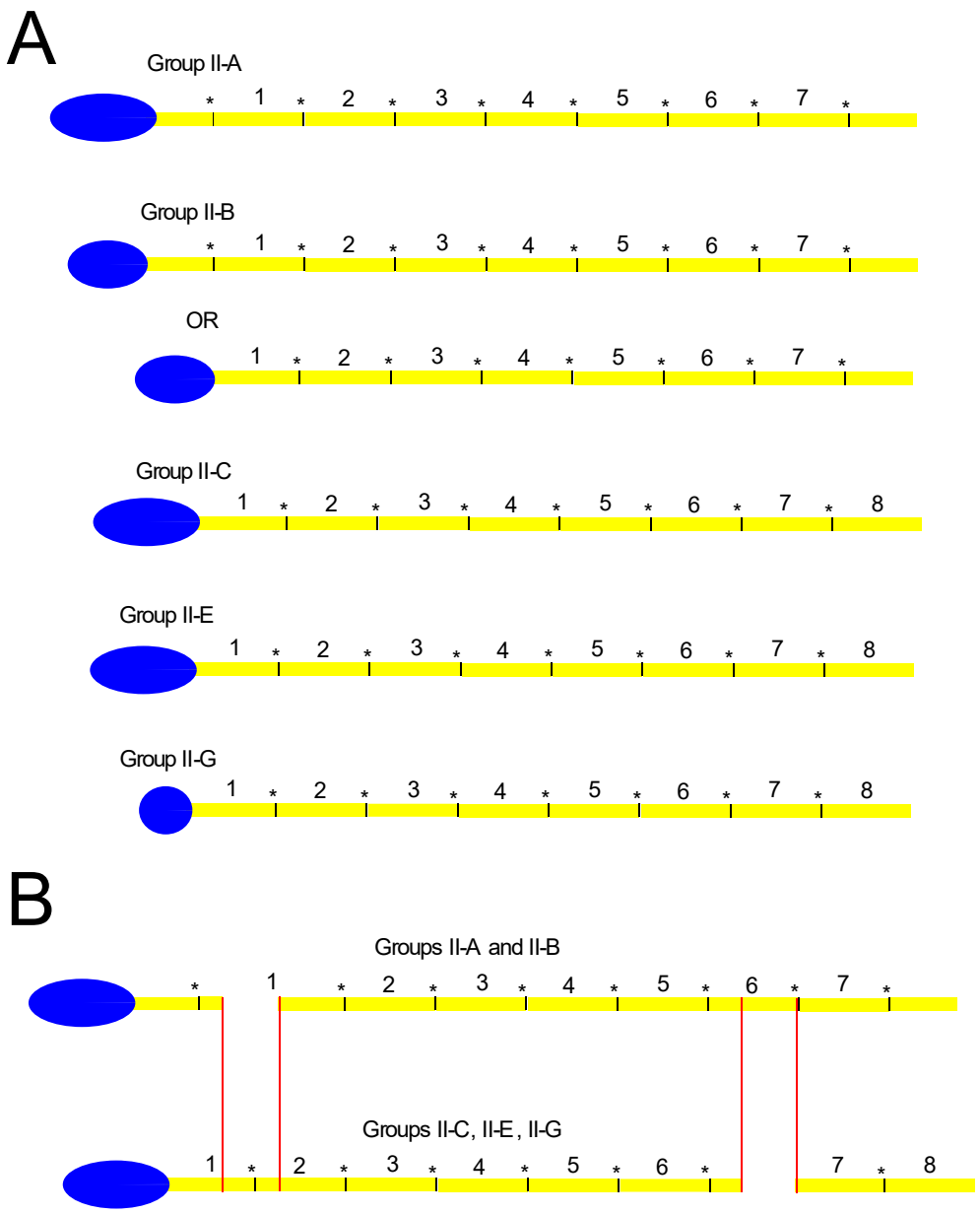

Schematic representation of excavate SFA domains. Head domains are in blue, rod domains are in yellow, and skip residues are represented by stars. Numbers indicate full heptad tetrad repeats. A) Structure of the excavate subgroup SFAs. All proteins have seven or eight full tetrad repeats, with varying head domain sizes. B) Groups II-A and II-B are shifted in their alignment with respect to Groups II-C, II-E, and II-G. Despite this alignment shift, both have similar

numbers of tetrad repeats, and the shift is not aligned with any tetrad, nor to any heptad within the heptad repeats.

Figure 1.5: AlphaFold predictions of SFA structure show similarity across different clades

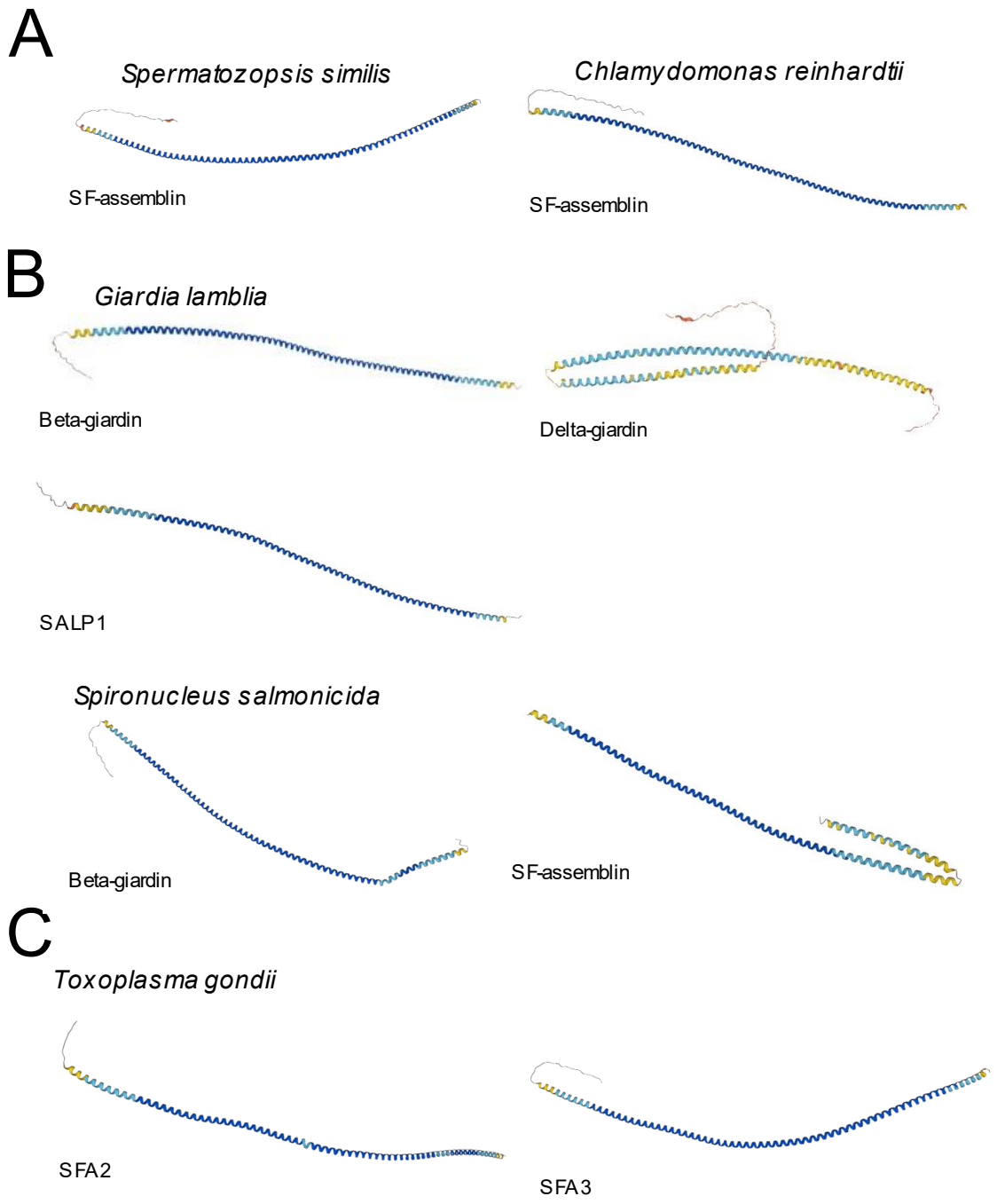

All structures were accessed from the from the AlphaFold Protein Structure Database (https://alphafold.ebi.ac.uk/). N-termini are displayed facing the left. For all SFAs except *Spironucleus* SF-assemblin, an unorganized head domain and coiled-coil rod domain of varying

lengths can be seen. Sample SFAs were drawn from green algae (A), excavates (B), and apicomplexans (C).

Table 1.1: SFA homologs used in phylogenetic analyses

Name	Group	Annotation	Species	Phylum
GFR51740.1	I-A	hypothetical_protein_Agub_g14186	Astrephomene_gubernaculifera	green_algae
CREI006755	I-A	CHLREDRAFT_127995	Chlamydomonas_reinhardtii	green_algae
XP_0429227	I-A	uncharacterized_protein_CHLRE_07g332950v5	Chlamydomonas_reinhardtii	green_algae
KAG1659271	I-A	hypothetical_protein_FOA52_008200	Chlamydomonas_sp._UWO_241	green_algae
KAG1677714	I-A	hypothetical_protein_FOA52_001026	Chlamydomonas_sp._UWO_241	green_algae
QDZ20397.1	I-A	SF-assemblin	Chloropicon_primus	green_algae
CAE3220305	I-A	unnamed_protein_product	Crustomastix_stigmatica	green_algae
KAF5831378	I-A	SF-assemblin_	Dunaliella_salina	green_algae
KAG2496805	I-A	hypothetical_protein_HYH03005212	Edaphochlamys_debaryana	green_algae
CAE5738847	I-A	unnamed_protein_product	Gloeochaete_wittrockiana	glaucocystophyte
KXZ45510.1	I-A	SFA_protein	Gonium_pectorale	green_algae
KFLA012908	I-A	kfl00570_0060_v1.1	Klebsormidium_flaccidum	green_algae
GAQ89864.1	I-A	hypothetical_protein_KFL_005700060	Klebsormidium_nitens	green_algae
CAE3381486	I-A	unnamed_protein_product	Micromonas_polaris	green_algae
CAD8515439	I-A	unnamed_protein_product	Micromonas_pusilla	green_algae
XP_0030577	I-A	predicted_protein	Micromonas_pusilla_CCMP1545	green_algae
MSPE000217	I-A	27396808_peptide_e_gw2.02.1017.1	Micromonas_species_RCC299	green_algae
MNEG010466	I-A	XP013900702.1	Monoraphidium_neglectum	green_algae
XP_0139007	I-A	SF-assemblin	Monoraphidium_neglectum	green_algae
CAF8252423	I-A	unnamed_protein_product	Nephroselmis_pyriformis	green_algae
OLUC007298	I-A	OSTLU_12738	Ostreococcus_lucimarinus_CCE9901	green_algae
CAD8579671	I-A	unnamed_protein_product	Ostreococcus_mediterraneus	green_algae
XP_0030804	I-A	SF-assemblin_	Ostreococcus_tauri	green_algae
CAG9460187	I-A	unnamed_protein_product	Pedinophyceae_sp._YPF-701	green_algae
CAE3157082	I-A	unnamed_protein_product	Prasinococcus_capsulatus	green_algae
CAE8057048	I-A	unnamed_protein_product	Pyramimonas_parkeae	green_algae
CAE8057050	I-A	unnamed_protein_product	Pyramimonas_parkeae	green_algae
GBF88940.1	I-A	SF-assemblin	Raphidocelis_subcapitata	green_algae
KAF6256136	I-A	SF-assemblin	Scenedesmus_sp._NREL_46B-D3	green_algae
KAF8061372	I-A	SF-assemblin	Scenedesmus_sp._PABB004	green_algae
P55925.1	I-A	SF-assemblin	Spermatozopsis_similis	green_algae
KAA6419680	I-A	striated_fiber_assemblin_	Trebouxia_sp._A1-2	green_algae
CAF7616551	I-A	unnamed_protein_product	uncultured_Micromonas	green_algae
CAF8479511	I-A	unnamed_protein_product	uncultured_Micromonas	green_algae
CAI0158030	I-A	unnamed_protein_product	uncultured_Micromonas	green_algae
CAI0310370	I-A	unnamed_protein_product	uncultured_Pyramimonadales	green_algae
CAF8361446	I-A	unnamed_protein_product	uncultured_Pyramimonas	green_algae
XP_0029589	I-A	SF-assemblin	Volvox_carteri_f._nagariensis	green_algae
CAE2616266	I-B	unnamed_protein_product	Chromera_velia	alveolate
CAH9751524	I-B	unnamed_protein_product	Chroomonas_cf._mesostigmatica	cryptophyte
CAE2408916	I-B	unnamed_protein_product	Chrysochromulina_rotalis	haptophyte
CAE3639370	I-B	unnamed_protein_product	Chrysoculter_rhomboideus	haptophyte
CAD8615716	I-B	unnamed_protein_product	Coccolithus_braarudii	haptophyte
CAD8634562	I-B	unnamed_protein_product	Cryptomonas_curvata	cryptophyte
CAD8268230	I-B	unnamed_protein_product	Diacronema_lutheri	haptophyte
KAG8458125	I-B	hypothetical_protein_KFE25_011656	Diacronema_lutheri	haptophyte
EHUX002750	I-B	EMIHUDRAFT_234082	Emiliania_huxleyi_CCMP1516	haptophyte
XP_0057815	I-B	hypothetical_protein_EMIHUDRAFT_234082	Emiliania_huxleyi_CCMP1516	haptophyte
CAD8498346	I-B	unnamed_protein_product	Hanusia_phi	cryptophyte
CAD8739285	I-B	unnamed_protein_product	Hemiselmis_andersenii	cryptophyte
CAE3467433	I-B	unnamed_protein_product	Hemiselmis_andersenii	cryptophyte
CAE3915042	I-B	unnamed_protein_product	Hemiselmis_virescens	cryptophyte
CAE5826815	I-B	unnamed_protein_product	Isochrysis_galbana	haptophyte
CAE5826816	I-B	unnamed_protein_product	Isochrysis_galbana	haptophyte
CAE5826817	I-B	unnamed_protein_product	Isochrysis_galbana	haptophyte
CAE5850507	I-B	unnamed_protein_product	Isochrysis_galbana	haptophyte
CAE5853982	I-B	unnamed_protein_product	Isochrysis_galbana	haptophyte
CAE4033660	I-B	unnamed_protein_product	Pavlova_gyrans	haptophyte
CAE2041804	I-B	unnamed_protein_product	Phaeocystis_antarctica	haptophyte
CAE2045570	I-B	unnamed_protein_product	Phaeocystis_antarctica	haptophyte
CAF6870094	I-B	unnamed_protein_product	Phaeocystis_sp._RCC851	haptophyte
CAF6870095	I-B	unnamed_protein_product	Phaeocystis_sp._RCC851	haptophyte
CAF6908054	I-B	unnamed_protein_product	Phaeocystis_sp._RCC851	haptophyte
CAG0577878	I-B	unnamed_protein_product	Prymnesium_neolepis	haptophyte
CAE2217919	I-B	unnamed_protein_product	Prymnesium_polylepis	haptophyte
CAE2242826	I-B	unnamed_protein_product	Prymnesium_polylepis	haptophyte

CAE5572172	I-B	unnamed_protein_product	Prymnesium_polylepis	haptophyte
CAE5583889	I-B	unnamed_protein_product	Prymnesium_polylepis	haptophyte
CAE2980514	I-B	unnamed_protein_product	Rhodomonas_lens	cryptophyte
CAE8104313	I-B	unnamed_protein_product	Rhodomonas_sp._CCMP768	cryptophyte
CAE3644260	I-B	unnamed_protein_product	Scyphosphaera_apsteinii	haptophyte
CAF6841921	I-B	unnamed_protein_product	uncultivated cryptophyte	cryptophyte
CAH9771101	I-B	unnamed_protein_product	uncultured_Geminigera	cryptophyte
CAH9771103	I-B	unnamed_protein_product	uncultured_Geminigera	cryptophyte
CAG1302811	I-B	unnamed_protein_product	uncultured_Isochrysis	haptophyte
CAG1302816	I-B	unnamed_protein_product	uncultured_Isochrysis	haptophyte
CAG1302826	I-B	unnamed_protein_product	uncultured_Isochrysis	haptophyte
CAH9584883	I-B	unnamed_protein_product	uncultured_Isochrysis	haptophyte
CAH9584885	I-B	unnamed_protein_product	uncultured_Isochrysis	haptophyte
CAH9584893	I-B	unnamed_protein_product	uncultured_Isochrysis	haptophyte
CAH9814007	I-B	unnamed_protein_product	uncultured_marine_Prymnesiales	haptophyte
CAF7741321	I-B	unnamed_protein_product	uncultured_Phaeocystis	haptophyte
CAF8319342	I-B	unnamed_protein_product	uncultured_Phaeocystis	haptophyte
CUF37707.1	II-A	SF_assemblin	Bodo_saltans	excavate
MONOS_2744	II-A	SF-assemblin	Monocercomoides_exilis	excavate
XP_0445591	II-A	uncharacterized_protein_FDP41006421	Naegleria_fowleri	excavate
XP_0026733	II-A	SF-assemblin	Naegleria_gruberi	excavate
XP_0445445	II-A	uncharacterized_protein_C9374_009962	Naegleria_lovaniensis	excavate
KAJ4456701	II-A	putative_Dynein_assembly_factor_3;_axonemal	Paratrimastix_pyriformis	excavate
KAJ4457334	II-A	putative_Ubiquitin-activating_enzyme_E11	Paratrimastix_pyriformis	excavate
CAE2765718	II-A	unnamed_protein_product	Percolomonas_cosmopolitus	excavate
KAA6380731	II-A	hypothetical_protein_EZS28_023745	Streblomastix_strix	excavate
KAA6399319	II-A	hypothetical_protein_EZS28_005153	Streblomastix_strix	excavate
XP_0093090	II-A	hypothetical_protein_DQ04_01441040	Trypanosoma_grayi	excavate
GKT26962.1	II-B	putative_multi-domain_containing_protein	Aduncisulcus_paluster	excavate
GKT34776.1	II-B	SF-assemblin/beta-giardin_like_protein	Aduncisulcus_paluster	excavate
KAG9392451	II-B	SF-assemblin_	Carpediemonas_membranifera	excavate
GL4410	II-B	SALP1	Giardia_lamblia_WBC6	excavate
GL4812	II-B	beta_giardin	Giardia_lamblia_WBC6	excavate
GL86676	II-B	delta_giardin	Giardia_lamblia_WBC6	excavate
GM12828	II-B	SALP1	Giardia_muris	excavate
GM13116	II-B	beta_giardin	Giardia_muris	excavate
GMRT_10130	II-B	delta_giardin	Giardia_muris	excavate
GIQ88493.1	II-B	SF-assemblin	Kipferlia_bialata	excavate
JAP92494.1	II-B	SF-assemblin,_partial	Trepomonas_sp._PC1	excavate
KAH0574774	II-B	SS5037722389	Spironucleus_salmonicida	excavate
KAH0569687	II-C	SS5037728643	Spironucleus_salmonicida	excavate
KAH0570349	II-C	SS5037728326	Spironucleus_salmonicida	excavate
KAH0573096	II-C	SS5037725214	Spironucleus_salmonicida	excavate
KAH0573097	II-C	SS5037725215	Spironucleus_salmonicida	excavate
JAP92908.1	II-C	SF-assemblin	Trepomonas_sp._PC1	excavate
JAP93695.1	II-C	hypothetical_protein_TPC113926	Trepomonas_sp._PC1	excavate
CAE4684474	II-D	unnamed_protein_product	Alexandrium_monilatum	dinoflagellate
CAE4460744	II-D	unnamed_protein_product	Amphidinium_carterae	dinoflagellate
CAE3108057	II-D	unnamed_protein_product	Amphidinium_massartii	dinoflagellate
CAE0441837	II-D	unnamed_protein_product	Aplanochytrium_stocchinoi	stramenopile
ALIM002419	II-D	SF_assemblin	Aurantiochytrium_limacinum_ATCC_MYA-1381	stramenopile
CVEL005213	II-D	Cvel_3613	Chromera_velia_CCMP2878	alveolate
CTOB011575	II-D	KOO32357.1	Chrysochromulina_tobin_strain_CCMP291	haptophyte
CAE6590376	II-D	unnamed_protein_product	Karlodinium_veneficum	dinoflagellate
CAF5575919	II-D	unnamed_protein_product	Lingulodinium_polyedra	dinoflagellate
CAF5575921	II-D	unnamed_protein_product	Lingulodinium_polyedra	dinoflagellate
CAF8253086	II-D	unnamed_protein_product	Nephroselmis_pyriformis	green_algae
CAF5868878	II-D	unnamed_protein_product	Oxyrrhis_marina	dinoflagellate
PMAR011027	II-D	hypothetical_protein_Pmar_PMAR017098	Perkinsus_marinus_ATCC_50983	alveolate
PPER010730	II-D	PPERSA_11603	Pseudocohnilembus_persalinus	ciliate
CAE8012516	II-D	unnamed_protein_product	Pyramimonas_parkeae	green_algae
SAGG005750	II-D	SF-assemblin	Schizochytrium_aggregatum_ATCC_28209	stramenopile
SMIC011006	II-D	OLP83335.1	Symbiodinium_microadriaticum	dinoflagellate
SMIN008102	II-D	symbB.v1.2.007143.t1symbB.v1.2.007143	Symbiodinium_minutum	dinoflagellate
CAF9825513	II-D	unnamed_protein_product	Symbiodinium_sp._CCMP2430	dinoflagellate
CAF9370132	II-D	unnamed_protein_product	Symbiodinium_sp._Mp	dinoflagellate
CAI0112908	II-D	unnamed_protein_product	uncultured_Symbiodinium	dinoflagellate

VBRA011124	II-D	Vbra_4325	Vitrella_brassicaformis_CCMP3155	alveolate
LAF67753.1	II-E	Giardin_subunit_beta-like_protein	Aduncisulcus_paluster	excavate
LAF70811.1	II-E	Giardin_subunit_beta-like_protein	Aduncisulcus_paluster	excavate
KAG9390376	II-E	hypothetical_protein_J82737726	Carpediemonas_membranifera	excavate
KAG9390884	II-E	chromosome_segregation_protein	Carpediemonas_membranifera	excavate
KAG9393993	II-E	putative_IQ_calmodulin-binding_motif_family_protein	Carpediemonas_membranifera	excavate
KAG9394854	II-E	Leucine_Rich_repeats	Carpediemonas_membranifera	excavate
KAG9395165	II-E	putative_IQ_calmodulin-binding_motif_family_protein	Carpediemonas_membranifera	excavate
KAG9396064	II-E	putative_IQ_calmodulin-binding_motif_family_protein	Carpediemonas_membranifera	excavate
KAG9397592	II-E	hypothetical_protein_J82730722	Carpediemonas_membranifera	excavate
GIQ81117.1	II-E	hypothetical_protein_KIPB_002026	Kipferlia_bialata	excavate
KAJ4455429	II-E	putative_IQ_calmodulin-binding_motif_protein	Paratrimastix_pyriformis	excavate
KAJ4461698	II-E	putative_IQ_calmodulin-binding_motif_protein	Paratrimastix_pyriformis	excavate
CAG9315837	II-F	unnamed_protein_product	Blepharisma_stoltei	ciliate
CAG9319033	II-F	unnamed_protein_product	Blepharisma_stoltei	ciliate
CAG9328128	II-F	unnamed_protein_product	Blepharisma_stoltei	ciliate
CAG9332670	II-F	unnamed_protein_product	Blepharisma_stoltei	ciliate
CAG9334056	II-F	unnamed_protein_product	Blepharisma_stoltei	ciliate
CAG9334318	II-F	unnamed_protein_product	Blepharisma_stoltei	ciliate
CAG9334362	II-F	unnamed_protein_product	Blepharisma_stoltei	ciliate
GTHE002649	II-F	GUITHDRAFT_164214	Guillardia_theta_CCMP2712	cryptophyte
TNV71154.1	II-F	hypothetical_protein_FGO68_gene8873	Halteria_grandinella	ciliate
TNV73886.1	II-F	hypothetical_protein_FGO68_gene10156	Halteria_grandinella	ciliate
IMUL002535	II-F	IMG5_092570	Ichthyophthirius_multifiliis_(strain_G5)	ciliate
IMUL004704	II-F	IMG5_012190	Ichthyophthirius_multifiliis_(strain_G5)	ciliate
OTRI007269	II-F	OXYTRI_18485	Oxytricha_trifallax	ciliate
OTRI015469	II-F	OXYTRI_03485	Oxytricha_trifallax	ciliate
PTET000850	II-F	GSPATT00038461001	Paramecium_tetraurelia	ciliate
PTET002657	II-F	GSPATT00019407001	Paramecium_tetraurelia	ciliate
PTET007714	II-F	GSPATT00027846001	Paramecium_tetraurelia	ciliate
PTET007969	II-F	GSPATT00007561001	Paramecium_tetraurelia	ciliate
PTET008182	II-F	GSPATT00007501001	Paramecium_tetraurelia	ciliate
PTET008231	II-F	GSPATT00022901001	Paramecium_tetraurelia	ciliate
PTET009984	II-F	GSPATT00019127001	Paramecium_tetraurelia	ciliate
PTET011392	II-F	GSPATT00007157001	Paramecium_tetraurelia	ciliate
PTET012679	II-F	GSPATT00017968001	Paramecium_tetraurelia	ciliate
PTET016467	II-F	GSPATT00006705001	Paramecium_tetraurelia	ciliate
PTET016625	II-F	GSPATT00001424001	Paramecium_tetraurelia	ciliate
PTET017311	II-F	GSPATT00017301001	Paramecium_tetraurelia	ciliate
PTET017536	II-F	GSPATT00020993001	Paramecium_tetraurelia	ciliate
PTET018342	II-F	GSPATT00012690001	Paramecium_tetraurelia	ciliate
PTET018349	II-F	GSPATT00012840001	Paramecium_tetraurelia	ciliate
PTET019156	II-F	GSPATT00023935001	Paramecium_tetraurelia	ciliate
PTET020125	II-F	GSPATT00015816001	Paramecium_tetraurelia	ciliate
PTET021474	II-F	GSPATT00016516001	Paramecium_tetraurelia	ciliate
PTET021686	II-F	GSPATT00020504001	Paramecium_tetraurelia	ciliate
PTET022684	II-F	GSPATT00004428001	Paramecium_tetraurelia	ciliate
PTET025570	II-F	GSPATT00002244001	Paramecium_tetraurelia	ciliate
PTET027899	II-F	GSPATT00025723001	Paramecium_tetraurelia	ciliate
PTET029222	II-F	GSPATT00008270001	Paramecium_tetraurelia	ciliate
PTET031528	II-F	GSPATT00013823001	Paramecium_tetraurelia	ciliate
PTET032324	II-F	GSPATT00015215001	Paramecium_tetraurelia	ciliate
PTET032466	II-F	GSPATT00015160001	Paramecium_tetraurelia	ciliate
PTET033051	II-F	GSPATT00002620001	Paramecium_tetraurelia	ciliate
PTET034196	II-F	GSPATT00014874001	Paramecium_tetraurelia	ciliate
PTET035634	II-F	GSPATT00013148001	Paramecium_tetraurelia	ciliate
PTET038287	II-F	GSPATT00027352001	Paramecium_tetraurelia	ciliate
PTET038790	II-F	GSPATT00023644001	Paramecium_tetraurelia	ciliate
PTET039287	II-F	GSPATT00038112001	Paramecium_tetraurelia	ciliate
PPER007463	II-F	PPERSA_10114	Pseudocohnilembus_persalinus	ciliate
PPER007785	II-F	PPERSA_01648	Pseudocohnilembus_persalinus	ciliate
PPER011715	II-F	PPERSA_01794	Pseudocohnilembus_persalinus	ciliate
SCOE001793	II-F	OMJ66752.1	Stentor_coeruleus	ciliate
SCOE004544	II-F	OMJ69503.1	Stentor_coeruleus	ciliate
SCOE005515	II-F	OMJ70474.1	Stentor_coeruleus	ciliate
SCOE014352	II-F	OMJ79311.1	Stentor_coeruleus	ciliate
SCOE015279	II-F	OMJ80238.1	Stentor_coeruleus	ciliate

SCOE015911	II-F	OMJ80870.1	Stentor_coeruleus	ciliate
SCOE023604	II-F	OMJ88563.1	Stentor_coeruleus	ciliate
SCOE029686	II-F	OMJ94645.1	Stentor_coeruleus	ciliate
SLEM019335	II-F	Contig13004.g13866	Stylonychia_lemnae	ciliate
TTHE005067	II-F	TTHERM_00354600	Tetrahymena_thermophila	ciliate
TTHE017977	II-F	TTHERM_00941400	Tetrahymena_thermophila	ciliate
TTHE021997	II-F	TTHERM_00588900	Tetrahymena_thermophila	ciliate
LAF69892.1	II-G	Giardin_subunit_beta-like_protein	Aduncisulcus_paluster	excavate
LAF80264.1	II-G	Giardin_subunit_beta-like_protein	Aduncisulcus_paluster	excavate
KAH0574824	II-G	SS5037722439	Spironucleus_salmonicida	excavate
IMUL001643	II-H	IMG5_195310	Ichthyophthirius_multifiliis_(strain_G5)	ciliate
CAE6663912	II-H	unnamed_protein_product	Karlodinium_veneficum	dinoflagellate
PTET003259	II-H	GSPATT00008626001	Paramecium_tetraurelia	ciliate
PTET008435	II-H	GSPATT00022867001	Paramecium_tetraurelia	ciliate
PTET009940	II-H	GSPATT00019065001	Paramecium_tetraurelia	ciliate
PTET015389	II-H	GSPATT00010780001	Paramecium_tetraurelia	ciliate
PTET016220	II-H	GSPATT00006766001	Paramecium_tetraurelia	ciliate
PTET017405	II-H	GSPATT00020957001	Paramecium_tetraurelia	ciliate
PTET019175	II-H	GSPATT00024123001	Paramecium_tetraurelia	ciliate
PTET022598	II-H	GSPATT00004373001	Paramecium_tetraurelia	ciliate
PTET027647	II-H	GSPATT00014274001	Paramecium_tetraurelia	ciliate
PTET030785	II-H	GSPATT00014806001	Paramecium_tetraurelia	ciliate
PTET036829	II-H	GSPATT00005889001	Paramecium_tetraurelia	ciliate
PTET037654	II-H	GSPATT00026454001	Paramecium_tetraurelia	ciliate
PPER005530	II-H	PPERSA_13160	Pseudocohnilembus_persalinus	ciliate
PPER006940	II-H	PPERSA_00932	Pseudocohnilembus_persalinus	ciliate
TTHE020027	II-H	TTHERM_00388620	Tetrahymena_thermophila	ciliate
TTHE020106	II-H	TTHERM_01151610	Tetrahymena_thermophila	ciliate
IMUL000851	II-I	IMG5_160360	Ichthyophthirius_multifiliis_(strain_G5)	ciliate
IMUL000896	II-I	IMG5_166490	Ichthyophthirius_multifiliis_(strain_G5)	ciliate
IMUL003032	II-I	IMG5_172770	Ichthyophthirius_multifiliis_(strain_G5)	ciliate
IMUL004886	II-I	IMG5_180510	Ichthyophthirius_multifiliis_(strain_G5)	ciliate
IMUL007272	II-I	IMG5_192870	Ichthyophthirius_multifiliis_(strain_G5)	ciliate
CAE2445079	II-I	unnamed_protein_product	Litonotus_pictus	ciliate
CAE2449857	II-I	unnamed_protein_product	Litonotus_pictus	ciliate
CAE2462106	II-I	unnamed_protein_product	Litonotus_pictus	ciliate
OTRI001009	II-I	OXYTRI_17902	Oxytricha_trifallax	ciliate
OTRI003192	II-I	OXYTRI_15526	Oxytricha_trifallax	ciliate
OTRI004310	II-I	OXYTRI_18742	Oxytricha_trifallax	ciliate
OTRI016134	II-I	OXYTRI_10490	Oxytricha_trifallax	ciliate
PTET001558	II-I	GSPATT00015408001	Paramecium_tetraurelia	ciliate
PTET004630	II-I	GSPATT00003161001	Paramecium_tetraurelia	ciliate
PTET005728	II-I	GSPATT00033989001	Paramecium_tetraurelia	ciliate
PTET006418	II-I	GSPATT00038161001	Paramecium_tetraurelia	ciliate
PTET007184	II-I	GSPATT00002032001	Paramecium_tetraurelia	ciliate
PTET007783	II-I	GSPATT00036963001	Paramecium_tetraurelia	ciliate
PTET010537	II-I	GSPATT00000453001	Paramecium_tetraurelia	ciliate
PTET016679	II-I	GSPATT00001334001	Paramecium_tetraurelia	ciliate
PTET018928	II-I	GSPATT00032447001	Paramecium_tetraurelia	ciliate
PTET021211	II-I	GSPATT00020721001	Paramecium_tetraurelia	ciliate
PTET022036	II-I	GSPATT00011977001	Paramecium_tetraurelia	ciliate
PTET023741	II-I	GSPATT00004838001	Paramecium_tetraurelia	ciliate
PTET024579	II-I	GSPATT00017545001	Paramecium_tetraurelia	ciliate
PTET025126	II-I	GSPATT00029782001	Paramecium_tetraurelia	ciliate
PTET025316	II-I	GSPATT00021211001	Paramecium_tetraurelia	ciliate
PTET026014	II-I	GSPATT00028132001	Paramecium_tetraurelia	ciliate
PTET030727	II-I	GSPATT00014618001	Paramecium_tetraurelia	ciliate
PTET032056	II-I	GSPATT00024832001	Paramecium_tetraurelia	ciliate
PTET033490	II-I	GSPATT00022821001	Paramecium_tetraurelia	ciliate
PTET033753	II-I	GSPATT00003756001	Paramecium_tetraurelia	ciliate
PTET034856	II-I	GSPATT00034181001	Paramecium_tetraurelia	ciliate
PTET035114	II-I	GSPATT00025686001	Paramecium_tetraurelia	ciliate
PTET035426	II-I	GSPATT00029521001	Paramecium_tetraurelia	ciliate
PTET036441	II-I	GSPATT00030915001	Paramecium_tetraurelia	ciliate
PTET036850	II-I	GSPATT00006108001	Paramecium_tetraurelia	ciliate
PTET037130	II-I	GSPATT00021965001	Paramecium_tetraurelia	ciliate
PTET038947	II-I	GSPATT00034929001	Paramecium_tetraurelia	ciliate

PPER003953	II-I	PPERSA_07262	Pseudocohnilembus_persalinus	ciliate
PPER006804	II-I	PPERSA_12590	Pseudocohnilembus_persalinus	ciliate
PPER011526	II-I	PPERSA_12480	Pseudocohnilembus_persalinus	ciliate
SCOE003242	II-I	OMJ68201.1	Stentor_coeruleus	ciliate
SCOE006035	II-I	OMJ70994.1	Stentor_coeruleus	ciliate
SCOE022480	II-I	OMJ87439.1	Stentor_coeruleus	ciliate
SCOE024428	II-I	OMJ89387.1	Stentor_coeruleus	ciliate
SCOE030816	II-I	OMJ95775.1	Stentor_coeruleus	ciliate
SLEM001141	II-I	Contig9480.g10143	Stylonychia_lemnae	ciliate
SLEM001284	II-I	Contig4675.g4991	Stylonychia_lemnae	ciliate
SLEM014422	II-I	Contig10456.g11163	Stylonychia_lemnae	ciliate
SLEM017231	II-I	Contig4912.g5251	Stylonychia_lemnae	ciliate
TTHE005816	II-I	TTHERM_00312820	Tetrahymena_thermophila	ciliate
TTHE010052	II-I	TTHERM_00188980	Tetrahymena_thermophila	ciliate
TTHE013964	II-I	TTHERM_00688560	Tetrahymena_thermophila	ciliate
TTHE014011	II-I	TTHERM_00688340	Tetrahymena_thermophila	ciliate
CAF8347265	II-I	unnamed_protein_product	uncultured_Stichotrichia	ciliate
CAD9452223	II-J	unnamed_protein_product	Alexandrium_andersonii	dinoflagellate
CAE4373397	II-J	unnamed_protein_product	Alexandrium_fundyense	dinoflagellate
CAE2829706	II-J	unnamed_protein_product	Alexandrium_minutum	dinoflagellate
CAE4689249	II-J	unnamed_protein_product	Alexandrium_monilatum	dinoflagellate
CAE4476565	II-J	unnamed_protein_product	Amphidinium_carterae	dinoflagellate
CAE3127802	II-J	unnamed_protein_product	Amphidinium_massartii	dinoflagellate
CAE8792104	II-J	unnamed_protein_product	Apocalathium_aciculiferum	dinoflagellate
CVEL014478	II-J	Cvel_872	Chromera_velia_CCMP2878	alveolate
CAE5122565	II-J	unnamed_protein_product	Crypthecodinium_cohnii	dinoflagellate
CAE5193973	II-J	unnamed_protein_product	Crypthecodinium_cohnii	dinoflagellate
CAE3217288	II-J	unnamed_protein_product	Gambierdiscus_australes	dinoflagellate
CAE3266839	II-J	unnamed_protein_product	Gymnodinium_catenatum	dinoflagellate
CAE3336549	II-J	unnamed_protein_product	Gymnodinium_catenatum	dinoflagellate
CAE3361292	II-J	unnamed_protein_product	Gymnodinium_catenatum	dinoflagellate
CAE3365312	II-J	unnamed_protein_product	Gymnodinium_catenatum	dinoflagellate
CAE4314211	II-J	unnamed_protein_product	Heterocapsa_arctica	dinoflagellate
CAE6443765	II-J	unnamed_protein_product	Karlodinium_veneficum	dinoflagellate
CAF6424941	II-J	unnamed_protein_product	Karlodinium_veneficum	dinoflagellate
CAF6424942	II-J	unnamed_protein_product	Karlodinium_veneficum	dinoflagellate
CAH9448249	II-J	unnamed_protein_product	Mesodinium_pulex	ciliate
CAE0880366	II-J	unnamed_protein_product	Oxyrrhis_marina	dinoflagellate
CAF5667497	II-J	unnamed_protein_product	Oxyrrhis_marina	dinoflagellate
CAE4096310	II-J	unnamed_protein_product	Pelagodinium_beii	dinoflagellate
CAE4126052	II-J	unnamed_protein_product	Pelagodinium_beii	dinoflagellate
CAE2712428	II-J	unnamed_protein_product	Polarella_glacialis	dinoflagellate
CAE4434025	II-J	unnamed_protein_product	Polarella_glacialis	dinoflagellate
CAE4441444	II-J	unnamed_protein_product	Polarella_glacialis	dinoflagellate
CAE1139080	II-J	unnamed_protein_product	Prorocentrum_minimum	dinoflagellate
CAE1301842	II-J	unnamed_protein_product	Prorocentrum_minimum	dinoflagellate
CAE2183888	II-J	unnamed_protein_product	Protoceratium_reticulatum	dinoflagellate
CAE8052863	II-J	unnamed_protein_product	Pyramimonas_parkeae	green_algae
CAD8351842	II-J	unnamed_protein_product	Pyrodinium_bahamense	dinoflagellate
CAE8480673	II-J	unnamed_protein_product	Scrippsiella_hangoei	dinoflagellate
CAE0280914	II-J	unnamed_protein_product	Spumella_elongata	stramenopile
SMIC040213	II-J	OLQ12543.1	Symbiodinium_microadriaticum	dinoflagellate
CAF9811355	II-J	unnamed_protein_product	Symbiodinium_sp._CCMP2430	dinoflagellate
CAG1209552	II-J	unnamed_protein_product	Symbiodinium_sp._clade_A	dinoflagellate
CAG1149607	II-J	unnamed_protein_product	Symbiodinium_sp._clade_D	dinoflagellate
CAF9517847	II-J	unnamed_protein_product	Symbiodinium_sp._Mp	dinoflagellate
CAE2576721	II-J	unnamed_protein_product	Togula_jolla	dinoflagellate
CAE2586399	II-J	unnamed_protein_product	Togula_jolla	dinoflagellate
CAF7393136	II-J	unnamed_protein_product	uncultured_Amoebophrya	dinoflagellate
CAF8363843	II-J	unnamed_protein_product	uncultured_Pyramimonas	green_algae
CAH9772033	II-J	unnamed_protein_product	uncultured_Symbiodinium	dinoflagellate
CAH9941684	II-J	unnamed_protein_product	uncultured_Symbiodinium	dinoflagellate
CAI0204430	II-J	unnamed_protein_product	uncultured_Symbiodinium	dinoflagellate
CAD9066976	II-J	unnamed_protein_product	Vitrella_brassicaformis	alveolate
VBRA003628	II-J	Vbra_17011	Vitrella_brassicaformis_CCMP3155	alveolate
CAE4569842	III-A	unnamed_protein_product	Alexandrium_monilatum	dinoflagellate
CAD7923881	III-A	unnamed_protein_product	Amoebophrya_sp._A120	dinoflagellate

CAE4466579	III-A	unnamed_protein_product	Amphidinium_carterae	dinoflagellate
CAE4466580	III-A	unnamed_protein_product	Amphidinium_carterae	dinoflagellate
CAE8663566	III-A	unnamed_protein_product	Apocalathium_aciculiferum	dinoflagellate
CVEL030024	III-A	Cvel_12806	Chromera_velia_CCMP2878	alveolate
OEH79472.1	III-A	putative_SF-assemblin	Cyclospora_cayetanensis	apicomplexan
XP_0261910	III-A	SF-assemblin_	Cyclospora_cayetanensis	apicomplexan
PHJ25868.1	III-A	sf-assemblin_beta_giardin_protein	Cystoisospora_suis	apicomplexan
CAE1604586	III-A	unnamed_protein_product	Dinophysis_acuminata	dinoflagellate
XP_0132333	III-A	SF-assemblin,_putative	Eimeria_tenella	apicomplexan
CAE4150788	III-A	unnamed_protein_product	Gonyaulax_spinifera	dinoflagellate
CAE4188600	III-A	unnamed_protein_product	Gonyaulax_spinifera	dinoflagellate
CAE3268772	III-A	unnamed_protein_product	Gymnodinium_catenatum	dinoflagellate
CAH9401899	III-A	unnamed_protein_product	Karenia_brevis	dinoflagellate
CAF6458793	III-A	unnamed_protein_product	Karlodinium_veneficum	dinoflagellate
CAF5663926	III-A	unnamed_protein_product	Lingulodinium_polyedra	dinoflagellate
CEL66178.1	III-A	SF-assemblin,_putative	Neospora_caninum_Liverpool	apicomplexan
CAE0888733	III-A	unnamed_protein_product	Oxyrrhis_marina	dinoflagellate
CAF5829093	III-A	unnamed_protein_product	Oxyrrhis_marina	dinoflagellate
CAE4087226	III-A	unnamed_protein_product	Pelagodinium_beii	dinoflagellate
CAE4090152	III-A	unnamed_protein_product	Pelagodinium_beii	dinoflagellate
PMAR021127	III-A	hypothetical_protein_Pmar_PMAR006803	Perkinsus_marinus_ATCC_50983	alveolate
PMAR021207	III-A	hypothetical_protein_Pmar_PMAR006886	Perkinsus_marinus_ATCC_50983	alveolate
KAF4687452	III-A	hypothetical_protein_FOZ60_003976	Perkinsus_olseni	alveolate
CAE2746773	III-A	unnamed_protein_product	Polarella_glacialis	dinoflagellate
CAE8588971	III-A	unnamed_protein_product,_partial	Polarella_glacialis	dinoflagellate
CAE8654859	III-A	unnamed_protein_product	Polarella_glacialis	dinoflagellate
CAE8668265	III-A	unnamed_protein_product	Polarella_glacialis	dinoflagellate
CAE1072150	III-A	unnamed_protein_product	Prorocentrum_minimum	dinoflagellate
CAG1240125	III-A	unnamed_protein_product	Symbiodinium_sp._clade_A	dinoflagellate
KAF4642657	III-A	SF-assemblin/beta_giardin_protein	Toxoplasma_gondii	apicomplexan
CAE8225281	III-A	unnamed_protein_product	uncultivated dinoflagellate	dinoflagellate
CEM10756.1	III-A	unnamed_protein_product	Vitrella_brassicaformis_CCMP3155	alveolate
VBRA005471	III-A	Vbra_15012	Vitrella_brassicaformis_CCMP3155	alveolate
CAD9482361	III-B	unnamed_protein_product	Alexandrium_andersonii	dinoflagellate
CAD9130930	III-B	unnamed_protein_product	Alexandrium_catenella	dinoflagellate
CAE2828235	III-B	unnamed_protein_product	Alexandrium_minutum	dinoflagellate
CAE4644624	III-B	unnamed_protein_product	Alexandrium_monilatum	dinoflagellate
CAD7924247	III-B	unnamed_protein_product	Amoebophrya_sp._A120	dinoflagellate
CAD7925753	III-B	unnamed_protein_product	Amoebophrya_sp._A120	dinoflagellate
CAE3126157	III-B	unnamed_protein_product	Amphidinium_massartii	dinoflagellate
CAE3136077	III-B	unnamed_protein_product	Amphidinium_massartii	dinoflagellate
CAE8659391	III-B	unnamed_protein_product	Apocalathium_aciculiferum	dinoflagellate
CAE8795196	III-B	unnamed_protein_product	Apocalathium_aciculiferum	dinoflagellate
XP_0127674	III-B	sf-assemblin/beta_giardin_family_protein	Babesia_bigemina	apicomplexan
CAD9550707	III-B	unnamed_protein_product	Brandtodinium_nutricula	dinoflagellate
KAF8823115	III-B	SF-assemblin/beta_giardin_protein	Cardiosporidium_cionae	apicomplexan
CVEL018337	III-B	Cvel_6796	Chromera_velia_CCMP2878	alveolate
CAE5189144	III-B	unnamed_protein_product	Crypthecodinium_cohnii	dinoflagellate
OLQ18936.1	III-B	SF-assemblin/beta_giardin	Cryptosporidium_hominis	apicomplexan
XP_0021402	III-B	SF-assemblin/beta_giardin_family_protein	Cryptosporidium_muris_RN66	apicomplexan
CPAI001734	III-B	cgd6_3620	Cryptosporidium_parvum_Iowa_II	apicomplexan
XP_627703.	III-B	SF-assemblin	Cryptosporidium_parvum_Iowa_II	apicomplexan
XP_0225902	III-B	SF-assemblin	Cyclospora_cayetanensis	apicomplexan
PHJ22352.1	III-B	sf-assemblin_beta_giardin_protein	Cystoisospora_suis	apicomplexan
CAE1619670	III-B	unnamed_protein_product	Dinophysis_acuminata	dinoflagellate
XP_0132319	III-B	SF-assemblin,_putative	Eimeria_tenella	apicomplexan
CAE3176840	III-B	unnamed_protein_product	Gambierdiscus_australes	dinoflagellate
CAE4162403	III-B	unnamed_protein_product	Gonyaulax_spinifera	dinoflagellate
GNIP004410	III-B	GNI_136160	Gregarina_niphandrodes	apicomplexan
CAE3267885	III-B	unnamed_protein_product	Gymnodinium_catenatum	dinoflagellate
CAE3274404	III-B	unnamed_protein_product	Gymnodinium_catenatum	dinoflagellate
CAH9398175	III-B	unnamed_protein_product	Karenia_brevis	dinoflagellate
CAE6671092	III-B	unnamed_protein_product	Karlodinium_veneficum	dinoflagellate
CAF6433464	III-B	unnamed_protein_product	Karlodinium_veneficum	dinoflagellate
CAF5653207	III-B	unnamed_protein_product	Lingulodinium_polyedra	dinoflagellate
CAF5674730	III-B	unnamed_protein_product	Lingulodinium_polyedra	dinoflagellate
XP_0038856	III-B	hypothetical_protein_NCLIV_060590	Neospora_caninum_Liverpool	apicomplexan

XP_0038857	III-B	hypothetical_protein_NCLIV_061500_		Neospora_caninum_Liverpool	apicomplexan
CAE0867684	III-B	unnamed_protein_product		Oxyrrhis_marina	dinoflagellate
CAE4114874	III-B	unnamed_protein_product		Pelagodinium_beii	dinoflagellate
CAE4168036	III-B	unnamed_protein_product		Pelagodinium_beii	dinoflagellate
KAF4676029	III-B	hypothetical_protein_FOL47006830		Perkinsus_chesapeaki	alveolate
PMAR010141	III-B	hypothetical_protein_Pmar_PMAR010141		Perkinsus_marinus_ATCC_50983	alveolate
KAF4663496	III-B	hypothetical_protein_FOZ61001600		Perkinsus_olseni	alveolate
KAF4695811	III-B	hypothetical_protein_FOZ60_003406		Perkinsus_olseni	alveolate
KAF4745785	III-B	hypothetical_protein_FOZ63007701		Perkinsus_olseni	alveolate
KOB84806.1	III-B	hypothetical_protein_PFDG_00109		Plasmodium_falciparum_Dd2	apicomplexan
KOB60531.1	III-B	hypothetical_protein_PFHG_02318		Plasmodium_falciparum_HB3	apicomplexan
KNG76006.1	III-B	sf-assemblin_		Plasmodium_falciparum_IGH-CR14	apicomplexan
CAE2690847	III-B	unnamed_protein_product		Polarella_glacialis	dinoflagellate
CAE4428725	III-B	unnamed_protein_product		Polarella_glacialis	dinoflagellate
CAE8630113	III-B	unnamed_protein_product,_partial		Polarella_glacialis	dinoflagellate
CAE8634770	III-B	unnamed_protein_product		Polarella_glacialis	dinoflagellate
CAE1312606	III-B	unnamed_protein_product		Prorocentrum_minimum	dinoflagellate
CAE1347330	III-B	unnamed_protein_product		Prorocentrum_minimum	dinoflagellate
SMIC011118	III-B	OLP83447.1		Symbiodinium_microadriaticum	dinoflagellate
SMIN003981	III-B	symbB.v1.2.003501.t1symbB.v1.2.003501		Symbiodinium_minutum	dinoflagellate
SMIN023467	III-B	symbB.v1.2.020701.t1symbB.v1.2.020701		Symbiodinium_minutum	dinoflagellate
CAE7385687	III-B	unnamed_protein_product		Symbiodinium_natans	dinoflagellate
CAE6935604	III-B	unnamed_protein_product		Symbiodinium_sp._CCMP2592	dinoflagellate
CAG1254524	III-B	unnamed_protein_product		Symbiodinium_sp._clade_A	dinoflagellate
CAE7946234	III-B	unnamed_protein_product		Symbiodinium_sp._KB8	dinoflagellate
TANN003114	III-B	CAI76245		Theileria_annulata	apicomplexan
XP_952869.	III-B	filament_assemblin_protein,_putative		Theileria_annulata	apicomplexan
CAE2609386	III-B	unnamed_protein_product		Togula_jolla	dinoflagellate
CAE8190341	III-B	unnamed_protein_product		uncultivated dinoflagellate	dinoflagellate
CAD9064092	III-B	unnamed_protein_product		Vitrella_brassicaformis	alveolate
CEL98015.1	III-B	unnamed_protein_product		Vitrella_brassicaformis_CCMP3155	alveolate
VBRA001315	III-B	Vbra_7792		Vitrella_brassicaformis_CCMP3155	alveolate
COKA008017	III-C	Cok_S_s045_7593.t1		Cladosiphon_okamuranus	stramenopile
ESIL005803	III-C	Ec-08_004740		Ectocarpus_siliculosus	stramenopile
RLN95441.1	III-C	hypothetical_protein_BBJ28_00008141		Nothophytophthora_sp._Chile5	stramenopile
OTRI007613	III-C	OXYTRI_04999		Oxytricha_trifallax	ciliate
OTRI024204	III-C	OXYTRI_16775		Oxytricha_trifallax	ciliate
PPER009876	III-C	PPERSA_03880		Pseudocohnilembus_persalinus	ciliate
SCOE008613	III-C	OMJ73572.1		Stentor_coeruleus	ciliate
SCOE030418	III-C	OMJ95377.1		Stentor_coeruleus	ciliate
TTHE016431	III-C	TTHERM_00263309		Tetrahymena_thermophila	ciliate
BNAT007617	III-D	JGI_V11134269		Bigelowiella_natans_CCMP2755	rhizaria
Filo_g623.	III-D	SF_assemblin,_putative		Filoreta_ramosa	rhizaria
PBRA001446	III-D	PBRA_001486		Plasmodiophora_brassicae	rhizaria
ETO20168.1	III-D	hypothetical_protein_RFI_17050		Reticulomyxa_filosa	rhizaria
CAE3671600	III-D	unnamed_protein_product		Scyphosphaera_apsteinii	haptophyte
CAG1079421	III-E	unnamed_protein_product		Aulacoseira_subarctica	stramenopile
KAA0154653	III-E	hypothetical_protein_FNF2902184		Cafeteria_roenbergensis	stramenopile
KAA0172597	III-E	hypothetical_protein_FNF2705950		Cafeteria_roenbergensis	stramenopile
CAE3766644	III-E	unnamed_protein_product		Chaetoceros_cf._neogracilis	stramenopile
CAE0458037	III-E	unnamed_protein_product		Chaetoceros_debilis	stramenopile
CAE3977936	III-E	unnamed_protein_product		Chaetoceros_dichaeta	stramenopile
GFH53576.1	III-E	hypothetical_protein_CTEN210_10052		Chaetoceros_tenuissimus	stramenopile
CAE4892120	III-E	unnamed_protein_product		Chattonella_subsalsa	stramenopile
CAD8713953	III-E	unnamed_protein_product		Chromulina_nebulosa	stramenopile
COKA017692	III-E	Cok_S_s298_16366.t1		Cladosiphon_okamuranus	stramenopile
CBJ31109.1	III-E	SF-assemblin_		Ectocarpus_siliculosus	stramenopile
ESIL002371	III-E	Ec-04_000800		Ectocarpus_siliculosus	stramenopile
CAB1116569	III-E	unnamed_protein_product		Ectocarpus_sp._CCAP_1310/34	stramenopile
GAX13180.1	III-E	hypothetical_protein_FisN_17Hh110		Fistulifera_solaris	stramenopile
GAX20159.1	III-E	hypothetical_protein_FisN_17Lh110		Fistulifera_solaris	stramenopile
KAI2493309	III-E	hypothetical_protein_MHU86_21230		Fragilaria_crotonensis	stramenopile
FCYL004101	III-E		68924	Fragilariopsis_cylindrus_CCMP_1102	stramenopile
FCYL016920	III-E		272105	Fragilariopsis_cylindrus_CCMP_1102	stramenopile
OEU16234.1	III-E	hypothetical_protein_FRACYDRAFT_268924_		Fragilariopsis_cylindrus_CCMP1102	stramenopile
CAD9296254	III-E	unnamed_protein_product		Grammatophora_oceanica	stramenopile
CAE0635969	III-E	unnamed_protein_product		Heterosigma_akashiwo	stramenopile

GBG29552.1	III-E	SF-assemblin	Hondaea_fermentalgiana	stramenopile
CAD9556458	III-E	unnamed_protein_product	Leptocylindrus_danicus	stramenopile
EWM27934.1	III-E	SF-assemblin	Nannochloropsis_gaditana	stramenopile
NGAD000371	III-E	Nga00374	Nannochloropsis_gaditana_CCMP526	stramenopile
KAG7353152	III-E	SF-assemblin/beta_giardin_domain_containing_protein	Nitzschia_inconspicua	stramenopile
KAG7367182	III-E	SF-assemblin/beta_giardin_domain_containing_protein	Nitzschia_inconspicua	stramenopile
CAE5940461	III-E	unnamed_protein_product	Paraphysomonas_imperforata	stramenopile
CAH0365244	III-E	unnamed_protein_product	Pelagomonas_calceolata	stramenopile
CAH0374357	III-E	unnamed_protein_product	Pelagomonas_calceolata	stramenopile
XP_0021854	III-E	predicted_protein_	Phaeodactylum_tricornutum_CCAP_1055/1	stramenopile
PTRI008187	III-E	Phatr3J50558.p1	Phaeodactylum_tricornutum_CCAP1055/1	stramenopile
CAD8260385	III-E	unnamed_protein_product	Pinguiococcus_pyrenoidosus	stramenopile
VEU40600.1	III-E	unnamed_protein_product	Pseudo-nitzschia_multistriata	stramenopile
CAE0277283	III-E	unnamed_protein_product	Spumella_elongata	stramenopile
CAE2987624	III-E	unnamed_protein_product	Stephanopyxis_turris	stramenopile
EJK57126.1	III-E	hypothetical_protein_THAOC_22869	Thalassiosira_oceanica	stramenopile
TPSE009080	III-E	THAPSDRAFT_23177	Thalassiosira_pseudonana_CCMP1335	stramenopile
XP_0022911	III-E	predicted_protein	Thalassiosira_pseudonana_CCMP1335	stramenopile
KAG5178294	III-E	SF-assemblin	Tribonema_minus	stramenopile
CAF7518603	III-E	unnamed_protein_product	Triparma_pacifica	stramenopile
CAG1134680	III-E	unnamed_protein_product	uncultured_Dinobryon	stramenopile
CAG1134682	III-E	unnamed_protein_product	uncultured_Dinobryon	stramenopile
OQR87478.1	III-F	SF-assemblin	Achlya_hypogyna	stramenopile
AAST024954	III-F	OG0006921	Aphanomyces_astaci	stramenopile
XP_0098267	III-F	hypothetical_protein_H25704040	Aphanomyces_astaci	stramenopile
KAG9402267	III-F	hypothetical_protein_AC1031006894	Aphanomyces_cochlioides	stramenopile
KAF0734008	III-F	hypothetical_protein_Ae201684_009181	Aphanomyces_euteiches	stramenopile
KAH9107600	III-F	hypothetical_protein_AeMF1017091	Aphanomyces_euteiches	stramenopile
XP_0088691	III-F	hypothetical_protein_H310_06063	Aphanomyces_invadans	stramenopile
KAF0684981	III-F	hypothetical_protein_As57867022939	Aphanomyces_stellatus	stramenopile
RLN52230.1	III-F	hypothetical_protein_BBJ28_00010615	Nothophytophthora_sp._Chile5	stramenopile
RLN86757.1	III-F	hypothetical_protein_BBJ28_00022434	Nothophytophthora_sp._Chile5	stramenopile
KAG6959258	III-F	hypothetical_protein_JG688_00010152	Phytophthora_aleatoria	stramenopile
KAG7398257	III-F	hypothetical_protein_PHYBOEH_011430	Phytophthora_boehmeriae	stramenopile
KAF1791140	III-F	SF-assemblin_	Phytophthora_cactorum	stramenopile
KAG2760723	III-F	hypothetical_protein_Pcac1g27320	Phytophthora_cactorum	stramenopile
KAG3022183	III-F	hypothetical_protein_PC120_g8247	Phytophthora_cactorum	stramenopile
KAG1689428	III-F	hypothetical_protein_DVH05_002230	Phytophthora_capsici	stramenopile
KAG6592733	III-F	SF-assemblin	Phytophthora_cinnamomi	stramenopile
KAE8888657	III-F	hypothetical_protein_PF003g27206	Phytophthora_fragariae	stramenopile
PINF001918	III-F	PITG_01027T0	Phytophthora_infestans_T30-4	stramenopile
XP_0029095	III-F	SF-assemblin,_putative	Phytophthora_infestans_T30-4	stramenopile
KAG2530344	III-F	protein_JM18_002224	Phytophthora_kernoviae	stramenopile
RLN62338.1	III-F	hypothetical_protein_BBJ29007581	Phytophthora_kernoviae	stramenopile
KAF4320206	III-F	hypothetical_protein_G195_004307	Phytophthora_kernoviae_00238/432	stramenopile
OWY99759.1	III-F	SF-assemblin	Phytophthora_megakarya	stramenopile
KUF76468.1	III-F	SF-assemblin	Phytophthora_nicotianae	stramenopile
POM77246.1	III-F	SF-assemblin	Phytophthora_palmivora_var._palmivora	stramenopile
ETI30596.1	III-F	hypothetical_protein_F44322269	Phytophthora_parasitica_P1569	stramenopile
KAG7385932	III-F	hypothetical_protein_PHYPSEUDO_000894	Phytophthora_pseudosyringae	stramenopile
KAH7476474	III-F	SF-assemblin	Phytophthora_ramorum	stramenopile
KAE9047711	III-F	hypothetical_protein_PR002_g863	Phytophthora_rubi	stramenopile
XP_0095232	III-F	hypothetical_protein_PHYSODRAFT_558872	Phytophthora_sojae	stramenopile
PHAL008594	III-F	CEG48322_4781.0	Plasmopara_halstedii	stramenopile
XP_0245846	III-F	filament_assemblin	Plasmopara_halstedii	stramenopile
TYZ66038.1	III-F	hypothetical_protein_PybrP1003661	Pythium_brassicum	stramenopile
GAY03884.1	III-F	hypothetical_protein_PINS_011710	Pythium_insidiosum	stramenopile
TMW57470.1	III-F	hypothetical_protein_Poli38472_003395	Pythium_oligandrum	stramenopile
PULT000575	III-F	PYU1T009530	Pythium_ultimum_DAOM_BR144	stramenopile
XP_0086143	III-F	hypothetical_protein_SDRG_10108	Saprolegnia_diclina_VS20	stramenopile
SPAR006418	III-F	SPRG_05844	Saprolegnia_parasitica_CBS_223.65	stramenopile
XP_0121998	III-F	hypothetical_protein_SPRG_05844	Saprolegnia_parasitica_CBS_223.65	stramenopile
OQS04842.1	III-F	SF-assemblin	Thraustotheca_clavata	stramenopile

References

1. Ferreira, J. L. & Frischknecht, F. Parasite microtubule arrays. *Curr. Biol.* **33**, R845–R850 (2023).

2. Reber, S., Singer, M. & Frischknecht, F. Cytoskeletal dynamics in parasites. *Curr. Opin. Cell Biol.* **86**, 102277 (2024).

3. Lechtreck, K. F. & Melkonian, M. Striated microtubule-associated fibers: identification of assemblin, a novel 34-kD protein that forms paracrystals of 2-nm filaments in vitro. *J. Cell Biol.* **115**, 705–716 (1991).

4. Galati, D. F. *et al.* DisAp-dependent striated fiber elongation is required to organize ciliary arrays. *J. Cell Biol.* **207**, 705–715 (2014).

5. Crossley, R. & Holberton, D. V. Characterization of proteins from the cytoskeleton of *Giardia lamblia*. *J. Cell Sci.* **59**, 81–103 (1983).

6. Nabi, A., Yano, J., Valentine, M. S., Picariello, T. & Van Houten, J. L. SF-Assemblin genes in Paramecium: phylogeny and phenotypes of RNAi silencing on the ciliary-striated rootlets and surface organization. *Cilia* **8**, 2 (2019).

7. Preisner, H. *et al.* The Cytoskeleton of Parabasalian Parasites Comprises Proteins that Share Properties Common to Intermediate Filament Proteins. *Protist* **167**, 526–543 (2016).

8. Crossley, R. & Holberton, D. V. Selective Extraction With Sarkosyl And Repolymerization *In Vitro* Of Cytoskeleton Proteins From *Giardia*. *J. Cell Sci.* **62**, 419–438 (1983).

9. Lechtreck, K.-F. Analysis of striated fiber formation by recombinant SF-assemblin in Vitro. *J. Mol. Biol.* **279**, 423–438 (1998).

10. Soh, A. W. J. *et al.* Ciliary force-responsive striated fibers promote basal body connections and cortical interactions. *J. Cell Biol.* **219**, e201904091 (2020).

11. Harper, J. D. I., Thuet, J., Lechtreck, K. F. & Hardham, A. R. Proteins related to green algal striated fiber assemblin are present in stramenopiles and alveolates. *Protoplasma* **236**, 97–101 (2009).

12. Weber, K. *et al.* SF-assemblin, the structural protein of the 2-nm filaments from striated microtubule associated fibers of algal flagellar roots, forms a segmented coiled coil. *J. Cell Biol.* **121**, 837–845 (1993).

13. Dutcher, S. K. Elucidation of Basal Body and Centriole Functions in *Chlamydomonas reinhardtii*. *Traffic* **4**, 443–451 (2003).

14. Lechtreck, K. F. & Melkonian, M. SF-assemblin, striated fibers, and segmented coiled coil proteins. *Cell Motil. Cytoskeleton* **41**, 289–296 (1998).

15. Lechtreck, K. F. & Silflow, C. D. SF-assemblin in Chlamydomonas: sequence conservation and localization during the cell cycle. *Cell Motil. Cytoskeleton* **36**, 190–201 (1997).

16. Palm, D. *et al.* Developmental changes in the adhesive disk during Giardia differentiation. *Mol. Biochem. Parasitol.* **141**, 199–207 (2005).

17. Allen, R. D. Fine Structure, Reconstruction and Possible Functions of Components of the Cortex of *Tetrahymena pyriformis*. *J. Protozool.* **14**, 553–565 (1967).

18. Allen, R. D. THE MORPHOGENESIS OF BASAL BODIES AND ACCESSORY STRUCTURES OF THE CORTEX OF THE CILIATED PROTOZOAN *TETRAHYMENA PYRIFORMIS*. *J. Cell Biol.* **40**, 716–733 (1969).

19. Holberton, D., Baker, D. A. & Marshall, J. Segmented α-helical coiled-coil structure of the protein giardin from the Giardia cytoskeleton. *J. Mol. Biol.* **204**, 789–795 (1988).

20. Einarsson, E., Ma'ayeh, S. & Svärd, S. G. An up-date on Giardia and giardiasis. *Curr. Opin. Microbiol.* **34**, 47–52 (2016).

21. Schwartz, C. L., Heumann, J. M., Dawson, S. C. & Hoenger, A. A Detailed, Hierarchical Study of Giardia lamblia's Ventral Disc Reveals Novel Microtubule-Associated Protein Complexes. *PLoS ONE* **7**, e43783 (2012).

22. Feely, D., Holberton, D. V. & Erlandsen, S. The Biology of Giardia. In: Meyer EA, editor. *Giardiasis Amst. Elsevier* 11–50 (1990).

23. Kim, J. & Park, S.-J. Role of gamma-giardin in ventral disc formation of Giardia lamblia. *Parasit. Vectors* **12**, 227 (2019).

24. Lechtreck, K.-F. Striated fiber assemblin in apicomplexan parasites. *Mol. Biochem. Parasitol.* **128**, 95–99 (2003).

25. Francia, M. E. *et al.* Cell Division in Apicomplexan Parasites Is Organized by a Homolog of the Striated Rootlet Fiber of Algal Flagella. *PLoS Biol.* **10**, e1001444 (2012).

26. Crossley, R. & Holberton, D. Assembly of 2·5 nm filaments from giardin, a protein associated with cytoskeletal microtubules in *Giardia*. *J. Cell Sci.* **78**, 205–231 (1985).

27. Walshaw, J., Shipway, J. M. & Woolfson, D. N. Guidelines for the assembly of novel coiled-coil structures: α-sheets and α-cylinders. *Biochem. Soc. Symp.* **68**, 111–123 (2001).

Chapter 2

Disc-associated proteins mediate the unusual hyperstability of the ventral disc in *Giardia lamblia*

Christopher Nosala*, Kari D. Hagen*, Nicholas Hilton*, Tiffany M. Chase, Kelci Jones, Rita Loudermilk, Kristofer Nguyen and Scott C. Dawson

* These authors contributed equally to this work

© 2020. Published by The Company of Biologists Ltd | Journal of Cell Science (2020) 133, jcs227355. doi:10.1242/jcs.227355

RESEARCH ARTICLE

Disc-associated proteins mediate the unusual hyperstability of the ventral disc in *Giardia lamblia*

Christopher Nosala*, Kari D. Hagen*, Nicholas Hilton*, Tiffany M. Chase, Kelci Jones, Rita Loudermilk, Kristofer Nguyen and Scott C. Dawson‡

ABSTRACT

Giardia lamblia, a widespread parasitic protozoan, attaches to the host gastrointestinal epithelium by using the ventral disc, a complex microtubule (MT) organelle. The 'cup-like' disc is formed by a spiral MT array that scaffolds numerous disc-associated proteins (DAPs) and higher-order protein complexes. In interphase, the disc is hyperstable and has limited MT dynamics; however, it remains unclear how DAPs confer these properties. To investigate mechanisms of hyperstability, we confirmed the disc-specific localization of over 50 new DAPs identified by using both a disc proteome and an ongoing GFP localization screen. DAPs localize to specific disc regions and many lack similarity to known proteins. By screening 14 CRISPRi-mediated DAP knockdown (KD) strains for defects in hyperstability and MT dynamics, we identified two strains – DAP5188KD and DAP6751KD – with discs that dissociate following high-salt fractionation. Discs in the DAP5188KD strain were also sensitive to treatment with the MT-polymerization inhibitor nocodazole. Thus, we confirm here that at least two of the 87 known DAPs confer hyperstable properties to the disc MTs, and we anticipate that other DAPs contribute to disc MT stability, nucleation and assembly.

KEY WORDS: Giardia, Microtubule-associated protein, MAP, Microtubule inner protein, MIP, Microtubule, Organelle

INTRODUCTION

Many microbial eukaryotes possess complex interphase microtubule (MT) organelles that offer a unique perspective into the abilities of MT polymers to generate diverse forms and functions in cells. Such MT organelles are often defined by intricate higher order MT assemblies and contain proteins that lack similarity to well-studied MT-binding proteins in other eukaryotes (Hagen et al., 2011; Hu et al., 2006; Preisner et al., 2016). Novel MT-associated proteins may provide structural stability, facilitate organelle motility or have unknown functions required for organelle synthesis or maintenance.

The widespread protistan intestinal parasite *Giardia lamblia* is defined by one such elaborate MT organelle, the cup-shaped ventral disc (Crossley and Holberton, 1983a, 1985; Feely et al., 1982; Friend, 1966; Holberton, 1973, 1981). Infectious *G. lamblia* cysts are commonly ingested from contaminated water (Einarsson et al., 2016) and excyst into flagellated trophozoites. Using the ventral disc, trophozoites attach to the intestinal microvilli to resist being dislodged by peristalsis (Elmendorf et al., 2003; Nosala and Dawson, 2015). Colonization leads to acute or chronic diarrheal disease in humans and other animals (Nosala and Dawson, 2015). Although the molecular mechanisms of attachment are not well understood, *G. lamblia* trophozoites are thought to attach through hydrodynamic suction-based forces that result in a pressure differential underneath the disc relative to the outside medium (Hansen et al., 2006; Holberton, 1974). Conformational changes of regions of the disc may also create or modulate attachment forces (Dawson et al., 2007; Woessner and Dawson, 2012).

The parallel MTs of the ventral disc scaffold an intricate architecture of associated structural elements (Fig. 1) first described over 50 years ago (Cheissin, 1964; Friend, 1966). Approximately 100 uniformly spaced, singlet disc MTs spiral one-and-a-quarter turns to form a domed organelle 8 µm in diameter (Brown et al., 2016). An overlap zone occurs between the upper and lower parts of the spiral, and a raised ventral groove region lies adjacent to the ventral flagella (Fig. 1A,B,E). An associated structure at the disc periphery, the lateral crest (Fig. 1C), forms a seal with surfaces in early attachment (Feely et al., 1990, 1982; House et al., 2011). Overall, the disc MTs comprise >1.2 mm of polymerized tubulin (Brown et al., 2016), yet the disc MT array is unaffected by treatment with the MT-polymerization inhibitor nocodazole or the MT stabilizer Taxol (Dawson et al., 2007), implying that it is a stable structure with limited interphase MT dynamics.

The first 3D high-resolution structure was obtained using cryo-electron tomography (cryo-ET) of whole isolated ventral discs with sub-tomogram averaging (Schwartz et al., 2012). The work by Schwartz and colleagues further articulated the elaborate cytoskeletal architecture, which is highlighted by repetitive complexes comprising microribbons (MRs) and crossbridges (CBs) that coat almost every protofilament of the MT spiral array (Fig. 1). Unusual, yet regularly-spaced, microtubule-associated protein (MAP) complexes (e.g. sidearms and paddles) (Fig. 1A) and three protein densities associated with the MT lumen – i.e. the MT inner proteins (MIPs) *g*MIP5, *g*MIP7 and *g*MIP8 – were also defined (Schwartz et al., 2012).

Interphase MT organelles in protists represent an untapped reservoir of non-canonical MT-binding proteins that may govern MT assembly, nucleation or dynamics (Dawson and Paredez, 2013). Although a handful of disc-associated proteins (DAPs) termed 'giardins' were isolated from the disc two decades after the initial disc structures had been described (Crossley and Holberton, 1983a), the identities of many of the proteins composing the unique MT-associated disc structure remained elusive. In a comprehensive proteomic analysis of detergent-extracted, isolated ventral discs, we have previously identified nearly twenty new DAPs that localize to regions of the ventral disc or lateral crest (Hagen et al., 2011).

Department of Microbiology and Molecular Genetics, University of California, Davis, One Shields Avenue, Davis, CA 95616, USA.
*These authors contributed equally to this work

‡Author for correspondence (scdawson@ucdavis.edu)

C.N., 0000-0002-0179-8101; K.D.H., 0000-0001-9673-2481; T.M.C., 0000-0001-9931-7697; R.L., 0000-0001-9970-5112; K.N., 0000-0001-8520-4835; S.C.D., 0000-0002-0843-1759

Handling Editor: David Stephens
Received 31 October 2018; Accepted 29 June 2020

Journal of Cell Science (2020) 133, jcs227355. doi:10.1242/jcs.227355

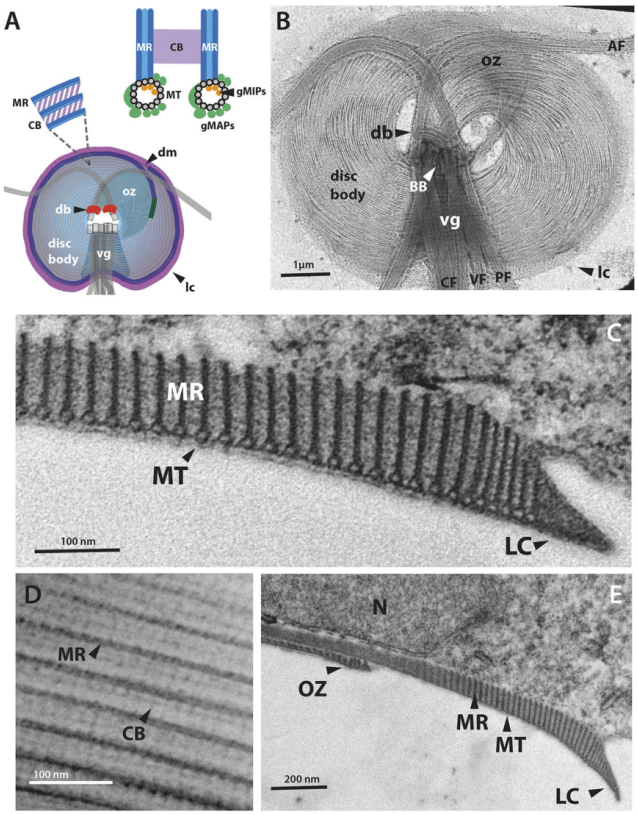

Fig. 1. Elaborate and unique protein complexes associated with the disc microtubule array. (A) Schematic of the ventral disc indicating the primary structural elements, including the disc MT array (disc body), disc margin (dm), dense bands (db), overlap zone (oz), ventral groove (vg), and lateral crest (lc). The inset shows a cross section of the MR–CB complex (MT, microtubules; MR, microribbons; CB, crossbridges) and the *G. lamblia* MAPs (*g*MAPs, green) or MIPs (gMIPs, orange). (B) Negative-stained cytoskeletal preparation of the ventral disc, highlighting the primary structural elements, basal bodies (BB), and regions of the eight cytoplasmic axonemes (AF, anterior flagella; CF, caudal flagella; PF, posteriolateral flagella; VF, ventral flagella). (C) Transmission electron microscopy of thin sections of whole embedded trophozoites showing the lateral crest (LC) and microribbons (MRs) associated with each MT of the spiral array. (D) Negative-stained preparation of the disc highlighting MRs linked to regularly spaced crossbridges (CBs). (E) The overlap zone (OZ) of the MT spiral array, together with the MR–CB complexes, are shown in cross section (N, nucleus).

Despite our emerging view of the complexity of ventral disc architecture and composition (Brown et al., 2016), we still know little about the functional basis of the unusual stability and limited MT dynamics of the disc. Thirty-four DAPs have been identified previously by using proteomic or protein-tagging approaches (Davids et al., 2008; Ebneter and Hehl, 2014; Ellis et al., 2003; Hagen et al., 2011; Lauwaet et al., 2007, 2011; Lourenço et al., 2012; Palm et al., 2005; Weiland et al., 2005). Combining a new disc proteome with a high-throughput GFP-tagging approach, we now identify an additional 53 DAPs, bringing the total number of confirmed DAPs to 87. Approximately two-thirds of all DAPs localize exclusively to the disc; the remainder also localize to other MT organelles, such as the flagella or median body. Some DAPs are conserved homologs of MAPs and MIPs (Nosala et al., 2018) known to stabilize ciliary doublet and triplet MTs (Ichikawa and Bui, 2018; Stoddard et al., 2018). Most DAPs, however, lack identifiable MT-binding domains; thus, the disc is primarily composed of proteins with ankyrin-repeat domains or proteins that lack similarity to other proteins in diverse eukaryotes.

Molecular genetics and functional analyses of the newly identified DAPs are central to understand the overall disc architecture, assembly and dynamics. Many of these DAPs are likely to stabilize singlet MTs in the spiral array or limit interphase disc MT dynamics. Here, we confirm that specific DAPs are required to confer the unusual hyperstable properties of the disc that limit MT dynamics during interphase. Although we have previously reported that the disc is insensitive to MT drugs (Dawson et al., 2007), we show here that CRISPRi-mediated knockdown (KD) of the ankyrin-repeat-containing DAP5188 causes the disc to become sensitive to the MT-polymerization inhibitor nocodazole. Moreover, KD of either DAP5188 or the novel protein DAP6571 causes ventral discs to lose some of their hyperstable properties and to dissociate during high-salt extraction. We anticipate that other recently identified DAPs – together with conserved MAPs and MIPs that are known to stabilize MTs – also confer hyperstable properties to the disc, which are required for its function of attachment to the host.

RESULTS

Biochemical fractionation and shotgun proteomic analysis of the *G. lamblia* cytoskeleton enabled the identification of over 50 new DAPs

Detergent extraction of trophozoites removes the membrane and cytosol, resulting in isolation of the entire MT cytoskeleton, including intact ventral discs and axonemes (Fig. 1B). This cytoskeletal preparation is stable in PHEM buffer for weeks (Crossley and Holberton, 1983a,b, 1985; Holberton and Ward, 1981). By using cryo-ET of such detergent-extracted cytoskeletons,

Journal of Cell Science (2020) 133, jcs227355. doi:10.1242/jcs.227355

Brown et al. have recently defined specific variations of the ventral disc architecture in the ventral groove, disc margin and overlap zone regions (Fig. 1) (Brown et al., 2016). We hypothesized that the protein density disparities observed in these distinct disc regions represent the targeting of specific DAPs to these regions.

To attempt to dissociate DAPs that confer disc structural stability or integrity, we modified a prior biochemical fractionation protocol and disrupted the cytoskeleton to obtain a disc-enriched fraction (Crossley and Holberton, 1983b; Holberton and Ward, 1981). Ventral discs were extracted with 1% Triton X-100 and 1 M KCl (Fig. S1), which facilitated the removal of contaminating proteins associated with the nuclei and cytosol, as observed by negative-staining EM. The disc and flagellar cytoskeletons (and occasionally median bodies) were retained following this high-salt extraction (Fig. S1B). Negative staining of the P1 fraction (Fig. S1D) showed loss of the majority of nuclei and retention of the disc, flagella and funis. Subsequent extractions alternating Tris-EDTA and HEPES buffers destabilized and released the disc from the axonemes and basal bodies, resulting in supernatant or pellet fractions (S2, P2, S3 and P3). These additional treatments produced a fraction enriched for ventral discs (fraction S3, Fig. S1E,F) and resulted in relaxation of the normally domed, closed ventral disc spiral (Fig. S1E,F). Many structural components of flagella were also removed in fraction S3 (Fig. S1E,F and Table S1). SDS-PAGE resolved proteins enriched in each pellet (P1, P2, P3) and supernatant (S2, S3) fraction (Fig. S1G).

Proteomic analysis of fractions enriched in ventral disc or flagellar proteins

The compositions of the initial cytoskeletal preparation (P1), two supernatant fractions (S2, S3) and the final pellet remaining after extraction (P3) were determined by mass spectrometry. Proteins with fewer than five peptides were excluded and the four fractions were compared (Fig. S1H and Table S1). One hundred and fifty-seven proteins were identified with at least five peptides in any fraction (Table S1). Tubulins, giardins, median body protein and GASP-180 family proteins were among the most commonly identified proteins. Thirty-five proteins (33 DAPs, one α- and one β-tubulin isoform) occurred in every fraction examined. The 33 DAPs included three striated fiber (SF)–assemblins (β-giardin, δ-giardin and SALP-1) (Baker et al., 1988; Jenkins et al., 2009; Palm et al., 2005), the MR protein γ-giardin (Kim and Park, 2019; Nohria et al., 1992), 11 ankyrin-repeat proteins and 14 DAPs without any known motifs (Table S1). Ten DAPs were unique to the P1 fraction; 24 proteins were enriched in the S2 fraction and nine were enriched in the P3 fraction as compared to other fractions.

Tagging of selected proteins allowed us to identify new DAPs. Forty-nine DAPs were present in the P1, S2 or S3 fractions. Although no DAPs were exclusive to the S3 fraction (Fig. S1H and Table S1), 25 proteins in the S3 fraction had disc localization and only four localized to the flagella. Approximately three quarters of the 22 confirmed flagellum-localizing proteins (basal bodies or axonemes) were present in the P1 or S2 fractions only. Lateral crest DAPs were primarily in the P1 fraction. Twenty-three DAPs identified and confirmed in this proteome had also been identified in prior disc-enriched proteome studies (Hagen et al., 2011; Lourenço et al., 2012) (Table S2). Three DAPs had been identified in other cytoskeletal proteomes (Lauwaet et al., 2011). Thirty-five DAPs had been previously identified solely by localization-based tagging methods (Davids et al., 2008; Ebneter and Hehl, 2014; Ellis et al., 2003; Hagen et al., 2011; Lauwaet et al., 2007, 2011; Palm et al., 2005; Weiland et al., 2005). Twenty-six DAPs had been identified exclusively in the ongoing GFP-tagging project of our laboratory (Nosala et al., 2018), yet were below a threshold abundance in the disc-enriched proteome (Tables S1 and S2). The 35 DAPs that lack current proteomic support were, nonetheless, included in subsequent analyses of ventral disc composition (Figs 2 and 3; Table S2).

A revised inventory of disc-associated proteins that lack known MT-binding motifs

To determine the subcellular localization of new candidate DAPs, we fused GFP to the C-terminal end of each protein and expressed the candidate DAP-GFP fusions using their native promoters (Figs 2, 3 and Figs S2–5). The disc-specific localization of 53 new DAPs was confirmed, bringing the total number of verified DAPs to 87 (Fig. 2A and Table S2). Only two of these 87 DAPs possess known outer MT-binding motifs (Fig. 2B and Table S2). One is kinesin-6a (DAP102455), which localized to the disc margin region and is the only kinesin associated with the disc. The other, DAP5374, has a CAP-GLY domain (Weisbrich et al., 2007) and localized to four disc regions (Fig. 2B and Table S2). Of the remaining confirmed DAPs, 25 lack similarity to any known protein in other eukaryotes (Fig. 2B). Each novel protein has a distinct localization pattern; not all localize to the same disc or lateral crest region. An additional 27 DAPs contain only predicted ankyrin-repeat domains (Fig. 2B and Table S2) and, like the novel proteins, were found in various regions of the disc. Several DAPs are members of conserved protein families, including: three SF-assemblins (Palm et al., 2003); four annexins, e.g. α-giardins (Bauer et al., 1999; Peattie, 1990; Weiland et al., 2005, 2003) and 13 NEK kinases (Fig. 2 and Table S2). Nine of the 13 NEKs lack conserved catalytic residues (Nosala et al., 2018). Other DAPs include those possessing a WD40-repeat domain (DAP15218), a DUF1126 domain (DAP41512), an Mlf1IP domain (DAP16424), an ENTH domain (DAP3256) (Ebneter and Hehl, 2014) or SHIPPO-repeat domains (DAP103164 and DAP9148).

DAP localization to other MT organelles and to distinct ventral disc regions

Forty-two of the 87 known DAPs localized only to specific regions of the ventral disc and not to other cytoskeletal structures (Fig. 2C). However, many of the newly identified DAPs localized to the disc and to at least one other MT structure, including the median body (Fig. 2D,F; 23 DAPs in total), the eight axonemes and basal bodies (Fig. 2E,F,H; 31 DAPs in total), or the lateral crest, a repetitive structure separate from the disc that surrounds the disc MT array (Fig. 2G,H; four DAPs in total). Eleven DAPs localized to all of the primary MT-based structures including the disc, flagella and median body (Fig. 2F).

Because ventral disc-specific GFP localization patterns varied, we further categorized the localizations of all 87 DAP-GFP strains, defining five distinct regions within the disc itself: the disc body, the disc margin, the overlap zone, the ventral groove and the dense bands (Fig. 3 and Table S2). The majority of the 87 DAPs localized to more than one disc region: 44 DAPs localized to the disc body, 37 DAPs to the disc margin, 34 DAPs to the overlap zone, 33 DAPs to the ventral groove and seven DAPs to the dense bands (Fig. 3 and Table S2). Thirty-six of the 87 DAPs localized to only one of the disc regions: six DAPs localized to the disc body only, three localized to the overlap zone only, 21 to the disc margin, four to the dense bands and two localized only to the ventral groove. Although six DAPs in total localized to the lateral crest, only two localized solely to the lateral crest and not to other disc or cytoskeletal elements (Fig. 2 and Table S2). There are also subtle, yet noticeable,

Journal of Cell Science (2020) 133, jcs227355. doi:10.1242/jcs.227355

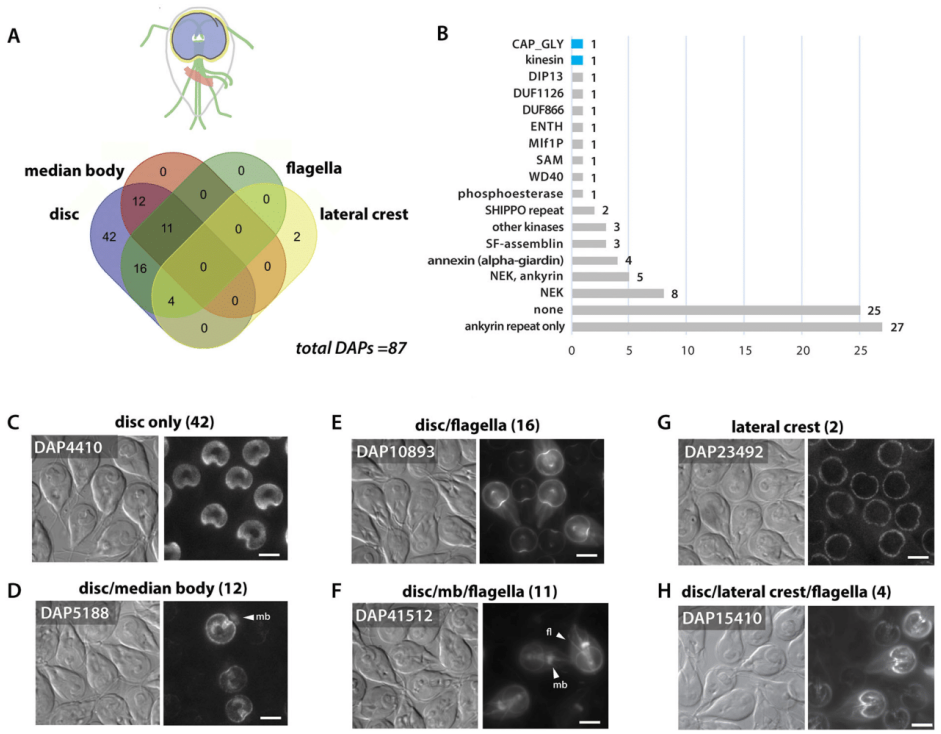

Fig. 2. Disc-associated proteins localize to dynamic and to stable MT organelles. The subcellular localizations of 87 DAP C-terminal GFP fusion proteins identified by fractionation and mass spectrometry (Fig. S1) were categorized. (A) Venn diagram indicating DAPs with overlapping localizations to the disc, flagella, median body and lateral crest. Some DAPs localized exclusively to the disc (*n*=42), whereas others localized to both the disc and other cytoskeletal structures, including the flagella (*n*=31), median body (*n*=12) and lateral crest (*n*=4). (B) PFAM domains of the 87 confirmed *G. lamblia* DAPs were summarized and ranked by abundance. A CAP_GLY domain (blue) and a kinesin motor domain (blue) are the only known MT-binding motifs that were identified in the 87 DAPs. (C–F) Representative localizations are shown for 42 DAPs localizing solely to the disc (C), for the 12 DAPs localizing to both the disc and median body (mb) (D), the 16 DAPs localizing to both the disc and flagella (fl) (E), and the 11 DAPs localizing to the disc, median body and flagella (F). (G) Two DAPs localized only to the lateral crest. (H) Four DAPs localized to the lateral crest, disc, and flagella. The flagella category includes localizations to the basal bodies and/or the cytoplasmic or membrane-bound regions of the flagella. Scale bars: 5 µm.

variations in localizations within any particular disc region in the DAP-GFP strains; for example, some strains with disc body or disc margin localizations lacked localization at the ventral groove region (Figs S2–S5).

Using CRISPRi-mediated KD to identify new DAPs associated with structural and functional defects of the ventral disc

Our lab recently developed CRISPR-Cas9-mediated transcriptional KD (CRISPRi) for *G. lamblia* (McInally et al., 2019a,b), enabling genetic analyses of the many unique disc proteins and protein complexes. Using morpholino or CRISPRi-mediated KD, we previously observed dramatic defects in the disc that highlight the structural and functional roles of the disc-associated median body protein (MBP) (Woessner and Dawson, 2012; McInally et al., 2019a,b). Here, we screened 14 CRISPRi KD strains to evaluate the contributions of specific DAPs to stabilizing the disc or limiting disc MT dynamics. These DAPs were chosen based on their limited and representative localizations to one of the disc regions defined in Figs 2,3. CRISPRi KD was performed in the mNGβtubNeo background strain, which contains a single integrated copy of mNeonGreen-tagged β-tubulin to allow easy visualization of disc MT defects. Initial visual screening and hyperstability assays indicated that 13 KD strains (all but DAP5188+288R) had discs with a wild-type appearance and 12 strains (all but DAP5188+288R and DAP6751+17R) had discs that retained wild-type stability. The 12 DAP KD strains in this initial screen with wild-type appearing, hyperstable discs were excluded from further analysis for this study (DAP3951+17R, DAP4410+618R, DAP5489+23R, DAP5883+62R, DAP9515+11R, DAP11554+17R, DAP16263+48R, DAP16342+44R, DAP17053+65R, DAP17551+11R, DAP23492+15R and DAP40016+30R). Two remaining KD strains (DAP5188+288R and DAP6751+17R) were examined further (see Fig. 2B and Fig. S4). Knockdown of DAP5188, an ankyrin-repeat protein, in the mNGβtubNeo background strain resulted in discs with an open, flattened conformation with less overall tubulin localization than the mNGβtubNeo non-specific gRNA (nsgRNA) strain (Fig. 4A–C). Population-level quantitative reverse transcription (qRT)-PCR of three independent electroporations of the DAP5188+288R strain indicated an average of ∼47% KD of DAP5188 transcription (normalized to

Journal of Cell Science (2020) 133, jcs227355. doi:10.1242/jcs.227355

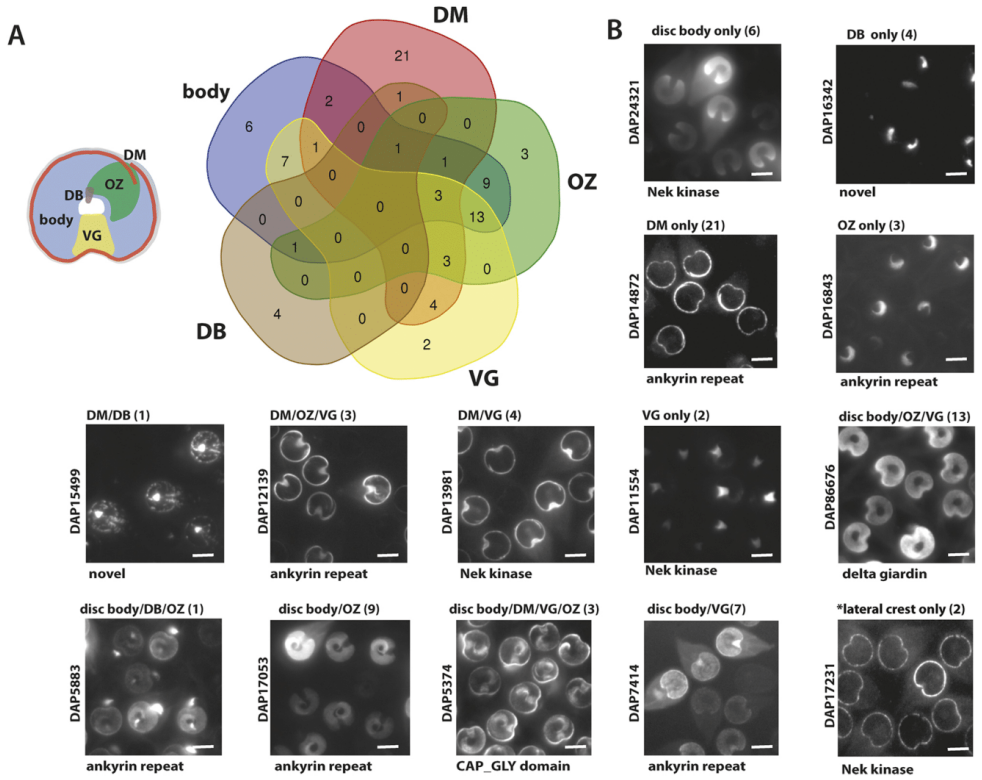

Fig. 3. DAPs localize to structurally distinct regions of the ventral disc. (A) Venn diagram showing the categorization of DAPs by their localization to distinct regions of the disc, including the MT spiral array (body), disc margin (DM), ventral groove (VG), dense bands (DB) and overlap zone (OZ). (B) Shown are 14 representative DAPs that define each of the localization categories. Whereas a representative lateral crest image is included, the last image (*) indicates that – in order to simplify the representation – six DAPs with lateral crest localization were not included in the Venn diagram. Also omitted was a representative image for the disc body/lateral crest category. Scale bars: 5 µm.

GAPDH expression) as compared to the average, normalized DAP5188 expression in three independent non-specific guide (nsgRNA) strains (Fig. 4D). Immunostaining of the DAP5188KD strain with anti-Cas9 antibody showed that the catalytically inactive Cas9 variant (dCas9) localized to the nuclei of ~25% of the trophozoites in the population (Fig. 4E). Nearly 15% of all cells in the DAP5188KD population had ventral disc defects as compared to the nsgRNA strain, yet aberrant disc phenotypes were >40% penetrant when correlated with dCas9-positive cells (Fig. 4F), supporting the population-level estimates of overall decreased DAP5188 expression observed using qRT-PCR (Fig. 4C). Knockdown of DAP6751, a novel protein, did not result in obvious visual structural defects (Fig. 4B), thus the aberrant disc phenotypic penetrance was not significantly higher than any disc phenotypic variance in the nsgRNA strain. Using qRT-PCR of three independent electroporations of the DAP6751+17R strain, we found an average KD of ~23% of DAP6751 expression (normalized to GAPDH expression) as compared to DAP6751 normalized expression in three independent non-specific guide (nsgRNA) strains. dCas9 was also detected in the nuclei of ~25% of the DAP6751KD strain population.

Ventral discs in the DAP5188 KD strain are sensitive to drugs that limit MT dynamics

We have previously shown that, in interphase, the ventral disc is insensitive to drugs that limit MT dynamics (Dawson et al., 2007), yet the MTs of the eight flagella, median body and mitotic spindles are sensitive to MT drugs (Dawson et al., 2007). Here, we developed quantitative imaging assays to evaluate the sensitivity of the MT organelles of CRISPRi KD strains to drugs that stabilize or inhibit MT polymerization (Fig. 5). After separate treatments of trophozoites with Taxol or nocodazole, we quantified the area and overall structure of the disc body, overlap zone and central bare area. As we have previously reported, the area and conformation of the ventral disc are unaffected by treatment with MT drugs (Fig. 5A,B); however, the MTs of other MT organelles (e.g. the flagella or median body) were sensitive to these MT drugs as indicated by differences in the sizes of these organelles following drug treatments (Fig. 5C).

DAP5188 localized to the disc body, disc margin, overlap zone and ventral groove (Fig. 4 and Fig. S4). To evaluate the effects of MT drugs after DAP5188 KD, the DAP5188KD and nsgRNA

Journal of Cell Science (2020) 133, jcs227355. doi:10.1242/jcs.227355

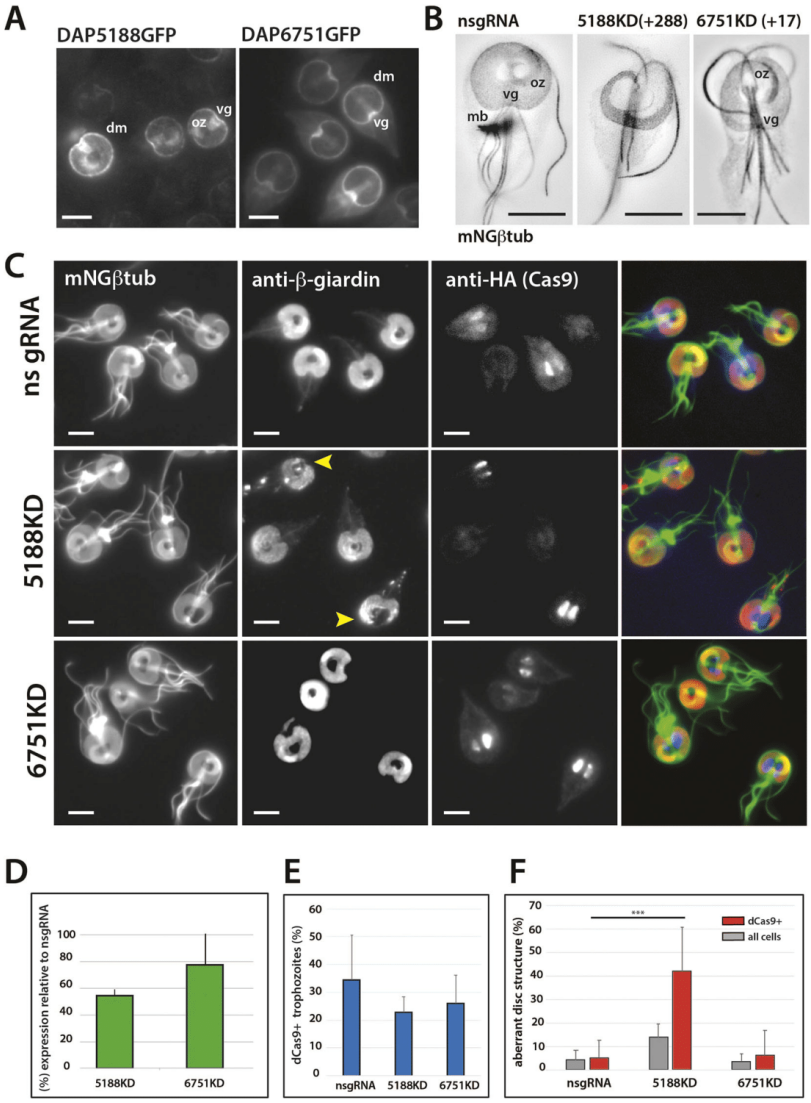

Fig. 4. Stable CRISPRi-mediated knockdowns of the disc margin proteins DAP5188 and DAP6751 have structural defects in the ventral disc. (A) C-terminal GFP fusions of the ankyrin-repeat domain protein DAP5188 and the newly identified protein DAP6751 localize to the disc margin (dm) and ventral groove (vg) regions of the ventral disc. DAP5188GFP also localizes to the disc body and overlap zone (oz). (B) High resolution SIM images of the cytoskeletal structure after CRISPRi-mediated KD of DAP5188 and DAP6751 in the mNGβtubNeo strain (inverted grayscale). (C) CRISPRi KDs of DAP5188 and DAP6751 (5188KD and 6751KD, respectively) in the mNGβtubNeo strain, immunostained with antibodies against β-giardin (microribbons) and HA (3×HA-tagged dCas9). (D) Quantification of the average expression of DAP5188 and DAP6751, normalized to the average expression of GAPDH in each strain. Error bars indicate +s.e. and correspond to the three independent electroporations of each strain. (E,F) Quantification of dCas9, as well as the penetrance of the aberrant disc phenotype within single cells. Aberrant discs in both the DAP5188KD(+288) and DAP6751KD(+17) strains are correlated with the presence of dCas9 nuclear staining, as compared to the nsgRNA control (see arrows in C). The normalized average expression of DAP5188 and DAP6751 in the KD strains is presented as a percentage of DAP5188 or DAP6751 normalized expression in the non-specific gRNA (nsgRNA) strain. dCas9 penetrance was quantified for the three independent electroporations of CRISPRi in both DAP KD strains. Of cells in each CRISPRi strain, ~25% express dCas9 (E), and aberrant disc phenotypes are strongly correlated with dCas9 expression (F) for the DAP5188KD (n=311) as compared to the nsgRNA strain (n=282). Few aberrant discs were visually observed for the DAP6751KD strain (n=148), such that a similar phenotypic correlation with dCas9 presence was not possible. In E and F, means and the corresponding confidence intervals (mean±c.i.) are presented for each experimental condition. Statistical significance was assessed using the unpaired t-test with ***$P \leq 0.05$. Scale bars: 5 µm.

Journal of Cell Science (2020) 133, jcs227355. doi:10.1242/jcs.227355

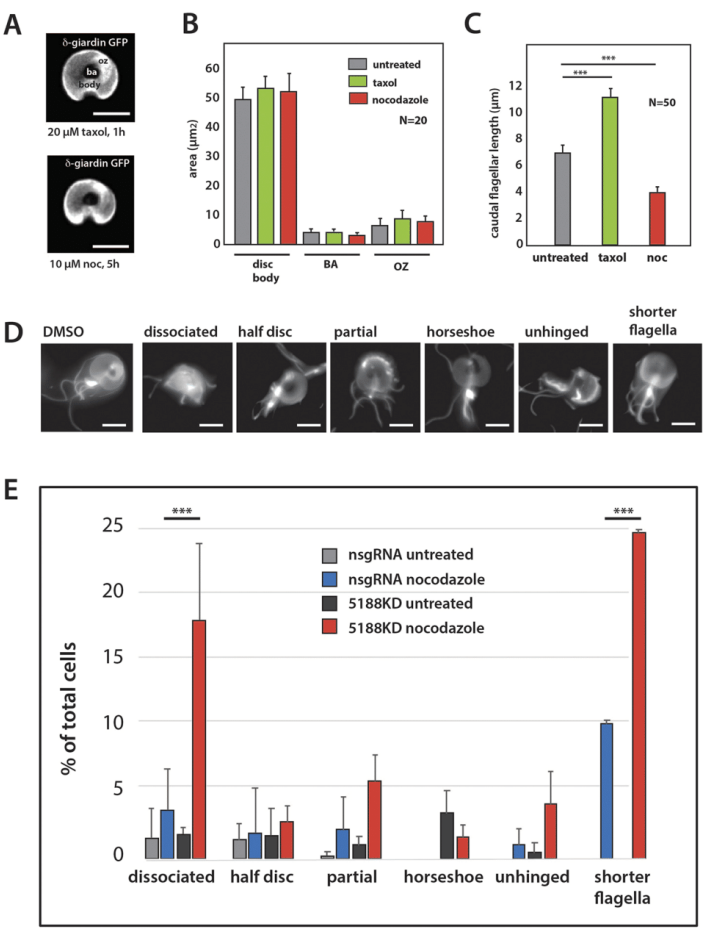

Fig. 5. Disc MT disassembly is increased in the DAP5188KD strain after nocodazole treatment. Trophozoite interphase MT dynamics are normally limited to the flagellar tips and the median body (Dawson et al., 2007). (A,B) Quantification of the effects of MT drugs on the area and overall structure of the disc body (body), overlap zone (oz) and central bare area (ba) in live cells following treatment with 10 µM nocodazole (5 h) or 20 µM Taxol (1 h). (C) Under the same treatment conditions, the eight flagella are sensitive to MT drugs and either lengthen (Taxol) or shorten (nocodazole). (D,E) Ventral discs of the DAP5188KD strain are sensitive to treatment with 10 µM nocodazole. Nocodazole treatment resulted in five distinct disc disassembly categories that were scored in fixed trophozoites (representative images are shown in D). (E) Discs in nocodazole-treated DAP5188KD cells (n=119) and untreated DAP5188KD DMSO vehicle control cells (n=127) were scored, and compared to treated (n=106) and untreated nsgRNA strain controls (n=135). Flagellar lengths were also more sensitive to length dynamics in the DAP5188KD strain (shorter flagella category). Means are presented with corresponding confidence intervals (mean±c.i.) for biological replicates of each experimental condition. Significance was assessed using the unpaired t-test with ***$P \leq 0.05$. Scale bars: 5 µm.

strains were each treated with nocodazole, and control cells were incubated with DMSO. Cells were then fixed and imaged by light microscopy, and ventral disc structural phenotypes were scored. In contrast to the nsgRNA strain, nocodazole treatment of the DAP5188KD strain resulted in an enrichment of five distinct phenotypic classes associated with increased levels of MT depolymerization in the disc (Fig. 5D). These MT drug-sensitive phenotypes included ‘dissociated’, in which the disc was largely disassembled; ‘half disc’, in which 50% of the disc was present; ‘partial’, in which the disc spiral was disrupted but the overlap zone was left intact; ‘horseshoe’, with an opened and flattened disc lacking an overlap zone; and ‘unhinged’, typified by a disc lacking an overlap zone, allowing the two ends of the disc spiral to rotate freely. We also determined the proportion of cells with ‘shorter flagella’, which was scored separately from the five categories described above. More than 25% of nocodazole-treated DAP5188KD trophozoites had a scorable phenotype, with the majority having dissociated (18%) or partial (~6%) disc phenotypes. Other scorable phenotypes (e.g. half disc, horseshoe and unhinged) were present but less abundant in the population of nocodazole-treated cells (Fig. 5E). Only ~5% of the untreated DAP5188KD (DMSO only) control trophozoites had scorable phenotypes. Furthermore, after nocodazole treatment, cells with shorter flagella were at least twice as abundant in the DAP5188KD strain as in the nsgRNA strain (Fig. 5E).

CRISPRi-mediated KD of the ankyrin-repeat protein DAP5188 or the novel protein DAP6751 limits hyperstable properties of the disc

To determine whether DAPs are required to maintain the hyperstable properties of the core disc ultrastructure, we adapted the biochemical fractionation protocol used to identify new disc proteins as an assay for disc integrity in various DAP KD strains. Whole intact discs were first extracted from cells using PHEM with detergent and a high-salt concentration (2 M KCl) indicating that the disc is ‘hyperstable’. Increased salt concentration had little effect on the dissociation of DAPs – as indicated by SDS-PAGE (Fig. 6A); and GFP-tagged disc proteins, such as DAP16343 (MBP), remain

Journal of Cell Science (2020) 133, jcs227355. doi:10.1242/jcs.227355

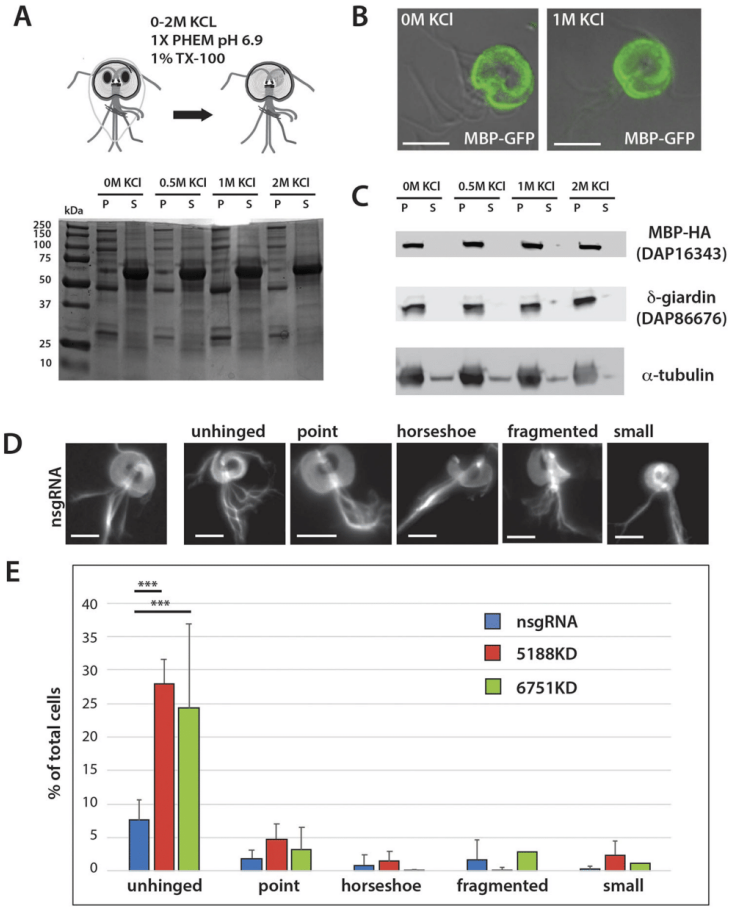

Fig. 6. Ventral discs from DAP5188KD and DAP6751KD strains dissociate after fractionation with high-salt and detergent. (A) SDS-PAGE of fractions (pellet P1 and supernatant S1) from extractions with 0–2 M KCl indicating that increased concentrations of KCl have little effect on the distribution of proteins from the fractionated discs. (B) In support, the GFP-tagged disc protein MBP (green) remains fluorescent and associated with the disc, even after extraction with 1 M KCl. (C) Western blot analysis of the SDS-PAGE shown in A, showing that α-tubulin, the MR protein δ-giardin (DAP86676), and HA-tagged MBP (DAP16343) (Woessner and Dawson, 2012) remain associated with the pelleted fraction regardless of the salt concentration (0–2 M KCl). Five categories of disc-dissociation phenotypes are observed in DAP5188KD and DAP6751KD strains after treatment. (D) Representative disc-dissociation categories are shown for the DAP5188KD strain; similar categories were observed and scored for the DAP6751KD strain (see Materials and Methods). (E) Disc-dissociation phenotypes were ranked and quantified for extracted discs from each of the three independent electroporations of the nsgRNA (blue; *n*=342), DAP5188KD (red; *n*=348) and DAP6751KD (green; *n*=635) strains. Means are presented with corresponding confidence intervals (mean ±c.i.) for biological replicates of each experimental condition. Significance was assessed using the unpaired *t*-test with ***$P \leq 0.05$. Scale bars: 5 µm.

associated with the disc even after extraction with 2 M KCl (Fig. 6B). α-tubulin and δ-giardin (a component of the MRs) also remain associated with the disc following high-salt extraction (Fig. 6C).

Stability and integrity of discs in the two CRISPRi KD strains were also evaluated following high-salt and detergent extraction (Fig. S1). Discs from the mNGβtubNeo strain retain fluorescence after extraction, allowing straightforward visual phenotypic scoring of hundreds of extracted discs. In both the CRISPRi DAP5188KD and DAP6751KD strains, we categorized five distinct phenotypic classes on the basis of severity of disc structural defects observed following disc fractionation with 2 M KCl. The least severe was 'fragmented', typified by an intact overlap zone and fully enclosed bare area, with disruption to small parts of the disc. This was followed by 'point', which lacked most of the overlap zone but retained enough to hold the two ends of the disc spiral together; 'unhinged', with flattened, open discs that lacked an overlap zone but appeared to have the same tubulin content as wild-type discs; and 'horseshoe', characterized by flattened open discs that lacked an overlap and had less tubulin than the unhinged phenotype. The most severe phenotype was 'small', in which only the central region of disc was maintained (Fig. 6D). As compared to the nsgRNA strain, >30% of CRISPRi 5188KD trophozoites had a scorable phenotype, with <30% of discs having an 'unhinged' disc phenotype (Fig. 6E). Other less-abundant phenotypic categories were 'point' or 'small'. Of CRISPRi DAP6751KD discs, ∼30% also had an aberrant phenotype following high-salt extraction. Phenotypes of the DAP6751KD strain were less severe, yet ∼25% of discs had an 'unhinged' structure after high-salt extraction; ∼5% of the DAP6751KD disc phenotypes included other categories, such as 'point' or 'fragmented'.

DISCUSSION

Cytoskeletal innovation is widespread in eukaryotic cells (Dawson and Paredez, 2013) and the elaborate architecture of the ventral disc in *G. lamblia* highlights the unique functional properties of diverse MT organelles (Russell et al., 2017). Ventral disc MTs scaffold the numerous novel and repetitive protein densities that make up the complex disc ultrastructure (Brown et al., 2016; Cheissin, 1964; Schwartz et al., 2012); however, the protein composition and

Journal of Cell Science (2020) 133, jcs227355. doi:10.1242/jcs.227355

functional roles of the repetitive MT-binding complexes governing the stability and functioning of the disc are not well understood.

By using a modified biochemical extraction protocol with shotgun proteomic analyses, combined with an ongoing subcellular localization screen, we identified and confirmed 53 new disc-associated proteins (DAPs) (Fig. 2), bringing the known DAPs to 87 in total. This study nearly triples the number of previously described DAPs (Hagen et al., 2011; Lourenço et al., 2012). Twenty-seven new DAPs are present in the detergent-extracted disc proteome, whereas the additional 26 identified by localization alone were below a threshold abundance of at least five peptides in the proteomic analyses (Table S2). Of the 87 DAPs, 85 lack similarity to known MT-associated proteins (Fig. 2) and close to one-third lack any similarity to proteins outside of *Giardia* species (Andersson et al., 2007).

Our subcellular localization of the 87 DAPs defined strikingly varied, yet distinct, localization patterns (Figs S2 and S3) that mirror the structural regions in the disc recently defined by cryo-ET (Brown et al., 2016). Specific DAPs localize to the disc margin, the dense bands, ventral groove and overlap zone regions, or the entire disc body (Fig. 3 and Figs S2–S5). DAPs associated with particular regions of the disc MT structure might, therefore, confer specific structural or functional properties (e.g. limited MT dynamics or hyperstability) that define particular regions of the disc architecture.

A new role for DAPs in limiting disc MT dynamics during interphase

Like other protists, *G. lamblia* simultaneously modulates the dynamics and stability of its MT organelles during interphase, cell division and encystation and/or excystation (Dawson et al., 2007). Although the two spindles, median body and eight flagella of *G. lamblia* exhibit both interphase and mitotic MT dynamics, such dynamics are severely limited in the interphase disc (Dawson et al., 2007; Fig. 5). Singlet MTs, such as those that comprise the mitotic spindle, typically exhibit dynamic instability – the property of MT plus ends to stochastically switch between growing and shrinking states (Mitchison and Kirschner, 1984). Dynamic instability can be stabilized or modulated by the activities of various MT plus-end-binding proteins (e.g. EB1, XMAP215) (Akhmanova and Steinmetz, 2015; Bowne-Anderson et al., 2015). Such MT plus-end-tracking proteins (+TIPs) accumulate at growing MT plus ends, where they modulate and couple dynamic MT movements to cellular structures (Akhmanova and Hoogenraad, 2005).

Here, we identified 38 DAPs that localize to the disc margin, i.e. the region of the disc that is the primary location of the MT plus ends (Brown et al., 2016). The majority of disc margin-localizing DAPs have ankyrin-repeat domains (15 DAPs) or NEK domains (six DAPs) but ten disc margin DAPs lack similarity to any known protein. Twenty-one DAPs localize exclusively to this region (Fig. 3 and Fig. S3), yet we have not identified *G. lamblia* homologs of conserved plus-end-binding proteins like EB1 (Dawson et al., 2007) or XMAP215 at the disc margin. Other MT plus ends are present in the terminal edge of the overlap zone region, to which 34 DAPs also localize. The majority of these 'overlap zone' DAPs also localize to the disc margin or disc body (Fig. S5).

The genetic interrogation of protein function in *G. lamblia* has been generally limited due to a lack of robust genetic tools and the presence of two diploid nuclei. Our recent adaptation of CRISPR interference (CRISPRi) in *G. lamblia* allows for the rapid evaluation of loss-of-function phenotypes (McInally et al., 2019a,b). CRISPRi employs the catalytically inactive Cas9 variant dCas9 to block transcription and/or elongation, resulting in stable, inducible or reversible gene KD in eukaryotes (Larson et al., 2013; Piatek et al., 2015) or bacteria (Kaczmarzyk et al., 2018; Larson et al., 2013; Liu et al., 2017; Tao et al., 2017; Zhang et al., 2016; Zuberi et al., 2017). Precise targeting is achieved using a complementary guide RNA to direct the inactive dCas9 to a specific genomic locus. CRISPRi is an effective alternative to RNAi transcriptional silencing in many systems and has been shown to have significantly fewer off-target effects (Larson et al., 2013; Smith et al., 2017; Stojic et al., 2018). Our recent demonstration of CRISPRi in *G. lamblia* showed that we could stably KD the transcription of endogenous and exogenously expressed proteins (McInally et al., 2019a,b). The *G. lamblia* CRISPRi KD plasmid can be electroporated into an existing strain that has an integrated subcellular marker, such as the mNGβtubNeo strain used here to screen and visualize defects in disc, flagellar or median body organization.

One possible role for the newly described disc margin and overlap zone DAPs is to specifically limit dynamic instability at the plus ends of ventral disc MTs in these regions, resulting in the stable interphase disc structure that is insensitive to nocodazole or Taxol (Fig. 5A). To test this idea, we created and screened several CRISPRi-mediated KDs of disc margin DAPs and determined that one, DAP5188, has a significant impact in limiting MT dynamics in the disc during interphase (Fig. 5). DAP5188 localizes to the disc margin as well as the overlap zone, disc body and ventral groove region (Fig. 4, Fig. S4 and Table S2), and is one of 32 DAPs with at least one ankyrin-repeat domain (Fig. 2B, Table S2). Structurally, DAP5188 is defined by one N-terminal and one C-terminal ankyrin repeat. Knockdown of DAP5188 results in discs with an open flattened disc conformation (Fig. 4). We have previously shown similar phenotypes with morpholino or CRISPRi-based KDs of the overlap zone protein DAP16343 (or median body protein), which results in discs with flattened open conformations and parasites with significant attachment defects (McInally et al., 2019a,b; Nosala et al., 2018; Woessner and Dawson, 2012). Many *G. lamblia* proteins that we identified in this or previous studies localize to disc regions with known MT plus-end termini (Brown et al., 2016) and might play a similar role in MT plus-end binding or in modulating plus-end dynamics in the disc.

Nocodazole-induced inhibition of MT polymerization has been used widely as an indication of high-affinity MT binding (Hoebeke et al., 1976). Nocodazole binds free tubulin dimers, preventing their incorporation into growing plus ends of MTs. During nocodazole treatment, MT-binding proteins stabilize MT dynamics at the MT plus ends, thus protecting growing MTs from steady-state cellular processes favoring MT depolymerization. Here, we defined a cellular role for DAP5188 in stabilizing disc MT dynamics. Unlike wild-type discs that are insensitive to MT drugs (Fig. 5A,B), discs in the DAP5188KD strain are sensitive to nocodazole (Fig. 5D,E). Following nocodazole treatment, discs in the DAP5188KD strain were partially to almost completely disassembled (Fig. 5D).

Stable interphase lengths of each of the four *G. lamblia* flagellar pairs were maintained through assembly by intraflagellar transport (IFT) mechanisms, counterbalanced by disassembly mechanisms mediated at flagellar tips by the depolymerizing MT motor kinesin-13 (Dawson et al., 2007; McInally et al., 2019a,b). Nocodazole treatment generally limits MT assembly and, thus, shifts the balance towards MT disassembly at flagellar tips, resulting in shorter flagella (Fig. 5C; see also Dawson et al., 2007; McInally et al., 2019a,b). Here, we observed that nocodazole treatment doubled the number of shortened flagella in the DAP5188KD strain as compared to the nocodazole-treated nsgRNA control strain

Journal of Cell Science (2020) 133, jcs227355. doi:10.1242/jcs.227355

(Fig. 5D,E). We interpret this difference as the loss of MT-stabilizing DAP5188 in KD mutants, causing flagellar tips MT to become more susceptible to the activity of constitutive MT-depolymerizing proteins, such as kinesin-13 (Dawson et al., 2007; McInally et al., 2019a,b). This increased susceptibility of flagella to MT depolymerization might, thereby, result in the increased number of trophozoites with shorter flagella lengths. Therefore, we suggest that DAP5188 acts as a more-general plus-end-binding protein, stabilizing both the disc and flagellar MT plus ends by limiting MT depolymerization during interphase.

A functional role for an ankyrin-repeat protein in selectively stabilizing MT plus ends has not been identified previously; however, a synthetically designed ankyrin-repeat protein (DARPin) that interferes with MT assembly by binding to exposed MT plus ends has been created (Pecqueur et al., 2012). Whereas ankyrin repeat proteins generally mediate protein–protein interactions and protein stability (Li et al., 2006), some ankyrin proteins have been shown to interact directly or indirectly with MTs. For example, ankyrin proteins found in human erythrocytes, muscles and neurons stabilize subsets of MTs, and can directly interact with tubulin *in vitro* (Bennett and Davis, 1981; Davis and Bennett, 1984). Furthermore, in the elaborate conoid MT organelle of the apicomplexan protist *Toxoplasma gondii*, an ankyrin-repeat protein (CPH1) links structural and motor proteins, and may interact with the tubulin-rich conoid fibers (Long et al., 2017). Whether other disc margin or overlap zone DAPs have similar properties in limiting assembly at the plus ends of disc MTs remains to be determined. The abundance of ankyrin-repeat proteins localized to the disc suggests that *G. lamblia* ankyrin-repeat proteins play similar and essential roles in limiting disc MT dynamics or stability.

The specific mechanism by which the ankyrin-repeat protein DAP5188 stabilizes MTs may also offer insight into the mechanisms of drug resistance to the benzimidazole class of compounds used to treat giardiasis, including both nocodazole and albendazole (Lindquist, 1996; Upcroft et al., 1996). Nocodazole and other benzimidazoles are potent inhibitors of cell division in *G. lamblia* and might also limit disc-mediated attachment to the host intestinal epithelium (Morgan et al., 1993). Albendazole resistance has been reported in *G. lamblia*, yet the mechanism of resistance is unknown. Albendazole resistance in helminths has been correlated to mutations in β-tubulin, yet similar mutations in *G. lamblia* β-tubulin are not associated with albendazole resistance (Lindquist, 1996; Upcroft et al., 1996). Resistant strains possess aberrant MT structures, including enlarged median bodies (Upcroft et al., 1996) indicative of unregulated MT dynamics. Thus, rather than β-tubulin mutations, it is possible that the reported resistance to commonly used benzimidazoles in *G. lamblia* is associated with mutations in MT-associated proteins, particularly those that modulate the affinity or activity of DAPs that limit MT dynamics, such as DAP5188.

DAPs are important for the hyperstability of the ventral disc

The singlet MTs of the curved, domed disc spiral array must withstand intense mechanical forces – much like the mechanical forces acting on axonemal doublet MTs during ciliary beating (Linck et al., 2014). The hyperstability of cilia, centrioles and basal bodies is thought to derive from the overall stabilizing ultrastructure of the doublet and triplet MTs (Linck et al., 2014), as well as from MAPs binding to the outside of protofilaments. MIPs form a scaffold inside the lumen of ciliary MTs, possibly enabling both MT stability and flexibility (Ichikawa and Bui, 2018). Various post-translational modifications of tubulin (PTMs) also directly or indirectly influence MT stability by regulating the localization of MAPs or other proteins that affect MT dynamics in various MT organelles (Garnham and Roll-Mecak, 2012). In contrast to cilia, the ventral disc is composed of singlet, not doublet, MTs and, thus, the disc MT ultrastructure alone is not sufficient for MT stability.

How, then, is hyperstability of the singlet disc MTs achieved? Almost all protofilaments of the disc MTs are coated with regularly spaced DAPs and higher order structures, such as the MR–CB complex (Fig. 1) (Brown et al., 2016). MR–CB complexes (Fig. 1) in particular have been implicated in the stabilization of the domed disc conformation (Holberton and Ward, 1981; Nosala et al., 2018). Three MR DAPs are SF-assemblin homologs, which stabilize both ciliary root structures in ciliated protists (Nabi et al., 2019; Weber et al., 1993) and MTs of the *Toxoplasma* apical complex (Francia et al., 2012). It is reasonable to suspect that disc hyperstability is mediated not only by MRs, but also through the other DAPs closely associated with the disc MTs.

G. lamblia lacks homologs of many canonical MAPs, such as tektin or tau, which are known to stabilize MTs (Amos, 2004, 2008; Morrison et al., 2007). To evaluate the roles of the many novel or ankyrin-repeat DAPs in *G. lamblia* that stabilize the disc architecture, we tested the integrity of discs in 14 CRISPRi DAP KD strains following high-salt and detergent extraction (Fig. 6A,B) (Crossley and Holberton, 1983b; Holberton and Ward, 1981). In contrast to discs from a nsgRNA control strain, we identified two DAP CRISPRi-mediated KD strains – DAP5188KD and DAP6751KD – whose discs were destabilized or dissociated following high-salt fractionation (Fig. 6D,E). Thus, DAP5188 and DAP6751 help to mediate hyperstability through direct or indirect interactions with the disc MTs. Discs from the DAP5188KD strain showed even greater dissociation following extraction than discs from the DAP6751KD strain (Fig. 6E). Because DAP6751 lacks similarity to other proteins, the mechanism by which DAP6751 helps to stabilize the disc remains unclear; however, the localization of both DAP6751 and DAP5188 to the disc margin could imply that the stabilization of the disc periphery is necessary to limit overall destabilization of the disc during fractionation as previously proposed (Holberton, 1981).

Conserved MIPs might also contribute to disc stability and flexibility

In addition to outer binding MAPs, an inner luminal scaffold formed by MIPs in MTs is thought to strengthen tubulin dimer and protofilament coherence, and promote MT stability and/or elasticity during ciliary beating to limit MT breakage (Ichikawa and Bui, 2018). MIPs also stabilize the singlet subpellicular MTs of the malarial parasite *Plasmodium*, enabling the stable, yet highly elastic, sporozoite cytoskeleton to flex as the parasites squeeze through host tissues (Cyrklaff et al., 2007). The three MIPs (gMIPs) that periodically repeat in the lumen of the disc singlet MTs might also support the structural integrity and extreme stability of the disc (Schwartz et al., 2012). Although the molecular identities of gMIPs remain unknown, we confirmed that DAP41512 – a Rib72 homolog with a DUF1126 domain – localizes to the disc margin, flagella and median body (Figs 2, 3; Fig. S3). Rib72 homologs may be globular MIPs, and *Tetrahymena* RIB72A and RIB72B are essential for the assembly of A-tubule MIPs in cilia (Stoddard et al., 2018). FAP52 is another widely conserved MIP that has recently been shown to localize to the inner junction of doublet MTs (Owa et al., 2018). The two FAP52 homologs (DAP15218 and DAP15956) in *G. lamblia* also localize to the stable singlet MTs of the disc and median body, as well as to the doublet axonemal MTs (Fig. 2). These localizations

Journal of Cell Science (2020) 133, jcs227355. doi:10.1242/jcs.227355

of *G. lamblia* Rib72 and FAP52 MIP homologs to the stable singlet MTs of the disc, and to the more-dynamic median body MTs support a more-general role for MIPs in promoting the stability and elasticity of interphase singlet MTs, in addition to stabilizing doublet and triplet MTs in axonemes. Moreover, two newly identified DAPs (DAP9148 and DAP103164) that localize to both the disc and axonemes (Fig. 3 and Table S2) are homologous to SHIPPO-repeat domain proteins. Although not studied outside of metazoans, SHIPPO-repeat proteins have been predicted to stabilize and add rigidity to MTs of the mammalian sperm tail (Egydio de Carvalho et al., 2002).

Additional functions of DAPs in promoting disc assembly, MT nucleation or parasite attachment to the host epithelium

Disc MTs are thought to nucleate primarily at a series of perpendicular bands termed the dense-band nucleation zone, as disc MT minus ends do not directly contact the basal bodies (Brown et al., 2016). The three distinct dense bands comprise two regions of tightly packed MTs that spiral into the nearly flat single plane at the base of the spiral disc MT array. Although we have now identified six DAPs localizing to the dense-band region (Fig. 3), the mechanism by which the dense bands support MT nucleation is unknown. Additionally, novel DAPs could mediate MT nucleation in the disc margin, as ∼39% of disc MTs nucleate from this region, possibly through a branching nucleation-type mechanism (Brown et al., 2016).

Disc-associated proteins, like DAP5188 or DAP6751, might also regulate dorsal daughter disc assembly and parental disassembly during division and encystation, resulting in the observed aberrant disc structural or stability phenotypes. During the rapid mitosis and cytokinesis of *G. lamblia* (Hardin et al., 2017), two daughter discs are assembled *de novo* on the anterior dorsal side of the parent cell, with the ventral sides of the new discs exposed on the cell surface (Tůmová et al., 2007). Other DAPs may also contribute to disc assembly. *G. lamblia* has an expanded repertoire of >70 NIMA-related kinases (or NEKs) (Manning et al., 2011) and 13 NEKs localize to various regions of the disc (Table S2). Members of the NEK family regulate centrosome separation, spindle assembly and cytokinesis during cell division through targeted phosphorylation of proteins associated with the MT cytoskeleton (Fry et al., 2017). Two disc NEKs are putatively cell cycle-specific (Davids et al., 2011). In addition to putative regulatory roles, the disc associated NEKs may contribute to disc architecture and stability or even to attachment dynamics.

Some of the newly identified DAPs might have less obvious roles in disc architecture, hyperstability, or MT dynamics. Presumably, DAPs are also required for the generation of forces by the disc for attachment to the host. DAPs could contribute to facilitating curvature and doming of the disc, or to regulating the functional properties of the disc necessary for attachment. We anticipate that the ongoing use of newly developed genetic tools, such as CRISPR interference (CRISPRi), to repress both single or multiple endogenous genes in *G. lamblia* (McInally et al., 2019a,b) will continue to uncover unique functions of DAPs regarding disc architecture, stability and flexibility during attachment-mediated infection in this widespread parasite.

MATERIALS AND METHODS

Strains and culture conditions

The *Giardia lamblia* strain WBC6 (ATCC 50803) was used to construct the DAP-GFP strains and the mNGβtubNeo background strain for CRISPRi KD s. All KD or control strains were routinely cultured in sterile 16 ml screw-capped disposable tubes (BD Falcon) containing 12 ml modified TYI-S-33 medium supplemented with bovine bile and 5% adult bovine serum and 5% fetal bovine serum (House et al., 2011). Cultures were incubated upright at 37°C without shaking and screened regularly for bacterial contamination. Puromycin was added to culture medium at a final concentration of 50 µg/ml to select for episomal plasmids in GFP and CRISPRi KD strains.

C-terminal GFP tagging of candidate disc-associated proteins

The construction of the median body protein (MBP)-GFP strain used to assess detergent extraction and dissociation of the disc with increasing KCl concentrations was described previously (Woessner and Dawson, 2012). All other *G. lamblia* DAP-GFP strains were created using Gateway cloning as previously described (Hagen et al., 2011). To add C-terminal GFP fusion tags to candidate DAPs, PCR forward primers were designed to bind 200 bp upstream of the gene to include the *G. lamblia* native promoter. Full-length genes lacking stop codons were amplified from *G. lamblia* strain WBC6 genomic DNA using either PfuTurbo Hotstart PCR Master Mix or Easy-A High Fidelity PCR Master Mix (Agilent) and were cloned into the Thermo Fisher Scientific Gateway entry vectors pENTR/D-TOPO (for blunt-end, directional TOPO cloning) or pCR8/GW/TOPO (for efficient TOPO TA cloning), respectively. Inserts were sequenced to confirm gene identity and correct orientation. To generate DAP-GFP fusions, entry vectors were recombined with the *E. coli* and *G. lamblia* Gateway destination vector pcGFP1Fpac (GenBank #MH048881) (Dawson and House, 2010) through LR recombination by using LR Clonase II Plus (Thermo Fisher Scientific). Clones were screened by AscI digest and the Plasmid Plus Midi Kit (Qiagen) was used to prepare bulk plasmid DNA. To create *G. lamblia* strains that express GFP-tagged candidate DAPs, plasmid DNA (20 µg) was introduced into 1×10^7 *G. lamblia* strain WBC6 (ATCC 50803) trophozoites by electroporation using a Bio-Rad GenePulserXcell as previously described (Dawson et al., 2007). Transfectants were initially selected with 10 µg/ml puromycin; the antibiotic concentration was increased to 50 µg/ml once cultures reached 50% confluence (typically 7–10 d). Cultures were maintained with selection for at least two weeks prior to the preparation of frozen stocks.

Construction of the *G. lamblia* mNGβtubNeo background strain for CRISPRi KDs

To generate *G. lamblia* strain mNGβtubNeo, which expresses N-terminally tagged mNeonGreen-β-tubulin from a plasmid integrated at the β-tubulin (GL50803_101291) locus, mNeonGreen with a C18 flexible linker was amplified from pjet1.2mNG_C18 (Hardin et al., 2017) and fused to the N-terminal end of β-tubulin (GL50803_101291). Gibson assembly was used to flank the gene fusion with 200 bp sequences immediately up- and downstream of the β-tubulin gene to provide the native promoter and terminator sequences, as well as to introduce the resulting fragment into NotI- and EcoRI-digested pKS_mNeonGreen-N11_NEO (Hardin et al., 2017). The resulting plasmid, pKSmNGβtubNeo, was linearized for recombination at a unique NruI site within β-tubulin (Gourguechon and Cande, 2011) and introduced into *G. lamblia* strain WBC6 by electroporation as described above. Trophozoites containing the integrated vector with a neomycin resistance marker were selected with 150 µg/ml of the neomycin analog G418 (Sigma-Aldrich) and maintained with 600 µg/ml G418. The mNeonGreen signal in the integrated mNGβtubNeo strain is retained in the absence of G418 selection.

Stable CRISPRi-based DAP KD strains

Fourteen DAPs were selected for CRISPRi knockdown (KD) based on regional localization. To create stable KD strains, gRNAs 20 nucleotide base pairs in length targeting the non-template strand of the coding region of each gene were selected using the CRISPR Guide RNA design tool (Benchling; https://benchling.com/crispr) as previously described (McInally et al., 2019a). Selection criteria for gRNAs included the minimization of predicted off-target effects, proximity to the start codon and absence of BbsI restriction enzyme sites within the gRNA sequence. One gRNA was tested for each DAP: DAP3951 (+17R: 5′-GGCTATGTCGTACGCTAT-AA-3′), DAP4410 (+618R: 5′-ACCCAGCAACAATCGTCTCG-3′), DAP5188 (+288R: 5′-GCGGCGTCCTCCCATCTGGA-3′), DAP5489 (+23R: 5′-CATGCGGCTCACAGTGAGGG-3′), DAP5883 (+62R: 5′-

Journal of Cell Science (2020) 133, jcs227355. doi:10.1242/jcs.227355

ACCGTTCTCATCGACTACAA-3′), DAP6751 (+17R: 5′-GGCTATGT-CGTACGCTATAA-3′), DAP9515 (+11R: 5′-CCAGTCTGCACTTGCC-TTAA-3′), DAP11554 (+17R: 5′-GTCACGATAGATCTGAGAGG-3′), DAP16263 (+48R: 5′-GAGACTCTAT-GAGTTTGACT-3′), DAP16342 (+44R: 5′-ACCGTTCACTTCCTCGACCA-3′), DAP17053 (+65R: 5′-C-GTGGGCAGTGCCTCCACGA-3′), DAP17551 (+11R: 5′-CCATTCCT-TAGAATCAGCTT-3′), DAP23492 (+15R: 5′-GATTTGGCGCCTCAAA-GTTG-3′), DAP40016 (+30R: 5′-CAGTGTCTCCATTAGCGTCA-3′). Annealed gRNA oligonucleotides with added four-base overhangs complementary to the ends of BbsI-digested dCas9g1pac were cloned as previously described (McInally et al., 2019a,b). The presence of the correct gRNA was confirmed using Sanger sequencing.

CRISPRi vectors (20 µg) were electroporated into *G. lamblia* strain mNGβtubNeo and selected with puromycin as described above. Two strains, DAP5188KD and DAP6751KD, with disc hyperstability defects (see Results above) were selected for further analysis after phenotypic screening; a total of three independent electroporations of each CRISPRi vector dCas5188gRNA288R, dCas6751gRNA17R and dCas9g1pac with a nonsense gRNA (nsgRNA) was performed as described previously (McInally et al., 2019a,b).

qRT-PCR of DAP gene expression in CRISPRi KD strains

Total RNA was extracted from three separate electroporations of each CRISPRi KD and nsgRNA control strain (1×10^7 trophozoites per extraction) using the Direct-Zol RNA Miniprep Kit (Zymo Research). Complementary DNA (cDNA) was generated from 1 µg of purified RNA using 5× All-In-One RT Master Mix (Applied Biological Materials). The quantitative reverse transcription (qRT)-PCR reaction was performed using *G. lamblia* cDNA from the KD or control strains (above) with the KiCqStart SYBR Green qPCR ReadyMix (Sigma) according to the manufacturer's instructions. The qRT-PCR reactions were performed with three technical replicates per condition and also included forward and reverse primers (each at a 0.3 µM final concentration) targeting the DAP5188, DAP6751 or GAPDH (positive control, GL50803_17043) genes. Primer sets were: 5188qPCR202F 5′-TACACGGCCATTATGCTTGC-3′ and 5188qPC-R373R 5′-AGATGAAGCGATTGTGGGGA-3′, 6751qPCR2442F 5′-TC-CGCAGCTATCTCAGACAG-3′ and 6751qPCR2596R 5′-CCAGGCTTA-GCGATGAAACC-3′, 17043qPCR120F 5′-CGCCATCAACAACAGGA-ACA-3′ and 17043qPCR304R 5′-ACACGGGCTTGTCATTGAAC-3′. The cDNA concentration was initially empirically determined and optimized for each primer set to minimize quantitative cycling error and variability, with 12.5 ng total used in reactions with the DAP5188 primer set, and 5 ng total used in reactions with the GAPDH and DP6751 primer sets. Quantitative RT-PCR was performed in a Roche LightCycler 480 II, with an initial melt at 95°C for 5 min, followed by 45 cycles of 95°C for 10 s, 60°C for 10 s, and 72°C for 10 s. Quantification measurements were taken during the annealing step. Following this, a melting curve was obtained by ramping from 65°C to 97°C at 0.11°C/sec. Crossing threshold (Ct) values were obtained using the Second Derivative Maximum method of calculation (Taylor et al., 2019). Quantitative data analysis was performed according to (Taylor et al., 2019). Normalized fold-expression values were averaged for three technical replicates for each of three electroporations of the same KD strain; the relative expression values (in %) for DAP5188 and DAP6751 were normalized relative to the GAPDH expression for that strain.

Immunostaining of CRISPRi KD strains

CRISPRi KD strain trophozoites (1×10^7 total cells) were immunostained as previously described (McInally et al., 2019a,b). Briefly, culture tubes were incubated on ice for 15 min and centrifuged at 900 ***g*** for 5 min. After three washes in 5 ml 1× HBS, trophozoites were resuspended in 1 ml warm 1× HBS. Aliquots (250 µl) were dispensed to warm coverslips and incubated at 37°C for 30 min in a humidified chamber to allow cells to attach. Cells were then fixed with 4% paraformaldehyde (PFA) in 1× HBS, washed three times with 2 ml PEM buffer pH 6.9 (0.1 M PIPES, 2 mM EGTA. 1 mM $MgSO_4$), quenched with 250 mM glycine and permeabilized with 0.1% Triton X-100 for 10 min. After three additional PEM washes, coverslips were blocked in 2 ml PEMBALG [100 mM PIPES pH 6.9, 1 mM EGTA, 0.1 mM $MgSO_4$, 1% BSA, 0.1% NaN_3, 100 mM lysine and 0.5% cold-water fish skin gelatin (Sigma G7765)] (Woessner and Dawson, 2012) for 30 min and incubated overnight at 4°C with anti-β-giardin (1:1000; gift from Mark Jenkins, USDA, Agricultural Research Service) and anti-CRISPRCas9 [7A9-3A3] (Abcam, ab191468, 1:1000) antibodies. Coverslips were washed three times in PEMBALG and incubated with goat anti-rabbit IgG (H+L) Cross-Adsorbed Secondary antibody Alexa Fluor 594 (A-11012, ThermoFisher/Invitrogen, 1:500) and/or goat anti-mouse IgG (H+L) Cross-Adsorbed Secondary antibody, Alexa Fluor 647 (A-11012, ThermoFisher/Invitrogen, 1:500) for 2 h at room temperature. Coverslips were then washed three times each with PEMBALG and PEM, mounted in Prolong Diamond antifade reagent (Thermo Scientific) and were allowed to cure overnight prior to imaging. Imaging was performed using differential interference contrast (DIC) and epifluorescence with a Leica DMI6000B wide-field inverted fluorescence microscope (Plan Apo 100×, NA 1.40 oil immersion objective). Optical sections were acquired at 0.2-µm intervals with a QImaging Rolera-MGi Plus EMCCD camera and MetaMorph acquisition software (MDS Analytical Technologies). Images were processed using FIJI (Schindelin et al., 2012).

Biochemical extraction and fractionation of the *G. lamblia* MT cytoskeleton

Detergent extraction of the MT cytoskeleton of *G. lamblia* was performed as previously described (Hagen et al., 2011) with several modifications (Fig. S1). Trophozoite cultures were iced and harvested as described above. Three pellets, each containing 2×10^8 cells, were washed three times with 5 ml of 1× HBS pH 7.0 (137 mM NaCl, 21 mM HEPES, 5.6 mM glucose, 5.0 mM KCl, 0.76 mM Na_2HPO_4) and centrifuged at 900 ***g*** and 4°C. To demembranate cytoskeletons, the washed pellets were resuspended in 1 ml of 0.5× HBS/1× PHEM (1× PHEM: 60 mM PIPES, 25 mM HEPES, 10 mM EGTA, 1 mM $MgCl_2$ pH 7.4) containing 1% Triton X-100, 1 M KCl and 1× HALT protease inhibitor cocktail (Roche) to prevent proteolysis. Suspensions were transferred to 1.8 ml Eppendorf tubes and vortexed continuously for 30 min (VWR Vortex-Genie2, vortex speed setting at 5) to extract the total cytoskeleton preparation 'T' (Fig. S1G). Preparation T was then centrifuged at 3000 ***g***, 25°C for 5 min. The resulting supernatant fraction was designated 'S1' and was saved for SDS-PAGE (Fig. S1G). The pellets, designated 'P1', were washed twice in 1 ml 0.5× HBS/1× PHEM lacking both 1% Triton X-100 and 1 M KCl. One P1 pellet was retained for analysis and was resuspended either in 200 µl 0.5× HBS/1× PHEM for immunostaining, negative-staining, or proteomics (Fig. S1C,D, H), or in 200 µl RIPA buffer (Sigma-Aldrich) for SDS-PAGE (Fig. S1G). The presence of intact, demembranated cytoskeletons (ventral disc with attached flagellar components) in P1 was confirmed by DIC microscopy (Fig. S1B), and immunostaining with anti-α-tubulin (anti-TAT1; Sigma-Aldrich, 0002091, 1:250) and anti-δ-giardin (gift from Mark Jenkins, USDA ARS, 1:1000) antibodies confirmed retention of the disc and flagella (Fig. S1C).

To further dissociate the cytoskeletons, the remaining two P1 pellets were resuspended in 1 ml of 10 mM Tris, 1 mM EDTA pH 7.7, incubated for 48 h at 4°C and centrifuged at 3000 ***g*** at 25°C for 5 min. The supernatant was retained for SDS-PAGE or proteomic analysis as the 'S2' fraction (Fig. S1A, G), and the 'P2' complexes were washed twice in 1 ml 10 mM Tris, 1 mM EDTA pH 7.7 and centrifuged at 3000 ***g*** as described above. One P2 pellet was resuspended in 200 µl RIPA buffer for SDS-PAGE, the second was resuspended in 1 ml of 10 mM HEPES, 5 mM EDTA pH 8.7 and incubated for an additional 48 h at 4°C. After the final incubation, the extracted complexes were centrifuged at 3000 ***g***, at 25°C for 5 min. The supernatant was retained as the 'S3' fraction, and the final 'P3' pellet was washed twice in 1 ml of 10 mM HEPES, 5 mM EDTA pH 8.7 and resuspended either in 200 µl 1× PHEM for immunostaining or proteomics or in 200 µl RIPA for SDS-PAGE. To confirm dissociation of axonemes from discs, an aliquot of the S3 fraction was immunostained using the anti-δ-giardin antibody and imaged using DIC and epifluorescence microscopy (Fig. S1E,F).

SDS-PAGE and western blotting

For SDS-PAGE of fractionated proteins (Fig. S1G), the total cytoskeletal preparation T and all supernatant fractions (S1, S2, S3) were mixed 1:1 with RIPA buffer. Aliquots (200 µl) of preparation T, supernatants S1, S2 and S3,

Journal of Cell Science (2020) 133, jcs227355. doi:10.1242/jcs.227355

and of the pellets resuspended in RIPA buffer (P1, P2, P3) were then sonicated (Heat Systems W-375, duty cycle 50%, output control 2, ten pulses). Protein concentrations were determined by the Pierce BCA assay (Thermo Scientific) using a Perkin-Elmer Victor ×3 plate reader. Cell lysate samples containing 2.4 µg of total protein were run on Precise Tris·HEPES protein gels (4–20%, ThermoFisher). Protein gels were stained with Instant Blue (Expedeon) for 1 h at room temperature and were destained overnight in MilliQ water when necessary (Fig. S1G).

For western blotting of cytoskeletal preparations, cell lysate samples (20 µg total protein) were electrophoresed as described above. After separation, proteins were transferred to 0.45 µm nitrocellulose membrane (Bio-Rad) using a Bio-Rad Mini Trans-Blot cell at 100 V for 2 h on ice. Membranes were blocked for 1 h at room temperature in 5% (w/v) milk in PBS with 0.05% Tween. Antibodies were diluted in 5% (w/v) milk in PBS or TBS with 0.05% Tween as follows: mouse monoclonal antibody against hemagglutinin (HA), clone HA-7 (Sigma, H9658, 1:5000); rabbit anti-δ-giardin (gift from Mark Jenkins, USDA ARS, 1:1000); mouse monoclonal antibody against α-tubulin (TAT1; Sigma-Aldrich, 00020911, 1:2500), goat anti-mouse IgG (H+L) HRP conjugate (Bio-Rad, 170516, 1:10000); goat anti-rabbit IgG (H+L) HRP conjugate (Bio-Rad, 170515, 1:5000). Amersham ECL Prime substrate (GE Healthcare) was used for chemiluminescence detection with a ProteinSimple AlphaImager documentation system.

Mass spectrometry and proteomic analysis

Fractions P1, S2, S3 and P3 (20 µg total protein in the fractionation buffers described above) were processed at the UC Davis Genome Center Proteomics Core facility for shotgun mass spectrometry analyses. All shotgun LC-MS/MS samples were analyzed the using X! Tandem search engine [The GPM, https://www.thegpm.org; version X! Tandem Alanine (2017.2.1.4)]. X! Tandem was used to search the uniprotgiardiaintestinalis_Craprev database (14528 entries) assuming the digestion enzyme trypsin and with a fragment ion mass tolerance of 20 p.p.m. and a parent ion tolerance of 20 p.p.m. X! Tandem variable specified amino acid modifications were Glu→pyro-Glu in the N-terminus, loss of NH_3 in the N-terminus, Gln→pyro-Glu in the N-terminus, deamidation of Asp and Gln, oxidation of Met and Trp, and dioxidation of Met and Trp. Scaffold Proteome software (version 4.8.4; Proteome Software Inc., Portland, OR) was used to validate MS/M-based peptide and protein identifications. Peptide identifications were accepted if they exceeded specific thresholds of the database search engine. Protein identifications were accepted if they contained at least five identified peptides. Proteins that contained similar peptides and could not be differentiated on the basis of MS/MS analysis alone were grouped, in order to satisfy the principles of parsimony. Proteins that shared substantial peptide evidence were grouped into clusters.

Live imaging of GFP-tagged DAP strains

DAP-GFP fusion strains were thawed from frozen stocks and cultured for 24 to 48 h prior to live imaging. Cells were iced and harvested as described above, resuspended in 1 ml warm (37°C) TYI-S-33, and 300 µl aliquots were incubated in 96-well black glass-bottomed imaging plates (Cellvis, Mountain View, CA) for ≤2 h at 37°C in a nitrogen-enriched atmosphere to promote attachment. 1 ml medium was replaced with 1× HBS, and trophozoites were incubated under the same conditions for 30 min. Additional warm (37°C) 1× HBS washes were performed as needed during imaging to remove detached cells. DIC and epifluorescence imaging was performed with a Leica DMI6000B microscope as described above. Images were processed using Fiji (Schindelin et al., 2012) and 2D maximum-intensity projections were created from the 3D data sets when required.

Structured illumination microscopy

Trophozoites (1×10^7 cells) from CRISPRi strains were iced, harvested and washed twice in 5 ml 1× HBS. Live trophozoites were resuspended in 1× HBS and allowed to attach to coverslips as described above. Attached cells were fixed *in situ* with 4% PFA in 1× HBS and quenched with 250 mM glycine. Coverslips were mounted with Prolong Diamond antifade (Thermo Scientific) and allowed to cure overnight prior to imaging. 3D stacks were collected at 0.125 µm intervals on a Nikon N-SIM Structured Illumination Super-resolution Microscope with a 100×/NA 1.49 objective, 100 EX V-R diffraction grating and an Andor iXon3 DU-897E EMCCD. Raw images were acquired in the 3D-SIM format (NIS-Elements, Nikon); reconstruction used three different diffraction grating angles each with five translations. Single-channel data spanned ∼5 µm depth and required acquisition times of ∼6 min. Image reconstruction was performed in NIS-Elements.

Transmission electron microscopy

Detergent extracted cytoskeletal preparations (see above) were applied to 400 mesh formvar/carbon coated glow-discharged grids. Negative staining was performed by applying 1% PTA pH 5.4, and grids were dried by blotting without washes. For thin sections, *G. lamblia* trophozoites that had been pelleted or had attached to ACLAR discs (Electron Microscopy Sciences) were fixed for 10 min in 4% PFA and fixed again for 1 h in 1% OsO_4. Cells were washed three times with cold doubly distilled water to remove fixative, dehydrated through ascending concentrations of ethanol (30%, 50%) and incubated for 1 h in 2% uranyl acetate in 50% ethanol. Dehydration continued through 70% ethanol and three changes of 95% ethanol and was completed with three changes in 100% ethanol for a minimum of 10 min each change. Cells were embedded in 1:1 epoxy resin: acetone overnight at room temperature. The next day the resin was removed and replaced with 100% resin twice for 2 h each. The ACLAR discs were placed at the bottom of a flat bottom beam capsule with the cells facing up and the capsule was filled with fresh resin. The blocks were polymerized at 70°C overnight. The blocks were trimmed and thin sections were cut with a Leica UCT ultramicrotome (Leica Ultracut UCT, Leica, Vienna, Austria), and stained with 2% uranyl acetate in 70% ethanol plus lead citrate before viewing in the Talos L120C electron microscope (FEI Company/Thermo Scientific, Hillsboro, OR; made in Eindhoven, The Netherlands) at 100KV. Images were acquired using the fully integrated Ceta CMOS camera.

Assay of disc hyperstability in CRISPRi KD strains after detergent and high-salt extraction

To determine whether the ventral discs of KD strains retained hyperstability, trophozoites from one confluent 12 ml culture (2×10^7 cells) of each DAP KD strain were harvested, resuspended in 1 ml 0.5× HBS/1× PHEM with 1% Triton X-100 and 2 M KCl and extracted with vortex mixing as described previously for fractionation of the cytoskeleton. P1 was resuspended in 200 µl 0.5× HBS/1× PHEM. For imaging, ∼100 µl of each detergent extracted cytoskeletal preparation was added to poly-L-lysine treated coverslips and allowed to settle for 15 min. The adhered cytoskeletons were fixed with 4% PFA in 1× HBS for 2 min and quenched with 250 mM glycine for 5 min. Coverslips were mounted on slides using Prolong Diamond antifade mounting medium and cured overnight. Cytoskeletons were examined with a Leica DMI 6000B fluorescence microscope and *z*-stacks of random fields were acquired. For scoring and presentation, 2D projections were created from acquired *z*-stacks. Twelve CRISPRi-mediated DAP KD strains that lacked aberrant disc phenotypes with this assay were excluded from further analysis. For DAP5188KD, DAP6751KD and the nsgRNA control strains, an average of 120 cytoskeletons were counted and evaluated for each independent electroporation (biological replicate).

For quantification of aberrant ventral discs, cytoskeletons were scored and assigned to six categories based on phenotype. Discs with a wild-type appearance had an intact overlap zone and an encircled bare area. 'Unhinged' discs lacked an intact overlap zone. Discs in the 'point' category were flattened and lacked an overlap zone, yet two tips of the disc spiral still touched at a single point. 'Horseshoe' discs lacked an overlap zone and had an opened bare area region no longer surrounded by disc MTs. The 'fragmented' category includes discs that were largely intact but had gaps or portions missing from the disc spiral. 'Small' describes discs with an enclosed, small bare area, lacking MTs on the outer half perimeter of the disc. Discs that did not clearly fall into one of the categories or were unscoreable (e.g. discs stacked upon each other, discs at an angle, or discs obscured by inorganic matter) were excluded from the count.

Assay of disc MT dynamics in CRISPRi KD strains using nocodazole or Taxol

For analyses of MT dynamics, the stable CRISPRi KD strain DAP5188KD and the control strain carrying a non-specific gRNA (nsgRNA) were thawed

and grown for 24 h at 37°C in TYI-S-33 medium. Cultures (12 ml) were then incubated on ice for 15 min, divided equally into two 8 ml screw-cap tubes (Fisher Scientific) and grown for an additional 16 h at 37°C. Following this incubation, one tube was incubated with a final concentration of 10 µM nocodazole in DMSO for 5 h, while the remaining tube was incubated with DMSO alone. Alternatively, one tube was incubated with 20 µM Taxol in DMSO for 1 h and the remaining tube was incubated with DMSO alone. Cells were then chilled for 15 min at 4°C and harvested by centrifugation (900 ***g***). The medium was decanted and pellets were washed three times with 1× HBS (4°C). After the final centrifugation step, the cell pellet was resuspended in 0.5 ml 1× HBS. Prior to imaging, trophozoites were allowed to attach to coverslips for 15 min at 37°C, then fixed in a final concentration of 4% PFA in 1× HBS for 2 min. Fixation was quenched by incubating coverslips in 250 mM glycine for 5 min. Coverslips were mounted on slides using Prolong Diamond antifade mountant and slides were cured overnight prior to imaging with a Leica DMI 6000B wide-field microscope as described above. For both the DAP5188KD and the nsgRNA control strain, three independent electroporations were imaged and scored. Images were captured of random fields and blind slide reading was performed to minimize investigator bias. Disc phenotypes were then scored for every trophozoite in a given frame. An average of 165 cells per electroporation were imaged.

Disc phenotypes following nocodazole treatment were assigned to six categories that described the range of variation of visually observable aberrant ventral disc MT architecture. As 'wild-type' discs are insensitive to nocodazole, they retained an intact 3D architecture with an overlap zone and a completely encircled bare area. 'Dissociated' discs were completely disrupted; cells in this category retained tubulin fluorescence in the anterior of the cell but lacked any disc structure whatsoever. 'Half discs' were those that had close to one half of the disc missing on the anterior-posterior axis. The 'partial' disc category included discs in which portions of the spiral were dissociated or fragmented. 'Horseshoe' category discs had an open and flattened U-shaped conformation with the bare area no longer enclosed. Lastly, 'unhinged' discs were flattened and lacked an intact overlap zone, which allowed the upper and sides of the disc to twist or rotate freely.

Acknowledgements
We thank Dr Alex Paredez (University of Washington, Seattle, WA) for plasmids pjet1.2-mNeonGreen_C18 and pKS_mNeonGreen-N11_NEO, and Dr Mark Jenkins (U.S. Department of Agriculture, Agricultural Research Service, Parasitic Diseases Laboratory) for *G. lamblia* anti-β-giardin and anti-δ-giardin antibodies. We thank Dr Michael Paddy (UC Davis MCB Microscopy Imaging Facility, UC Davis Campus Core Research Facility) for helpful advice and use of the 3i SDC and Nikon N-SIM microscopes. We also thank Patricia Kysar (UC Davis MCB Electron Microscopy Lab) for advice and TEM training and Michelle Salemi and Dr Brett Phinney (UCD Proteomics Core) for assistance with mass spectroscopy.

Competing interests
The authors declare no competing or financial interests.

Author contributions
Conceptualization: C.N., K.D.H., N.H., S.C.D.; Methodology: C.N., K.D.H., N.H., T.M.C., K.J., R.L., K.N.; Validation: C.N., K.D.H., N.H., T.M.C., R.L., K.N.; Formal analysis: C.N., K.D.H., N.H., S.C.D.; Investigation: C.N., K.D.H., N.H., T.M.C., S.C.D.; Resources: C.N., K.D.H., N.H., T.M.C.; Data curation: C.N., K.D.H., N.H., S.C.D.; Writing - original draft: C.N., K.D.H., N.H., S.C.D.; Writing - review & editing: C.N., K.D.H., N.H., S.C.D.; Visualization: C.N., K.D.H., N.H., K.N., S.C.D.; Supervision: S.C.D.; Project administration: S.C.D.; Funding acquisition: S.C.D.

Funding
This work was supported by the National Institutes of Health (grant number: NIH 5R01AI077571-11 to S.C.D.) and the Center for Comparative Medicine at University of California Davis School of Medicine (grant number: T32 AI060555 Animal Models of Infectious Diseases Training Program to C.N). Deposited in PMC for release after 12 months.

Data availability
Mass spectrometry data from each of the disc fractionations are deposited in the MassIVE database, with accession number MSV000085943.

Supplementary information
Supplementary information available online at
https://jcs.biologists.org/lookup/doi/10.1242/jcs.227355.supplemental

References
Akhmanova, A. and Hoogenraad, C. C. (2005). Microtubule plus-end-tracking proteins: mechanisms and functions. *Curr. Opin. Cell Biol.* **17**, 47-54. doi:10.1016/j.ceb.2004.11.001

Akhmanova, A. and Steinmetz, M. O. (2015). Control of microtubule organization and dynamics: two ends in the limelight. *Nat. Rev. Mol. Cell Biol.* **16**, 711-726. doi:10.1038/nrm4084

Amos, L. A. (2004). Microtubule structure and its stabilisation. *Org. Biomol. Chem.* **2**, 2153-2160. doi:10.1039/b403634d

Amos, L. A. (2008). The tektin family of microtubule-stabilizing proteins. *Genome Biol.* **9**, 229. doi:10.1186/gb-2008-9-7-229

Andersson, J. O., Sjögren, A. M., Horner, D. S., Murphy, C. A., Dyal, P. L., Svärd, S. G., Logsdon, J. M., Jr, Ragan, M. A., Hirt, R. P. and Roger, A. J. (2007). A genomic survey of the fish parasite Spironucleus salmonicida indicates genomic plasticity among diplomonads and significant lateral gene transfer in eukaryote genome evolution. *BMC Genomics* **8**, 51. doi:10.1186/1471-2164-8-51

Baker, D. A., Holberton, D. V. and Marshall, J. (1988). Sequence of a giardin subunit cDNA from *Giardia lamblia*. *Nucleic Acids Res.* **16**, 7177. doi:10.1093/nar/16.14.7177

Bauer, B., Engelbrecht, S., Bakker-Grunwald, T. and Scholze, H. (1999). Functional identification of alpha 1-giardin as an annexin of *Giardia lamblia*. *FEMS Microbiol. Lett.* **173**, 147-153. doi:10.1111/j.1574-6968.1999.tb13496.x

Bennett, V. and Davis, J. (1981). Erythrocyte ankyrin: immunoreactive analogues are associated with mitotic structures in cultured cells and with microtubules in brain. *Proc. Natl. Acad. Sci. USA* **78**, 7550-7554. doi:10.1073/pnas.78.12.7550

Bowne-Anderson, H., Hibbel, A. and Howard, J. (2015). Regulation of microtubule growth and catastrophe: unifying theory and experiment. *Trends Cell Biol.* **25**, 769-779. doi:10.1016/j.tcb.2015.08.009

Brown, J. R., Schwartz, C. L., Heumann, J. M., Dawson, S. C. and Hoenger, A. (2016). A detailed look at the cytoskeletal architecture of the *Giardia lamblia* ventral disc. *J. Struct. Biol.* **194**, 38-48. doi:10.1016/j.jsb.2016.01.011

Cheissin, E. M. (1964). Ultrastructure of lamblia duodenalis. I. Body surface, sucking disc and median bodies. *J. Protozool.* **11**, 91-98. doi:10.1111/j.1550-7408.1964.tb01725.x

Crossley, R. and Holberton, D. V. (1983a). Characterization of proteins from the cytoskeleton of *Giardia lamblia*. *J. Cell Sci.* **59**, 81-103.

Crossley, R. and Holberton, D. V. (1983b). Selective extraction with Sarkosyl and repolymerization in vitro of cytoskeleton proteins from *Giardia*. *J. Cell Sci.* **62**, 419-438.

Crossley, R. and Holberton, D. V. (1985). Assembly of 2.5 nm filaments from giardin, a protein associated with cytoskeletal microtubules in *Giardia*. *J. Cell Sci.* **78**, 205-231.

Cyrklaff, M., Kudryashev, M., Leis, A., Leonard, K., Baumeister, W., Menard, R., Meissner, M. and Frischknecht, F. (2007). Cryoelectron tomography reveals periodic material at the inner side of subpellicular microtubules in apicomplexan parasites. *J. Exp. Med.* **204**, 1281-1287. doi:10.1084/jem.20062405

Davids, B. J., Gilbert, M. A., Liu, Q., Reiner, D. S., Smith, A. J., Lauwaet, T., Lee, C., McArthur, A. G. and Gillin, F. D. (2011). An atypical proprotein convertase in *Giardia lamblia* differentiation. *Mol. Biochem. Parasitol.* **175**, 169-180. doi:10.1016/j.molbiopara.2010.11.008

Davids, B. J., Williams, S., Lauwaet, T., Palanca, T. and Gillin, F. D. (2008). *Giardia lamblia* aurora kinase: a regulator of mitosis in a binucleate parasite. *Int. J. Parasitol.* **38**, 353-369. doi:10.1016/j.ijpara.2007.08.012

Davis, J. Q. and Bennett, V. (1984). Brain ankyrin. A membrane-associated protein with binding sites for spectrin, tubulin, and the cytoplasmic domain of the erythrocyte anion channel. *J. Biol. Chem.* **259**, 13550-13559.

Dawson, S. C. and House, S. A. (2010). Imaging and analysis of the microtubule cytoskeleton in giardia. *Methods Cell Biol.* **97**, 307-339. doi:10.1016/S0091-679X(10)97017-9

Dawson, S. C. and Paredez, A. R. (2013). Alternative cytoskeletal landscapes: cytoskeletal novelty and evolution in basal excavate protists. *Curr. Opin. Cell Biol.* **25**, 134-141. doi:10.1016/j.ceb.2012.11.005

Dawson, S. C., Sagolla, M. S., Mancuso, J. J., Woessner, D. J., House, S. A., Fritz-Laylin, L. and Cande, W. Z. (2007). Kinesin-13 regulates flagellar, interphase, and mitotic microtubule dynamics in Giardia intestinalis. *Eukaryot. Cell* **6**, 2354-2364. doi:10.1128/EC.00128-07

Ebneter, J. A. and Hehl, A. B. (2014). The single epsin homolog in *Giardia lamblia* localizes to the ventral disk of trophozoites and is not associated with clathrin membrane coats. *Mol. Biochem. Parasitol.* **197**, 24-27. doi:10.1016/j.molbiopara.2014.09.008

Egydio de Carvalho, C., Tanaka, H., Iguchi, N., Ventela, S., Nojima, H. and Nishimune, Y. (2002). Molecular cloning and characterization of a complementary DNA encoding sperm tail protein SHIPPO 1. *Biol. Reprod.* **66**, 785-795. doi:10.1095/biolreprod66.3.785

Einarsson, E., Ma'ayeh, S. and Svard, S. G. (2016). An up-date on Giardia and giardiasis. *Curr. Opin. Microbiol.* **34**, 47-52. doi:10.1016/j.mib.2016.07.019

Ellis, J. G., Davila, M. and Chakrabarti, R. (2003). Potential involvement of extracellular signal-regulated kinase 1 and 2 in encystation of a primitive eukaryote, *Giardia lamblia*. Stage-specific activation and intracellular localization. *J. Biol. Chem.* **278**, 1936-1945. doi:10.1074/jbc.M209274200

Elmendorf, H. G., Dawson, S. C. and McCaffery, J. M. (2003). The cytoskeleton of *Giardia lamblia*. *Int. J. Parasitol.* **33**, 3-28. doi:10.1016/S0020-7519(02)00228-X

Feely, D. E., Schollmeyer, J. V. and Erlandsen, S. L. (1982). *Giardia* spp.: distribution of contractile proteins in the attachment organelle. *Exp. Parasitol.* **53**, 145-154. doi:10.1016/0014-4894(82)90100-X

Feely, D. E., Hoberton, D. V. and Erlandsen, S. L. (1990). The biology of *Giardia*. In *Giardiasis*, Vol. 3 (ed. E. A. Meyer), pp. 11-50. Amsterdam: Elsevier.

Francia, M. E., Jordan, C. N., Patel, J. D., Sheiner, L., Demerly, J. L., Fellows, J. D., de Leon, J. C., Morrissette, N. S., Dubremetz, J.-F. and Striepen, B. (2012). Cell division in Apicomplexan parasites is organized by a homolog of the striated rootlet fiber of algal flagella. *PLoS Biol.* **10**, e1001444. doi:10.1371/journal.pbio.1001444

Friend, D. S. (1966). The fine structure of *Giardia muris*. *J. Cell Biol.* **29**, 317-332. doi:10.1083/jcb.29.2.317

Fry, A. M., Bayliss, R. and Roig, J. (2017). Mitotic regulation by NEK KINASE NETWorks. *Front. Cell Dev. Biol.* **5**, 102. doi:10.3389/fcell.2017.00102

Garnham, C. P. and Roll-Mecak, A. (2012). The chemical complexity of cellular microtubules: tubulin post-translational modification enzymes and their roles in tuning microtubule functions. *Cytoskeleton (Hoboken)* **69**, 442-463. doi:10.1002/cm.21027

Gourguechon, S. and Cande, W. Z. (2011). Rapid tagging and integration of genes in Giardia intestinalis. *Eukaryot. Cell* **10**, 142-145. doi:10.1128/EC.00190-10

Hagen, K. D., Hirakawa, M. P., House, S. A., Schwartz, C. L., Pham, J. K., Cipriano, M. J., De La Torre, M. J., Sek, A. C., Du, G., Forsythe, B. M. et al. (2011). Novel structural components of the ventral disc and lateral crest in Giardia intestinalis. *PLoS Negl. Trop. Dis.* **5**, e1442. doi:10.1371/journal.pntd.0001442

Hansen, W. R., Tulyathan, O., Dawson, S. C., Cande, W. Z. and Fletcher, D. A. (2006). Giardia lamblia attachment force is insensitive to surface treatments. *Eukaryot. Cell* **5**, 781-783. doi:10.1128/EC.5.4.781-783.2006

Hardin, W. R., Li, R., Xu, J., Shelton, A. M., Alas, G. C. M., Minin, V. N. and Paredez, A. R. (2017). Myosin-independent cytokinesis in Giardia utilizes flagella to coordinate force generation and direct membrane trafficking. *Proc. Natl. Acad. Sci. USA* **114**, E5854-E5863. doi:10.1073/pnas.1705096114

Hoebeke, J., Van Nijen, G. and De Brabander, M. (1976). Interaction of oncodazole (R 17934), a new antitumoral drug, with rat brain tubulin. *Biochem. Biophys. Res. Commun.* **69**, 319-324. doi:10.1016/0006-291X(76)90524-6

Holberton, D. V. (1973). Fine structure of the ventral disk apparatus and the mechanism of attachment in the flagellate *Giardia muris*. *J. Cell Sci.* **13**, 11-41.

Holberton, D. V. (1974). Attachment of *Giardia*-a hydrodynamic model based on flagellar activity. *J. Exp. Biol.* **60**, 207-221.

Holberton, D. V. (1981). Arrangement of subunits in microribbons from *Giardia*. *J. Cell Sci.* **47**, 167-185.

Holberton, D. V. and Ward, A. P. (1981). Isolation of the cytoskeleton from *Giardia*. Tubulin and a low-molecular-weight protein associated with microribbon structures. *J. Cell Sci.* **47**, 139-166.

House, S. A., Richter, D. J., Pham, J. K. and Dawson, S. C. (2011). Giardia flagellar motility is not directly required to maintain attachment to surfaces. *PLoS Pathog.* **7**, e1002167. doi:10.1371/journal.ppat.1002167

Hu, K., Johnson, J., Florens, L., Fraunholz, M., Suravajjala, S., DiLullo, C., Yates, J., Roos, D. S. and Murray, J. M. (2006). Cytoskeletal components of an invasion machine–the apical complex of Toxoplasma gondii. *PLoS Pathog.* **2**, e13. doi:10.1371/journal.ppat.0020013

Ichikawa, M. and Bui, K. H. (2018). Microtubule inner proteins: a meshwork of luminal proteins stabilizing the doublet microtubule. *BioEssays* **40**, 1700209. doi:10.1002/bies.201700209

Jenkins, M. C., O'Brien, C. N., Murphy, C., Schwarz, R., Miska, K., Rosenthal, B. and Trout, J. M. (2009). Antibodies to the ventral disc protein δ-giardin prevent in vitro binding of *Giardia lamblia* trophozoites. *J. Parasitol.* **95**, 895-899. doi:10.1645/GE-1851R.1

Kaczmarzyk, D., Cengic, I., Yao, L. and Hudson, E. P. (2018). Diversion of the long-chain acyl-ACP pool in Synechocystis to fatty alcohols through CRISPRi repression of the essential phosphate acyltransferase PlsX. *Metab. Eng.* **45**, 59-66. doi:10.1016/j.ymben.2017.11.014

Kim, J. and Park, S.-J. (2019). Role of gamma-giardin in ventral disc formation of *Giardia lamblia*. *Parasit. Vectors* **12**, 227. doi:10.1186/s13071-019-3478-8

Larson, M. H., Gilbert, L. A., Wang, X., Lim, W. A., Weissman, J. S. and Qi, L. S. (2013). CRISPR interference (CRISPRi) for sequence-specific control of gene expression. *Nat. Protoc.* **8**, 2180-2196. doi:10.1038/nprot.2013.132

Lauwaet, T., Davids, B. J., Torres-Escobar, A., Birkeland, S. R., Cipriano, M. J., Preheim, S. P., Palm, D., Svärd, S. G., McArthur, A. G. and Gillin, F. D. (2007). Protein phosphatase 2A plays a crucial role in *Giardia lamblia* differentiation. *Mol. Biochem. Parasitol.* **152**, 80-89. doi:10.1016/j.molbiopara.2006.12.001

Lauwaet, T., Smith, A. J., Reiner, D. S., Romijn, E. P., Wong, C. C. L., Davids, B. J., Shah, S. A., Yates, J. R., III and Gillin, F. D. (2011). Mining the *Giardia* genome and proteome for conserved and unique basal body proteins. *Int. J. Parasitol.* **41**, 1079-1092. doi:10.1016/j.ijpara.2011.06.001

Li, J., Mahajan, A. and Tsai, M.-D. (2006). Ankyrin repeat: a unique motif mediating protein-protein interactions. *Biochemistry* **45**, 15168-15178. doi:10.1021/bi062188q

Linck, R., Fu, X., Lin, J., Ouch, C., Schefter, A., Steffen, W., Warren, P. and Nicastro, D. (2014). Insights into the structure and function of ciliary and flagellar doublet microtubules: tektins, Ca2+-binding proteins, and stable protofilaments. *J. Biol. Chem.* **289**, 17427-17444. doi:10.1074/jbc.M114.568949

Lindquist, H. D. (1996). Induction of albendazole resistance in *Giardia lamblia*. *Microb. Drug Resist.* **2**, 433-434. doi:10.1089/mdr.1996.2.433

Liu, X., Gallay, C., Kjos, M., Domenech, A., Slager, J., van Kessel, S. P., Knoops, K., Sorg, R. A., Zhang, J. R. and Veening, J. W. (2017). High-throughput CRISPRi phenotyping identifies new essential genes in Streptococcus pneumoniae. *Mol. Syst. Biol.* **13**, 931. doi:10.15252/msb.20167449

Long, S., Anthony, B., Drewry, L. L. and Sibley, L. D. (2017). A conserved ankyrin repeat-containing protein regulates conoid stability, motility and cell invasion in Toxoplasma gondii. *Nat. Commun.* **8**, 2236. doi:10.1038/s41467-017-02341-2

Lourenço, D., Andrade Ida, S., Terra, L. L., Guimarães, P. R., Zingali, R. B. and de Souza, W. (2012). Proteomic analysis of the ventral disc of *Giardia lamblia*. *BMC Res. Notes* **5**, 41. doi:10.1186/1756-0500-5-41

Manning, G., Reiner, D. S., Lauwaet, T., Dacre, M., Smith, A., Zhai, Y., Svard, S. and Gillin, F. D. (2011). The minimal kinome of Giardia lamblia illuminates early kinase evolution and unique parasite biology. *Genome Biol.* **12**, R66. doi:10.1186/gb-2011-12-7-r66

McInally, S. G., Hagen, K. D., Nosala, C., Williams, J., Nguyen, K., Booker, J., Jones, K. and Dawson, S. (2019a). Robust and stable transcriptional repression in *Giardia* using CRISPRi. *Mol. Biol. Cell* **30**, 119-130. doi:10.1091/mbc.E18-09-0605

McInally, S. G., Kondev, J. and Dawson, S. C. (2019b). Length-dependent disassembly maintains four different flagellar lengths in Giardia. *Elife* **8**, e48694. doi:10.7554/eLife.48694

Mitchison, T. and Kirschner, M. (1984). Dynamic instability of microtubule growth. *Nature* **312**, 237-242. doi:10.1038/312237a0

Morgan, U. M., Reynoldson, J. A. and Thompson, R. C. (1993). Activities of several benzimidazoles and tubulin inhibitors against Giardia spp. in vitro. *Antimicrob. Agents Chemother.* **37**, 328-331. doi:10.1128/AAC.37.2.328

Morrison, H. G., McArthur, A. G., Gillin, F. D., Aley, S. B., Adam, R. D., Olsen, G. J., Best, A. A., Cande, W. Z., Chen, F., Cipriano, M. J. et al. (2007). Genomic minimalism in the early diverging intestinal parasite *Giardia lamblia*. *Science* **317**, 1921-1926. doi:10.1126/science.1143837

Nabi, A., Yano, J., Valentine, M. S., Picariello, T. and Van Houten, J. L. (2019). SF-Assemblin genes in Paramecium: phylogeny and phenotypes of RNAi silencing on the ciliary-striated rootlets and surface organization. *Cilia* **8**, 2. doi:10.1186/s13630-019-0062-y

Nohria, A., Alonso, R. A. and Peattie, D. A. (1992). Identification and characterization of gamma giardin and the gamma giardin gene from *Giardia lamblia*. *Mol. Biochem. Parasitol.* **56**, 27-37. doi:10.1016/0166-6851(92)90151-9

Nosala, C. and Dawson, S. C. (2015). The critical role of the Cytoskeleton in the pathogenesis of giardia. *Curr. Clin. Microbiol. Rep.* **2**, 155-162. doi:10.1007/s40588-015-0026-y

Nosala, C., Hagen, K. D. and Dawson, S. C. (2018). 'Disc-o-Fever': getting down with giardia's groovy microtubule organelle. *Trends Cell Biol.* **28**, 99-112. doi:10.1016/j.tcb.2017.10.007

Owa, M., Uchihashi, T., Haruaki, H., Yamano, T., Iguchi, H., Fukuzawa, H., Wakabayashi, K., Ando, T. and Kikkawa, M. (2018). Inner lumen proteins stabilize doublet microtubules in cilia/flagella. *Nat. Commun.* **10**, 1143. doi:10.1038/s41467-019-09051-x

Palm, J. E. D., Weiland, M. E. L., Griffiths, W. J., Ljungstrom, I. and Svard, S. G. (2003). Identification of immunoreactive proteins during acute human giardiasis. *J. Infect. Dis.* **187**, 1849-1859. doi:10.1086/375356

Palm, D., Weiland, M., McArthur, A. G., Winiecka-Krusnell, J., Cipriano, M. J., Birkeland, S. R., Pacocha, S. E., Davids, B., Gillin, F., Linder, E. et al. (2005). Developmental changes in the adhesive disk during *Giardia* differentiation. *Mol. Biochem. Parasitol.* **141**, 199-207. doi:10.1016/j.molbiopara.2005.03.005

Peattie, D. A. (1990). The giardins of *Giardia lamblia*: genes and proteins with promise. *Parasitol. Today* **6**, 52-56. doi:10.1016/0169-4758(90)90070-K

Pecqueur, L., Duellberg, C., Dreier, B., Jiang, Q., Wang, C., Plückthun, A., Surrey, T., Gigant, B. and Knossow, M. (2012). A designed ankyrin repeat protein selected to bind to tubulin caps the microtubule plus end. *Proc. Natl. Acad. Sci. USA* **109**, 12011-12016. doi:10.1073/pnas.1204129109

Piatek, A., Ali, Z., Baazim, H., Li, L., Abulfaraj, A., Al-Shareef, S., Aouida, M. and Mahfouz, M. M. (2015). RNA-guided transcriptional regulation in planta via synthetic dCas9-based transcription factors. *Plant Biotechnol. J.* **13**, 578-589. doi:10.1111/pbi.12284

Preisner, H., Karin, E. L., Poschmann, G., Stuhler, K., Pupko, T. and Gould, S. B. (2016). The cytoskeleton of parabasalian parasites comprises proteins that share properties common to intermediate filament proteins. *Protist* **167**, 526-543. doi:10.1016/j.protis.2016.09.001

Russell, J. J., Theriot, J. A., Sood, P., Marshall, W. F., Landweber, L. F., Fritz-Laylin, L., Polka, J. K., Oliferenko, S., Gerbich, T., Gladfelter, A. et al. (2017). Non-model model organisms. *BMC Biol.* **15**, 55. doi:10.1186/s12915-017-0391-5

Schindelin, J., Arganda-Carreras, I., Frise, E., Kaynig, V., Longair, M., Pietzsch, T., Preibisch, S., Rueden, C., Saalfeld, S., Schmid, B. et al. (2012). Fiji: an open-source platform for biological-image analysis. *Nat. Methods* **9**, 676-682. doi:10.1038/nmeth.2019

Schwartz, C. L., Heumann, J. M., Dawson, S. C. and Hoenger, A. (2012). A detailed, hierarchical study of *Giardia lamblia's* ventral disc reveals novel microtubule-associated protein complexes. *PLoS ONE* **7**, e43783. doi:10.1371/journal.pone.0043783

Smith, I., Greenside, P. G., Natoli, T., Lahr, D. L., Wadden, D., Tirosh, I., Narayan, R., Root, D. E., Golub, T. R., Subramanian, A. et al. (2017). Evaluation of RNAi and CRISPR technologies by large-scale gene expression profiling in the Connectivity Map. *PLoS Biol.* **15**, e2003213. doi:10.1371/journal.pbio.2003213

Stoddard, D., Zhao, Y., Bayless, B. A., Gui, L., Louka, P., Dave, D., Suryawanshi, S., Tomasi, R. F.-X., Dupuis-Williams, P., Baroud, C. N. et al. (2018). Tetrahymena RIB72A and RIB72B are microtubule inner proteins in the ciliary doublet microtubules. *Mol. Biol. Cell* **29**, 2566-2577. doi:10.1091/mbc.E18-06-0405

Stojic, L., Lun, A. T. L., Mangei, J., Mascalchi, P., Quarantotti, V., Barr, A. R., Bakal, C., Marioni, J. C., Gergely, F. and Odom, D. T. (2018). Specificity of RNAi, LNA and CRISPRi as loss-of-function methods in transcriptional analysis. *Nucleic Acids Res.* **46**, 5950-5966. doi:10.1093/nar/gky437

Tao, W., Lv, L. and Chen, G.-Q. (2017). Engineering Halomonas species TD01 for enhanced polyhydroxyalkanoates synthesis via CRISPRi. *Microb Cell Fact* **16**, 48. doi:10.1186/s12934-017-0655-3

Taylor, S. C., Nadeau, K., Abbasi, M., Lachance, C., Nguyen, M. and Fenrich, J. (2019). The ultimate qPCR experiment: producing publication quality, reproducible data the first time. *Trends Biotechnol.* **37**, 761-774. doi:10.1016/j.tibtech.2018.12.002

Túmová, P., Kulda, J. and Nohýnková, E. (2007). Cell division of *Giardia intestinalis*: assembly and disassembly of the adhesive disc, and the cytokinesis. *Cell Motil. Cytoskeleton* **64**, 288-298. doi:10.1002/cm.20183

Upcroft, J., Mitchell, R., Chen, N. and Upcroft, P. (1996). Albendazole resistance in Giardia is correlated with cytoskeletal changes but not with a mutation at amino acid 200 in beta-tubulin. *Microb. Drug Resist.* **2**, 303-308. doi:10.1089/mdr.1996.2.303

Weber, K., Geisler, N., Plessmann, U., Bremerich, A., Lechtreck, K. F. and Melkonian, M. (1993). SF-assemblin, the structural protein of the 2-nm filaments from striated microtubule associated fibers of algal flagellar roots, forms a segmented coiled coil. *J. Cell Biol.* **121**, 837-845. doi:10.1083/jcb.121.4.837

Weiland, M. E.-L., Palm, J. E., Griffiths, W. J., McCaffery, J. M. and Svärd, S. G. (2003). Characterisation of alpha-1 giardin: an immunodominant *Giardia lamblia* annexin with glycosaminoglycan-binding activity. *Int. J. Parasitol.* **33**, 1341-1351. doi:10.1016/S0020-7519(03)00201-7

Weiland, M. E.-L., McArthur, A. G., Morrison, H. G., Sogin, M. L. and Svärd, S. G. (2005). Annexin-like alpha giardins: a new cytoskeletal gene family in *Giardia lamblia*. *Int. J. Parasitol.* **35**, 617-626. doi:10.1016/j.ijpara.2004.12.009

Weisbrich, A., Honnappa, S., Jaussi, R., Okhrimenko, O., Frey, D., Jelesarov, I., Akhmanova, A. and Steinmetz, M. O. (2007). Structure-function relationship of CAP-Gly domains. *Nat. Struct. Mol. Biol.* **14**, 959-967. doi:10.1038/nsmb1291

Woessner, D. J. and Dawson, S. C. (2012). The Giardia median body protein is a ventral disc protein that is critical for maintaining a domed disc conformation during attachment. *Eukaryot. Cell* **11**, 292-301. doi:10.1128/EC.05262-11

Zhang, B., Liu, Z.-Q., Liu, C. and Zheng, Y.-G. (2016). Application of CRISPRi in Corynebacterium glutamicum for shikimic acid production. *Biotechnol. Lett.* **38**, 2153-2161. doi:10.1007/s10529-016-2207-z

Zuberi, A., Misba, L. and Khan, A. U. (2017). CRISPR Interference (CRISPRi) Inhibition of luxS Gene Expression in E. coli: An Approach to Inhibit Biofilm. *Front. Cell Infect. Microbiol.* **7**, 214. doi:10.3389/fcimb.2017.00214

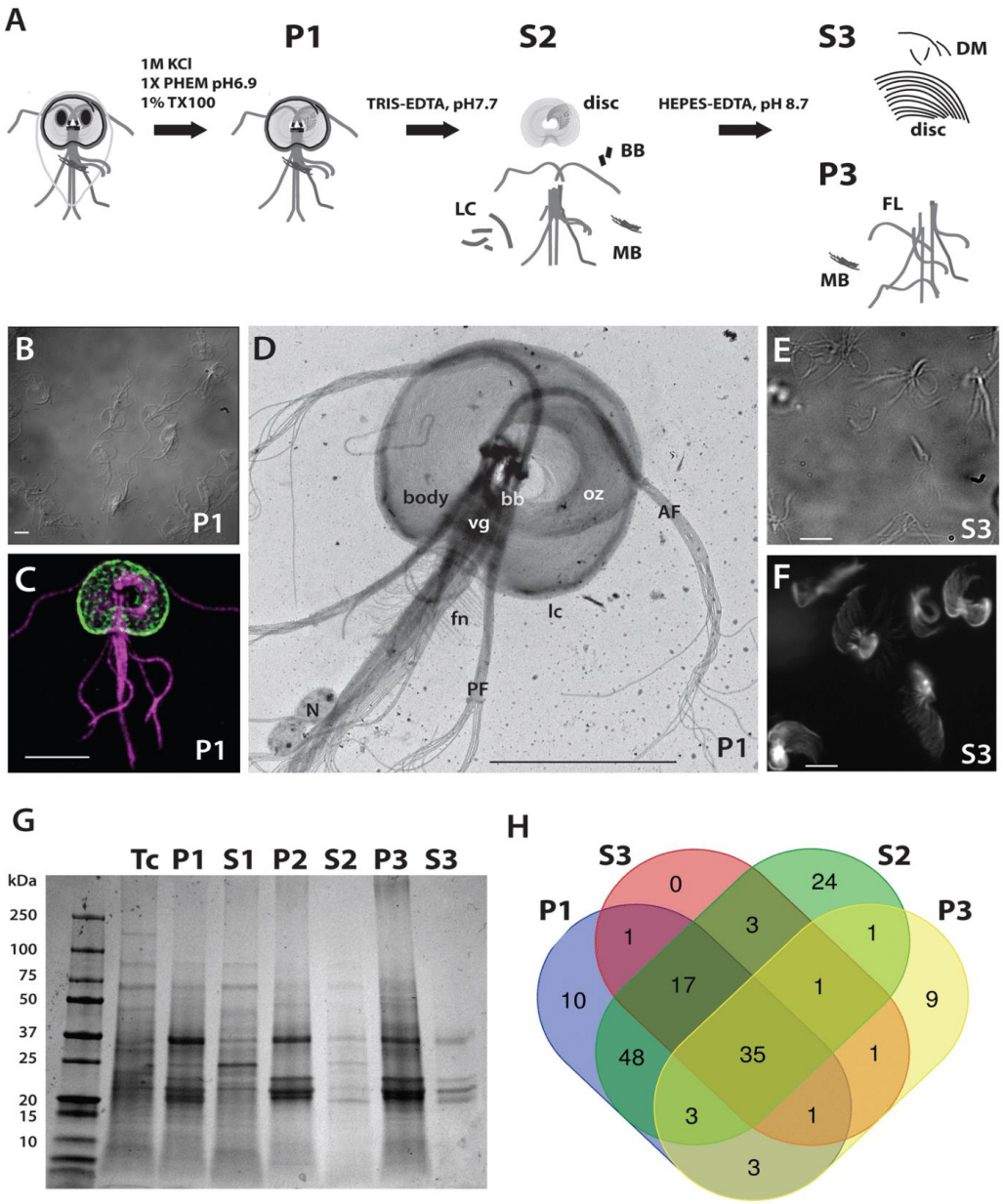
A
P1
S2
S3
1M KCl
1X PHEM pH6.9
1% TX100
TRIS-EDTA, pH7.7
HEPES-EDTA, pH 8.7
disc
BB
LC
MB
DM
disc
P3
FL
MB
B
P1
C
P1
D
body
bb
oz
vg
AF
fn
lc
PF
N
P1
E
S3
F
S3
G
Tc P1 S1 P2 S2 P3 S3
kDa
250
100
75
50
37
25
20
15
10
H
S3
S2
P1
P3
0
24
1
3
1
17
1
10
9
48
35
1
3
1
3

Figure S1.

Biochemical fractionation readily extracts disc and axoneme proteins for shotgun proteomic analysis and mass spectrometry. Extraction of *Giardia* trophozoites with detergent and high salt (A) removed membrane and cytosol from the microtubule cytoskeleton (P1). Subsequent extractions with Tris-EDTA and HEPES further disrupted the disc resulting in the S2, P2, S3 and P3 fractions. Immunostaining of the P1 fraction (B, C) shows that the disc (green, anti-δ-giardin) and flagella (magenta, anti-alpha-tubulin) were retained. Negative staining of the P1 fraction (D) confirms the retention of the disc (body, vg, oz, lc), flagella (AF, PF) and the funis (fn); greater dissociation of the disc from the axonemes is evident in the S3 fraction as shown by δ-giardin immunostaining (E, F). SDS-PAGE resolves proteins that are enriched in total cell pellet (T) and each pellet (P1, P2, P3) and supernatant (S1, S2, S3) fraction. Following mass spectrometry of fractions (P1, P3, S2, S3), the Venn diagram comparison indicates some overlap between proteins in the various fractions (H).

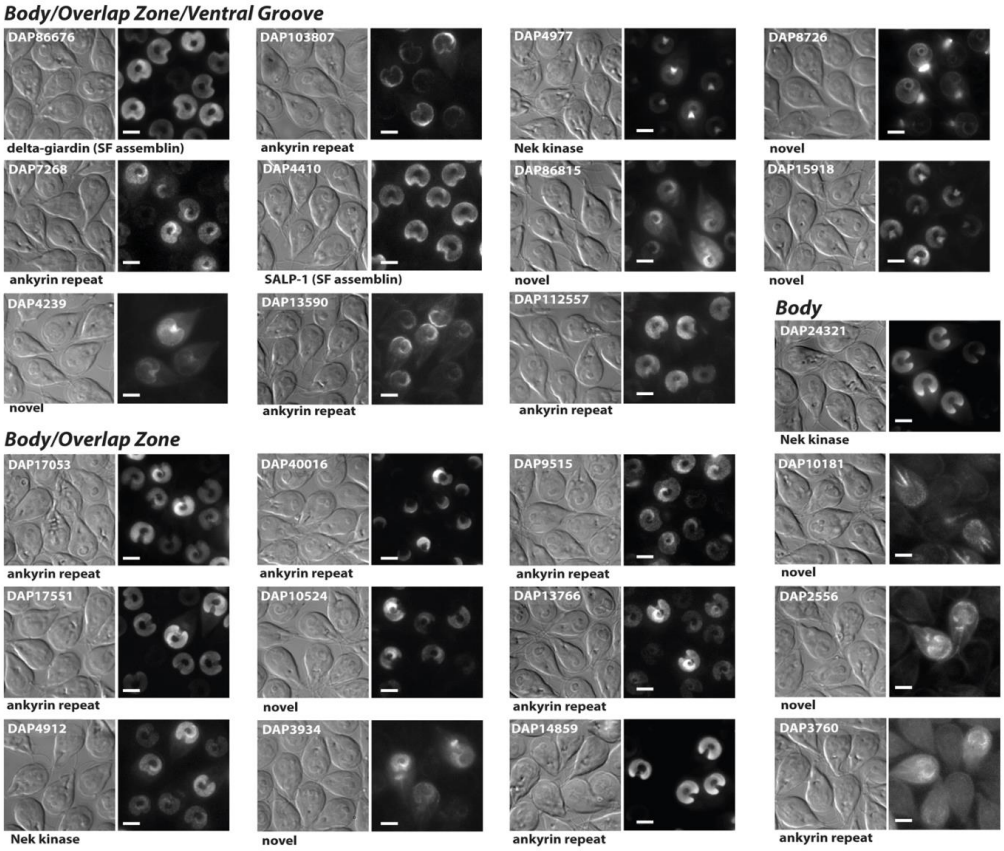

Figure S2.

Representative disc-specific localization of Body/Overlap Zone/Ventral Groove and Body/ Overlap zone DAPs. Left image is DIC; Right is DAP-GFP localization using epifluorescence.

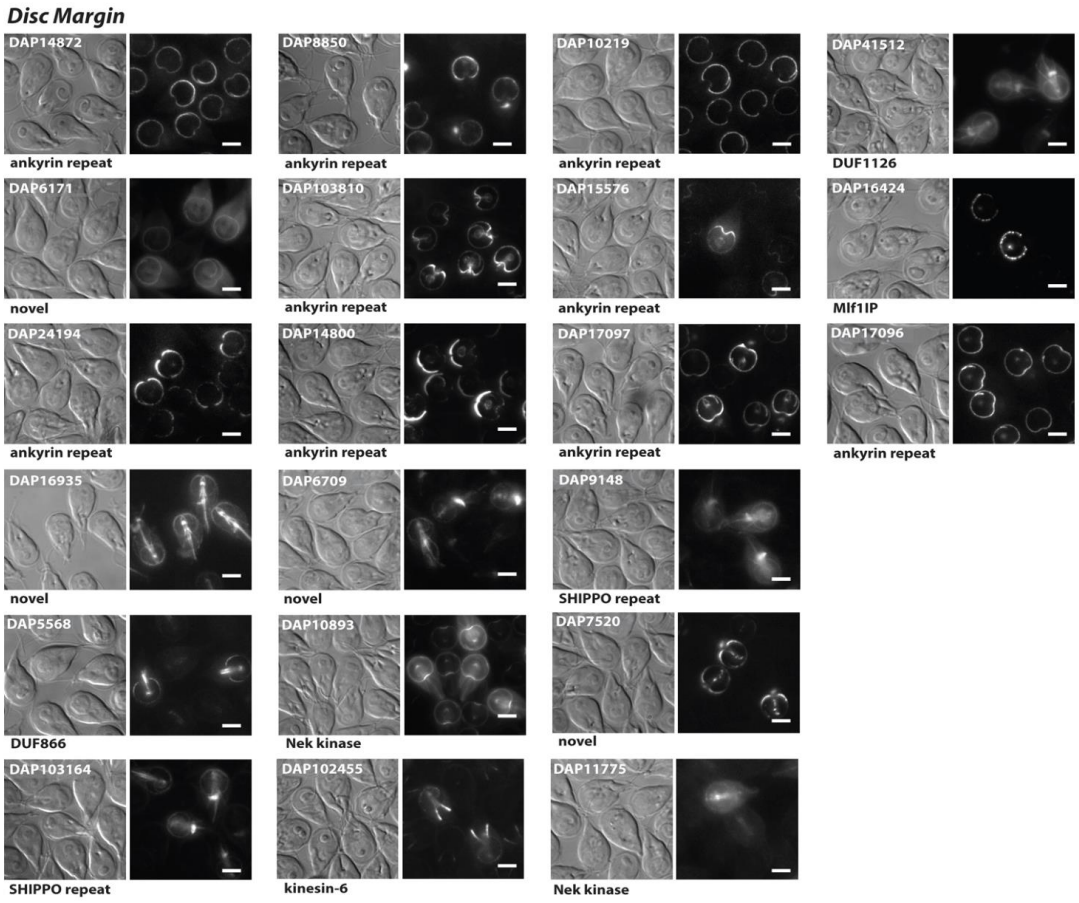

Figure S3.

Representative disc-specific localization of Disc Margin DAPs. Left image is DIC; Right is DAP-GFP localization using epifluorescence.

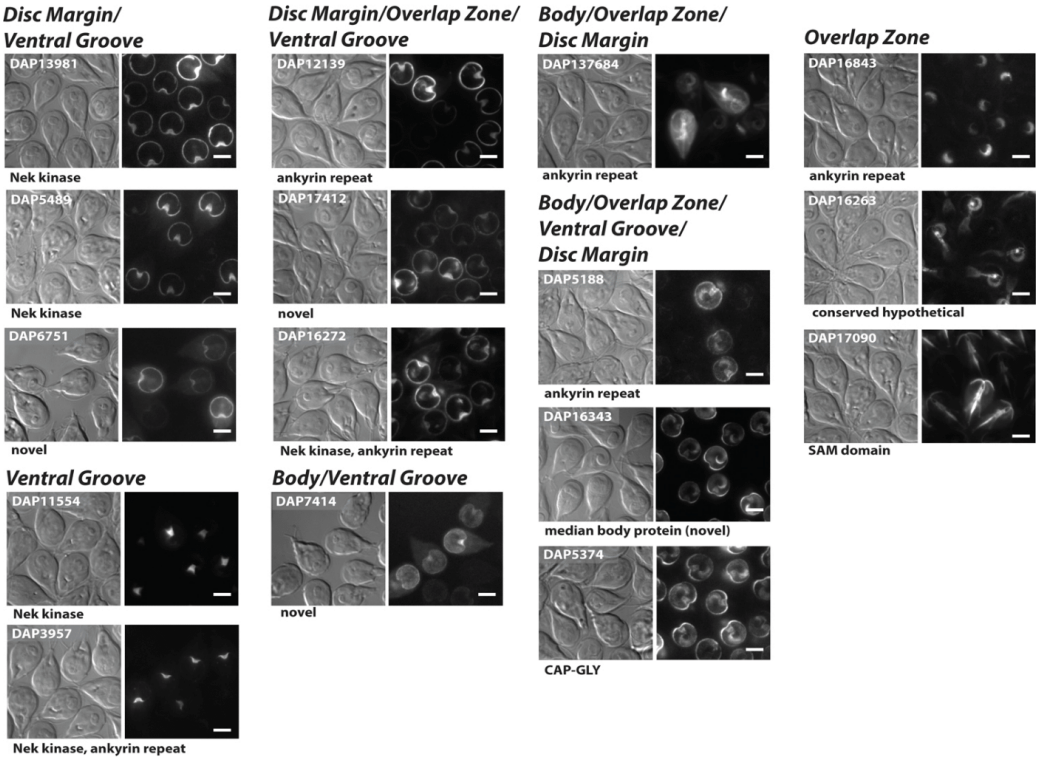

Figure S4.

Representative disc-specific localizations DAPs localizing to the more than one region of the Disc Margin, Ventral Groove, Overlap Zone, or disc body. Left image is DIC; Right is DAP-GFP localization using epifluorescence.

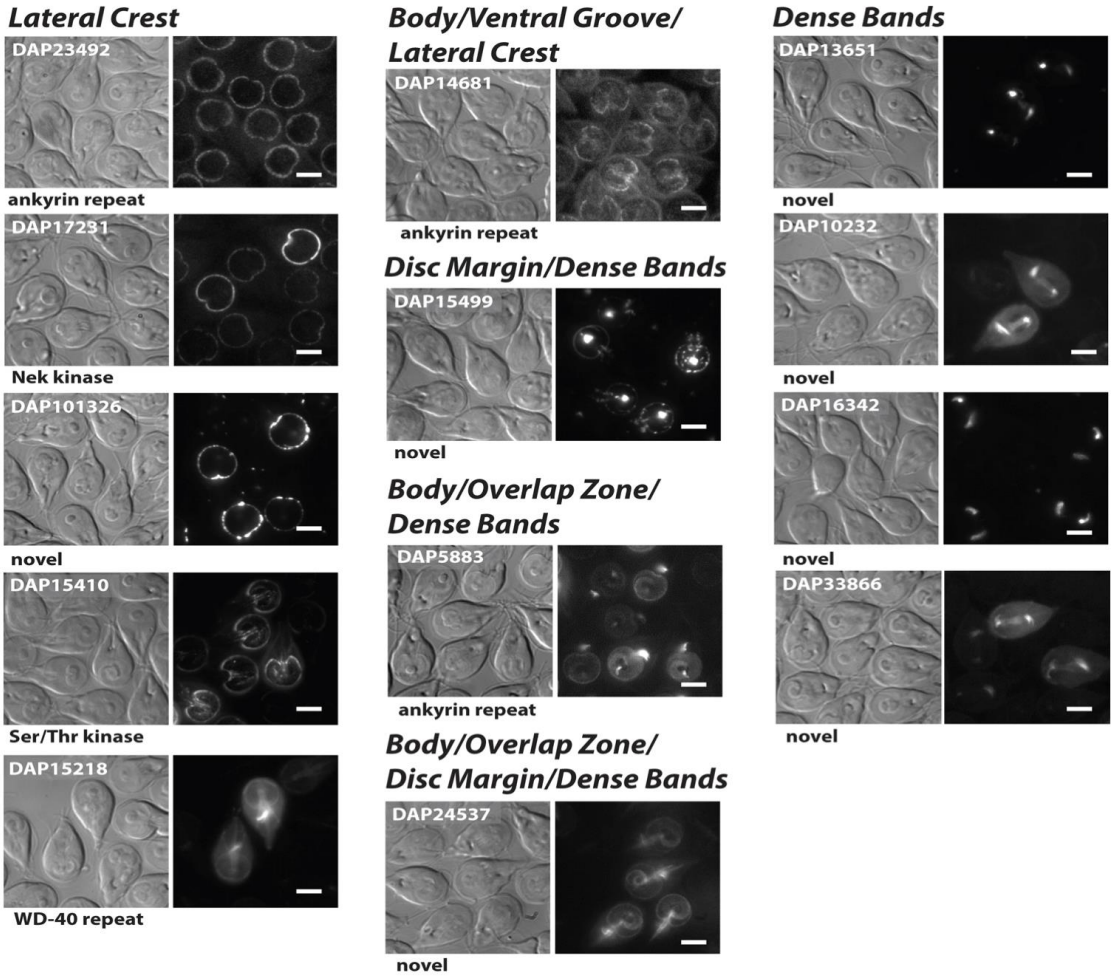

Figure S5.

Representative disc-specific localizations DAPs localizing to the lateral crest, dense bands, as well as to the Disc Margin, Ventral Groove, Overlap Zone, or disc body regions. Left image is DIC; Right is DAP-GFP localization using epifluorescence.

Chapter 3

Microribbons stabilize the microtubule spiral of *Giardia*'s domed ventral disc, enabling attachment

Nicholas Hilton, Kari D. Hagen, and Scott Dawson

Abstract

Giardia lamblia is a single-celled eukaryotic parasite that colonizes the small intestine and causes significant diarrheal disease worldwide. Motile trophozoites attach to intestinal villi with the ventral disc, a cup-shaped microtubule (MT) organelle that enables extracellular parasite attachment. A current model of attachment proposes that a flexible disc modulates its dome shape to create a seal on the host cell surface. The ventral disc is a highly ordered and complex spiral MT array. Novel protein complexes such as the microribbon-crossbridge (MR-CB) complex bind to the disc MT at regular intervals, almost completely coating all MT protofilaments. Aside from the ventral disc's role in infection, understanding how complex MT organelles are assembled and evolve can shed light on how morphological diversity evolved in eukaryotes. Prior research has identified nearly 90 disc-associated proteins (DAPs), yet we still know very little about how the composition of protein complexes associated with the disc either enables stability and flexibility or mediates attachment. In particular, the functional and structural roles of the conspicuous MR-CB complexes remain unknown. Several DAPs localize to the MRs, including three homologs of the Striated Fiber (SF)-assemblins. SF-assemblins are structural proteins known to polymerize in vitro and to be associated with flagellar root structures in other protists. Here, we show that MR-CB complexes play a role in maintaining the disc spiral structure. We show that the MR-CB complex stabilizes the conformation of the disc spiral MT array required for parasite attachment to the host. We determine the structural and functional roles of the MR-CB complexes by creating stable CRISPR knockouts of known MR-CB proteins and evaluating mutant disc structure and function with light microscopy. Furthermore, we use biophysical attachment assays to assess disc function. Understanding the MR-CB complex will also shed light on the disc as a whole and guides us towards key insights into how the disc flexes during attachment. This work also contributes to our knowledge of how

cells construct and maintain complex MT organelles and in particular, help to define the roles of SF-assemblins in complex MT structures.

Introduction

Giardia lamblia is a single celled eukaryotic parasite that colonizes the small intestine and causes the significant diarrheal disease giardiasis worldwide[1]. It can infect both humans and animals[1] via oral consumption of cysts present in contaminated food or water. The burden of giardiasis is heavier where water sanitation is lacking, and can lead to malnutrition or delayed development in children[1]. When consumed, cysts remain dormant until passing through the host stomach, and excyst into a trophozoite form when emerging into the small intestine[1]. During colonization, motile trophozoites attach to intestinal villi with the ventral disc, a cup-shaped microtubule organelle that enables extracellular parasite attachment to the host gastrointestinal tract[2]. Attachment is thought to be necessary for the resistance of peristaltic flow and the successful establishment of infection[1]. The current model of attachment suggests that the attachment force is generated by the movement of specific ventral disc substructural elements combined with hydrodynamic flow produced by flagellar beating[3]. While the exact mechanisms of *Giardia* disc-mediated attachment remain controversial, parasites are able to reversibly attach to inert and biological surfaces such as intestinal epithelium, glass coverslips, and culture tubes. This supports a biophysical mechanism of disc-mediated attachment driven by the dynamic movements of the ventral disc rather than a ligand-dependent adhesive mechanism.

To better understand the process and essential components of disc-driven, reversible attachment we can closely examine *Giardia's* ventral disc structure and composition. The ventral disc is a highly ordered and complex spiral microtubule array[2]. Approximately 100 parallel, uniformly spaced microtubules spiral to form a dome, with an overlap zone between the upper and lower portions[2]. The disc is an unusually stable structure in interphase, and notably,

the detergent extraction of *Giardia* with high salt results in a preparation of intact or "hyperstable" discs[4]. The interphase disc is also not sensitive to drugs that affect microtubule dynamics[4,5]. Novel protein complexes such as the microribbon-crossbridge (MR-CB) complex[6,7], and the repetitive sidearm and paddle complexes bind to the disc microtubules at regular intervals, almost completely coating all microtubule protofilaments[8]. It is proposed that the MR-CB complex may thereby mediate disc hyperstability[8,9]. The perimeter of the spiral microtubule array is defined by the disc margin, which contacts the ventral surface, and includes a gap or "opening" at the point of the overlap zone[2]. A fibrillar structure, the lateral crest, surrounds the periphery of the ventral disc[10] and has been proposed to create a seal to maintain hydrodynamic suction during attachment[11–15].

Several microtubule-associated proteins termed 'giardins' were isolated from the disc two decades after the initial disc structures were described[16], However, through comprehensive proteomic analysis of detergent-extracted, isolated ventral discs and ongoing protein-tagging projects, we have identified nearly 90 disc-associated proteins (now referred to as DAPs, rather than giardins) that localize to regions of the ventral disc or the lateral crest[11]. Despite our emerging view of the complexity of ventral disc architecture[9], we still know very little about how the composition of protein complexes associated with the disc enables hyperstability or mediates attachment forces.

In particular, the functional and structural roles of the conspicuous MR-CB complex remain unknown. The prominent trilaminar microribbon (MR) complex is associated with the entire length of the MT spiral and extends 400 nm dorsally into the cytoplasm[7,17]. Parallel microribbons are linked together laterally by crossbridges (CBs)[17]. The MR-CB complex includes five regions: the outer layer and inner core layers of the trilaminar MR, the MR-MT interacting densities, the MR-CB connector densities, and the CBs themselves. The MR-CB complex may play a role in maintaining the curved or "domed" disc structure and ultimately

attachment. Furthermore, the crossbridges themselves are proposed to be flexible and thus could mediate disc movement during attachment[2].

Three DAPs that localize to the MRs are homologs of the Striated Fiber (SF)-assemblins. SF-assemblins are structural proteins that polymerize *in vitro* and are associated with flagellar root structures in other protists[18]. The *Giardia* SF-assemblin homologs beta-giardin, delta-giardin, and SALP1[19] are proposed to polymerize into the initial MR complex that enables other MR-associated proteins to later assemble into the MR-CB complex[10]. The precise location and abundance of known MR proteins in the 3D disc architecture of the trilaminar MRs is still unknown, and no candidate crossbridge (CB) protein has been identified. We anticipate that there are additional DAPs associated with the trilaminar MR structure, the MR-MT interactors, the MR-CB connectors that remain to be discovered.

Genetic analyses of DAPs are essential to building a foundational understanding of disc architecture, assembly, and dynamics. Functional studies of the disc have lagged behind that of microtubule organelles in other parasites due to a lack of molecular genetic tools in *Giardia*. In particular, the critical role of disc-mediated attachment in Giardia pathogenesis has received remarkably little attention in the last 50 years, and prior work has been largely descriptive[2]. However, we have developed transformative CRISPR-Cas9 mediated knockdown (CRISPRi) and knockout (CRISPR) systems in the “double diploid” *Giardia*[20,21], enabling genetic analyses of the many unique disc proteins and protein complexes.

Here, I define the role of the MR-CB complexes in stabilizing and maintaining the disc domed conformation. Using new genetic tools to create disc mutants, I show that the presence of intact microribbons is required for proper formation of the microtubule spiral of the disc. This implies that the MR-CB complex is necessary for disc MT assembly which in turn scaffolds the overall disc architecture, rather than alternative, non-MR-CB complex DAPs. Through a domain analysis of the disc SFAs, I build on early work characterizing the ability of *Chlamydomonas* SF-

assemblin to self-assemble into fibers[22] to show that specific head or tail domains are of the three SFAs are required for disc assembly. Using three MR DAP knockout lines with aberrant disc structure, I show that the intact MR-CB complex is required for attachment. Lastly, I show that the MR SFAs are necessary for disc stability, and, in turn, that disc stability is necessary for *Giardia* attachment.

Results

Giardia's three SF-assemblin homologs localize to the trilaminar microribbon structure of the ventral disc

Giardia's ventral disc consists of a spiral of microtubules overlaid by a dense protein network named the microribbon-crossbridge complex[7,8,17] (Figure 3.1A). The microribbons trace the microtubule spiral of the disc, are trilaminar, and extend dorsally up to 400 nm into the cell body. Crossbridges connect adjacent microribbons regularly down their length[8,9]. There are no direct microtubule-microtubule connections, though the microtubules of the disc are decorated with a variety of Microtubule Associated Proteins and Microtubule Inner Proteins. Prior studies in *Giardia* determined the localization of beta-giardin, delta-giardin, and SALP1 to the trilaminar microribbons of the disc[16,19,23] (Figure 3.1B), but have not elucidated where within this structure these SF-assemblin homologs reside.

Beta-giardin, delta-giardin, and SALP1 are conserved structurally yet evolutionarily distinct

While beta-giardin, delta-giardin, and SALP1 have been identified, the remaining makeup of the MR-CB complex is unknown. Common features of SF-assemblin homologs are an unstructured N-terminal head domain, followed by a tail domain consisting of a series of coiled coil

repeats[19,22,23] (see Chapter 1). AlphaFold predictions of these protein's structure aligned with an unstructured head domain and coiled-coil tail domain (Figure 3.1C).

We conducted a phylogenetic and structural analysis of the SFA family of proteins (see Chapter 1) and found that SFAs cluster into three main groups, with numerous subgroups (Figure 3.1D). In particular, *Giardia's* three SFA homologs cluster together into Group II-B (Figure 3.1E). The three *Giardia* SFAs also form a cluster distinct from some SFAs from closely related organisms, such as *Spironucleus salmonicida* (Figure 3.1E).

Beta-giardin knockout cells fail to properly localize delta-giardin to the ventral disc

A quadruple beta-giardin KO line (bGKO) was stained with an anti-delta-giardin antibody to assess the impact of beta-giardin on microribbon structure (Figure 3.2A, 2B). Delta-giardin signal was not contained to the ventral disc, as compared to the wild-type control, but delta-giardin localizes instead throughout the cell body (Figure 3.2A, 2B). Complementing beta-giardin KO cells with an exogenously expressed beta-giardin (bGKO+bG) restored proper delta-giardin signal localization (Figure 3.2A).

bGKO ventral discs are longer and thinner than wild-type discs

bGKO discs were measured to determine the impact of beta-giardin on the disc microtubule spiral. The bGKO strain was stained with an anti-alpha-tubulin antibody to visualize the tubulin spiral, and measurements were taken with this stain (Figure 3.2C). No alteration of flagellar length nor defects in basal bodies were observed in bGKO cells. bGKO discs have a lengthened anterior-posterior axis, and a shortened side-to-side axis when compared to wild-type and Cas9-only (beta-giardin gRNA) negative control strains (Figure 3.2D). bGKO+bG cells did not have wild-type disc dimensions, although bGKO+bG discs were significantly shorter than bGKO discs (Figure 3.2D). To track dimensional change within cells and distinguish between aggregate length and width changes, we examined the length:width ratio of discs, and found

that bGKO cells were closer to a 1:1 ratio than negative controls (Figure 3.2E). The bGKO+bG complement line had a wild-type length:width ratio in the disc, however (Figure 3.2E).

Delta-giardin KO discs are destabilized and fail to maintain an evenly spaced disc spiral

Trophozoites from the delta-giardin (dGKO) quadruple knockout strain were stained with an anti-beta-giardin antibody to determine the impact of delta-giardin on the ventral disc microribbon-crossbridge architecture (Figure 3.3A, 3B). Discs possessed various distorted or disordered disc phenotypes (Figure 3.3C). Aberrant discs were quantified and categorized based on the following characteristics: disc with full structure present, indistinguishable from wild-type (full disc); arms of the disc spiral breaking apart and becoming disjointed (frayed disc); loss of disc material such that a full disc cannot be formed (horseshoe); intact arms of spiral but overlap zone has come undone (unhinged) (Figure 3.3C). Wild-type cells possessed almost exclusively full disc phenotypes, with approximately 3% falling into any of the other categories (Figure 3.3C). The dGKO line had a little over 40% full discs, with frayed discs (34%) and unhinged discs (18%) featuring prominently amongst the remaining percentages (Figure 3.3C).

dGKO discs are elongated as compared to wild-type

Similar dimensional analyses were performed on the dGKO discs as was done for the bGKO line. dGKO discs are longer than wild-type and Cas9 only (delta-giardin gRNA) controls, but are not significantly thinner than wild-type, unlike the dGKO line (Figure 3.3D). Complementation of KO cells with an exogenously expressed delta-giardin (dGKO+dG) does not fully restore wild-type dimensions and is both significantly longer than wild-type but shorter than the uncomplemented KO (Figure 3.3D). We also examined the individual disc length:width ratio and found that dGKO discs are closer to a ratio of 1:1 than the negative controls (Figure 3.3E). dGKO+dG disc dimensions were lower in length:width ratio than both the uncomplemented KOs and the wild-type lines (Figure 3.3E).

dGKO discs are both larger and have larger bare areas than wild-type discs

To further characterize disc structural defect in mutants, the disc area measurements were taken in FIJI (ImageJ) software using the “Thresholding” and “Particle Analysis” functions (Figure 3.3F, 3G). dGKO cells possess a larger disc area than wild-type cells (Figure 3.3F); this measurement did not include the bare area as part of the total area. The disc bare area of the dGKO line was also larger than a wild-type negative control (Figure 3.3G).

dGKO discs lose hyperstability

In order to test the maintenance or loss of disc hyperstability, we extracted cytoskeletons as performed previously[4]. Discs were stained with anti-beta-giardin to visualize the disc. Wild-type discs remained intact, but dGKO discs were further degraded by the extraction procedure (Figure 3.3H). Discs in the dGKO line were observed to have sections of disc material missing from the disc interior, both adjacent and nonadjacent to the bare area.

SALP1 KO discs have similar defects to delta-giardin KO strain discs

SALP1 quadruple KO (SALPKO) cells were stained with an anti-beta-giardin antibody to highlight the microribbons and were observed to be visually distinct from wild-type discs (Figure 3.4A, 4B). The same categorization scheme that was applied to the dGKO cells was employed to sort SALPKO discs (Figure 3.3C, 4C). About half of SALPKO cells had a full disc phenotype, with roughly 50% of cells matching this criterion (Figure 3.4C). Of the remaining categories, frayed disc (25%), and unhinged (16%) were the most prominent (Figure 3.4C). Both the SALPKO and dGKO lines had only a small percentage of discs fall under the horseshoe category (Figure 3.3C, 4C). SALPKO discs were also stained with anti-delta-giardin to observe whether the knockout effects observed were consistent across different microribbon proteins. We found the same disc phenotypes, as described above, in anti-delta-giardin stained SALPKO cells (Figure 3.4D).

SALPKO discs are longer than wild-type discs

Like the other SF-assemblin KO lines, disc length and width measurements were quantified for the SALPKO strain discs. SALPKO discs were elongated as compared to wild-type or Cas9-only (SALP1 gRNA) strain controls, but SALPKO disc widths were not significantly different (Figure 3.4E). Complementation of SALPKO cells with an exogenously expressed SALP1 (SALPKO+SALP) did not restore wild-type length, but complemented discs were both significantly longer than wild-type and significantly shorter than SALPKO discs (Figure 3.4E). Like the other knockout lines, disc length:width ratio in SALPKO discs is closer to 1:1 than negative controls (Figure 3.4F). Complementation of SALP1 did restore a wild-type disc length:width ratio (Figure 3.4F).

SALPKO cells have no significant change in disc area or bare area

The same disc area measurements performed on dGKO cells (Figure 3.3F, 3G) were applied to SALPKO cells. Despite trending larger, SALPKO cells were not found to possess a larger disc area nor bare area when compared to wild-type cells (Figure 3.4G, 4H).

SALPKO disc hyperstability is also lost

The same disc extraction procedure performed on dGKO cells was performed on SALPKO cells. Discs were stained with anti-beta-giardin to visualize the disc. SALPKO discs were highly affected by the extraction protocol, showing a high degree of structure breakdown (Figure 3.4I). Some discs were completely disassembled and only remained as a diffuse signal.

SF-assemblin mutants have attachment defects

To determine the impact of attachment defects in the SF-assemblin mutant strains, we used a shear-force assay to quantify attachment on an *in vitro* substrate. Briefly, cells were injected into a flow chamber filled with buffer and given time to attach. Afterwards, cells were subject to

continuous shear force from buffer pumped at a constant rate into the chamber (Figure 3.5A). Number of initial cells and number of cells remaining attached after flow challenge was quantitated and compared between wild-type and MR SFA homologue lines (Figure 3.5B). This can be visualized by overlaying images taken before and after the flow challenge, and false coloring them red and green, respectively (Figure 3.5B). Cells false-colored red were unable to resist shear forces and detached; cells in yellow remained attached; and cells in green attached after flow rates were stopped.

All SF-assemblin DAP KO lines are less resistant to shear flow forces than wild-type

The number of cells remaining attached after challenge in wild-type, Cas9 only, and quadruple KO lines was quantitated (Figure 3.5C, 5D, 5E). Approximately 80% of wild-type cells remained attached after flow, while roughly 45% of bGKO cells stayed attached (Figure 3.5C). However, bGKO cells were not significantly worse at remaining attached than their Cas9 only negative control (Figure 3.5C). The bGKO+bG line did not regain wild-type attachment (Figure 3.5C).

dGKO cells were significantly worse at remaining attached than both the wild-type and their Cas9 only line (Figure 3.5D). dGKO cells were only able to remain attached approximately 20% of the time (Figure 3.5D), a much more severe defect than the bGKO line. Similarly, dGKO+dG complement cells were not able to regain wild-type attachment (Figure 3.5D). Finally, the SALPKO line had the most severe attachment defect, with less than 20% of cells able to remain attached (Figure 3.5E), significantly less than the wild-type and SALP1 Cas9 only lines. SALPKO+SALP cell attachment was partially restored, SALPKO+SALP resisted flow better than SALPKO cells, but were worse than wild-type (Figure 3.5E).

Exogenously expressed head or tail domains were insufficient to restore disc structure, except the SALP1 tail domain

To assess domain function, head and tail partial complements were inserted into SFA KO lines. The structure of Striated Fiber Assemblin homologs includes an unstructured head domain at the N terminus, followed by a series of coiled-coil repeats forming a rod domain at the tail end[18], (Figure 3.6A). It has been theorized that head and tail domains from adjacent SF-assemblins interact to form a Striated Fiber[22] (Figure 3.6A); this was proposed by work done in *Chlamydomonas* which has a sole SF-assemblin homolog. To determine the potential roles of head and tail domains on disc structure and function, we first identified head and tail domains for the three microribbon SFA homologues[19,22–24], and see Chapter 1. Head or tail domains were expressed in the cognate SF-assemblin quadruple KO lines and phenotypes were quantified with respect to disc structure and localization of other assemblins and the beta/delta giardins.

The beta-giardin tail domain is insufficient to restore visual wild-type phenotype, but partially restores delta-giardin localization

Full beta-giardin and tail domain only constructs were exogenously expressed in bGKO (lines bGKO+bG and bGKO+bGtail, respectively), and compared when visualized with an anti-delta-giardin stain (Figure 3.6B). bGKO+bG discs were visually indistinguishable from wild-type cells, and had delta-giardin localization in the disc (Figure 3.6B). bGKO+bGtail cells failed to restore wild-type disc structure, however (Figure 3.6B). Delta-giardin localization in bGKO+bGtail was partially restored, some cells had proper disc localization, in others, delta-giardin was still present outside of the disc. Overall, delta-giardin mislocalization in bGKO+bGtail was not as severe as in bGKO (Figure 3.6B). bGKO+bGtail discs had similar dimensions to the dGKO line and were significantly different from wild-type cells in width and length:width ratio (Figure 3.6D), but not in length (Figure 3.6C).

The delta-giardin head domain does not restore wild-type disc structure or dimensions

For delta-giardin complementation analyses, exogenous expression of full-length delta-giardin and head-only domain complements (lines dGKO+dG and dGKO+dGhead, respectively) were compared when visualized with anti-beta-giardin immunostaining (Figure 3.6E). dGKO+dG cells possessed discs that are visually indistinguishable from wild-type cells (Figure 3.6E). The dGKO+dGhead line failed to restore wild-type apparent cells (Figure 3.6E). dGKO+dGhead discs had similar dimensions to the dGKO line (Figure 3.6F) and were significantly different from wild-type cells in length and length:width ratio (Figure 3.6F, 6G).

The SALP1 tail domain, but not the head domain, is sufficient to restore wild-type disc appearance but not disc dimensions

Lastly, to interrogate the role of SALP1 head and tail domains in disc structure, cell lines expressing exogenous full length SALP1, SALP1 head domain only, and SALP1 tail domain only complements were created (SALPKO+SALP, SALPKO+SALPhead, SALPKO+SALPtail, respectively). The aforementioned lines were stained with anti-beta-giardin to determine beta-giardin localization and disc structure (Figure 3.6H). Both the SALPKO+SALP and the SALPKO+SALPtail lines had discs that were structurally indistinguishable from wild-type cells (Figure 3.6H). SALPKO+SALPhead discs were more similar in appearance to the SALPKO line (Figure 3.6H). None of the complement lines restored wild-type disc length (Figure 3.6I) or length:width ratio (Figure 3.6J). However, SALPKO+SALP had a significantly shorter disc length than the KO line (Figure 3.6I), and SALPKO+SALP, SALPKO+SALPhead, and SALPKO+SALPtail all had a lower length:width ratio than the SALPKO line (Figure 3.6J).

Expression of full beta-giardin or beta-giardin tail domain failed to restore wild-type flow resistance

bGKO+bG and bGKO+bGtail lines were challenged by flow as described previously. Both lines have significantly decreased attachment as compared to wild-type cells, with bGKO+bG

remaining attached approximately 50% of the time, and bGKO+bGtail remaining attached approximately 25% of the time (Figure 3.7A).

dGKO+dG and dGKO+dGhead cells also failed to remain adhered when challenged by flow

When dGKO+dG cells were challenged by flow, about 30% remained attached (Figure 3.7B). Sixty percent of dGKO+dGhead cells resisted flow challenge, and both lines were significantly worse at remaining attached when compared to a wild-type control (Figure 3.7B).

Expression of SALP1 head and tail domains in SALPKO did not restore wild-type attachment

SALPKO+SALP cells did not recover wild-type attachment rates but were significantly better at remaining attached than SALPKO cells (Figure 3.7C). SALPKO+SALPhead cell attachment was indistinguishable from SALPKO attachment, and significantly worse than wild-type (Figure 3.7C). Despite restoring visual wild-type disc appearance, SALPKO+SALPtail cells did not return to wild-type flow resistance (Figure 3.7C). However, SALPKO+SALPtail cells did remain attached significantly more than SALPKO cells.

Discussion

Giardia microribbon proteins provide insight into ventral disc mediated attachment

The critical role of disc-mediated attachment in Giardia pathogenesis has received remarkably little attention in the last 50 years, and prior work has been largely descriptive[2]. The work we have completed in this study on disc structure and function allow us to address a fundamental question in parasitology – how does Giardia attach to the host via the ventral disc? MR-CB DAPs are among the most abundant proteins in the disc[2], and the conspicuous MR-CB complex

associated with the entire ventral disc MT spiral array has been described for 50 years[25], yet its structural or functional role in attachment has only recently been discussed[26].

SF-assemblins perform structural roles across organism clades

Three out of the four known microribbon proteins are SF-assemblins[19]. Thus, we can compare the activity of Striated Fiber Assemblins in other organisms to the role these proteins play in *Giardia*. The SF-assemblin of the green algae *Chlamydomonas reinhardtii* is associated with the flagellar root microtubules[18], which help organize the flagella and coordinate the cytoskeleton during mitosis[27]. It was the self-assembly properties of *Chlamydomonas* SFA that was characterized *in vitro* with a domain analysis, which described the head domain as essential for assembly[22]. Striated Fibers in the ciliate *Tetrahymena thermophila*, also called kinetodesmal fibers in this organism, are necessary for proper cytoskeletal organization by providing physical bracing against the forces of ciliary beating[28]. Specifically, a *Tetrahymena* SFA, called DisAp, is required for maintenance of the ciliary array[28,29]. In *Giardia*, *Chlamydomonas*, and *Tetrahymena*, SFAs are responsible for maintaining cytoskeletal morphology.

Prior work targeted specifically at understanding the role of the SFA homologues in *Giardia*, is scarce. However, current hypotheses propose that beta-giardin, delta-giardin, and SALP1 polymerize into the initial MR complex that enables other MR-associated proteins to later assemble into the MR-CB complex[10]. The lack of known MR-CB proteins has restricted functional experiments targeting the MRs, and prevented functional work on the CBs. Only one non-SFA protein, gamma-giardin, is known to be part of the Microribbons[30], and there are currently no confirmed Crossbridge proteins. Finding additional MR proteins and identifying CB proteins is a key step to further understanding MR-CB structure and the ventral disc as a whole.

Structural impacts of SFA knockouts on the MR-CB complex

The inability of MR SFA KO cells to form wild-type discs suggests a key role for the MR-CB complex in stabilizing the disc structure. At minimum, beta-giardin, delta-giardin, and SALP1 are needed to maintain the disc's shape, and these proteins, or the microribbons as a whole, may play a role in disc formation during development of new discs during cell replication. One question about ventral disc formation has been whether the MR-CB complex is responsible for shaping the microtubule spiral, or whether other MAPs and MIPs are responsible for the curved microtubules, and the MR-CB complex forms on top. Our work has shown that microribbon proteins are necessary to maintain the typical shape of the microtubule spiral, suggesting that it is the MR-CB complex that shapes the tubulin spiral.

In all three microribbon protein knockout lines, the length:width ratio of the discs grew closer to 1, when compared to the negative control lines. If microtubules in the wild-type disc are under strain and the unique shape of the disc is maintained by the microribbons and crossbridges, any perturbation of this connection could "loosen" the disc spiral. It is possible that the knockout discs are "relaxing" into a more circular shape.

When thinking about the critical role of MR-CB proteins, and how different MR SFA knockdowns have different phenotypes, examining MR and CB substructure may provide insight. Different regions of the MR-CB complex (Figure 3.8B, 8C) may be associated with different functions, and we expect different structural and functional phenotypes dependent on their localization within the trilaminar MR-CB complex. As discussed in the Introduction, microribbons are trilaminar and an outer and inner layer. Additionally, microribbons are attached to the microtubule disc, but it is unknown if *Giardia* SFAs bind directly to tubulin or if there are intermediary proteins. Certain microribbon proteins may specialize in binding the crossbridges but play no role in the formation of the microribbons themselves. Thus, we predict specific MR-CB and disc phenotypes associated with knockdowns of proteins of various MR-CB

sublocalization (Figure 3.8B, 8C). Notably, we predict loss of disc three-dimensional dome shape in all hypothetical KOs, as connections between parallel MRs are severed or weakened.

bGKO cells either specifically mislocalize delta-giardin, or fail to properly form microribbons

Delta-giardin fails to localize properly in bGKO cells which supports an interaction between these SFAs. Specifically, there is no clearly defined disc in the bGKO strain, and delta-giardin signal is distributed throughout the cell body, with occasional foci. Thinking about the trilaminar microribbon structure, beta-giardin could be a core microribbon protein (Figure 3.8B), without which microribbon formation fails to take place. Cells without proper MR-CB complex formation to flatten out and become unable to maintain the disc dome shape. On the other hand, beta-giardin could have a much more specific role in the periphery, working closely in tandem with delta-giardin, and is needed for specifically delta-giardin localization. Alpha-tubulin staining in both wild-type and knockout cells only highlights the periphery of the disc, and does not penetrate into the disc body. Thus, we see that at least the outer portion of the disc is intact in bGKO cells, albeit with an altered shape. Taken in tandem with the idea that the MR-CB drives the tubulin spiral formation, this suggests that microribbons are at least present at the disc edge. At 400 nm, microribbons are at the limit of resolution by super resolution light microscopy, so direct visual examination of the microribbons would require additional imaging using electron microscopy.

Delta-giardin and SALP1 play a similar role in the microribbons and may localize to the same substructural region

The dGKO and SALPKO lines had similar phenotypes, and the microribbons were visible with a beta-giardin stain. Unlike the bGKO line, delta-giardin localized properly in the SALPKO line. In these lines, degradation of the disc occurred in both the MR-CB complex and in the microtubule

spiral, as visualized with an alpha-tubulin stain. If microribbons are forming properly, then delta-giardin and SALP1 could have a role in connecting microribbons and crossbridges necessary for the disc shape. It is also possible that delta-giardin and SALP1 are in the outer microribbon layer (Figure 3.8C) and beta-giardin in the inner layer (Figure 3.8B). Thus beta-giardin would properly localize and form the initial microribbon structure, but further development would cease (Figure 3.8B). dGKO discs and bare areas being larger in area than wild-type supports the "loosening spiral" hypothesis, where microtubules are relaxing into a more circular shape. Overall, the dGKO and SALPKO lines suggest a break in the MR-CB connection, but further study with electron microscopy is needed to see whether microribbon formation is occurring fully.

Role of SFA domain structure on disc assembly

In order to analyze the impact of different domains on the selected microribbon protein function, we performed a domain complementation analysis on the MR SFA knockout lines. As mentioned previously, SF-assemblins have a disorganized head domain followed by a series of coiled-coil repeats[22,23]. Work by Lechtreck[22] found that both the head and coiled-coil domains were necessary for the formation of fibrous structures by *Chlamydomonas* SF-assemblin *in vitro* (Figure 3.8D). Following up on his work, we decided to see if exogenous expression of only head or tail domains of the microribbon proteins could restore a wild-type disc phenotype in the associated KO line. We also complemented our KOs with a full-length version of the respective protein. Full gene complements restored visual wild-type appearance in all our KO lines but did not restore wild-type disc dimensions. Daughter discs are formed *de novo* during cellular replication, so it is unlikely that structural inheritance is preventing restoration of wild-type measurements. Complement copies of the gene were expressed exogenously, with an unknown number of plasmids retained by *Giardia* cells to withstand selection. Therefore, a difference in

the number of complement copies of the gene and the number of copies that were knocked out might explain the differences in measurements seen.

Expressing only the beta-giardin tail domain in the bGKO line was insufficient to restore wild-type appearance. Discs with enlarged bare areas and detached overlap zones were prominent in the population. Interestingly, the beta-giardin tail domain was sufficient to partially restore delta-giardin localization. In bGKO+bGtail cells, some cells had ventral discs visible by delta-giardin staining; mislocalization was limited to streaks or clumps of signal outside the disc, in contrast to the full cell stain in bGKO cells. It is possible that delta-giardin, or other micoribbon proteins interact with the beta-giardin tail domain, thus the presence of this fragment is enough to recruit them to the disc. However, the lack of wild-type disc formation suggests the beta-giardin head domain plays a key role in this process.

Expressing the delta-giardin head domain was unable to restore wild-type disc appearance in dGKO cells. The delta-giardin head domain is a small fragment of the full protein size, and the tail domain is a necessary component of this protein's function.

The SALP1 tail domain by itself was enough to restore a wild-type disc appearance in SALPKO cells. While disc dimensions remained significantly different than wild-type cells, it appears that the SALP1 tail domain is able to function sufficiently on its own. This contrasts our findings with the beta-giardin tail domain and may reflect the evolutionary difference between these two proteins. Alternatively, SALP1 may have a more peripheral role, either literally at the outer edge of the microribbons, or is otherwise more easily compensated for, such that these discs are able to remain intact. As anticipated, SALP1 head domain expression was unable to restore SALPKO discs.

The MR-CB complex contributes to disc hyperstability

The disc as a hyperstable microtubule organelle was discussed in prior research[4]. Briefly, wild-type ventral discs are neither affected by the tubulin drugs Taxol or nocodazole, nor extraction with detergent and 2M KCl[4]. Knocking out disc proteins may make the disc vulnerable, as was seen previously. dGKO and SALPKO discs were extracted following the previous protocol[4], and stained with anti-beta-giardin to determine if further disc breakdown occurred beyond the phenotypes discussed in Figure 3.3C, 4C. Our observations of greater disc disruption, especially in the SALPKO line, suggests that delta-giardin and SALP1 contribute to hyperstability. The MR-CB complex in general may also shield the disc microtubules from the dynamic instability found in other organisms.

Implications of the MR-CB on disc contraction and/or attachment

Early work on *Giardia* attachment put forth a “hydrodynamic model” whereby fluid, drawn by beating flagella, would flow through channels in an immotile disc producing a current-based suction[3]. However, a more recent study examining mutants with flagellar motility defects found that attachment does not require flagellar beat[31]. Thus, novel attachment hypotheses shift focus to the disc as the primary agent of attachment. A new study has shown evidence for a “disc contraction” hypothesis, where a flexible disc compresses or constricts arms of the microtubule spiral to physically change disc conformation and generate suction force[26].

To connect the impact that microribbon protein KO disc phenotypes have on the disc’s ability to attach to a surface and the role of microribbons in attachment, we performed a quantitative flow assay by challenging our KO lines to shear flow stress. In all MR SFA KO lines, we observe a decrease in attachment ability when compared to a wild-type control. Thus, we confirm that an intact disc is an essential component of *Giardia* attachment. We also see that the dGKO and SALPKO lines are more heavily impacted in their ability to attach than the bGKO line. It is possible that this finding supports a more peripheral role for beta-giardin, and a linear relationship between severity of disc phenotype and attachment ability. Notably, not all cells

were detached by flow, even in the dGKO and SALPKO lines, and this may connect to the variation in phenotype observed in these lines.

Overall significance

Our work has shown that the MR-CB complex is an essential component of disc organization and is responsible for maintaining the unique structure of the disc microtubule spiral. In particular, the proteins beta-giardin, delta-giardin, and SALP1 all play key roles in disc stability and maintenance, which in turn, is essential for cell attachment. This study has opened the door for further work on beta-giardin, delta-giardin, and SALP1, to understand the mechanisms and protein interactions behind disc assembly, and perhaps on the nature of SFA self-assembly as a whole. Additionally, the close association of the MR SFAs with the disc microtubule spiral is ripe for exploring to understand how the rigorous conformation of these microtubules is manipulated and maintained.

Materials and Methods

Giardia culture, electroporation, and creation of KO mutants

Giardia lamblia trophozoites (strain WBC6, ATCC 50803) were grown at 37°C in 16 ml screw cap culture tubes (BD Falcon), no shaking. Culture medium was 12 ml modified TYI-S-33 with added bovine bile, 5% adult and 5% fetal bovine serum. Either at full confluence, or after a 48-hour period, tubes were placed on ice for 15 minutes and subcultured by transferring unattached trophozoites (1 ml) to fresh medium.

Electroporation of plasmids or linear homology-directed repair (HDR) templates into *Giardia* were performed as previously described[4]. 40 µg DNA and 1 x 10^7 trophozoites were used in each electroporation. After electric shock, cells were moved to culture tubes as

described above, and incubated at 37°C. Media was exchanged for fresh media every 48 hours. Initial concentration of antibiotic used for selection were as follows: puromycin (12.5 µg/ml), blasticidin (75 µg/ml), hygromycin B gold (600 µg/ml), and G418 (150 µg/ml). Upon reaching 50% confluency or greater, a higher concentration of antibiotic was used as follows: puromycin (50 µg/ml), blasticidin (150 µg/ml), hygromycin B gold (1200 µg/ml), and G418 (600 µg/ml).

To get clonal lines, we used dilution in 96 well tissue culture plates (Corning). Cells were diluted to 0.5 cells/well, and plates were incubated at 37°C in Mitsubishi AnaeroPack 2.5L jars with a Mitsubishi AnaeroPack-Anaero Gas Generator (ThermoScientific) for 7 days. Wells were screened for cell growth, and plates were incubated on ice for 1 hour to detach cells. Samples were taken for PCR screening, and the remainder was transferred to 8 ml screw cap culture tubes (BD Falcon) at 37°C. Upon reaching 50% confluence, cells were incubated on ice for 15 minutes, and 2 ml of trophozoites were transferred to a standard culture tube for continued culturing.

Creation of the Cas9/gRNA vector and HDR templates for MR DAP knockout lines

The Cas9/gRNA vector used has been described previously[21]. Using the CRISPR 'Design and Analyze Guides' tool from Benchling (https://benchling.com/crispr), we selected 20 nt gRNA sequences with an NGG PAM sequence from the *Giardia lamblia* ATCC 50803 genome (GenBank Assembly GCA_000002435.1). The following gRNA oligo sequences were selected and ordered: beta-giardin forward (5'-caaaCCGTACGCTCACCCAGACGA-3'), beta-giardin reverse (5'-aaacTCGTCTGGGTGAGCGTACGG-3'), delta-giardin forward (5'-caaa ACTTTCACGAGGACTTCAAG-3'), delta-giardin reverse (5'-aaac CTTGAAGTCCTCGTGAAAGT-3'), SALP1 forward (5'-caaaCGATGACCGCGAGCTACGTG-3'), and SALP1 reverse (5'-aaacCACGTAGCTCGCGGTCATCG-3'). These included 4-base overhangs to complement the vector overhangs when annealed and ligated.

HDR templates for the beta-giardin and delta-giardin knockouts were the 750 bp up and downstream of the double stranded break site, combined with either the blasticidin or hygromycin B gold cassette described previously[26]. The SALP1 HDR template used 610 bp upstream and 415 bp downstream of the double stranded break, combined with the templates above, to minimize impact on surrounding genes in the *Giardia* genome. Mutations were made within the gRNA target site to prevent HDR cutting by Cas9. The HDR templates were synthesized (Twist Biosciences), and linear templates for use in electroporation were PCR amplified using Phusion DNA polymerase (New England Biolabs) with M13 Forward and M13 Reverse primers. PCR product was purified and concentrated with Zymo Research Clean and Concentrator-25 columns.

Generation of MR DAP quadruple knockout lines

The completed Cas9/gRNA plasmid specific to each MR DAP was electroporated into wild type WBC6, as described above. The Cas9/gRNA was maintained through constant puromycin selection. The linear HDR templates were introduced into their respective Cas9/gRNA lines via two sequential electroporations, first the modified blasticidin HDR, then the modified hygromycin HDR. After the second HDR cassette was introduced, cells were cloned out (see above) and clones were sampled. Samples were analyzed by PCR with a PHIRE Tissue Direct PCR Master Mix kit (ThermoScientific), using primers beta-giardinLeftF (5'-TGCTTTGGAAGCTTACGCAC-3'), beta-giardinRightR (5'-GCTTTGTGACCATCGAGAGG-3'), delta-giardinLeftF (5'-CGGCGTTTAAGGGACCAGTG-3'), delta-giardinRightR (5'-TAAGCTCTCCCAAGGCAGCG-3'), SALP1LeftF (5'-TCTGGATCGCATACCTCTGC-3'), and SALP1RightR (5'-TGGCCACTTCAGAGTCTAGC-3'). The insertion of HDR cassettes was detected by the presence of longer amplicons than what was amplified from wild type gene sequences. Quadruple knockouts were detected by absence of any amplicons that corresponded in length

to wild type gene sequences. Quadruple knockout clones were selected as follows: beta-giardin KO (3G2), delta-giardin KO (1B4), SALP1 KO (1D1).

Design and creation of MR DAP complement lines

Complement lines were described as full-length complement, head domain only, or tail domain only. Head domains were defined by consulting relevant literature and examining the structure of the three MR DAPs. The general structure of SF-assemblins has been described previously[19,22–24]. Holberton[23] described the beta-giardin head domain as 19 amino acids, and Lechtreck[22] found that a deletion of 19 amino acid residues from the N-terminus of beta-giardin was sufficient to disrupt *in vitro* paracrystal formation. In this paper, we defined the following sequence as the beta-giardin head domain (N-MDKPDDLTRSATETAVKLS-C). The tail domain for beta-giardin, and all tail domains in this paper, was defined as the remaining sequence of amino acids not in the head domain. The delta-giardin head domain was defined by consulting an alignment of the *Giardia* SFAs found in the literature[19], and our own analysis (see Chapter 1). Comparing the beta-giardin and delta-giardin alignments, we defined delta-giardin's head domain as the first 31 amino acid residues (N-MTTVSTSFSLKDRLAKINSRVTDFHEDFKRQ-C). Palm[19] describes SALP1 as not possessing a head domain, but we observe a similar pattern in amino acid periodicity as the other *Giardia* SFAs, and defined the SALP1 head domain as the first 25 residues (N-MFSVRADPTKSRLNVIDSHTSEFMV-C). Head, tail, and full-length sequences were synthesized (Twist Biosciences), and inserted into an expression vector. Complementation vectors were electroporated into quadruple knockout lines, described above.

Immunofluorescence staining of MR DAP knockouts and other lines

Giardia to be immunostained were either allowed to attach live to coverslips or were fixed in culture medium and settled on coverslips. *Giardia* trophozoites were grown to confluence in 12 ml of culture medium at 37°C before harvesting. To attach cells to coverslips before fixation,

culture tubes were placed on ice for 15 minutes, then spun down at 900 x g for 5 minutes. Cells were washed three times with 5 ml HEPES-buffered saline (HBS, 137 mM NaCl, 21 mM HEPES, 5.55 mM glucose, 5 mM KCl, 0.76 mM Na_2HPO_4), resuspended in 1 ml of HBS, after which, cells were added to coverslips, 500 µl each, inside an 8 well plate. Cells were allowed to attach to coverslips inside a humidified chamber for 20 minutes at 37°C. After attachment, HBS was aspirated via pipette, and 2 ml of 4% paraformaldehyde in HBS, pH 7.4, was added onto each coverslip. Cells were fixed for 2 minutes, before being aspirated and washed three times with 2 ml PEM (100 mM PIPES [piperazine-N,N'-bis(2-ethanesulfonic acid)], 1 mM EGTA, 0.1 mM $MgSO_4$ pH 6.9).

To settle fixed *Giardia* on coverslips, 375 µl of 32% paraformaldehyde was added to a confluent 12 ml culture tube (1% final concentration) for 10 minutes at 37°C. After, the tube was spun down at 900 x g for 5 minutes and washed once with HBS. Cells were resuspended in 1 ml of HBS, added to 2 poly-L-lysine coated coverslips, 500 µl each, and incubated to 15 minutes at room temperature. Coverslips were then washed three times with 2 ml PEM.

Following the above, the protocol is the same for both attached and settled cells. Paraformaldehyde in fixed, washed cells was quenched for 5 minutes by incubating in 0.125 M glycine at room temperature. Cells were then washed again for three times with PEM, and permeabilized with 0.1% Triton X-100 for 10 minutes. Coverslips were washed three times with PEM and blocked with 2 ml PEMBLG (PEM with 1% bovine serum albumin, 100 mM lysine, 0.5% cold-water fish skin gelatin [Sigma, St Louis, MO]) for 30 minutes. Coverslips were incubated overnight at 4°C in one or more of the following antibodies: anti-beta-giardin (1:1000), anti-delta-giardin (1:1000), or anti-TAT1 (1:500). Anti-beta and delta-giardin are gifts of Mark Jenkins, USDA, and anti-TAT1 is a mouse monoclonal antibody against alpha-tubulin, and a gift of Keith Gull (University of Oxford, UK). Coverslips were washed three times in PEMBLG and incubated with the following for three hours at room temperature: goat anti-rabbit and/or goat

anti-mouse Alexa Flour 488, 594, or 647 antibodies (1:1000, Life Technologies). Coverslips were washed three times with PEMBLG, followed by three times with PEM and mounted in Prolong Diamond antifade reagent (Invitrogen). All imaging experiments were performed with at least three biologically independent samples.

Acquisition of wide-field fluorescence images and 3D SIM super-resolution images

Single or multi-focal plane images were acquired with a Leica DMI 6000 wide-field inverted fluorescence microscope, using the 100x or 40x objective, and μManager image acquisition software.

For super-resolution images of fluorescently tagged MR KO cell lines, 3D stacks were collected at 0.1 μm intervals using a Nikon N Structured Illumination Super-resolution Microscope with a 100x/NA 1.49 objective, 100 EX V-R diffraction grating, and an Andor iXon3 DU-897E EMCCD. Images were acquired and reconstructed using NIS-Elements software (Nikon), in the “3D-SIM” mode. Images were reconstructed in the “Reconstruct Slice” mode and were only used if the score was 8.

Assay quantifying attachment and resistance to shear flow force

Giardia trophozoites were cultured in 12 ml culture medium until full confluency. Cells were iced for 15 minutes, washed with HBS, and stained with either CellMask orange or green (ThermoFisher) for 10 minutes. Cells were then washed with HBS and added to an Ibidi mSlide VI 0.4 flow chamber. Images of cells at a concentration of 2 million per ml were taken with a 40x objective on a Leica DMI 6000 wide-field microscope. Fluorescent images were acquired of attached cells before and after flow challenge for 20 seconds at a rate of 3 ml/minute. DIC images were taken at a rate of 1 per second for 20 seconds pre-challenge, during challenge, and for 20 seconds post-challenge. Cells were permitted to attach for 5 minutes prior to challenge. Pre- and post-challenge fluorescence images were compared; cells that remained in

place were considered resisting flow, cells that did not remain in place were unable to resist flow.

Biochemical extraction of the ventral disc

In order to test whether SFA knockouts affected the hyperstable nature of *Giardia*'s ventral disc, we performed a biochemical disc isolation as previously described[4,11]. One tube of *Giardia* trophozoites per cell line were cultured as described above until fully confluent. Cells were then washed with HBS and resuspended in 1 ml of 0.5x HBS/1x PHEM (60 mM PIPES, 25 mM HEPES, 10 mM EGTA, 1 mM $MgCl_2$, pH 7.4) containing 1% Triton X-100, 1 M KCl and 1× HALT protease inhibitor cocktail (Roche). The resuspensions were transferred to 1.8 ml Eppendorf tubes and vortexed for 30 min (VWR Vortex-Genie2, vortex speed setting at 5) to extract cytoskeletons. Extracted cytoskeletons were centrifuged at 3000 x g for 5 minutes. The supernatant was discarded and the pellets were washed twice in 1 ml 0.5x HBS/1x PHEM, before being resuspended in 1 ml 0.5x HBS/1x PHEM. To image the state of the extracted discs, 500 µl of the isolated cytoskeletons was added each to two poly-L-lysine treated coverslips and settled for 15 minutes. The cytoskeletal preparations were fixed with 4% paraformaldehyde in HBS for 2 minutes and quenched with 250 mM glycine for 5 minutes, before proceeding with the remaining immunofluorescence protocol.

Acknowledgements

This work was supported by an R01AI077571 award to SCD. We graciously thank the UC Davis MCB Microscopy Core for helpful advice on the SIM microscopes. We also thank Katie Chun and Alec Juliano for their contributions to this work.

Figures

Figure 3.1: Giardia possesses three SF-assemblin homologs in its ventral disc

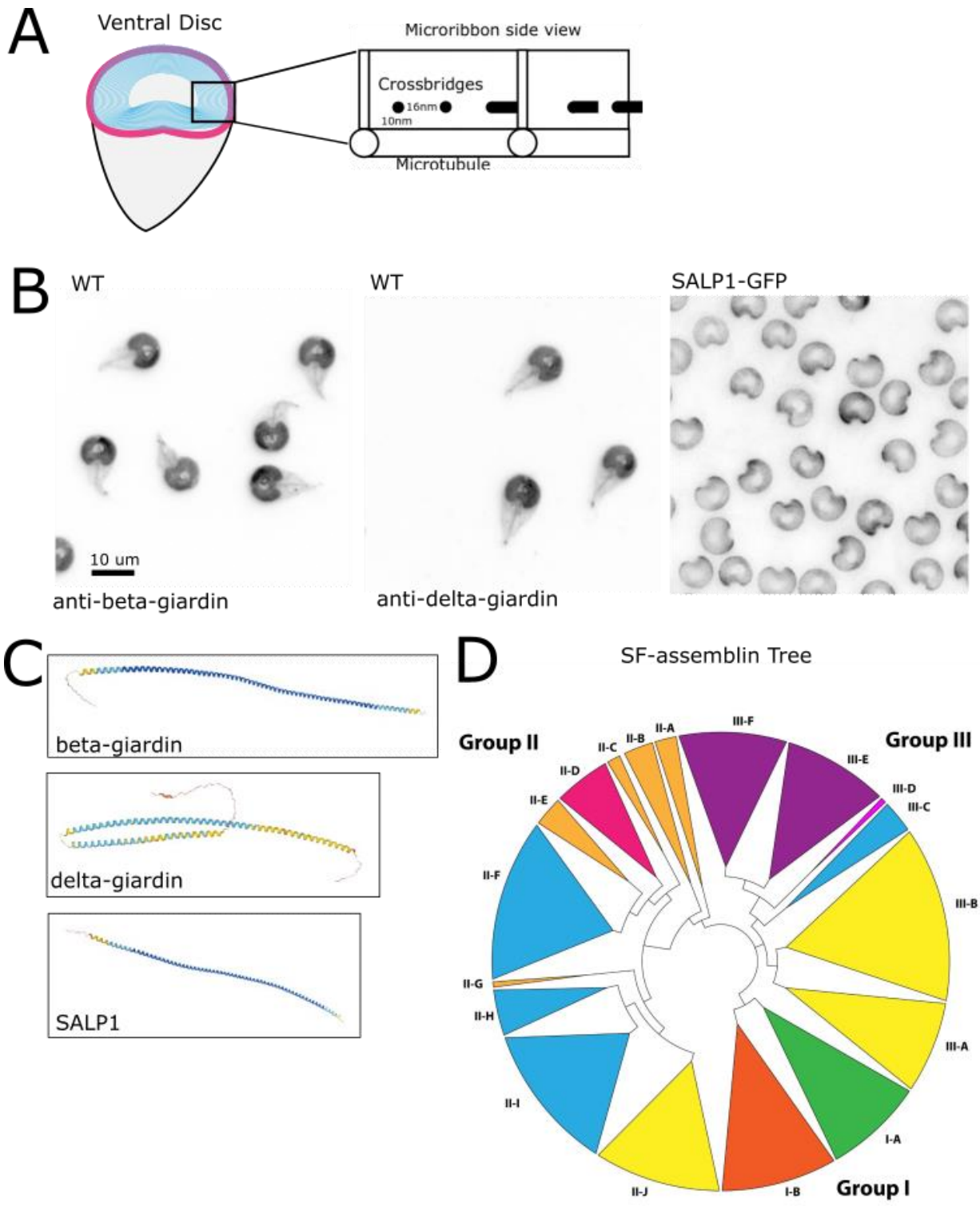

E

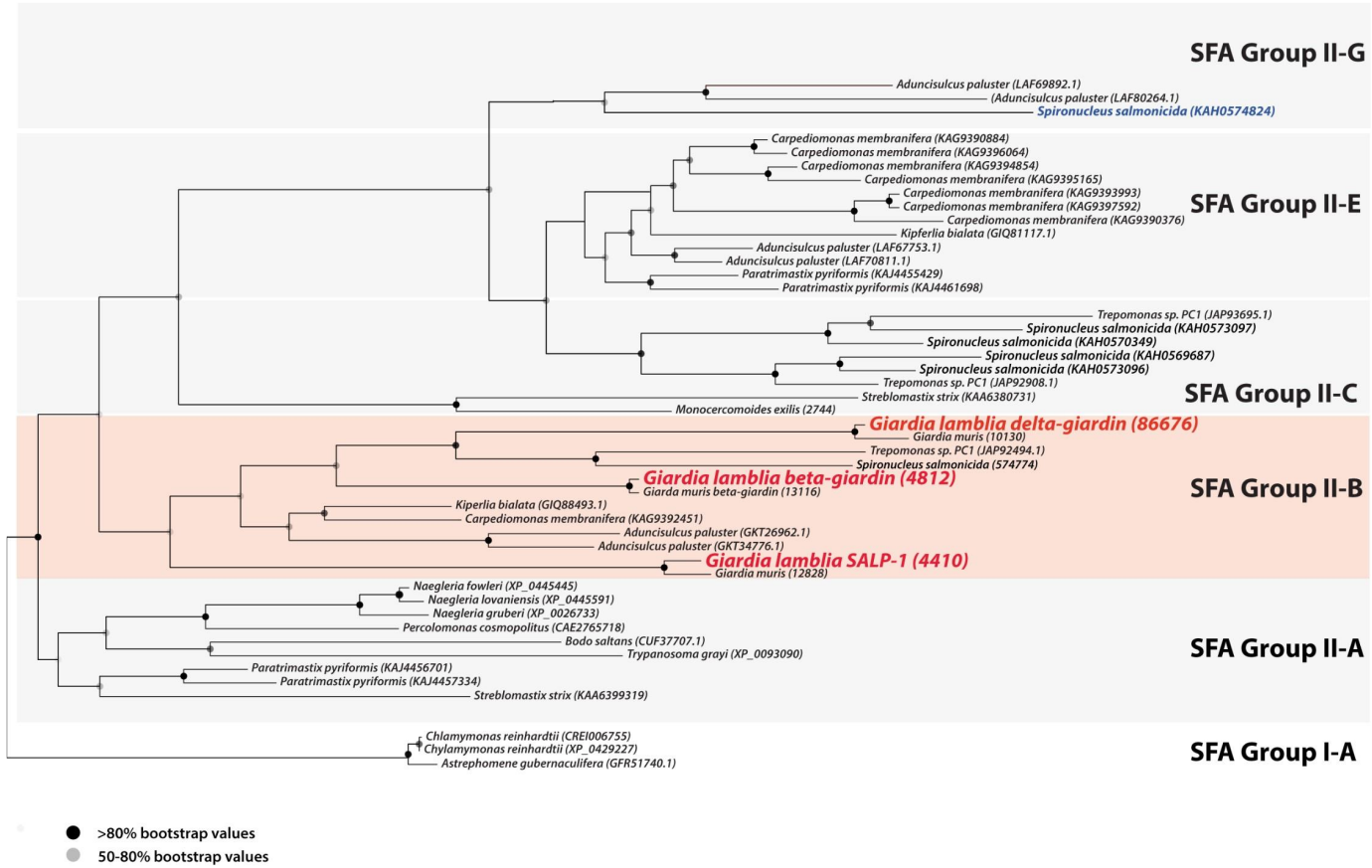
SFA Group II-G
Aduncisulcus paluster (LAF69892.1)
(Aduncisulcus paluster (LAF80264.1)
Spironucleus salmonicida (KAH0574824)
SFA Group II-E
Carpediomonas membranifera (KAG9390884)
Carpediomonas membranifera (KAG9396064)
Carpediomonas membranifera (KAG9394854)
Carpediomonas membranifera (KAG9395165)
Carpediomonas membranifera (KAG9393993)
Carpediomonas membranifera (KAG9397592)
Carpediomonas membranifera (KAG9390376)
Kipferlia bialata (GIQ81117.1)
Aduncisulcus paluster (LAF67753.1)
Aduncisulcus paluster (LAF70811.1)
Paratrimastix pyriformis (KAJ4455429)
Paratrimastix pyriformis (KAJ4461698)
SFA Group II-C
Trepomonas sp. PC1 (JAP93695.1)
Spironucleus salmonicida (KAH0573097)
Spironucleus salmonicida (KAH0570349)
Spironucleus salmonicida (KAH0569687)
Spironucleus salmonicida (KAH0573096)
Trepomonas sp. PC1 (JAP92908.1)
Streblomastix strix (KAA6380731)
Monocercomoides exilis (2744)
SFA Group II-B
Giardia lamblia delta-giardin (86676)
Giardia muris (10130)
Trepomonas sp. PC1 (JAP92494.1)
Spironucleus salmonicida (574774)
Giardia lamblia beta-giardin (4812)
Giardia muris beta-giardin (13116)
Kiperlia bialata (GIQ88493.1)
Carpediomonas membranifera (KAG9392451)
Aduncisulcus paluster (GKT26962.1)
Aduncisulcus paluster (GKT34776.1)
Giardia lamblia SALP-1 (4410)
Giardia muris (12828)
SFA Group II-A
Naegleria fowleri (XP_0445445)
Naegleria lovaniensis (XP_0445591)
Naegleria gruberi (XP_0026733)
Percolomonas cosmopolitus (CAE2765718)
Bodo saltans (CUF37707.1)
Trypanosoma grayi (XP_0093090)
Paratrimastix pyriformis (KAJ4456701)
Paratrimastix pyriformis (KAJ4457334)
Streblomastix strix (KAA6399319)
SFA Group I-A
Chlamymonas reinhardtii (CREI006755)
Chylamymonas reinhardtii (XP_0429227)
Astrephomene gubernaculifera (GFR51740.1)
>80% bootstrap values
50-80% bootstrap values

A) Schematic representation of a *Giardia* cell, with the ventral disc outlined in pink, and the disc MT spiral depicted in blue. A zoom in on the disc spiral reveals micoribbons extending down the length of disc MTs, and crossbridges regularly connecting microribbons. B) Wild-type cells were stained with anti-beta-giardin or anti-delta-giardin to depict the localization of these proteins to the ventral disc. A C-terminal GFP tagged SALP1 also shows this protein's localization to the ventral disc. C) AlphaFold predictions of beta-giardin, delta-giardin, and SALP1 structure. N-termini, oriented towards the left, all show an unstructured head domain. D) Schematic of SF-assemblin family tree (see Chapter 1). The SF-assemblin family of proteins breaks into three main groups, with various subgroups below. *Giardia*'s SFA homologs can be found in Group II-B. E) Detailed tree of excavate SFA proteins. The three *Giardia* SFAs have been highlighted in red.

Figure 3.2: bGKO mislocalizes delta-giardin and possesses altered disc dimensions

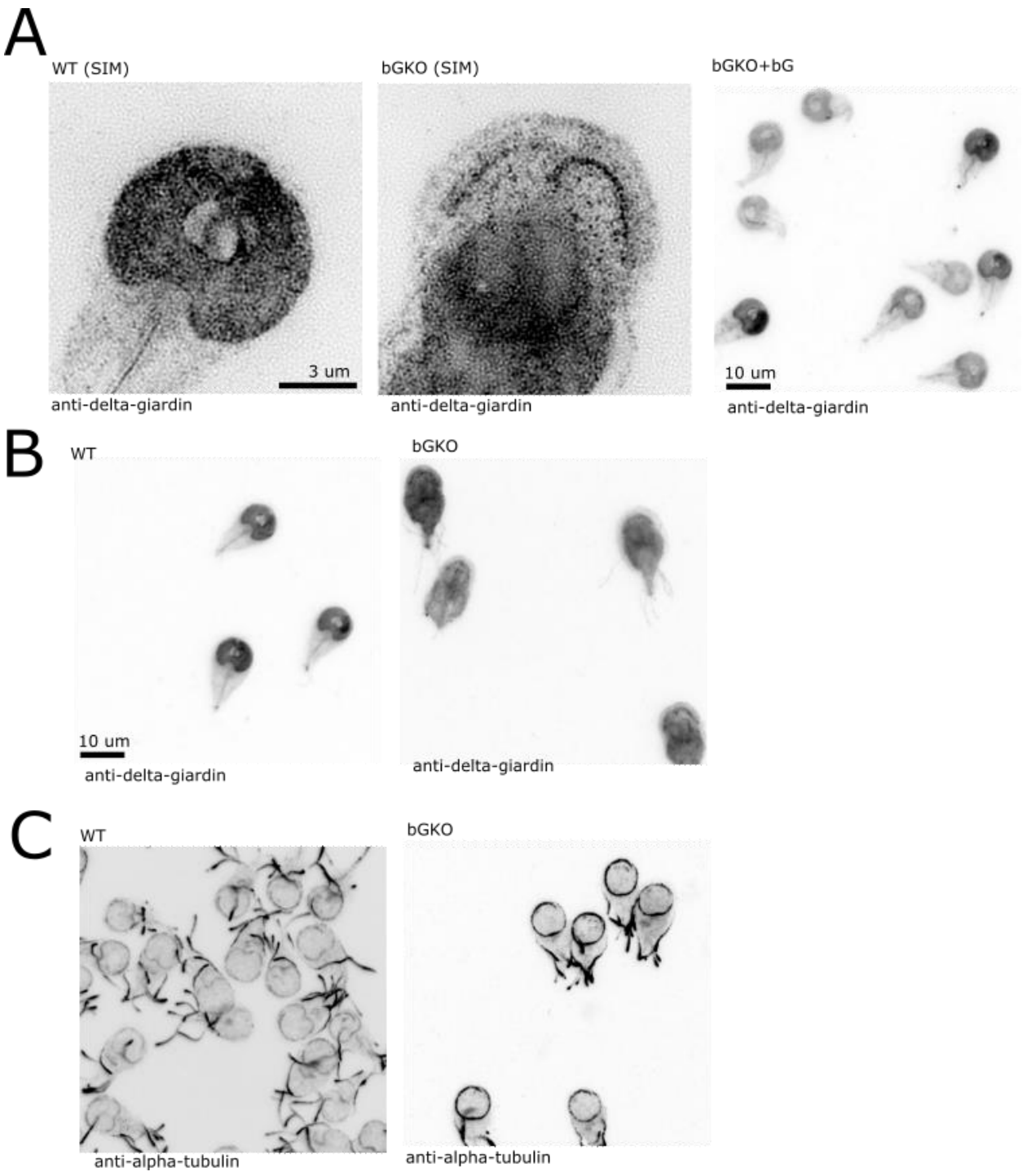

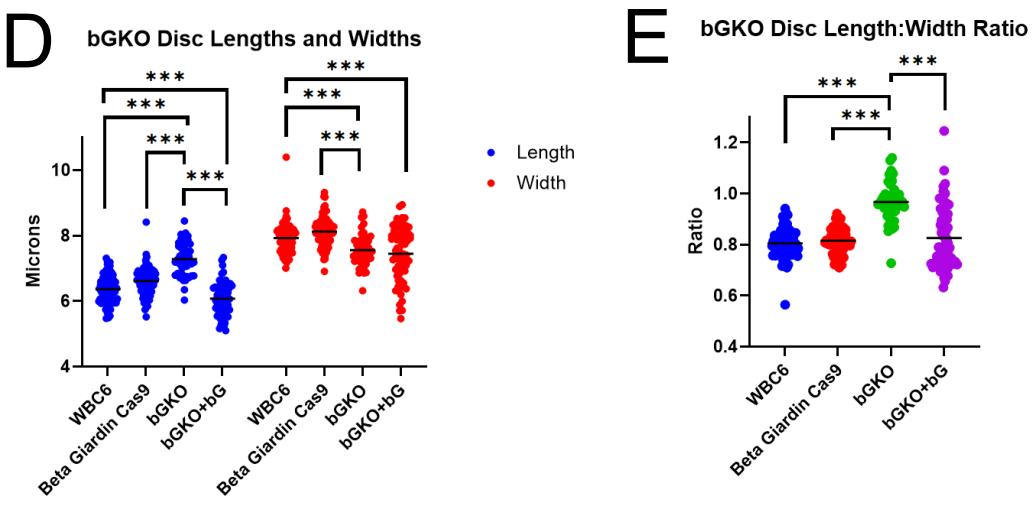

A) Structured Illumination Microscopy (SIM) imaging of wild-type and bGKO cells stained with anti-delta-giardin, to show mislocalization of delta-giardin in bGKO cells. Wide-field imaging of bGKO+bG cells to show restoration of anti-delta-giardin localization to the ventral disc. B) Wide-field image of wild-type and bGKO cells stained with anti-delta-giardin. C) Wide-field image of wild-type and bGKO cells stained with anti-alpha-tubulin, showing disc periphery, which was used for disc dimensional measurements in bGKO cells. D) Length and width measurements of discs in wild-type (WBC6), strains expressing only a Cas9 targeting beta-giardin, bGKO, and bGKO+bG lines, showing longer and thinner bGKO discs. *** represents p value <0.001. E) Disc lengths and widths were compared via a ratio; bGKO discs are more circular. Discs in wild-type (WBC6), strains expressing only a Cas9 targeting beta-giardin, bGKO, and bGKO+bG lines were measured.

Figure 3.3: dGKO has a disrupted disc spiral

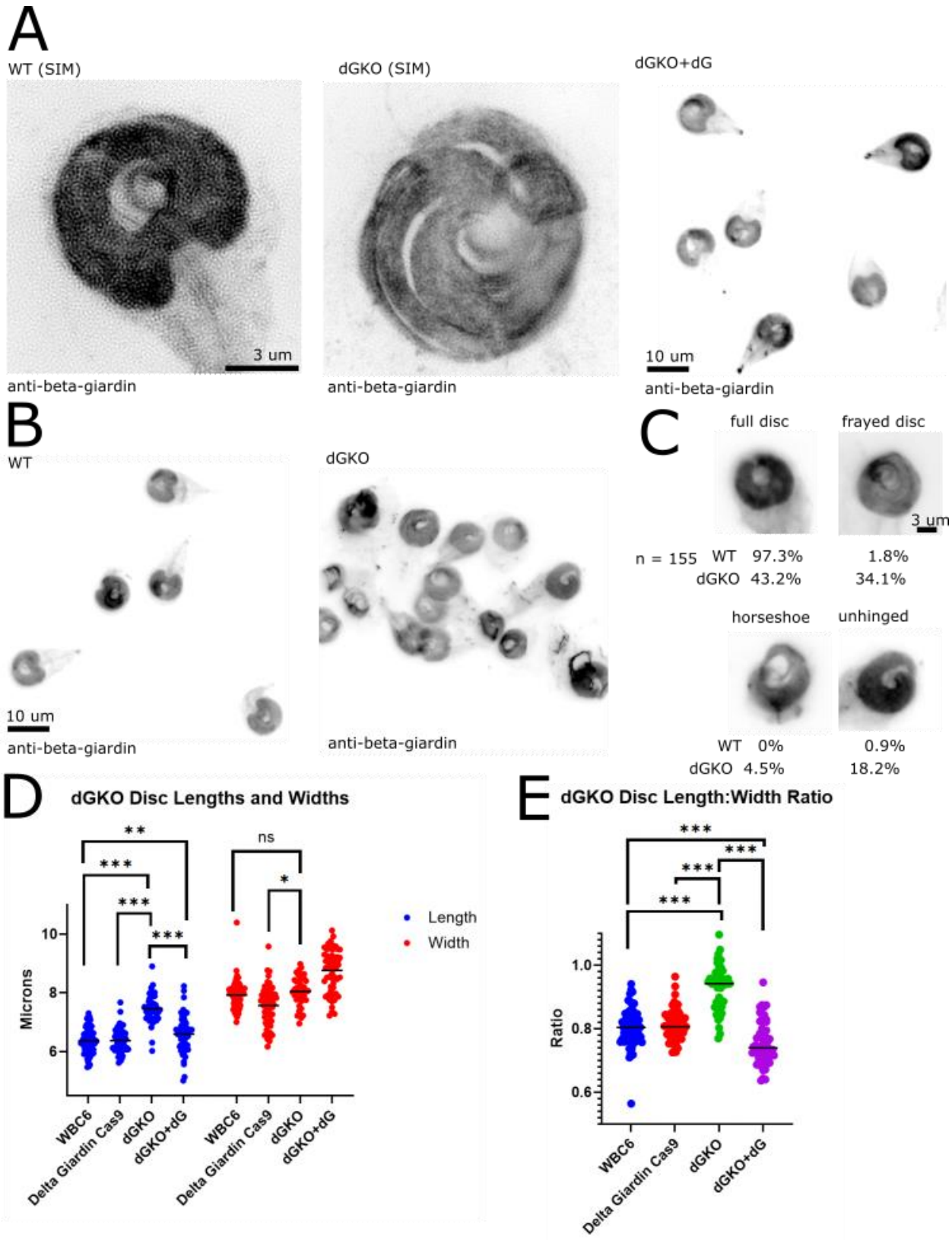

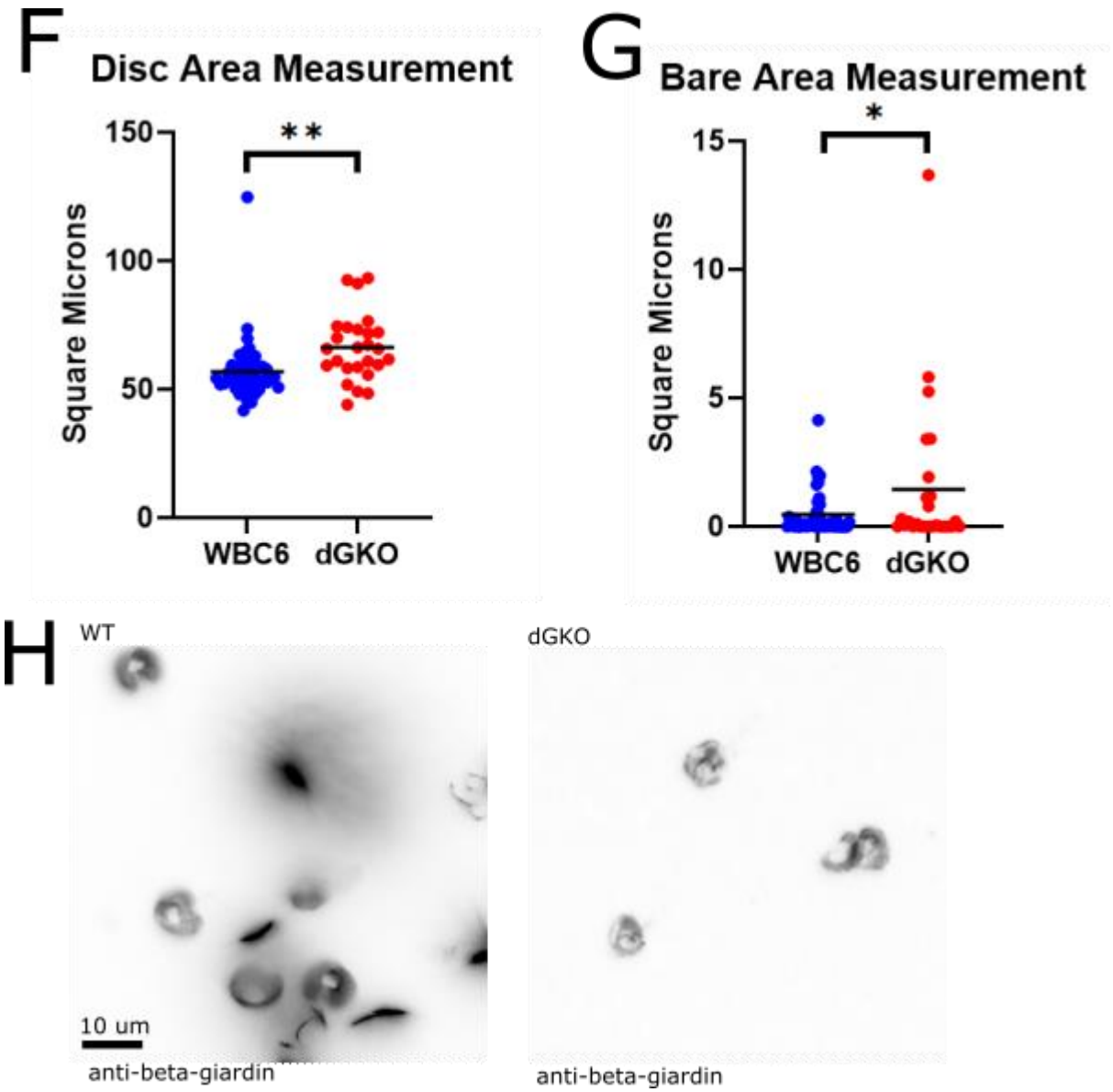

A) Structured Illumination Microscopy (SIM) imaging of wild-type and dGKO cells stained with anti-beta-giardin to illustrate a broken disc spiral. Wide-field imaging of dGKO+dG cells to show restoration of full disc phenotype. B) Wide-field image of wild-type and dGKO cells stained with anti-beta-giardin. C) Phenotype analysis of wild-type and dGKO strains stained with anti-beta-giardin. Discs were classified as the following: disc with full structure present, indistinguishable from wild-type (full disc); arms of the disc spiral breaking apart and becoming disjointed (frayed disc); loss of disc material such that a full disc cannot be formed (horseshoe); intact arms of

spiral, but overlap zone has come undone (unhinged). D) Length and width measurements of discs in wild-type (WBC6), strains expressing only a Cas9 targeting delta-giardin, dGKO, and dGKO+dG lines. * represents p value <0.05, ** represents p value <0.01, *** represents p value <0.001, and ns is not significant. E) Disc lengths and widths were compared via a ratio. Discs in wild-type (WBC6), strains expressing only a Cas9 targeting delta-giardin, dGKO, and dGKO+dG lines were measured. F) Disc area measurements were taken in Fiji (ImageJ) using the "Thresholding" and "Particle Analysis" features, excluding the space left by the bare area. Area measurements were performed using wild-type (WBC6) or dGKO cells stained with anti-beta-giardin. G) Area of the bare area was also measured using the same functions as in (F). H) A hyperstability analysis using detergent and salt to extract discs[4] was performed on wild-type and dGKO cells. Cells were stained with anti-beta-giardin for analysis.

Figure 3.4: SALPKO discs have a similar appearance to dGKO discs

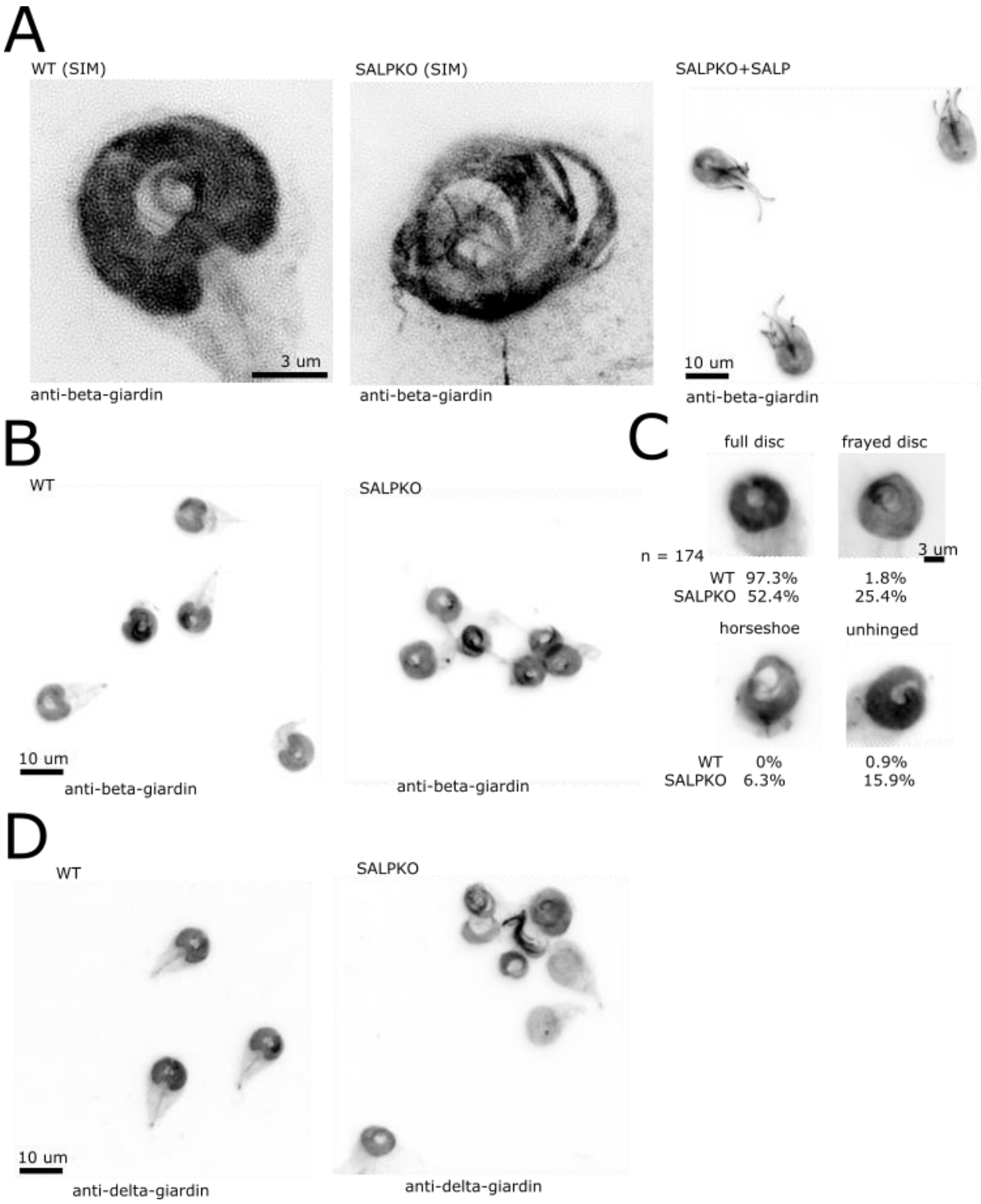

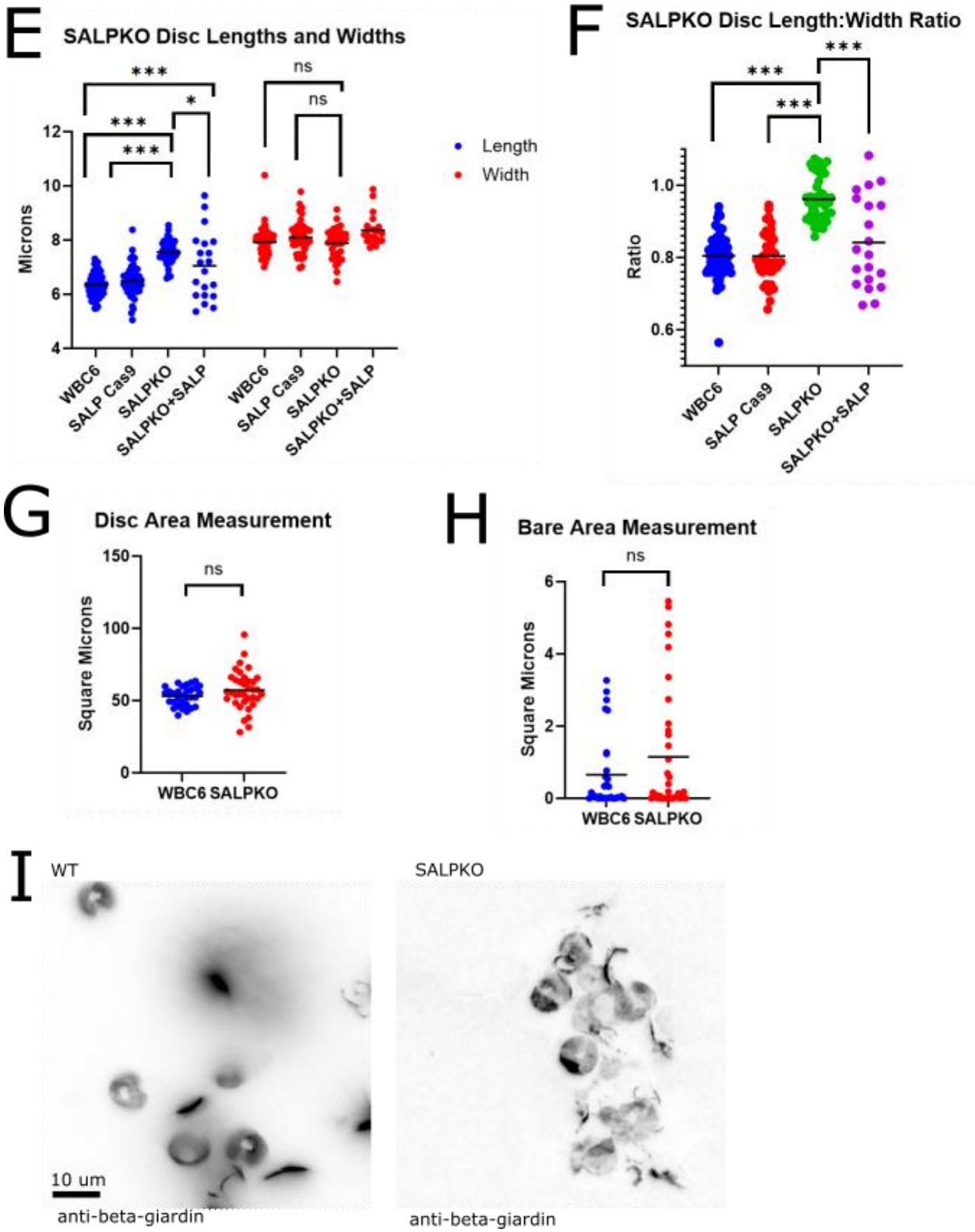
E
SALPKO Disc Lengths and Widths
Microns
Length
Width
WBC6
SALP Cas9
SALPKO
SALPKO+SALP
F
SALPKO Disc Length:Width Ratio
Ratio
G
Disc Area Measurement
Square Microns
WBC6 SALPKO
H
Bare Area Measurement
Square Microns
WBC6 SALPKO
I
WT
SALPKO
10 um
anti-beta-giardin
anti-beta-giardin

A) Structured Illumination Microscopy (SIM) imaging of wild-type and SALPKO cells stained with anti-beta-giardin showed similar phenotypes as dGKO cells. Wide-field imaging of SALPKO+SALP cells to show restoration of full disc phenotype. B) Wide-field image of wild-type and SALPKO cells stained with anti-beta-giardin. C) Phenotype analysis of wild-type and SALPKO strains stained with anti-beta-giardin. Discs were classified as the following: disc with full structure present, indistinguishable from wild-type (full disc); arms of the disc spiral breaking apart and becoming disjointed (frayed disc); loss of disc material such that a full disc cannot be formed (horseshoe); intact arms of spiral but overlap zone has come undone (unhinged). D) Wide-field imaging of wild-type and SALPKO cells stained with anti-delta-giardin to show consistency of microribbon appearance across available immunostains. E) Length and width measurements of discs in wild-type (WBC6), strains expressing only a Cas9 targeting SALP1, SALPKO, and SALPKO+SALP lines. * represents p value <0.05, *** represents p value <0.001, and ns is not significant. F) Disc lengths and widths were compared via a ratio. Discs in wild-type (WBC6), strains expressing only a Cas9 targeting SALP1, SALPKO, and SALPKO+SALP lines were measured. G) Disc area measurements were taken in Fiji (ImageJ) using the "Thresholding" and "Particle Analysis" features, excluding the space left by the bare area. Area measurements were performed using wild-type (WBC6) or SALPKO cells stained with anti-beta-giardin. H) Area of the bare area was also measured using the same functions as in (G). I) A hyperstability analysis using detergent and salt to extract discs[4] was performed on wild-type and SALPKO cells. Cells were stained with anti-beta-giardin for analysis.

Figure 3.5: A biophysical flow assay reveals a defect in MR SFA KO cell attachment

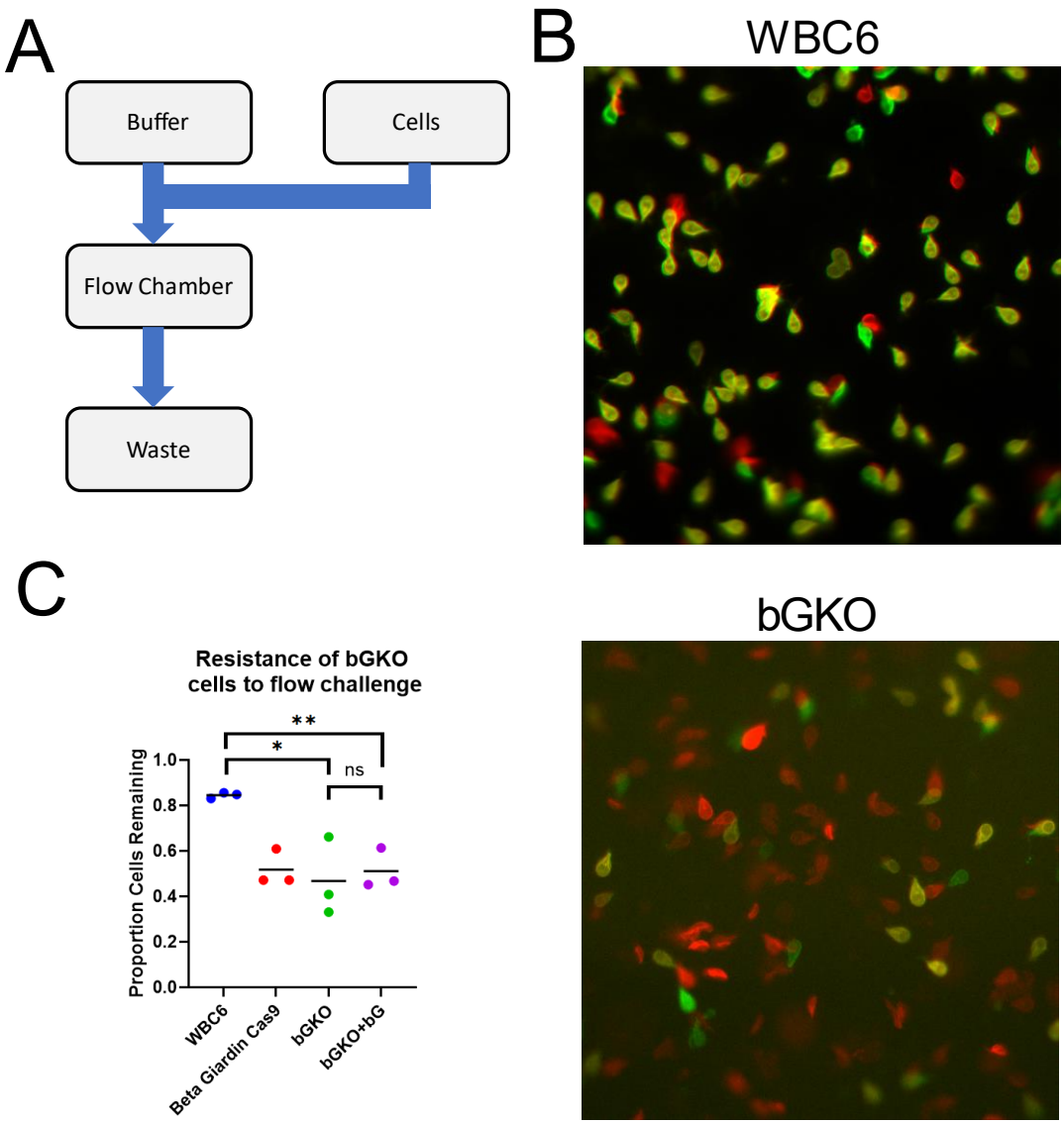

D

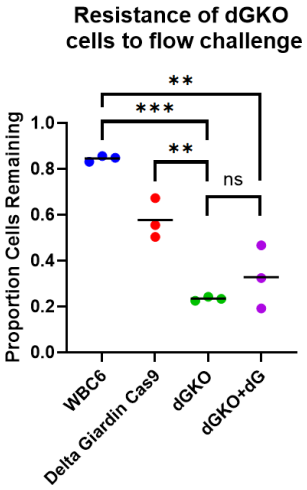

dGKO

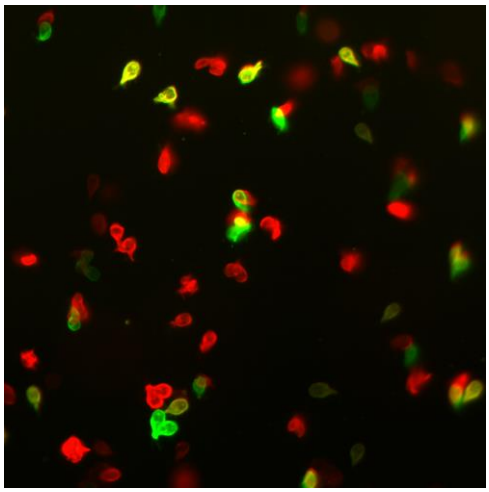

E

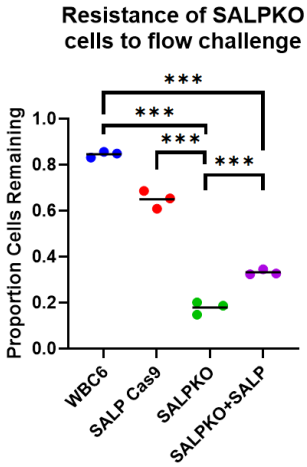

SALPKO

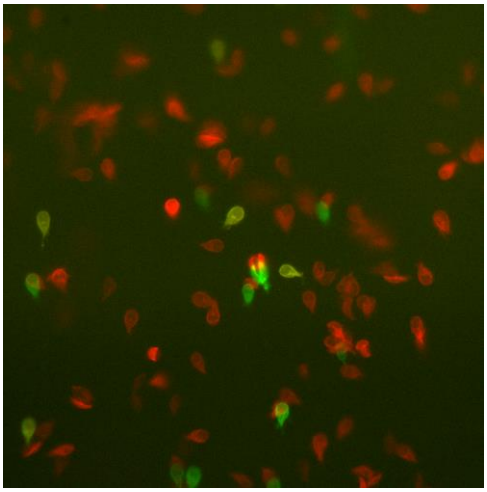

A biophysical flow assay was performed to gauge MR KO cells' ability to remain attached to a surface while experiencing shear flow force. A) Schematic of flow assay set up. *Giardia* cells are injected into a flow chamber allowed to attach for 5 minutes. The flow chamber is visualized on a wide-field microscope. Buffer is pumped into the flow chamber at a rate of 3 ml/minute for 20 seconds to gauge attachment ability, and cells and buffer are collected into a waste container. B) Visualization of attachment data for wild-type cells (WBC6). An image of cells stained with cellmask orange was aquired before flow challenge and false colored red. This image was

overlaid with an image taken immediately after flow challenge and false colored green. Yellow cells have remained in place before and after flow, red cells have been detached by flow, and green cells attached after flow was completed. C) Quantitation of wild-type (WBC6), a line expressing only a Cas9 construct targeting beta-giardin, bGKO, and bGKO+bG resistance to flow challenge. Only cells present before challenge were included in quantitation. Visualization of attachment data for bGKO in the manner described in (B). * represents p value <0.05, ** represents p value <0.01, and ns is not significant. D) Quantitation of wild-type (WBC6), a line expressing only a Cas9 construct targeting delta-giardin, dGKO, and dGKO+dG resistance to flow challenge. Only cells present before challenge were included in quantitation. Visualization of attachment data for dGKO in the manner described in (B). *** represents p value <0.001. E) Quantitation of wild-type (WBC6), a line expressing only a Cas9 construct targeting SALP1, SALPKO, and SALPKO+SALP resistance to flow challenge. Only cells present before challenge were included in quantitation. Visualization of attachment data for SALPKO in the manner described in (B).

Figure 3.6: The head domain is necessary for restoration of bGKO cells, but not for SALPKO cells

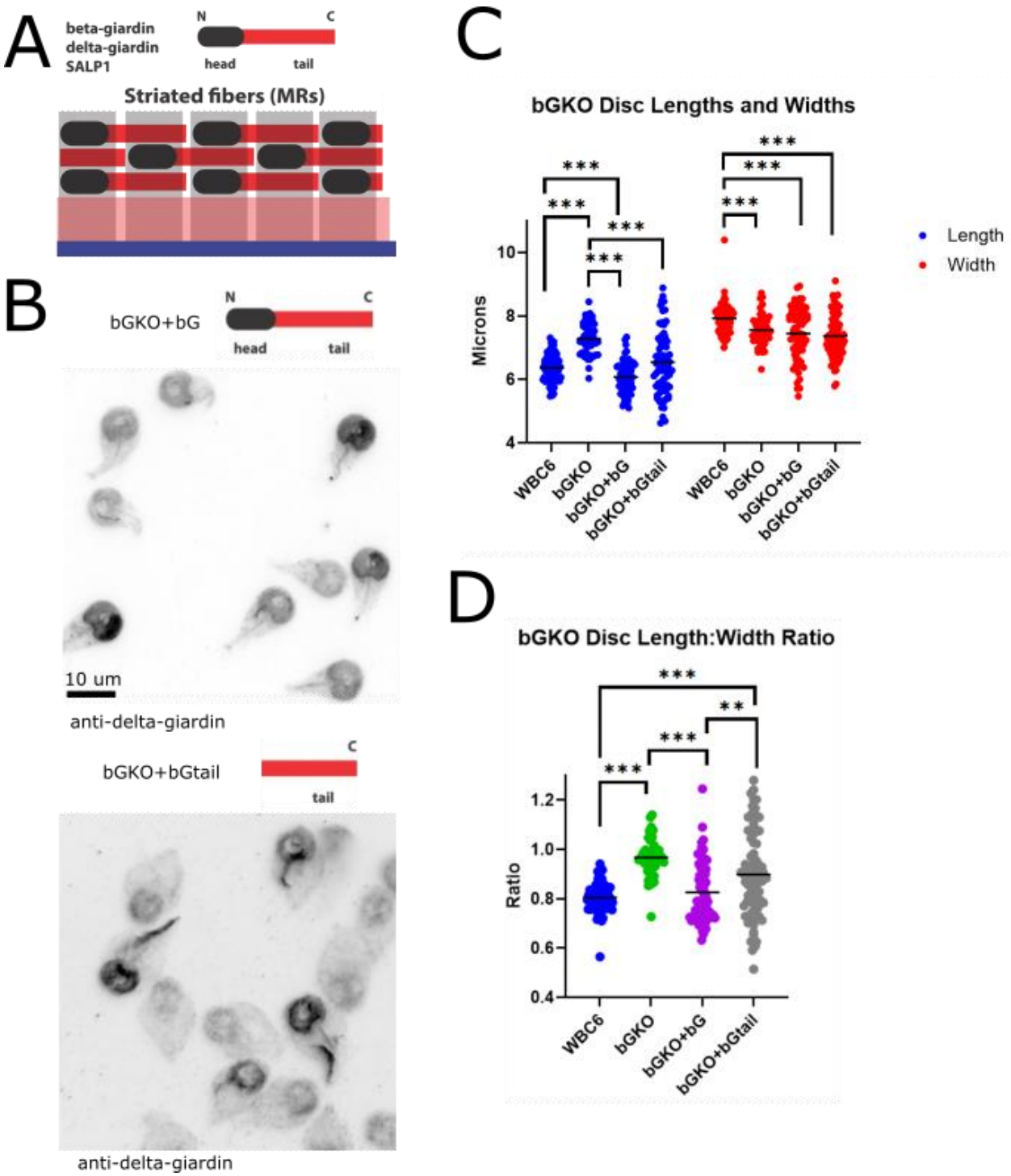

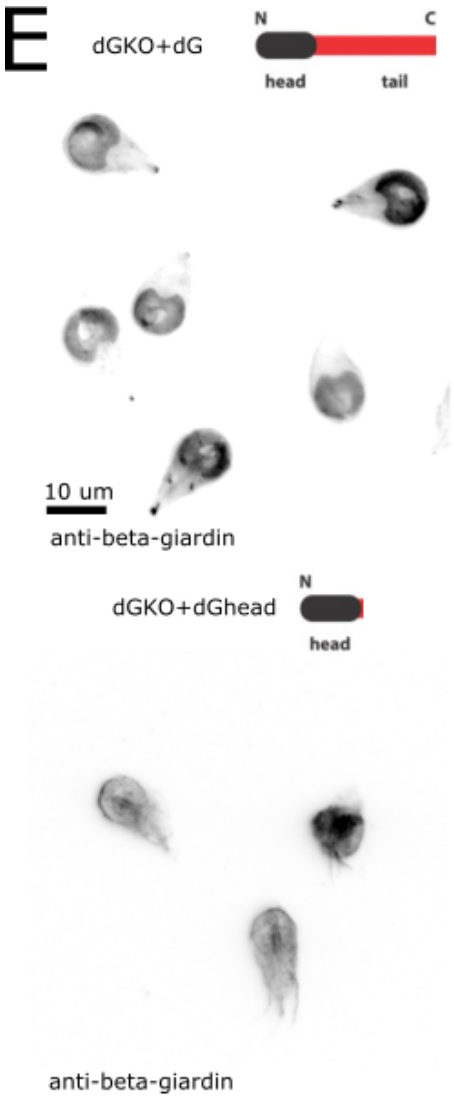
E
dGKO+dG
N
C
head
tail
10 um
anti-beta-giardin
dGKO+dGhead
N
head
anti-beta-giardin

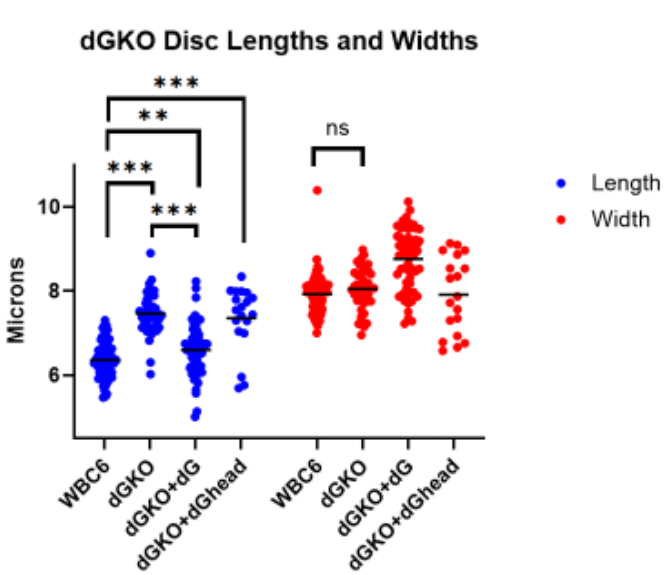
F
dGKO Disc Lengths and Widths
***
**
***
***
ns
Microns
10
8
6
WBC6
dGKO
dGKO+dG
dGKO+dGhead
WBC6
dGKO
dGKO+dG
dGKO+dGhead
Length
Width

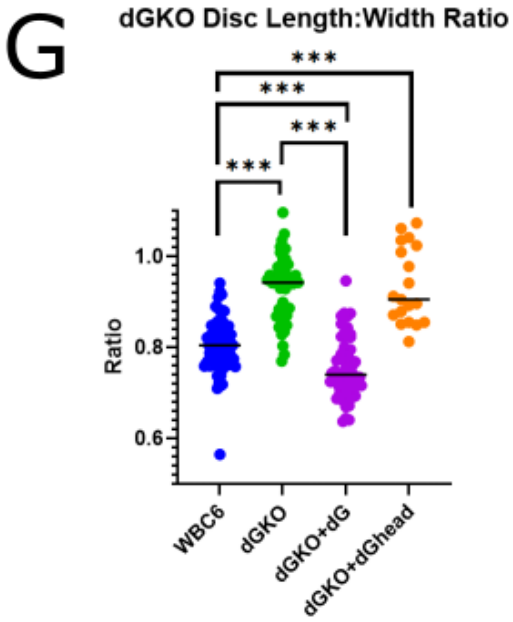
G
dGKO Disc Length:Width Ratio
***
***
***
***
Ratio
1.0
0.8
0.6
WBC6
dGKO
dGKO+dG
dGKO+dGhead

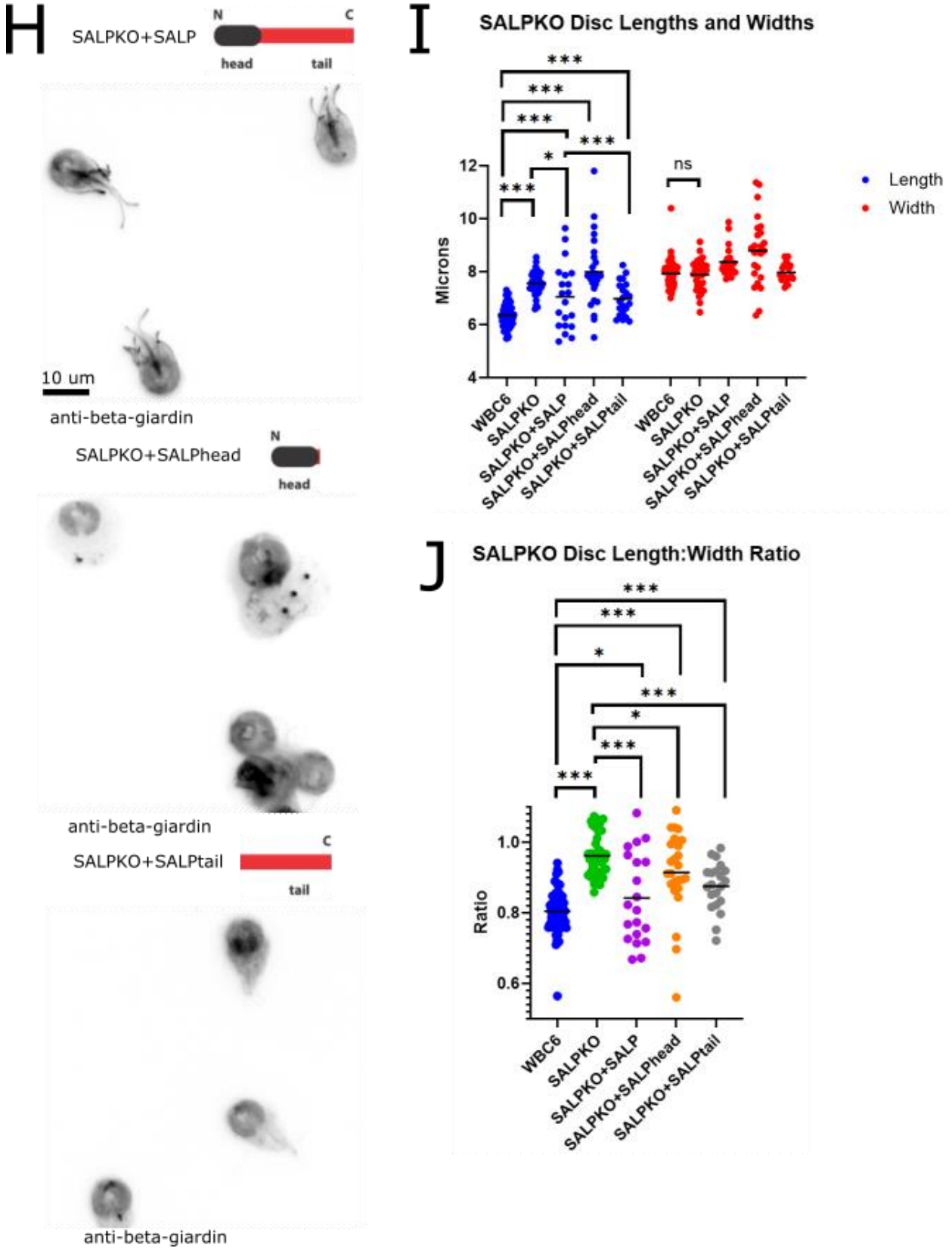
H
SALPKO+SALP
N
C
head
tail
10 um
anti-beta-giardin
SALPKO+SALPhead
N
head
anti-beta-giardin
SALPKO+SALPtail
C
tail
anti-beta-giardin
I
SALPKO Disc Lengths and Widths
Microns
Length
Width
ns
WBC6
SALPKO
SALPKO+SALP
SALPKO+SALPhead
SALPKO+SALPtail
J
SALPKO Disc Length:Width Ratio
Ratio
WBC6
SALPKO
SALPKO+SALP
SALPKO+SALPhead
SALPKO+SALPtail

To determine the role of the SFA head and tail domains with respect to *Giardia* MR proteins, a series of partial SFA protein expression lines were constructed. A) Schematic of the general SF-assemblin layout: unstructured N-terminal head domain, and a coiled coil tail domain. One hypothesis of SFA self-assembly is a head-tail interaction[22] to form fibers, which in *Giardia* would be the microribbons. B) Anti-delta-giardin staining of bGKO+bG and bGKO+bGtail. Delta-giardin properly localized to the ventral disc in the bGKO+bG line, and in some bGKO+bGtail cells. However, streaks of anti-delta-giardin signal were still visible in the cytoplasm of some bGKO+bGtail cells, and bGKO+bGtail ventral discs still had defects. C) Ventral disc length and width measurements in the wild-type (WBC6), bGKO, bGKO+bG, and bGKO+bGtail lines. Measurements were performed on cells stained with anti-alpha-tubulin. ** represents p value <0.01, and *** represents p value <0.001. D) Ventral disc length and width ratio in the wild-type (WBC6), bGKO, bGKO+bG, and bGKO+bGtail lines. Measurements were performed on cells stained with anti-alpha-tubulin. E) Anti-beta-giardin staining of dGKO+dG and dGKO+dGhead. dGKO+dGhead cells still had defects in their ventral discs. F) Ventral disc length and width measurements in the wild-type (WBC6), dGKO, dGKO+dG, and dGKO+dGhead lines. Measurements were performed on cells stained with anti-beta-giardin. ns represents not significant. G) Ventral disc length and width ratio in the wild-type (WBC6), dGKO, dGKO+dG, and dGKO+dGhead lines. Measurements were performed on cells stained with anti-beta-giardin. H) Anti-delta-giardin staining of SALPKO+SALP, SALPKO+SALPhead, and SALPKO+SALPtail. SALPKO+SALPhead cells still had defects in their ventral discs, but SALPKO+SALPtail cells were visually similar to SALPKO+SALP cells. I) Ventral disc length and width measurements in the wild-type (WBC6), SALPKO, SALPKO+SALP, SALPKO+SALPhead, and SALPKO+SALPtail lines. Measurements were performed on cells stained with anti-beta-giardin. * represents p value <0.05. J) Ventral disc length and width ratio in the wild-type (WBC6), SALPKO, SALPKO+SALP, SALPKO+SALPhead and SALPKO+SALPtail lines. Measurements were performed on cells stained with anti-beta-giardin.

Figure 3.7: Exogenously expressed partial SFA constructs were unable to restore resistance to flow

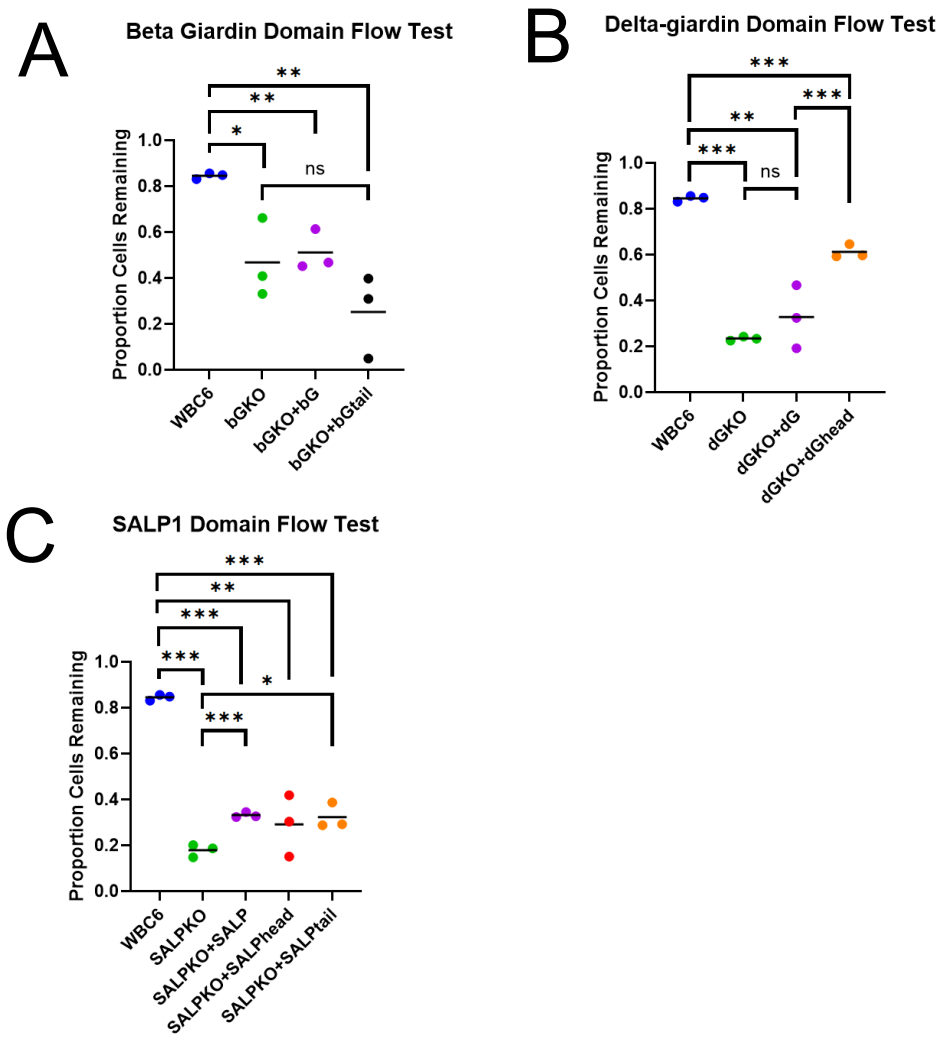

Shear flow challenge assay was performed against the exogenously expressed SFA domain analysis lines. A) bGKO, bGKO+bG, and bGKO+bGtail cells were compared to a wild-type (WBC6) control. B) dGKO, dGKO+dG, and dGKO+dGhead cells were compared to a wild-type (WBC6) control. C) SALPKO, SALPKO+SALP, SALPKO+SALPhead, and SALPKO+SALPtail cells were compared to a wild-type (WBC6) control.

Figure 3.8: MR SFAs may play different roles depending on sub-MR-CB localization

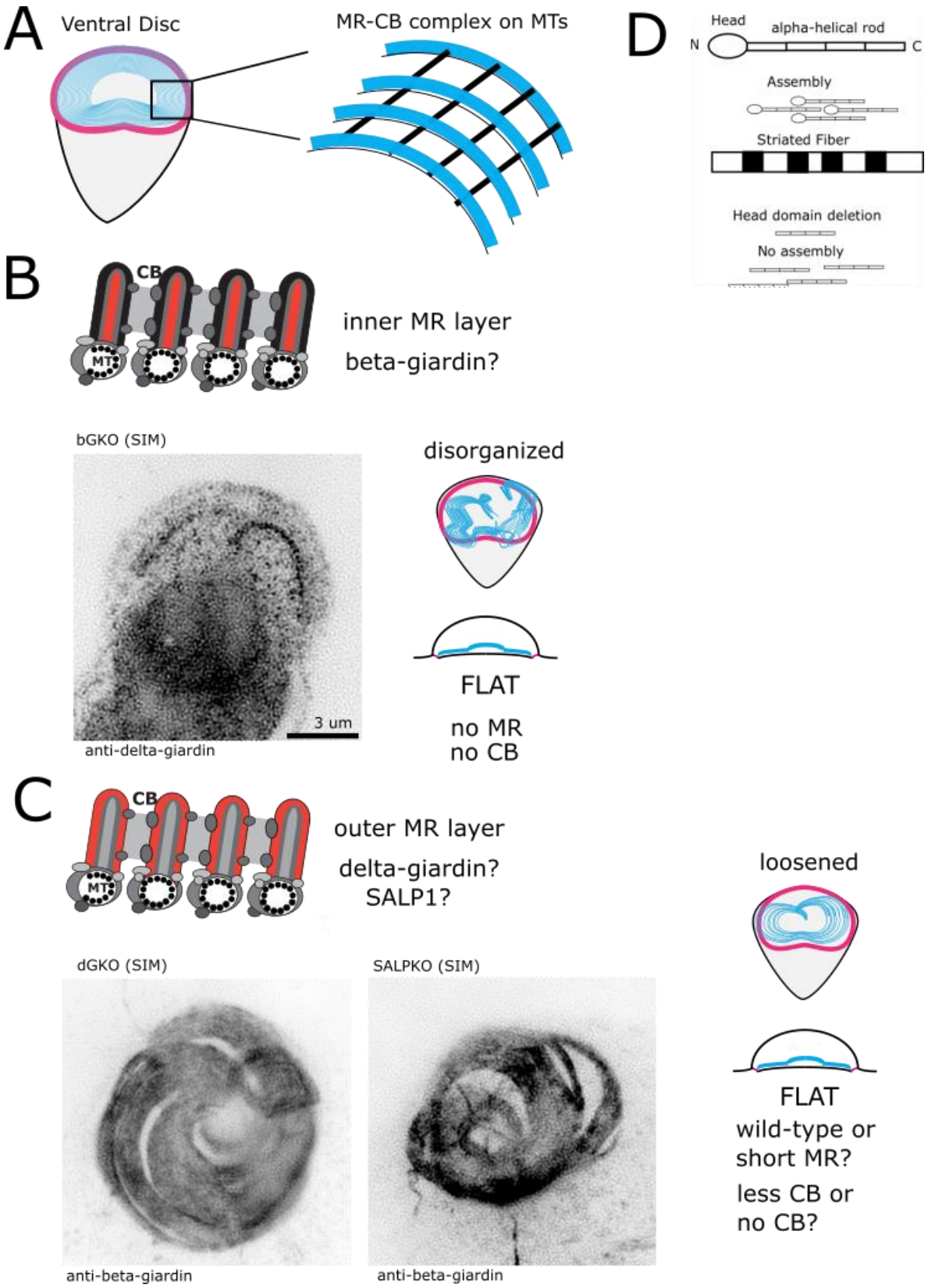

E

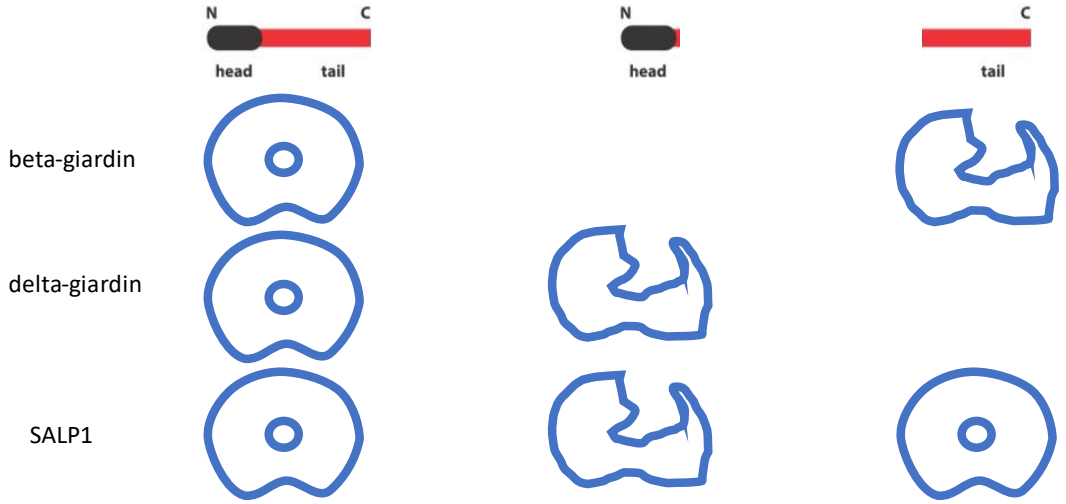

A) Schematic representation of the ventral disc and zoom in on the MR-CB complex. B) As discussed in the Introduction, microribbons are trilaminar and have an outer and inner layer. Knockout lines targeting core microribbon proteins and proteins involved with binding the MR-CB complex to the disc may highly disrupt MR-CB and disc formation. Beta-giardin could be a core MR protein; bGKO mislocalized delta-giardin, and this could be indicative of failure to form MRs. C) Outer MR proteins, and MR proteins that specialize in binding the crossbridges but play no role in the formation of the microribbons themselves may have less severe KO phenotypes. Delta-giardin and SALP1 could be outer MR proteins or bind CB proteins. Notably, we predict loss of disc three-dimensional dome shape in all hypothetical KOs, as connections between parallel MRs are severed or weakened. D) Diagram depicting SFA head and tail domain hypothesis of Striated Fiber formation. E) Summary of MR SFA domain analysis, showing restoration of wild-type disc appearance in bGKO+bG, dGKO+dG, SALPKO+SALP, and SALPKO+SALPtail lines. bGKO+bGtail, dGKO+dGhead, and SALPKO+SALPhead lines retained disrupted disc structure. bGKO+bGhead and dGKO+dGtail lines are a work in progress.

References

1. Einarsson, E., Ma'ayeh, S. & Svärd, S. G. An up-date on Giardia and giardiasis. *Curr. Opin. Microbiol.* **34**, 47–52 (2016).

2. Nosala, C., Hagen, K. D. & Dawson, S. C. 'Disc-o-Fever': Getting Down with Giardia's Groovy Microtubule Organelle. *Trends Cell Biol.* **28**, 99–112 (2018).

3. Holberton, D. V. Attachment of *Giardia* - A Hydrodynamic Model Based on Flagellar Activity. *J. Exp. Biol.* **60**, 207–221 (1974).

4. Nosala, C. *et al.* Disc-associated proteins (DAPs) mediate the unusual hyperstability of *Giardia* 's ventral disc. *J. Cell Sci.* jcs.227355 (2020) doi:10.1242/jcs.227355.

5. Dawson, S. C. *et al.* Kinesin-13 Regulates Flagellar, Interphase, and Mitotic Microtubule Dynamics in *Giardia intestinalis*. *Eukaryot. Cell* **6**, 2354–2364 (2007).

6. Holberton, D. V. & Ward, A. P. Isolation of the cytoskeleton from *Giardia* . tubulin and a low-molecular-weight protein associated with microribbon structures. *J. Cell Sci.* **47**, 139–166 (1981).

7. Holberton, D. V. Arrangement of subunits in microribbons from *Giardia*. *J. Cell Sci.* **47**, 167–185 (1981).

8. Schwartz, C. L., Heumann, J. M., Dawson, S. C. & Hoenger, A. A Detailed, Hierarchical Study of Giardia lamblia's Ventral Disc Reveals Novel Microtubule-Associated Protein Complexes. *PLoS ONE* **7**, e43783 (2012).

9. Brown, J. R., Schwartz, C. L., Heumann, J. M., Dawson, S. C. & Hoenger, A. A detailed look at the cytoskeletal architecture of the Giardia lamblia ventral disc. *J. Struct. Biol.* **194**, 38–48 (2016).

10. Feely, D., Holberton, D. V. & Erlandsen, S. The Biology of Giardia. In: Meyer EA, editor. *Giardiasis Amst. Elsevier* 11–50 (1990).

11. Hagen, K. D. *et al.* Novel Structural Components of the Ventral Disc and Lateral Crest in Giardia intestinalis. *PLoS Negl. Trop. Dis.* **5**, e1442 (2011).

12. Feely, D. E. & Erlandsen, S. L. Morphology of *Giardia agilis* : Observation by Scanning Electron Microscopy and Interference Reflexion Microscopy [1]. *J. Protozool.* **32**, 691–693 (1985).

13. Koudela, B. The ultrastructure of the intestinal microvillous border in the common vole (Microtus arvalis) naturally infected with Giardia microti. *Folia Parasitol. (Praha)* **41**, 241–245 (1994).

14. Narcisi, E. M., Paulin, J. J. & Fechheimer, M. Presence and localization of vinculin in Giardia. *J. Parasitol.* **80**, 468–473 (1994).

15. Chavez, B. & Martinez-Palomo, A. *Giardia lamblia:* Freeze-fracture Ultrastructure of the Ventral Disc Plasma Membrane. *J. Eukaryot. Microbiol.* **42**, 136–141 (1995).

16. Crossley, R. & Holberton, D. V. Characterization of proteins from the cytoskeleton of *Giardia lamblia*. *J. Cell Sci.* **59**, 81–103 (1983).

17. Holberton, D. V. Fine structure of the ventral disk apparatus and the mechanism of attachment in the flagellate *Giardia muris*. *J. Cell Sci.* **13**, 11–41 (1973).

18. Weber, K. *et al.* SF-assemblin, the structural protein of the 2-nm filaments from striated microtubule associated fibers of algal flagellar roots, forms a segmented coiled coil. *J. Cell Biol.* **121**, 837–845 (1993).

19. Palm, D. *et al.* Developmental changes in the adhesive disk during Giardia differentiation. *Mol. Biochem. Parasitol.* **141**, 199–207 (2005).

20. McInally, S. G. *et al.* Robust and stable transcriptional repression in *Giardia* using CRISPRi. *Mol. Biol. Cell* **30**, 119–130 (2019).

21. Hagen, K. *et al.* The domed architecture of *Giardia* 's ventral disc is necessary for attachment and host pathogenesis. Preprint at https://doi.org/10.1101/2023.07.02.547441 (2023).

22. Lechtreck, K.-F. Analysis of striated fiber formation by recombinant SF-assemblin in Vitro. *J. Mol. Biol.* **279**, 423–438 (1998).

23. Holberton, D., Baker, D. A. & Marshall, J. Segmented α-helical coiled-coil structure of the protein giardin from the Giardia cytoskeleton. *J. Mol. Biol.* **204**, 789–795 (1988).

24. Lechtreck, K. F. & Silflow, C. D. SF-assemblin in Chlamydomonas: sequence conservation and localization during the cell cycle. *Cell Motil. Cytoskeleton* **36**, 190–201 (1997).

25. Cheissin, E. M. ULTRASTRUCTURE OF LAMBLIA DUODENALIS. I. BODY SURFACE, SUCKING DISC AND MEDIAN BODIES. *J. Protozool.* **11**, 91–98 (1964).

26. Nosala, C. *et al.* Dynamic ventral disc contraction is necessary for *Giardia* attachment and host pathology. Preprint at https://doi.org/10.1101/2023.07.04.547600 (2023).

27. Dutcher, S. K. Elucidation of Basal Body and Centriole Functions in *Chlamydomonas reinhardtii*. *Traffic* **4**, 443–451 (2003).

28. Galati, D. F. *et al.* DisAp-dependent striated fiber elongation is required to organize ciliary arrays. *J. Cell Biol.* **207**, 705–715 (2014).

29. Soh, A. W. J. *et al.* Ciliary force-responsive striated fibers promote basal body connections and cortical interactions. *J. Cell Biol.* **219**, e201904091 (2020).

30. Kim, J. & Park, S.-J. Role of gamma-giardin in ventral disc formation of Giardia lamblia. *Parasit. Vectors* **12**, 227 (2019).

31. House, S. A., Richter, D. J., Pham, J. K. & Dawson, S. C. Giardia Flagellar Motility Is Not Directly Required to Maintain Attachment to Surfaces. *PLoS Pathog.* **7**, e1002167 (2011).

Chapter 4

A co-immunoprecipitation screen on microribbon proteins highlights new MR-CB candidate proteins

Nicholas Hilton and Scott C. Dawson

Abstract

Giardia lamblia is a protist parasite that colonizes the small intestine and causes significant diarrheal disease worldwide. Trophozoites attach to intestinal villi with the ventral disc, a dome-shaped microtubule (MT) organelle that allows the parasite to attach to the lining of the host small intestine. Currently, the “hydrodynamic model” of attachment suggests that the disc creates a seal on the host cell surface. The ventral disc is comprised of a spiral MT array, where parallel MTs turn clockwise to form the dome shape. The microribbon-crossbridge (MR-CB) complex is a novel protein structure bound to the disc MT at regular intervals, and covers, almost completely covers all disc MTs. Additionally, crossbridges are thought to be flexible and mediate the process of disc-based attachment. Not only is the ventral disc an essential feature of *Giardia* infection, understanding the evolution and structure of unique MT organelles can shed light on how morphological diversity evolved in eukaryotes. We currently know of over 90 disc-associated proteins (DAPs), yet the vast majority of these protein’s function in disc maintenance or attachment has not been characterized. While work on the MR-CB complex has begun to reveal its role in stabilizing the domed disc conformation, functional studies have been hampered by the small number of known MR-CB proteins. Four proteins, beta-giardin, delta-giardin, SALP1, and gamma-giardin are currently known to be part of the microribbons, but no crossbridge proteins have been identified. In this study, we conducted a co-immunoprecipitation assay on known microribbon proteins to identify a set of novel MR-CB candidate proteins. We localized these candidates using fluorescent tags, as well as targeted them with sTable 4.CRISPRi knockdowns and CRISPR knockouts. Mutant disc structure and function was assessed with light microscopy and a biophysical flow assay. In particular, a protein called GL50803_15376 shows promise, and has potential to be the first confirmed components of the crossbridges. We show that GL50803_15376 is essential for proper formation and maintenance of the disc spiral. Identifying new MR-CB proteins will help us understand the disc as a whole

and could provide key insights into the mechanisms of disc attachment. Generally, work on the ventral disc can also inform how cells build and maintain complex MT organelles. Lastly, identifying DAPs essential to the MR-CB complex would provide numerous new targets for drug treatment of Giardia.

Introduction

Giardia lamblia is an intestinal protozoan parasite that causes the diarrheal disease giardiasis[1]. *Giardia* colonizes the small intestine and can infect humans and animals worldwide[1] by the consumption of cysts contaminating the food or water supply. Giardiasis can cause malnutrition or delayed development in children, and is a particular problem in regions of the world where water sanitation is less developed[1]. *Giardia* remains in cyst form until passing through the host stomach and into the duodenum of the small intestine, where they excyst into a trophozoite form[1]. *Giardia* trophozoites are motile and possess a unique morphology. They are teardrop shaped, have four pairs of flagella, and a ventral disc, a cup-shaped microtubule organelle that permits the parasite to adhere to host intestinal epithelial cells[2]. Successful attachment is considered necessary for the normal process of infection, and resistance to host peristaltic flow[1]. Currently, it is thought that the force that drives attachment is generated by the movement of the ventral disc and disc substructural elements in concert with hydrodynamic flow generated by beating of the flagella[3]. Additionally, we are able to observe attachment on glass coverslips and culture tubes, which suggests ligand interactions are unnecessary for attachment. The exact cellular and biophysical mechanisms that enable *Giardia* trophozoites to attach remain to be discovered, yet work presented in my dissertation (see Chapters 2-3) implicate a role for disc-associated proteins (DAPs) and complexes in the disc structure, hyperstability, and function in attachment.

To better understand structural bases of *Giardia* attachment, I have focused on the understanding specific DAPs which are essential for building the molecular architecture of ventral disc. The disc is comprised of a highly organized spiral microtubule array with protein subcomplexes emerging dorsally from the microtubule spiral[2]. The spiral itself consists of roughly 100 parallel, equally distributed microtubules, twisting clockwise to form a dome[2]. A region where the upper and lower parts of the spiral cross is called the overlap zone[2]. The disc is highly sTable 4.in interphase, and treatment of *Giardia* cells with a high salt lysis buffer leaves intact discs behind[4] (see Chapter 2). The ventral disc is also not sensitive to drugs that alter microtubule dynamics[5]. Thus, we term the disc “hyperstable”. Beyond the microtubule spiral, the disc is decorated with the microribbon-crossbridge (MR-CB) complex[6,7], and repeating sidearm and paddle complexes, which nearly completely coat the disc microtubules[8]. The presence of such prominent structures has been proposed to mediate disc hyperstability[8,9].

Several decades after the disc was first defined, microtubule-associated proteins, called ‘giardins’ were isolated via a biochemical fractionation of the disc[10]. More recently, we have identified over 90 disc-associated proteins (DAPs) by proteomic analysis of isolated discs and used GFP tagging to localize DAPs to specific regions of the ventral disc[4,11]. However, while electron tomography has revealed many complex substructures of the disc[9], we still lack knowledge of the mechanisms which underlie disc hyperstability or generation of attachment force.

Furthermore, the function and structural contributions of the MR-CB complex remain a mystery. Microribbons are trilaminar, extending 400 nm into the cytoplasm, and trace the length of the microtubule spiral[7,12]. Parallel microribbons are linked by crossbridges, which repeat every 16 nm down the length of the microribbons[9,12]. The MR-CB complex as a whole can be divided into five parts: the outer and inner regions of the microribbons, MR-microtubule border, MR-CB connection, and the crossbridges themselves. A possible role for the MR-CB complex

might be to maintain the disc's three dimensional dome shape, and thus maintain attachment. Prior work has suggested that crossbridges could be flexible, and provide a mechanism for disc movement during the process of attachment[2]. Additionally, recent observation has shined light on the ventral disc's ability to contract, and theorized that the crossbridges could play a central role in disc contraction[13]. While there are over currently known 90 DAPs[11], there are only four known microribbon proteins: beta-giardin, delta-giardin, SALP1, and gamma-giardin[10,14,15]. There are no confirmed crossbridge proteins. We anticipate that not only the crossbridge proteins but additional DAPs associated with the MR-CB complex are yet to be discovered, as well as DAPs associated with the disc as a whole.

Genetic and functional assays of the ventral disc and disc proteins are essential to understanding and uncovering its functions and mechanisms during attachment. We have recently adapted dCas9/CRISPRi and Cas9/CRISPR technology for use in *Giardia* to generate knockdown and knockout cell lines[16,17]. To expand our list of potential MR-CB complex proteins, and identify DAPs interacting with the microribbons (including crossbridge proteins) I conducted a co-immunoprecipitation screen targeting two of the known MR proteins: beta-giardin and delta-giardin. Among the *Giardia* proteins highlighted by this screen is GL50803_15376, a novel protein. Both 15376 knockdowns and knockouts have severely disrupted disc morphology, suggesting an this is an additional MR-CB complex component essential for disc architecture.

Results

Co-immunoprecipitation of beta- and delta-giardin reveals novel components of the microribbon-crossbridge complex

Beta-giardin and delta-giardin are two of the four known MR proteins; thus, I reasoned that interacting proteins identified in a co-immunoprecipitation (co-IP) screen could also be part of

the MR-CB complex. Prior to immunoprecipitations, *Giardia* wild-type strain WBC6 trophozoites were grown and harvested according to the Methods (Figure 4.1A). Cell membranes were first permeabilized using a detergent extraction, and cytoskeletal structures (e.g, disc and flagella) were further disrupted with sonication (see Methods). Cytoskeletal lysates were then incubated with one of three options: 1) magnetic beads conjugated to anti-beta-giardin antibody (gift of Mark Jenkins, USDA) 2) beads conjugated to anti-delta-giardin antibody (gift of Mark Jenkins, USDA), or 3) unconjugated beads. After incubation, beads were washed three times and resuspended in a minimal volume of wash buffer (~50 µl, see Methods). All remaining material was sent to the UC Davis Proteomics Core where proteins were digested off the beads and analyzed via mass spectroscopy. Each immunoprecipitation condition (beta-giardin antibody, delta-giardin antibody, unconjugated) was performed on independently grown cultures and analyzed three times, for a total of nine co-IP runs.

Fractions were taken throughout the co-IP process for silver stain visualization of protein content (Figure 4.1B). The silver stain highlights the high amount of protein content in the whole cell digest (Wc), lysate supernatant (Ls), and wash 1 (W1) fractions (Figure 4.1B). In contrast, the final elution (Fe) fraction contains fewer and fainter bands under the anti-beta-giardin (b-giardin) and anti-delta-giardin (d-giardin) bead conditions, and no visible bands in the unbound bead (null bead) condition (Figure 4.1B).

Known microribbon DAPs and novel proteins were the most abundant interacting proteins by co-IP

Each protein identified in the mass spectroscopy analysis was assigned an intensity value for each of the bead condition repeats (Table 4.1). Intensity values corresponded to the number of peptides detected for a particular protein, as well as the peptide size. Intensity values across repeats of the same condition were averaged, and the null intensity values were subtracted from the beta- and delta-giardin values. Peptide hits were then sorted by both the average beta-

giardin intensity difference, and the delta-giardin intensity difference (Figure 4.2A). Proteins with an average intensity score of at least 1% of the top hit were considered for further analysis. Additionally, proteins with known ribosomal, nuclear, or other non-disc localization were removed from further analysis. At this stage, a total of 15 proteins were identified as top hits from either co-IP, three of which were found in the beta-giardin bead condition, three of which were in the delta-giardin bead condition, and nine were found in both conditions (Figure 4.2B). Overlapping hits included all four currently known microribbon proteins, and beta-giardin hits included the known disc edge localizing DAP, DAP12139[11]. The remaining hits were actin, and nine novel proteins which could be potential MR-CB DAPs.

Nine novel proteins highlighted in the co-IP screen are sublocalized to various parts of the Giardia cell

To determine whether any of the nine novel co-IP hits are components of the MR-CB complex, each were C-terminally tagged with mNeon-Green using episomal plasmids (see Methods) and electroporated into wild-type *Giardia* trophozoites (Figure 4.3). GL50803_16844 localized to the ventral disc. Two novel proteins, GL50803_15376 (15376) and GL50803_16443 were unable to be cloned and currently remain unlocalized. The remainder are not specific to the pull-down as they localize to other cellular regions. GL50803_5859 and GL50803_21628 both localized to the nuclei, GL50803_7233 localized to basal bodies of the caudal flagella, GL50803_31743 localized to the plasma membrane, and GL50803_92132 and GL50803_103205 localized to the cytoplasm (Figure 4.3).

Knockdowns and knockout of GL50803_15376 disrupts ventral disc structure

In parallel to protein-tagging, the nine novel protein hits were also targeted by specific CRISPRi knockdown constructs expressed in an mNeon-Green beta-tubulin cell line (mNG-bTubulin) and knockdown mutants were screened for ventral disc phenotypes. Of the nine KD lines, only the

15376 CRISPRi KD line, 15376KD, showed aberrant discs from the mNG-bTubulin line. A CRISPR knockout line for 15376 was also created, 15376KO, to achieve a more complete suppression of 15376 expression.

Generation of dCas9 CRISPRi knockdown lines followed a protocol described by McInally[16] (see Methods). We selected 20 nt gRNA sequences with a PAM site 47 bp from gene start, and prepped CRISPRi plasmids were electroporated into the mNG-bTubulin line. Creation of the 15376KO line followed the procedure described by Hagen[17] (see Methods). We selected a 20 nt gRNA sequence with a PAM site 46 bp from gene start. For a complete KO, we electroporated wild-type *Giardia* cells sequentially with the Cas9 plasmid, and two homologous repair templates, using three selection markers in the process (Puromycin, Blasticidin, Hygromycin, see Methods). Following that, we cloned out our partial KO line and screened for complete KOs via PCR on genomic DNA.

15376KO genomic DNA was also sent for nanopore sequencing (Figure 4.4) to confirm quadruple KO. When compared with the 15376 wild-type gene, we observed sequence coverage up to, and beyond, but not through the KO cassette insertion site (Figure 4.4A). We observed sequence coverage across the entirety of our two KO cassettes (Figure 4.4A, 4B, see Methods).

To observe the disc MT spiral in the 15376KO line, mutant and wild type discs were extracted[4] (see Chapter 2), and 15376KO discs were immunostained with an anti-alpha-tubulin antibody (Figure 4.5A, 5B). Discs were also immunostained with an anti-beta-giardin antibody to examine the microribbons (Figure 4.5C). Microribbon and disc tubulin spiral appearance were consistent within cell lines.

Several categories of of disrupted disc phenotypes were observed in the 15376KD and 15376KO lines and phenotypes and quantitated based on tubulin spiral appearance (Figure

4.5D). Discs were assigned to one of four categories: 1) no defects observed, indistinguishable from wild-type (Full Disc), 2) arms of the tubulin spiral have come undone, overlap zone is gone (Unhinged), 3) bare area increased in size, loss of disc material from the disc interior (Enlarged BA), and 4) loss of disc material from the exterior, or from both an enlarged bare area and from the disc periphery (Small Disc). 15376KO discs had a Full Disc phenotype 30% of the time, compared to 76% in 15376KD, and 77% in mNG-bTubulin (Figure 4.5D). 15376KO discs were primarily Unhinged, with 58% falling into this category, compared to 15% in 15376KD, and 12% in mNG-bTubulin. 15376KD discs were primarily Full Discs, that and other phenotype percentages were similar to mNG-bTubulin. Enlarged BA and Small Disc phenotypes remained within single digit percentages for all cell lines (Figure 4.5D).

15376KD and 15376KO discs are smaller but have varied disc interior (bare area) dimensions

Overall disc area, not including the bare area, was quantitated in the 15376KD, 15376KO, and mNG-bTubulin lines (Figure 4.5E) using the thresholding function in FIJI (ImageJ). Disc area was significantly reduced in both the 15376KD and 15376KO lines compared to the mNG-bTubulin (WT) control line. Disc areas were reduced by 8.5% in the 15376KD line, and 4% in the 15376KO line. Similarly, the bare area region was quantitated for 15376KD, 15376KO, and mNG-bTubulin (Figure 4.5F). 15376KD cells possess an enlarged bare area, while 15376KO cells have a reduced bare area. 15376KD bare areas were 39% larger, and 15376KO bare areas were 35% smaller than mNG-bTubulin bare areas.

15376KO cells do not have an attachment defect when compared to mNG-bTubulin

To quantify the effects of the 15376KO disc phenotypes and altered disc dimensions on attachment, a shear force flow assay was performed (Figure 4.6). The 15376KO cell line trends poorer in attachment than the mNG-bTubulin negative control, but not to a statistically significant

extent. The 15376KO line was highly variable, with some experimental repetitions remaining attached at a close to negative control rate, and other repetitions much worse at attachment.

Discussion

The search for new MR-CB complex components

Understanding the mechanisms behind ventral disc stability and the role disc dome shape plays in attachment remains a work in progress. To answer questions about ventral disc form and function, genetic manipulation of disc proteins is a critical tool in the process of discovery. The ventral disc itself is comprised of a microtubule spiral, with the prominent MR-CB complex on top[2]. While prior work has identified over 90 disc associated proteins[11], there are only four known proteins specifically localized to the microribbons: beta-giardin, delta-giardin, SALP1 and gamma-giardin[10,14,15]. Furthermore, there are currently no identified crossbridge proteins, complicating our efforts to understand the MR-CB complex. We set out to identify and characterize new MR-CB proteins, which will hopefully lead to further discoveries about this unique cytoskeletal feature.

GL50803_15376 is a novel protein and a potential novel component of the MR-CB complex

15376 (accession number GL50803_0015376) is a novel protein that emerged as a strong hit in our delta-giardin co-IP assay (Figure 4.2B). The 15376 protein is 323 kDa in size, and lacks homology to any known protein in GenBank. Due to its length (8.7 Kb) the cloning of GL50803_15376 into a fluorescent tagging expression vector has proven a challenge and has not been completed as of yet. Yet, both knockdown and knockout strains show a clear disc structural phenotype. 15376KO cells have a destabilized ventral disc (Figure 4.5A – 5D) and both 15376KO and 15376KD cells have a smaller disc (Figure 4.5E). These disc-associated

phenotypes support that 15376 plays a role in maintaining disc morphology and is a bonafide component of the disc.

Microribbons are trilaminar, with an inner layer, and two external layers on either side[8]. Additionally, the ventral end of the MRs interacts with disc MTs, and crossbridges interface with the MR periphery[8]. It is possible that various sub-microribbon regions have different roles, in particular, that the core MR layer is necessary for the formation of the rest of this structure, as discussed in Chapter 3. On the other hand, peripheral MR proteins may be necessary for proper MR-CB connection, but not for the formation of MRs themselves. I discussed the possibility of delta-giardin localizing to the outer MR layers in Chapter 3, based on its knockout phenotype. Because 15376 was only highlighted in our delta-giardin co-IP assay, and was not a high-ranking hit in our beta-giardin co-IP, I suggest that 15376 has a more peripheral MR localization. This notion is supported by the observation that the 15376KO disc phenotype (Figure 4.5A, 5B) closely resembles the delta-giardin KO phenotype (see Chapter 3), and microribbon proteins in the 15376KO line are able to localize to the disc (Figure 4.5C).

Crossbridges may be key to understanding Giardia disc attachment

Recent work has described disc contraction[13], a process that could be mediated by the purported contractile abilities of crossbridges, either acting independently or working in concert with microribbons. The mechanism of disc contraction, including whether microtubule spacing of the disc spiral is contracted, or whether the overlap zone within the disc slides. Earlier work has described striated fibers (composed of SF-assemblins), in *Chlamydomonas*, as noncontractile and rigid[18]. If the microribbons exist as a bracing pillar, holding the current disc conformation in place, then the crossbridges would have to contract or otherwise be motile to provide any change in disc shape. Identifying and confirming crossbridge proteins, of which 15376 may be associated, would aid in understanding mechanisms behind disc-driven attachment. The 15376 protein could be a good target for an additional co-IP screen to identify crossbridge proteins,

and more work defining the roles of this disc protein is disc architecture, hyperstability, or attachment is needed.

Materials and Methods

Giardia culture and electroporation

Giardia lamblia trophozoites (strain WBC6, ATCC 50803) were cultured as previously described[17]. Briefly, cells were kept at 37°C, and grown in 16 ml culture tubes (BD Falcon), without shaking. Media used for maintaining cultures was a modified TYI-S-33, with the addition of bovine bile, 5% adult and 5% fetal bovine serum. A 12 ml culture volume was maintained. When trophozoites reached either complete confluence, or after 48 hours of growth, culture tubes were iced for 15 minutes and 1 ml of unattached cells were transferred to fresh medium.

The electroporation of plasmids and linear homology-directed repair (HDR) templates into *Giardia* was completed as described by Nosala[4]. We began with 1 x 10^7 total cells and 40 µg of DNA for each individual electroporation. Cells were shocked, added to 12 ml fresh culture medium, and incubated at 37°C. Media was decanted and exchanged with fresh media every 48 hours. Antibiotic selection occurred in two stages, with a lower initial concentration, followed by a higher final concentration once cells reached 50% confluence or greater. Selection antibiotics and their concentrations were: puromycin (12.5 µg/ml initial, 50 µg/ml final), blasticidin (75 µg/ml initial, 150 µg/ml final), hygromycin B gold (600 µg/ml initial, 1200 µg/ml final), and G418 (150 µg/ml initial, 600 µg/ml final).

Conjugation of magnetic beads to antibodies

In order to selectively enrich for proteins associated with the microribbon-crossbridge complex, we conjugated anti-beta-giardin antibody and anti-delta-giardin antibody (both antibodies are

gifts of Mark Jenkins, USDA) to magnetic beads (Dynabeads Antibody Coupling Kit, Life Technologies). As a negative control, we also performed the conjugation protocol without the addition of any antibody (null bead condition). We followed the instruction manual provided by Life Technologies, summarized briefly here. 5 mg of beads per conjugation were washed with 1 ml of C1, adhered to a magnet for 1 minute, and wash aspirated via pipette. For beads with antibody, 240 µl of C1 and 10 µl of antibody were added and mixed. Beads without antibody received 250 µl of C1. Following mixing, 250 µl of C2 was added. Tubes with beads were sealed with parafilm and incubated at 37°C overnight with inversion. Beads were adhered to a magnet for 1 minute and liquid was aspirated out. Beads were then quickly washed with the following: 800 µl of HB, 800 µl LB, and 2x 800 µl SB. A third 800 µl SB was incubated on the beads for 15 minutes at room temperature with inversion. The final wash was aspirated and beads were resuspended in 500 µl SB and stored for up to 3 weeks at 4°C.

Co-immunoprecipitation in Giardia using antibody-conjugated magnetic beads

For each bead type, three rounds of co-immunoprecipitation were performed. $1x10^9$ WBC6 strain *Giardia* trophozoites were cultured as described above. Cultures were grown across a total of 50 culture tubes, each reaching $2x10^7$ cells when fully confluent. To harvest, tubes were iced for 15 minutes, followed by a 5 minute centrifugation at 900 x g and 4°C. The supernatant was decanted, and cells were resuspended in 1 ml HBS (137 mM NaCl, 21 mM HEPES, 5.6 mM glucose, 5.0 mM KCl, 0.76 mM Na_2HPO_4, pH 7.0). Cells from 10 tubes were combined into a single tube and washed with 5 ml of HBS. After washing, pellets were resuspended in 1 ml HBS and transferred from the culture tube to a 1.5 ml tube, centrifuged again, and supernatant aspirated with a pipette. Pellets were immediately snap-frozen in liquid nitrogen and stored at -80°C.

All steps of the following protocol were performed on ice. Cell pellets were thawed and resuspended in 100 µl of lysis buffer (80 mM K-PIPES, 1 mM $MgCl_2$, 1 mM EGTA, 10%

Glycerol, 0.2% Triton X-100, 5 µg/ml DNAse I, 1 mM DTT, 0.1 mM ATP, 1 mM GTP, 0.2 mM PMSF, 5 µg/ml Leupeptin, 1 µg/ml Pepstatin A, 1 µg/ml Aprotinin). Pellets from five separate tubes were combined into one fresh 1.5 ml tube. Cells were lysed on ice for 30 minutes; every 10 minutes lysate was mixed by pipetting up and down. Lysates were then further broken up by sonication (Heat Systems W-375, duty cycle 50%, output control 2, ten pulses). A 50 µl sample was saved at -20°C and labeled “whole cell” (Wc). Lysates were then clarified by a 10 minute centrifugation at 17000 x g and 4°C. To prepare the conjugated magnetic beads, 25 µl of beads were washed with 500 µl wash buffer (10 mM Tris/Cl pH 7.5, 150 mM NaCl, 0.5 mM EDTA, 0.05% NP-40) and mixed by inversion. Cell lysate supernatant was transferred to a fresh tube, 500 µl ice cold dilution buffer (10 mM Tris/Cl pH 7.5, 150 mM NaCl, 0.5 mM EDTA) was added, and a 50 µl sample was saved as “lysate supernatant” (Ls). The beads were placed alongside a magnet for 1 minute, and the liquid aspirated. The lysate supernatant was then transferred into the bead tube. Tubes were sealed with parafilm and incubated for 1 hour at room temperature, with inversion.

After incubation, the beads were put alongside a magnet for 1 minute, and the supernatant was removed and saved as “wash 1” (W1). Beads were washed twice with 500 µl wash buffer before being transferred into a fresh 1.5 ml tube during the second wash. 450 µl of the second wash was removed; the beads were then resuspended in the remaining buffer by gently flicking the tube. Beads were either kept on ice and immediately taken to the proteomics core at the University of California, Davis for mass spectroscopy analysis, or run on a protein gel for silver staining.

Protein gel and silver stain of samples from co-immunoprecipitation

Samples from the above protocol were diluted 1:20 in 1x Laemmli Sample Buffer (Bio-Rad) with 5% beta-mercaptoethanol. The diluted samples were then boiled for 5 minutes and 10 µl was

loaded onto a Mini-PROTEAN TGX Gel (4-10%, 15 well, Bio-Rad). Gels were run at 200 V until sample front reached the bottom, then extracted and put into a tray for silver staining.

To perform a silver stain, we used a Pierce Silver Stain Kit (ThermoScientific) and followed the associated protocol. For all incubation steps, gels were placed on an orbiting mixer. Briefly, gels were washed twice for 5 minutes in water, then fixed for 30 minutes in a 30% ethanol:10% acetic acid solution, with fixation solution exchanged once after 15 minutes. Gels were washed twice for 5 minutes with 10% ethanol, followed by two 5 minute washes with water. Gels were sensitized for 1 minute with a Sensitizer Working Solution (50 µl Sensitizer, 25 ml water), then washed twice for 1 minute with water. Gels were then stained for 30 minutes with a Stain Working Solution (0.5 ml Enhancer, 25 ml Stain). Gels were washed twice for 20 seconds in water, then developed for 2 minutes, using a Developer Working Solution (0.5 ml Enhancer, 25 ml Developer). Finally, development was stopped with 5% acetic acid for 10 minutes. Gels were imaged immediately following the completion of the stop incubation.

Mass spectroscopy analysis and proteomic data analysis

Samples were analyzed at the UC Davis Proteomics Core using a Bruker timsTOF system, which gave a list of protein hits for each of the bead conditions. Proteins were automatically assigned an intensity value based primarily on peptide abundance.

Intensity values of protein hits were used to highlight and prioritize further investigation of possible beta- and delta-giardin interactors. To create a protein priority list, we took all proteins which appeared in the anti-beta-giardin or anti-delta-giardin bead lists and averaged their intensity values across three repeats. Proteins who also appeared in the null bead list had their average null intensity subtracted from their anti-beta-giardin or anti-delta-giardin values. The adjusted intensity values were then sorted high to low, and the proteins with an intensity value of at least 1% of the highest hit were considered for further study (Figure 4.2A). Additional

prioritization factored in if proteins were of unknown function or contained structural domains. Known non-ventral disc proteins were excluded from further study.

Creation of N-terminally tagged Neon Green co-IP hit lines for novel protein localizations, as well as a Neon Green beta-tubulin line for observation of disc phenotypes in knockdown and knockout lines

A vector containing resistance to the antibiotic G418, the mNeonGreen gene without a stop codon, and a C18 linker immediately following mNeonGreen (gift of Alexander Paredez, University of Washington) was used as the base construct. Sequence of each individual co-IP hit with native terminator was PCR amplified from genomic DNA extracted from wild-type *Giardia* trophozoites. The gene sequence was inserted immediately after the C18 linker and plasmid sequence was confirmed by Sanger sequencing. Completed plasmids were electroporated into WBC6 *Giardia* cells as described above, and localization was determined by wide-field light microscopy.

Beta-tubulin sequence was amplified and inserted into plasmid as described above, and beta-tubulin sequence was confirmed by Sanger sequencing. Completed plasmids were electroporated into WBC6 *Giardia* cells as described above, and proper localization was confirmed by wide-field light microscopy.

Creation of the 15376 knockdown and knockout lines

Generation of dCas9 CRISPRi knockdown lines in *Giardia* and the dCas9/gRNA vector used was described by McInally[16]. Briefly, using the CRISPR 'Design and Analyze Guides' tool from Benchling (https://benchling.com/crispr), we selected 20 nt gRNA sequences with an NGG PAM sequence from the *Giardia lamblia* ATCC 50803 genome (GenBank Assembly GCA_000002435.1). The sequences selected and ordered targeted at site 47 bp from gene start, and were 15376KD Forward (5'-caaaCCAAGGGGTACAAGACACGG-3') and 15376KD

Reverse (5'-aaacCCGTGTCTTGTACCCCTTGG-3'). These include a four-base overhang to complement vector overhangs when annealed and ligated. After vector preparation, plasmids were electroporated into mNeonGreen-beta-tubulin tagged *Giardia* trophozoites as described above.

Generation of Cas9 CRISPR knockout lines in *Giardia* and the Cas9/gRNA vector used has been described by Hagen[17]. To summarize, the CRISPR 'Design and Analyze Guides' tool was used to obtain a suiTable 4.20 nt gRNA sequence with an NGG PAM. The following sequences were selected and synthesized in order to target a cut site immediately before the 46th bp from gene start: 15376KO Forward (5'-caaaACCCAGTAGATGCCCCCAAG-3') and 15376KO Reverse (5'-aaacCTTGGGGGCATCTACTGGGT-3').

To obtain HDR templates for a 15376 knockout line, we selected 750 bp up and downstream of the double stranded break site, and combined those sequences with either the blasticidin or hygromycin B gold cassette described by Hagen[17]. Mutations were made in the gRNA target site to stop Cas9 from cutting within the HDR. HDR templates were synthesized (Twist Bioscience), and the hygromycin HDR was further modified by PCR amplifying and inserting the N-terminally tagged Neon Green-beta-tubulin gene described above. Linear templates to use for electroporation were amplified via PCR reaction with Phusion DNA polymerase (New England Biolabs) and M13 Forward and Reverse primers. The resultant PCR product was purified and concentrated with a Zymo Research Clean and Concentrator-25 kit. To create the knockout line, the Cas9/gRNA plasmid, blasticidin HDR, and hygromycin HDR were electroporated sequentially into WBC6 *Giardia* cells.

To obtain clones of the 15376KO line post electroporation, we diluted cells and distributed them into a 96 well tissue culture plate (Corning) at 0.5 cells/well. Plates were incubated at 37°C in a Mitsubishi AnaeroPack 2.5L jar, with a Mitsubishi AnaeroPack-Anaero Gas Generator (ThermoScientific) for 7 days. Wells were screened for cell growth and plates

were incubated on ice for 1 hour to detach cells. Samples from each well with growth were screened by PCR for the presence of a quadruple KO, and the remainder was transferred to 8 ml culture tubes (BD Falcon) and incubated at 37°C. Upon reaching 50% confluence, cells were iced and 2 ml of trophozoites were transferred to a standard culture tube for continuous culturing as described above.

Immunofluorescence staining of 15376KD/KO and control lines

Initial fixation of *Giardia* cells for immunofluorescent staining and microscopic analysis was either performed on coverslips after cells attached live or fixation occurred by the addition of fixative to cells growing in culture medium and subsequently settled on coverslips. Confluent tubes of *Giardia* trophozoites were iced for 15 minutes, then spun at 900 x g for 5 minutes. Cells were washed three times with 5 ml HEPES-buffered saline (HBS, 137 mM NaCl, 21 mM HEPES, 5.55 mM glucose, 5 mM KCl, 0.76 mM Na_2HPO_4) and resuspended in 1 ml of HBS. Next, cells were transferred to coverslips placed inside an eight well plate at a volume of 500 µl per coverslip. Cells attached to coverslips inside a humidified chamber for 20 minutes at 37°C. Following coverslip adherence, HBS was aspirated, and 2 ml of 4% paraformaldehyde in HBS, pH 7.4 and warmed to 37°C, was added onto each coverslip. Fixation proceeded for 2 minutes, before the paraformaldehyde solution was aspirated and coverslips were washed three times with 2 ml PEM (100 mM PIPES [piperazine-N,N'-bis(2-ethanesulfonic acid)], 1 mM EGTA, 0.1 mM $MgSO_4$ pH 6.9).

Alternatively, to fix *Giardia* in a culture tube before adding to coverslips, 375 µl of 32% paraformaldehyde was added to a culture tube (1% final concentration) and incubated for 10 minutes at 37°C. Following this, the tube was spun down at 900 x g for 5 minutes, and washed once with HBS. Cells were resuspended in 1 ml of HBS and added to two precoated poly-L-lysine coverslips, at a volume of 500 µl per coverslip, for 15 minutes at room temperature. Coverslips were then washed three times with 2 ml PEM.

From here on, both fixation conditions follow the same protocol. Residual paraformaldehyde in fixed, washed cells was quenched for 5 minutes via incubation in 0.125 M glycine at room temperature. Coverslips were washed three times with PEM, and permeabilized with 0.1% Triton X-100 for 10 minutes. Cells were washed again three times with PEM, and blocked with 2 ml PEMBLG (PEM with 1% bovine serum albumin, 100 mM lysine, 0.5% cold-water fish skin gelatin [Sigma, St Louis, MO]) for 30 minutes. Staining with primary antibody took place overnight at 4°C in one or more of the following antibodies: anti-beta-giardin (1:1000), anti-delta-giardin (1:1000), or anti-TAT1 (1:500). Anti-beta and delta-giardin are gifts of Mark Jenkins, USDA, and anti-TAT1 is a mouse monoclonal antibody against alpha-tubulin, and a gift of Keith Gull (University of Oxford, UK). The next morning, coverslips were washed three times in PEMBLG and secondary antibody stain occurred for 3 hours at room temperature, in the dark, with goat anti-rabbit and/or goat anti-mouse Alexa Flour 488, 594, or 647 antibodies (1:1000, Life Technologies). Finally, coverslips were washed three times with PEMBLG, three times with PEM and mounted in Prolong Diamond antifade reagent (Invitrogen). All imaging experiments were performed with at least three biologically independent samples.

Acquisition of wide-field fluorescence images and 3D SIM super-resolution images

Single or multi-focal plane images were acquired with a Leica DMI 6000 wide-field inverted fluorescence microscope, using the 100x or 40x objective, and μManager image acquisition software.

To obtain super-resolution images of fluorescently tagged 15376KD or KO cell lines, 3D stacks were collected at 0.1 μm intervals using a Nikon N Structured Illumination Super-resolution Microscope with a 100x/NA 1.49 objective, 100 EX V-R diffraction grating, and an Andor iXon3 DU-897E EMCCD. Images were acquired and reconstructed using NIS-Elements software (Nikon), in the “3D-SIM” mode. Images were reconstructed in the “Reconstruct Slice” mode and were only used if the score was 8.

Quantifying attachment and resistance to shear flow forces

Giardia trophozoites were cultured in 12 ml culture medium until full confluency. Cells were iced for 15 minutes, washed with HBS, and stained with CellMask orange (ThermoFisher) for 10 minutes. Cells were then washed with HBS and added to an Ibidi mSlide VI 0.4 flow chamber. Images of cells at a concentration of 2 million per ml were taken with a 40x objective on a Leica DMI 6000 wide-field microscope. Fluorescent images were acquired of attached cells before and after flow challenge for 20 seconds at a rate of 3 ml/minute. DIC images were taken at a rate of 1 per second for 20 seconds pre-challenge, during challenge, and for 20 seconds post-challenge. Cells were permitted to attach for 5 minutes prior to challenge. Pre and post-challenge fluorescence images were compared; cells that remained in place were considered resisting flow, cells that did not remain in place were unable to resist flow.

Biochemical extraction of the ventral disc

In order to obtain clear immunofluorescent staining of the ventral disc microtubule spiral, we performed a biochemical disc isolation as previously described[4,11]. One tube of *Giardia* trophozoites per cell line were cultured as described above until fully confluent. Cells were then washed with HBS and resuspended in 1 ml of 0.5x HBS/1x PHEM (60 mM PIPES, 25 mM HEPES, 10 mM EGTA, 1 mM $MgCl_2$, pH 7.4) containing 1% Triton X-100, 1 M KCl and 1× HALT protease inhibitor cocktail (Roche). The resuspensions were transferred to 1.8 ml Eppendorf tubes and vortexed for 30 min (VWR Vortex-Genie2, vortex speed setting at 5) to extract cytoskeletons. Extracted cytoskeletons were centrifuged at 3000 x g for 5 minutes. The supernatant was discarded and the pellets were washed twice in 1 ml 0.5x HBS/1x PHEM, before being resuspended in 1 ml 0.5x HBS/1x PHEM. 500 µl of the isolated cytoskeletons was added each to two poly-L-lysine treated coverslips and settled for 15 minutes. The cytoskeletal preparations were fixed with 4% paraformaldehyde in HBS for 2 minutes and quenched with 250 mM glycine for 5 minutes, before proceeding with the remaining immunofluorescence protocol.

Prep and Nanopore sequencing to confirm quadruple KO of 15376

In order to confirm a quadruple KO of the 15376 gene in our 15376KO cells, we extracted genomic DNA from one tube of confluent cells using a Quick-DNA Miniprep Plus Kit (Zymo Research). Genomic DNA was amplified via PCR targeting sequences just outside of the HDR cassette. Specifically, the primers used were 15376LeftF (5'-GCATAAACATGCCGTTGCGAC-3'), and 15376RightR (5'-ACTATCCTTTGGGTCCGTGGC-3'). Amplified linear DNA was column purified and concentrated by a DNA Clean & Concentrator-25 kit (Zymo Research), and sent to the UC Berkeley DNA Sequencing Facility at the University of California, Berkeley for nanopore sequencing. 15376KO sequencing reads were compared to wild-type 15376 gene sequence using the Integrative Genome Viewer (igv.org).

Acknowledgements

This work was supported by an R01AI077571 award to SCD. We graciously thank the UC Davis MCB Microscopy Core for helpful advice on the SIM microscopes. We also thank the UC Davis Proteomics Core for performing the Mass Spectroscopy analysis. Finally, we thank Katie Chun, Alec Juliano, and Lawrence Fang for their contributions to this work.

Figures

Figure 4.1: A co-immunoprecipitation assay was performed on beta-giardin and delta-giardin

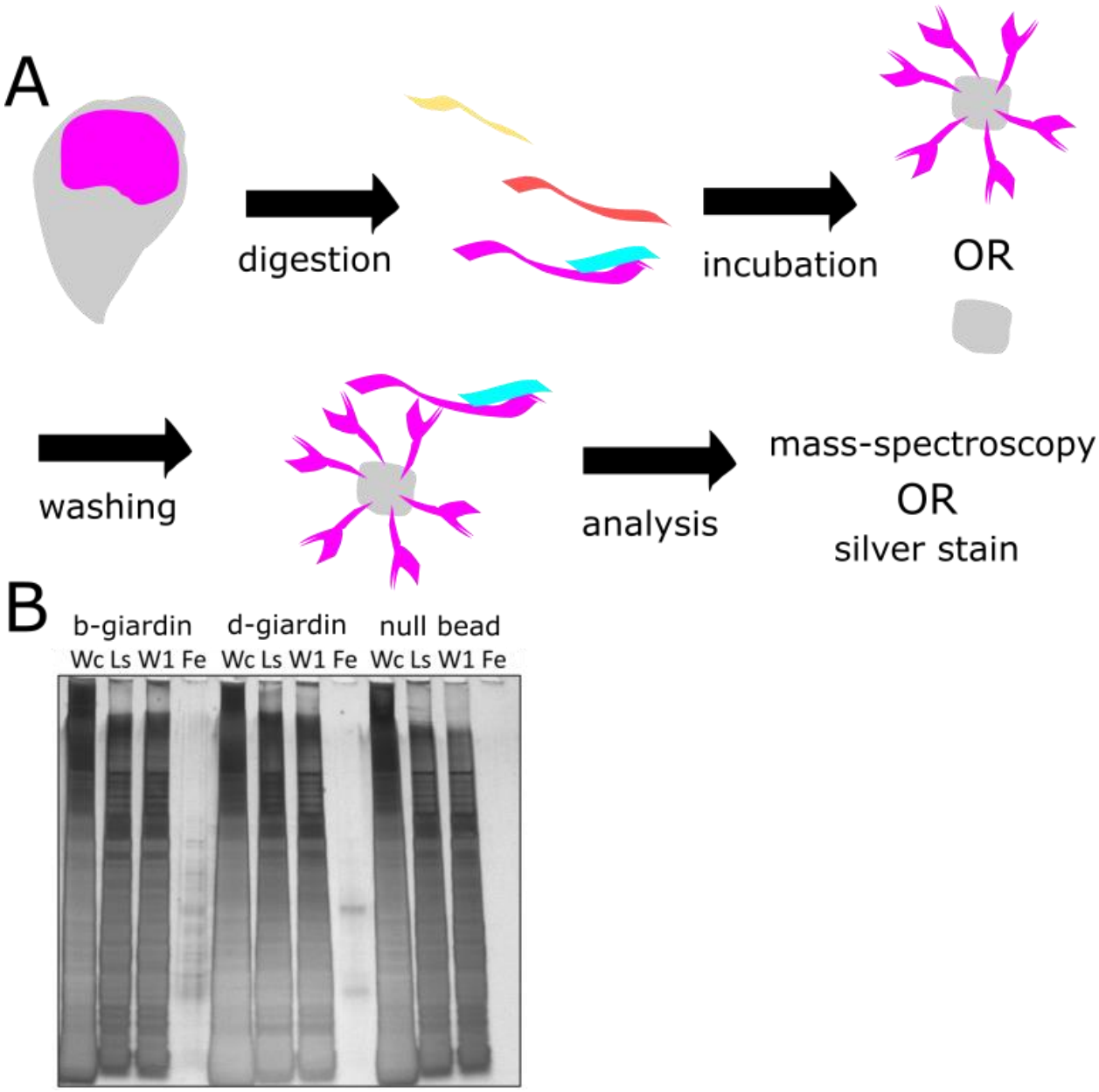

To obtain a list of potential novel MR-CB proteins, a co-immunoprecipitation (co-IP) assay using magnetic beads conjugated to either anti-beta-giardin or anti-delta-giardin was performed. Unconjugated beads were used as a negative control. A) Schematic representation of the steps

in the co-IP assay. Cells were digested and incubated with conjugated or unconjugated beads, followed by washing and either mass-spectroscopy or silver stain analysis. B) Silver stain of fractions taken during co-IP assay. Protein content in whole cell (Wc), lysate supernatant (Ls), and wash 1 (W1) is much higher than in the final eluate (Fe). Bands can be seen in the Fe column of the beta-giardin and delta-giardin beads, but not the unconjugated beads (null bead).

Figure 4.2: Top hits from co-IP assay were ranked and selected for further analysis

A

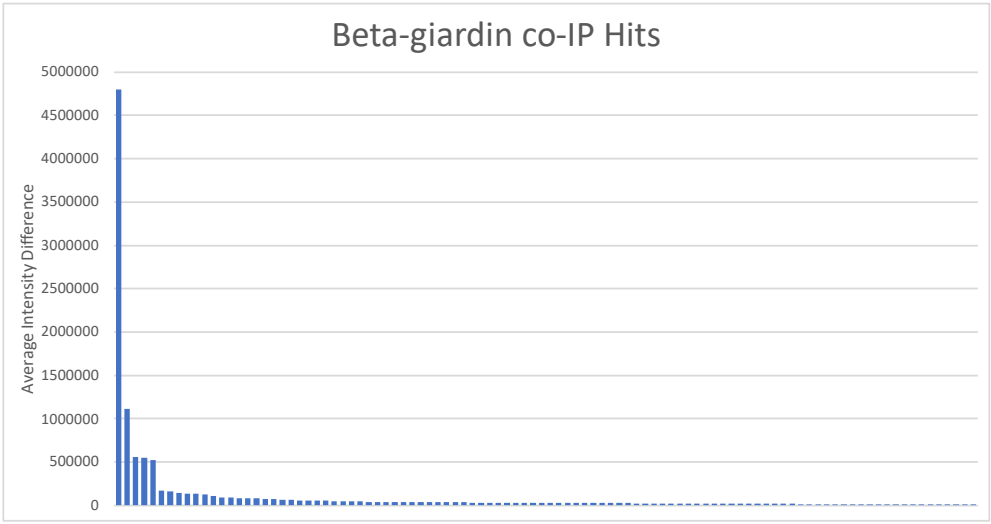

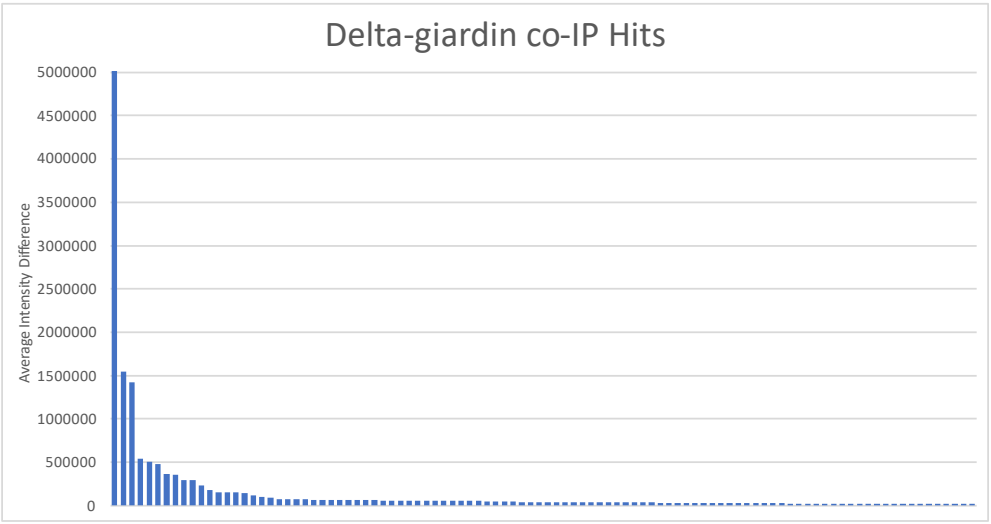

B

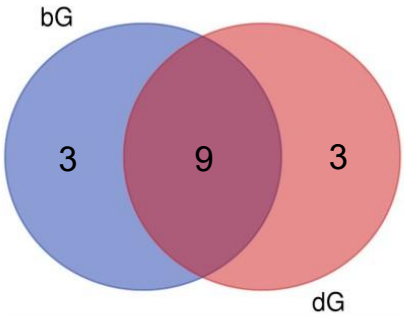

Beta-giardin hits	
DAP12139	GL50803_5859
GL50803_16844	

Overlapping hits	
SALP1	Beta-giardin
Gamma-giardin	Delta-giardin
Actin	GL50803_7233
GL50803_31743	GL50803_92132
GL50803_103205	

Delta-giardin hits	
GL50803_15376	GL50803_16443
GL50803_21628	

Proteins found in mass-spectroscopy analysis of co-IP were assigned an intensity value for each bead condition (beta-giardin, delta-giardin, null bead) repeat. Bead conditions were performed three times each. Intensity values corresponded to number of peptides identified for each protein, as well as size of those peptides. A) Intensity values for each bead condition were averaged for each protein, and the null intensities were subtracted from beta-giardin and delta-giardin intensities. Proteins were then ranked based on this average intensity difference. A few high ranking, high intensity proteins can be seen when visualized via a histogram. B) Proteins with an average intensity difference of at least 1% of the number one hit in the beta-giardin, delta-giardin, or both conditions are shown here. Of the 15 identified top hits, 9 are novel, 5 are known disc proteins, and the remaining protein is actin, which is unconfirmed to be part of the disc.

Figure 4.3: Tagging top hits from co-IP screen with a fluorescent marker reveals a variety of localizations

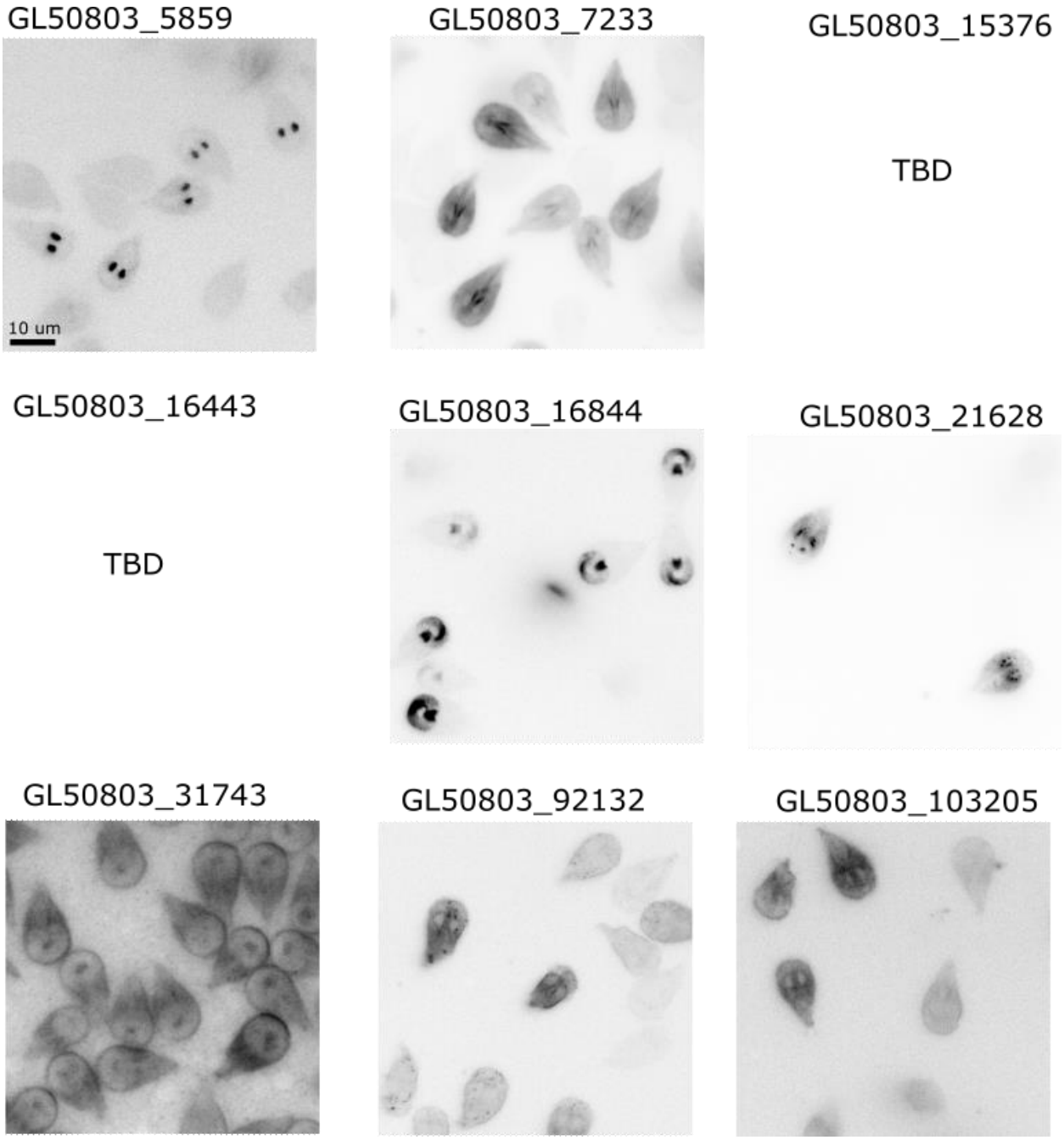

Novel co-IP hits were C-terminally tagged with mNeon-Green and expressed episomally in wild-type *Giardia*. GL50803_16844 localized to the ventral disc. Two proteins, GL50803_15376 and GL50803_16443 were unable to be cloned and currently remain unlocalized. GL50803_5859

and GL50803_21628 both localized to the nuclei, GL50803_7233 localized to basal bodies of the caudal flagella, GL50803_31743 localized to the plasma membrane, and GL50803_92132 and GL50803_103205 localized to the cytoplasm.

Figure 4.4: Confirmation of 15376 quadruple KO in 15376KO cells by nanopore sequencing

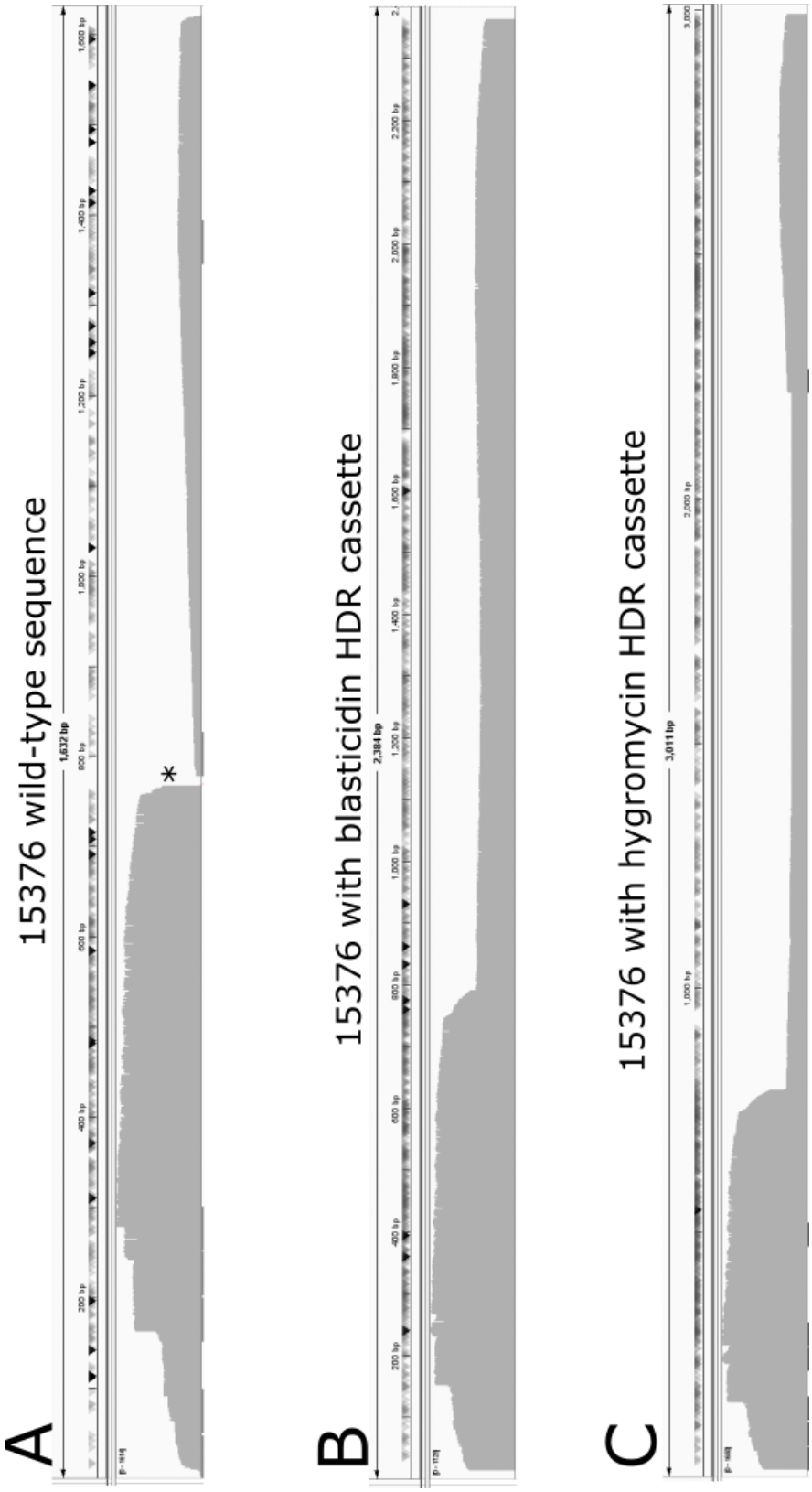

15376KO genomic DNA was sent for nanopore sequencing to confirm quadruple KO. Sequence reads were mapped to (A) 15376 wild-type sequence, (B) blasticidin HDR cassette, or (C) hygromycin HDR cassette (see Methods). The star in (A) marks the site at which the HDR cassettes were inserted; no reads bridge this region, confirming cassette insertion in all 15376 gene copies.

Figure 4.5: 15376KD and 15376KO show disruption of disc structure

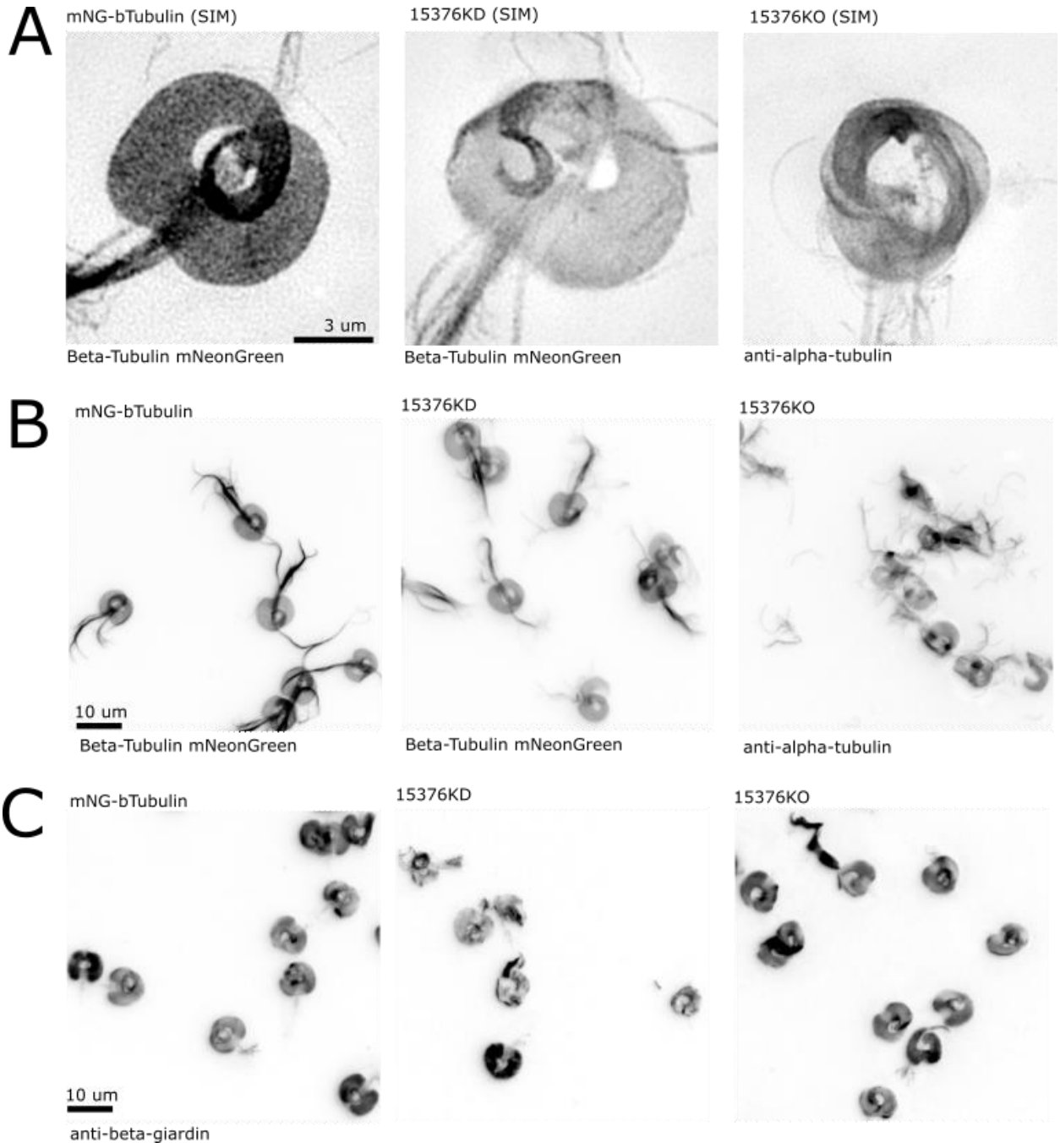

D

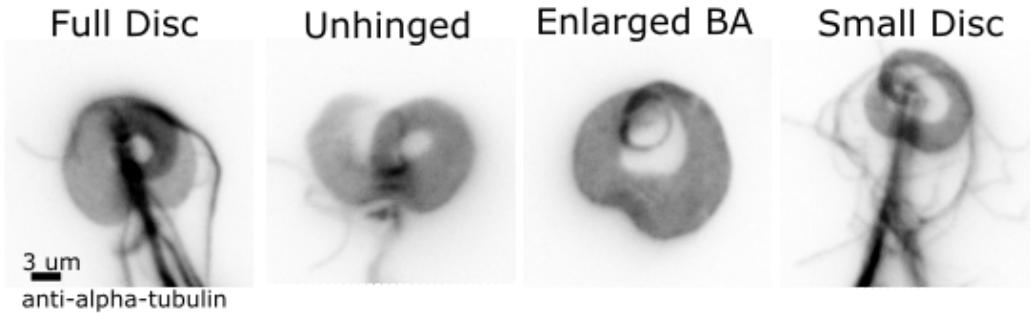

mNG-bTubulin	76.9%	12.0%	3.7%	7.4%
15376KD	76.4%	15.4%	4.1%	4.1%
15276KO	29.3%	57.9%	3.8%	9.0%

E

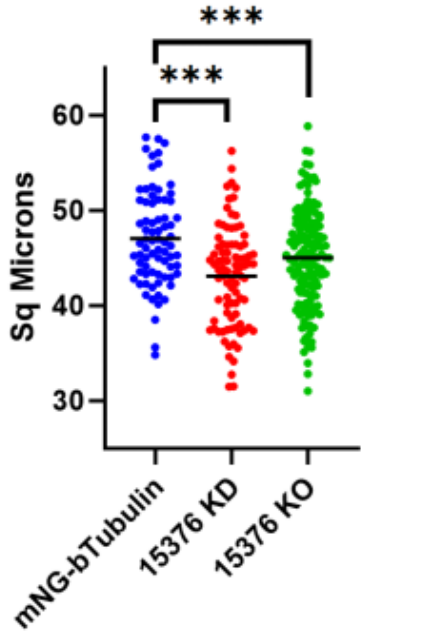

F

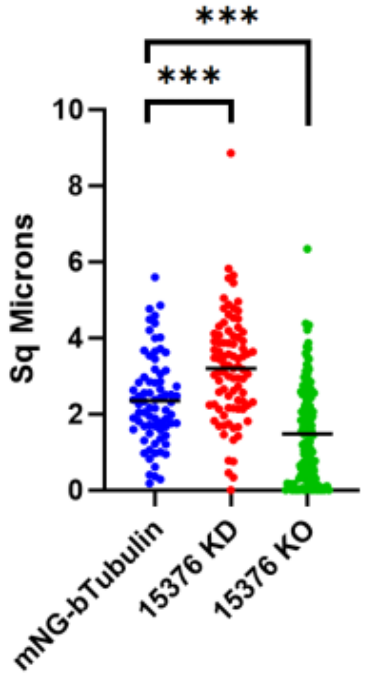

G

AlphaFold Prediction of 15376 Structure

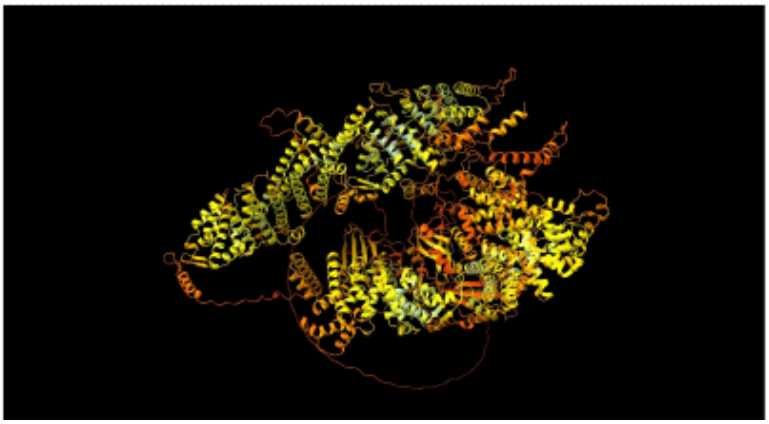

15376 was targeted with a CRISPRi KD and a CRISPR KO to functionally assess its role in disc stability. A) Structured Illumination Microscopy (SIM) imaging of mNG-bTubulin, 15376KD and 15376KO extracted cytoskeletons to illustrate a broken disc spiral. mNG-bTubulin and 15376KD were unstained, while 15376KO cytoskeletons were stained with anti-alpha-tubulin. B) Wide-field image of mNG-bTubulin, 15376KD and 15376KO extracted cytoskeletons. mNG-bTubulin and 15376KD were unstained, while 15376KO cytoskeletons were stained with anti-alpha-tubulin. C) Wide-field images of the three aforementioned lines, stained with anti-beta-giardin to demonstrate consistency in appearance between the MT spiral and microribbons. D) Phenotype analysis of the three cell lines was performed on unstained (mNG-bTubulin and 15376KD) or anti-alpha-tubulin stained (15376KO) cytoskeletons. Discs were classified as the following: disc with full structure present, indistinguishable from wild-type (Full Disc); intact arms of spiral, but overlap zone has come undone (Unhinged); enlarged bare area in middle of disc (Enlarged BA); loss of disc material from the exterior inward (Small Disc). E) Disc area measurements were taken in Fiji (ImageJ) using the “Thresholding” and “Particle Analysis” features, excluding the space left by the bare area. Area measurements were performed using whole cells, unstained mNG-bTubulin and 15376KD, and anti-alpha-tubulin stained 15376KO. *** represents p value <0.001. G) Area of the bare area was also measured using the same functions as in (E). G) AlphaFold prediction of 15376 structure.

Figure 4.6: 15376KO cells are not worse at resisting flow challenge when compared to a mNG-bTubulin negative control

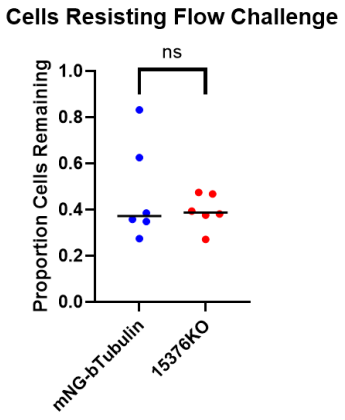

A biophysical flow assay was performed to asses the ability of 15376KO cells to remain attached when challenged with shear flow stress. 15376KO cells clustered at resisting flow at approximately 40% of the time, while the mNG-bTubulin cells were highly variable. No significant difference was detected between these two cell lines.

Table 4.1: descriptions and intensity values for top co-IP hits

Description	**Accession code**	**Average null intensity**	**Average beta-giardin intensity**	**Average delta-giardin intensity**
SALP-1	GL50803_4410	10518.94533	571892.6233	485466.32
Beta-giardin	GL50803_4812	65557.33433	4866459.867	6508207.167
Uncharacterized protein	GL50803_5859	0	136169.2333	38973.39667
Uncharacterized protein	GL50803_7233	8946.481667	116489.6967	191816.455

DAP12139 ankyrin repeat protein	GL50803_12139	0	72534.67267	22491.84
Uncharacterized protein	GL50803_15376	69719.27	8479.190667	1493161.833
Protein phosphatase 2A B' regulatory subunit Wdb1	GL50803_16443	154463.55	0	383495.5333
Uncharacterized protein	GL50803_16844	0	33452.028	24990.45833
Gamma giardin	GL50803_17230	38478.36633	1155164.033	1580788.2
Uncharacterized protein	GL50803_21628	91587.55967	106381.125	444621.0467
Uncharacterized protein	GL50803_31743	0	62461.54667	71513.46567
Actin related protein	GL50803_40817	14084.23833	140368.5123	164862.0833
Delta giardin	GL50803_86676	34303.582	579685.1433	578532.36
Uncharacterized protein	GL50803_92132	0	526909.85	502603.1033
Uncharacterized protein	GL50803_103205	0	51283.219	67452.33

References

1. Einarsson, E., Ma'ayeh, S. & Svärd, S. G. An up-date on Giardia and giardiasis. *Curr. Opin. Microbiol.* **34**, 47–52 (2016).

2. Nosala, C., Hagen, K. D. & Dawson, S. C. 'Disc-o-Fever': Getting Down with Giardia's Groovy Microtubule Organelle. *Trends Cell Biol.* **28**, 99–112 (2018).

3. Holberton, D. V. Attachment of *Giardia* - A Hydrodynamic Model Based on Flagellar Activity. *J. Exp. Biol.* **60**, 207–221 (1974).

4. Nosala, C. *et al.* Disc-associated proteins (DAPs) mediate the unusual hyperstability of *Giardia* 's ventral disc. *J. Cell Sci.* jcs.227355 (2020) doi:10.1242/jcs.227355.

5. Dawson, S. C. *et al.* Kinesin-13 Regulates Flagellar, Interphase, and Mitotic Microtubule Dynamics in *Giardia intestinalis*. *Eukaryot. Cell* **6**, 2354–2364 (2007).

6. Holberton, D. V. & Ward, A. P. Isolation of the cytoskeleton from *Giardia* . tubulin and a low-molecular-weight protein associated with microribbon structures. *J. Cell Sci.* **47**, 139–166 (1981).

7. Holberton, D. V. Arrangement of subunits in microribbons from *Giardia*. *J. Cell Sci.* **47**, 167–185 (1981).

8. Schwartz, C. L., Heumann, J. M., Dawson, S. C. & Hoenger, A. A Detailed, Hierarchical Study of Giardia lamblia's Ventral Disc Reveals Novel Microtubule-Associated Protein Complexes. *PLoS ONE* **7**, e43783 (2012).

9. Brown, J. R., Schwartz, C. L., Heumann, J. M., Dawson, S. C. & Hoenger, A. A detailed look at the cytoskeletal architecture of the Giardia lamblia ventral disc. *J. Struct. Biol.* **194**, 38–48 (2016).

10. Crossley, R. & Holberton, D. V. Characterization of proteins from the cytoskeleton of *Giardia lamblia*. *J. Cell Sci.* **59**, 81–103 (1983).

11. Hagen, K. D. *et al.* Novel Structural Components of the Ventral Disc and Lateral Crest in Giardia intestinalis. *PLoS Negl. Trop. Dis.* **5**, e1442 (2011).

12. Holberton, D. V. Fine structure of the ventral disk apparatus and the mechanism of attachment in the flagellate *Giardia muris*. *J. Cell Sci.* **13**, 11–41 (1973).

13. Nosala, C. *et al.* Dynamic ventral disc contraction is necessary for *Giardia* attachment and host pathology. Preprint at https://doi.org/10.1101/2023.07.04.547600 (2023).

14. Palm, D. *et al.* Developmental changes in the adhesive disk during Giardia differentiation. *Mol. Biochem. Parasitol.* **141**, 199–207 (2005).

15. Kim, J. & Park, S.-J. Role of gamma-giardin in ventral disc formation of Giardia lamblia. *Parasit. Vectors* **12**, 227 (2019).

16. McInally, S. G. *et al.* Robust and sTable 4.transcriptional repression in *Giardia* using CRISPRi. *Mol. Biol. Cell* **30**, 119–130 (2019).

17. Hagen, K. *et al.* The domed architecture of *Giardia* 's ventral disc is necessary for attachment and host pathogenesis. Preprint at https://doi.org/10.1101/2023.07.02.547441 (2023).

18. Lechtreck, K. F. & Melkonian, M. Striated microtubule-associated fibers: identification of assemblin, a novel 34-kD protein that forms paracrystals of 2-nm filaments in vitro. *J. Cell Biol.* **115**, 705–716 (1991).